DISPERSIVE FOURIER TRANSFORM SPECTROSCOPY IN THE FAR INFRARED

DAVID ANTHONY LEDSHAM

A Thesis submitted for the internal Degree of Doctor of Philosophy (Ph D) in the Faculty of Science, University of London

July 1977

ABSTRACT

The technique of dispersive Fourier transform spectroscopy (DFTS) permits the direct measurement of phase spectra, and thus removes a major limitation of conventional spectroscopy where the phase, which is required to determine the dielectric response, must be derived from a Kramers-Krönig analysis of the measured power reflectivity. DFTS studies between 300K and 100K using interferometers equipped with dielectric beam dividers have recently been reported, but the performance of such instruments at frequencies less than about 30 cm^{-1} is seriously impaired by interference effects in the dividers.

The acquisition of accurate data from this region is extremely important when investigating phase transitions in ferroelectric crystals such as KH_2PO_4 (KDP), characterised by a 'soft' mode whose frequency $\omega_i \rightarrow 0$. The development of polarising interferometers employing wire grid beam dividers has made low frequency dispersive studies feasible, although such measurements have been previously made only at ambient temperature.

In the present work a dispersive polarising interferometer has been constructed. The instrument has a working range of 20 - 235 cm^{-1} when used with a Golay detector and this can be extended to $\sim$ 2 cm^{-1} by using a liquid helium cooled Ge bolometer. The sample temperature may be held to $\sim$ ±0.1K anywhere between 90K and 300K. Consequently the interferometer permits low frequency temperature dependent DFTS studies of solids for the first time, simultaneously overcoming all the aforementioned problems.

The performance of the instrument was evaluated by measuring the complex reflectivity of CsI and CsBr at 100K and 300K. The results agree well with published data.

The complex reflectivity of KDP was measured from 300K down towards

the ferroelectric transition at 122K. The resultant 'c' axis dielectric functions were analysed in terms of the coupled mode formalism adopted by previous workers, whose work is briefly reviewed. The results are supplemented by transmission measurements performed with a conventional power interferometer on thin KDP crystals, whose 'c' axis spectra were found to exhibit a temperature dependent transmission window. Complex reflectivity spectra of antiferroelectric $NH_4H_2PO_4$ (ADP) are also presented.

The results illustrate the advantages to be obtained by using dispersive Fourier transform spectroscopy when accurate values of the complex dielectric response are required.

ACKNOWLEDGEMENTS

My sincerest thanks first go to Dr T J Parker for suggesting and supervising this research project and for his consistent help and encouragement. He has enlightened me through many discussions and rarely failed to provide solutions to the numerous problems I have laid before him.

I am greatly indebted to Dr G A Gledhill for the use of his interferometer, for much advice and for lessons in the game of squash. Thanks are also due to Dr W G Chambers for his enthusiastic help in all aspects of the computational work and to Dr J F Angress for thoughtful discussions from which I have greatly benefited.

It is a pleasure to thank the technical staff of the Physics Department for their invaluable assistance. Particular thanks are due to Mr P Heaver, the Chief Technician, Messrs J Oliver, J Beadle and W Howard of the engineering workshop, M Curati and E Dorfman of the electronics workshop and Mr R Collins for the unenviable task of crystal polishing.

I acknowledge also the help of Dr R W Martin for growing some of the KDP crystals, Mr J R Birch of the National Physical Laboratory for the loan of much equipment and Miss P Hultum for typing this manuscript.

I am exceedingly grateful for the tremendous support given me by my family and thank certain close friends for bearing with me for so long through some extremely difficult times.

To all these people, and others I have failed to mention, without whom completion of this work would have been impossible, I again express my most sincere gratitude.

I would finally like to acknowledge the financial support of the Science Research Council.

CONTENTS

CHAPTER 1

INTRODUCTION

The science of spectroscopy has its origins in the experiments of Sir Isaac Newton who produced an array of the colours of the rainbow on a screen by refracting sunlight with a glass prism. Nowadays spectroscopy is performed throughout the electromagnetic spectrum from radiowaves through to γ-rays and is an extremely important tool of the physicist.

Spectroscopy has proved invaluable in gaining an insight into the lattice dynamics of materials and provides information on many of their important physical properties, including the specific heat and the thermal and electrical conductivities. The foundations of the rigorous theory of lattice vibrations and the calculation of the possible modes of vibration of atomic lattices were laid at the beginning of this century by Born and Von Karman[1]. Their work followed earlier theories by Einstein[2] and Debye[3] and in their simplest model of a linear chain of equidistantly spaced atoms of identical mass the interatomic force constant and the atomic mass determine a maximum frequency that may be propagated through the chain. This frequency is of the order of 10^{13} Hz and thus lies in the infrared region of the spectrum. Hence even the simple linear chain model indicates the importance of IR experimental studies to obtain information on lattice dynamics.

However, until about 1950, the infrared region of the spectrum, and in particular the extreme infrared, was one of the most inaccessible to the spectroscopist due to the severe technical difficulties encountered when attempting measurements in this region. All this began to change with developments in IR sources and detectors, improvements in IR grating spectroscopy and later, the development of Fourier transform spectroscopy,

a technique which became feasible with the advent of the computer age. In future years, the tunable laser, which is at present under intense development, might prove to be the most powerful technique available for IR measurements, superceding the majority, if not all, of the techniques in present-day use.

Fourier transform spectroscopy (hereafter abbreviated to FTS) using Michelson-type interferometers, has been used to measure the IR power spectra of numerous solids, liquids and gases during the last decade and has become an extremely popular and valuable technique in the study of the vibrational properties of materials. Conventional power FTS does, however, have one particular disadvantage, a disadvantage suffered also by grating spectroscopy. Phase spectra, required to calculate the optical constants and the related dielectric functions, are not measured directly but must be constructed from a Kramers-Krönig (KK) mathematical analysis of the measured power spectra. Such an analysis is inevitably an approximate procedure when applied to the truncated spectral range covered in any FTS experiment.

The construction of phase spectra by KK analysis has proved successful in some experiments where data has been available from a wide spectral range by combining results obtained using FT and grating spectrometers. However, the method is inadequate for studies where accurate phase values are required over a restricted spectral range, particularly at frequencies near the truncation. An important example of such studies is the investigation of the phase transition in ferroelectric materials where temperature dependent changes in the optical constant and dielectric function values must be monitored via small changes, often $\sim 1^{\circ}$, in the measured phase spectra.

Recent years have seen the development of a major new technique in the field of FTS, a technique known as dispersive Fourier transform

spectroscopy (DFTS). The principal difference between this and conventional "power" FTS is that the sample under investigation is introduced into the optical path in one arm of the interferometer. This enables the complex reflectivity or transmissivity, that is both the amplitude and phase spectra, to be measured. The optical constants can then be determined from the measured phase spectra, thus avoiding the need for a KK analysis.

The technique of DFTS has been used by a number of workers to make ambient temperature measurements of solids, liquids and gases. The pioneering workers include Bell[4], Genzel (see for example Gast et al[5]) and Chamberlain[6]. Later measurements have been performed by Birch et al[7] and Gauss et al[8]. Measurements below ambient temperature introduce further difficulties which have however been overcome by Parker et al[9-12] who have performed DFTS studies down to 90K using an interferometer equipped with a dielectric beam divider. These additional problems were largely solved by use of an experimental technique termed the division of the field of view. This technique and the problems it solves are discussed in Chapter 4 of this thesis.

For many studies in solid state physics the ability to make measurements over a wide temperature range is important. In addition it is often extremely important to obtain data from the low frequency end of the far IR spectrum. This is particularly true for many ferroelectric materials since much of the information required to explain the mechanism of the phase transition, from paraelectric to ferroelectric, lies in this spectral region. However, the performance below $\sim$ 30 cm^{-1}, of interferometers equipped with dielectric beam dividers is seriously impaired by interference effects in the dividers. The effects lead to a strongly frequency-dependent transmissivity, rising from zero at zero frequency to a maximum and falling to zero again at a frequency inversely proportional to the beam divider thickness.

To overcome these difficulties Martin[13] devised a polarising interferometer employing wire grid beam dividers with a constant transmissivity up to a frequency inversely proportional to the grid spacing. The author has built a polarising interferometer for far IR reflection studies which employs two wire grid beam dividers in a configuration similar to that developed by Chamberlain[6]. The instrument has a working range of 20 - 235 cm^{-1} when used with a Golay detector and this can be extended to $\sim$ 2 cm^{-1} by using a liquid helium cooled Ge bolometer.

The design of the instrument permits measurements to be performed at any temperature between 90K and 300K. Thus the interferometer allows low frequency temperature dependent DFTS studies of solids to be made for the first time. Descriptions of the polarising interferometer and the severe technical problems involved in its construction are presented in Chapter 4.

Initial measurements made with the polarising interferometer were of the complex reflectivity spectra of the alkali halides CsBr and CsI. These materials were chosen partly because the reststrahlen band of each lies comfortably within the working range of the instrument and partly because their reflection spectra are comparatively well known from power measurements.

The main subject of study was the ferroelectric KH_2PO_4 (KDP) which has been investigated previously by a number of workers using Raman scattering techniques, grating spectroscopy and power FTS. The transition in KDP is characterised by a soft mode whose frequency $\omega_i \rightarrow 0$. Thus, use of a polarising interferometer is highly desirable when DFTS studies of KDP are being considered in order that the mode may be tracked into the low frequency region below $\sim$ 30 cm^{-1}, as the temperature is lowered towards the transition. Previcus work on KDP, both experimental and theoretical, is reviewed in Chapter 5.

The complex reflectivity spectrum of the KDP ferroelectric 'c' axis was measured from 300K down towards the transition temperature at 123K. The ensuing dielectric functions exhibit the expected soft mode behaviour and were analysed in terms of the coupled mode formalism of Barker and Hopfield[14]. These results are presented, discussed and compared to those obtained by other workers in Chapter 6. Room temperature measurements of the complex reflectivity spectra of the 'a' axis of KDP and both axes of antiferroelectric $NH_4H_2PO_4$ (ADP) are also presented.

The KDP results obtained with the polarising interferometer were supplemented by power transmission and reflection studies of KDP. These measurements were made from 300K down to below the transition temperature using a conventional interferometer with a mylar beam divider. The transmission measurements were made on thin crystals of KDP, the 'c' axis of which was found to exhibit a temperature dependent transmission window. This enabled a check to be made, in the region of the spectral window, on the accuracy of the phase values which were obtained directly using the polarising interferometer. These power FTS studies are described and the results presented and discussed in Chapter 7.

CHAPTER 2

THE THEORY OF FOURIER TRANSFORM SPECTROSCOPY

2.1 INTRODUCTION

The aim of this chapter is to give a brief description of the method of FTS. Following a few general comments on the technique, an outline of the theory involved is presented. The concepts of resolution, resolving power, étendue, apodisation, aliasing and the Fellgett and Jacquinot advantages, amongst others, are introduced and defined. The chapter is concluded with a discussion of the advanced technique of DFTS.

Throughout the chapter comparisons are made with the theory of a grating spectrometer to clarify certain points and to illustrate the advantages and disadvantages of the FTS method.

Much of the theoretical detail is omitted for the sake of brevity but can readily be found in various books; in particular an excellent review of FTS by Bell[15] and the Proceedings of the 1970 International Conference on Fourier Spectroscopy at Aspen, Colorado[16].

In describing the theory of FTS it is necessary from time to time to mention certain details of the apparatus used. The discussions in this chapter consequently assume an elementary knowledge of the Michelson interferometer, a knowledge which may be obtained from a vast number of sources including the majority of text books on optics.

The chief reason for the sudden rise of FTS to the front line of solid state experimental research lies with one of the basic procedures the method involves. The output from the optical instrument, in general a Michelson-type interferometer or one of its variants, is obtained in the form of an interferogram, a plot of recorded signal versus optical path difference, the path difference being related to the relative displacement

of the two mirrors in the two arms of the interferometer. This interferogram must undergo a point-by-point mathematical Fourier transformation to obtain the required spectral information. The task of performing this FT procedure by hand calculation was far too daunting a prospect to make FTS a viable proposition, until the advent of computers. Now, advances in program development and in particular the Fast Fourier transform algorithm, have turned this once mammoth task into a computational procedure which can be performed in a fraction of a second.

In conventional "power" FTS the role of the Michelson is similar to that of the IR grating spectrometer in that it defines a throughput spectrum $P(\nu)$, the intensity of IR radiation as a function of frequency. The profile of this power spectrum, which essentially dictates the pass-band of the instrument, is fixed by features in the instrumental design, the use of filters and the mode of operation of the recording electronics. Some of these factors which define the spectral profile are undesirable but are, unfortunately, in many cases unavoidable.

The throughput radiation from the Michelson is caused to be incident upon the sample under investigation and the output optics arranged so as to obtain either the power reflection or the power transmission spectrum by FT of the resulting interferogram. The phase spectrum is then obtained from the experimental power spectrum by use of a Kramers-Krönig (KK) mathematical analysis, the essential equations of which are presented in section 3.7. Information on the optical constants and the related dielectric parameters is then obtained using the Fresnel equations which are derived in section 3.4.

2.2 THE BASIC INTEGRAL FOR POWER FTS

On displacement of the moving mirror in one arm of the Michelson, each wavelength present produces its own characteristic interferogram. For a monochromatic source the flux of the combined radiation from the two arms is a cosine variation, a well-known FT result.

For a polychromatic source the interferogram is the sum of the fluxes of the patterns produced by each wavelength. The method of Fourier analysis unscrambles this interferogram to obtain the pattern for each frequency, and hence determines the magnitude of the flux at that frequency, the Fourier coefficient. Thus a record of signal versus frequency, ie a spectrum, is obtained.

The two coherent waves in the two arms of the interferometer, each a continuous distribution of frequencies, which have the same amplitude $g(\nu)$ at wave number ν and which are separated by a phase difference $2\pi\nu x$ where x is the optical path difference between the two waves, can be expressed as

$$E_1(z) = \int_{-\infty}^{\infty} g(\nu) \exp[2\pi i\nu z] \, d\nu$$

$$E_2(z) = \int_{-\infty}^{\infty} g(\nu) \exp[2\pi i\nu(z+x)] \, d\nu \qquad (2.1)$$

where z is the parameter defining position in the interferometer arms.

Providing the response of the system to a disturbance is linear, the principle of Linear Superposition can be applied to define the resultant field of the recombined waves in terms of the amplitude $g(\nu)$.

However, it is not the amplitude of the field but its intensity which is required in order to obtain an expression for the power spectrum. To derive such an expression an assumption must be made before we can justify applying the principle of Linear Superposition to the beam intensities.

We must assume that all wave packets in the beams are identical and

that they are both closely and randomly spaced in time, ie there is no phase relation between the fluxes of different frequencies at a given path difference from a polychromatic source.

We can then derive the basic equation of power FTS giving the intensity of the interferogram I(x) in terms of the power spectrum P(ν) (Bell[15])

$$I(x) = \int_0^\infty P(\nu) \cos 2\pi\nu x \, d\nu \qquad (2.2)$$

where x is the path difference between the two arms of the interferometer and ν is the wavenumber.

By use of the Fourier transform integral theorem we can invert (2.2) to obtain its Fourier "pair", an expression for the power spectrum

$$P(\nu) = \int_0^\infty I(x) \cos 2\pi\nu x \, dx \quad . \qquad (2.3)$$

2.3 FUNDAMENTAL DEFINITIONS OF FTS

(a) Resolution

We may obtain a simple expression for the resolution of the Michelson by considering the particular case of

$$P(\nu) = P_o \delta(\nu - \nu_o) \qquad (2.4)$$

ie a Dirac δ function or in physical terms, a purely monochromatic line. Thus

$$I(x) = \int_0^\infty P_o \delta(\nu - \nu_o) \cos 2\pi\nu x d\nu = P_o \cos 2\pi\nu_o x \quad . \qquad (2.5)$$

Now the mechanical limitations of the Michelson apparatus impose a restriction on the interferogram I(x). It is obviously impossible to record the interferogram to infinity and in practice we are restricted to a maximum displacement $0 \rightarrow x_o$. Owing to unavoidable asymmetry, double-sided interferograms are usually recorded and hence we are forced to

truncate the integral within the limits ±L where $L = x_o/2$. Hence the recovered spectrum is given by

$$P(\nu) = \int_{-L}^{L} P_o \cos 2\pi\nu_o x \cos 2\pi\nu x dx$$

$$= P_o L \left[\frac{\sin 2\pi(\nu+\nu_o)L}{2\pi(\nu+\nu_o)L} + \frac{\sin 2\pi(\nu-\nu_o)L}{2\pi(\nu-\nu_o)L} \right] . \qquad (2.6)$$

The first term is very small compared to the second, thus we can consider $P(\nu)$ as a sinc function which has zeros when

$$2\pi(\nu-\nu_o)L = \pm\pi \quad \text{or} \quad \nu = \nu_o \pm \frac{1}{2L} . \qquad (2.7)$$

Therefore we recover the δ function as a peak with full width

$$\Delta\nu = \frac{1}{L} . \qquad (2.8)$$

We may take (2.8) as a measure of the resolution of the interferometer. There can, however, be no fixed definition of the resolution of a Michelson, for a number of different viewpoints may be considered including the effect of apodisation, a discussion of which is left until section 2.3(c). However, in all cases the general result is obtained that the resolution is inversely proportional to the maximum path difference.

For the case of (2.6) one possible definition is obtained from the width of the sinc function at half its peak value, commonly termed the half-width. Fig 2.1 illustrates the function sinc z' versus z' and from this it can be determined that the intensity drops to half its peak value at $z' = \pm 0.607\pi$. Hence the full half-width is $\sim 1.21\pi$ and so, for $z' = 2\pi(\nu-\nu_o)L$, we obtain the resolution

$$\Delta\nu = \frac{1.21}{2L} . \qquad (2.9)$$

Another possible definition follows from the so-called Rayleigh criterion which defines the resolution in terms of the separation of two

lines of equal intensity. If we consider that each of the recovered lines is given by (2.6) then we can show (Bell[15] chapter 6)

$$\Delta\nu_{RC} = \frac{1}{2L} \quad . \tag{2.10}$$

As (2.9) and (2.10) differ by only 20%, the simpler expression of (2.10) will be used as a definition for the resolution for an unapodized interferogram in the derivation of further spectroscopic quantities.

The resolving power of an interferometer can be very large; eg relative mirror displacements of $\sim$ 2 metres have been obtained in practice leading to resolutions $\sim$ 0.0025 cm^{-1}.

(b) The Fellgett and Jacquinot Advantages

The potentially large resolving power of the interferometer may be practically realised as a consequence of two important properties of the instrument, the Fellgett and Jacquinot advantages.

The Fellgett (or Multiplex) advantage can be stated in the following way. Suppose we observe a spectrum of N elements in a time T, each spectral increment being equal to the resolution. With a grating spectrometer each element will be observed for a time T/N as it lies within the exit slit of the instrument. The signal-to-noise ratio in the observed spectrum will be proportional to the square root of the observation time, ie $(T/N)^{\frac{1}{2}}$. However, with an interferometer each element is observed all the time during a scan so that the signal-to-noise will be proportional to $T^{\frac{1}{2}}$. Thus the interferometric system is superior by the factor $N^{\frac{1}{2}}$ which is generally considerable, N being typically of the order of 100 or more.

Fig .2.2 shows an equivalent optical diagram of a Michelson interferometer where the two arms containing the mirrors have been superimposed and off-axis rays are included. This diagram is an aid to the understanding of the following discussion.

Prior to describing the Jacquinot or throughput advantage (étendue) we must define the maximum aperture we may use with a Michelson. This is a consequence of the well-known circular fringe pattern produced when the mirrors in the two arms, as illustrated in the equivalent diagram of Fig 2.2, are parallel. The rings shrink as the path difference (x) is increased causing the intensity at any point to vary sinusoidally from a maximum to a minimum. The aperture must therefore be limited to include only the central fringe in order that the interferogram exhibit a variation of intensity with x. Hence we set the aperture to the size of the central fringe spot at maximum path difference x = L.

Fig 2.2 shows an oblique ray incident on and reflected from the fixed and movable mirrors, at an angle α to the optic axis. The optical path difference (Δ) for this oblique ray is given by

$$\Delta = (2d/\cos\alpha) - 2d \tan\alpha\sin\alpha = 2d\cos\alpha \qquad (2.11)$$

where d is the mirror separation. However, the measured "there and back" optical path difference for a ray on the optic axis is x = 2d; thus we may write

$$\Delta = x\cos\alpha \quad . \qquad (2.12)$$

Modifying (2.2) to take account of the off-axis rays in the interferometer we write

$$I(\Delta) = \int_0^\infty P(\nu)\cos 2\pi\nu\Delta \, d\nu \quad . \qquad (2.13)$$

Therefore integrating over the solid angle Ω subtended by the source

$$I(x,\Omega) = \frac{1}{\Omega}\int_0^\infty P(\nu)\int_0^\infty [\cos(2\pi\nu x\cos\alpha)]\, d\Omega d\nu \quad . \qquad (2.14)$$

The size of the central fringe is governed by the term in (2.14)

$$\cos(2\pi\nu x\cos\alpha) \simeq \cos 2\pi\nu x \left(1 - \frac{\alpha^2}{2}\right) \quad \text{for small } \alpha \quad . \qquad (2.15)$$

The phase difference between the central ray ($\alpha = 0$) and the first intensity minimum is π, so the first minimum is given by

$$2\pi\nu x \frac{\alpha_m^2}{2} = \pi \quad \text{ie} \quad \alpha_m^2 = \frac{1}{\nu x} \quad . \qquad (2.16)$$

The solid angle subtended from the centre to the first intensity minimum, the size of the central fringe, is therefore

$$\Omega = \pi\alpha_m^2 = \frac{\pi}{\nu x} \quad . \qquad (2.17)$$

Thus the maximum aperture which is dictated by the size of the central fringe and which occurs for $x = L$, the maximum path difference and $\nu = \nu_{MAX}$, is

$$\Omega_m = \frac{\pi}{L\nu_{MAX}} \quad . \qquad (2.18)$$

A further limiting factor arises from the integration of (2.14). By use of the small angle expression $\cos\alpha \simeq (1 - \alpha^2/2)$, setting $\Omega = \pi\alpha^2$ and using trigonometric identities, evaluation of (2.14) yields

$$I(x,\Omega) = \int_0^\infty P(\nu)\ \mathrm{sinc}\left(\frac{\Omega\nu x}{2}\right)\cos\left(2\pi\nu x\left[1 - \frac{\Omega}{4\pi}\right]\right)d\nu \quad . \qquad (2.19)$$

The interferogram is now modulated by a sinc function which has its first zero at

$$\Omega = \frac{2\pi}{\nu x} \quad . \qquad (2.20)$$

On progressing beyond the first zero of the sinc function the phase of the fringes is reversed and energy is removed not added to the spectrum as x is increased. From these considerations, the maximum usable aperture is therefore

$$\Omega_c = \frac{2\pi}{L\nu_{MAX}} \quad . \qquad (2.21)$$

The aperture Ω_c is a limit imposed by the modulating sinc function and not that of (2.18) which was dictated by the size of the central fringe spot. For correct interferometry the smaller of the two apertures must be employed. Since $\Omega_m < \Omega_c$, it is Ω_m that is taken to define the maximum usable aperture for the interferometer.

The étendue for a particular optical system is a constant which determines the amount of light that can be transmitted by the system or the "throughput". It is defined as

$$E = A\Omega \tag{2.22}$$

where A is the area of the collimator and Ω is the solid angle subtended by the source.

The Jacquinot advantage states that we may consider the flux throughput at any point in a lossless optical system for, in such a system, the brightness of an object is equal to the brightness of an image. We may now compare the étendues of a Michelson and a grating spectrometer.

From (2.10) the resolution of a Michelson was defined as

$$d\nu = \frac{1}{2L} \quad .$$

We now define the resolving power as

$$R = \frac{\nu}{d\nu} \quad . \tag{2.23}$$

Thus, from (2.10) and (2.18) the maximum solid angle aperture of the Michelson is given by

$$\Omega_m = \frac{2\pi}{R} \quad . \tag{2.24}$$

Therefore the étendue of the Michelson

$$E_m = A_m \frac{2\pi}{R} \quad . \tag{2.25}$$

In the case of the grating spectrometer the throughput power is limited by the entrance slit. The grating solid angle is

$$\Omega_G = \frac{w\ell}{f^2} \qquad (2.26)$$

where f is the focal length of the collimator, w the width and ℓ the length of the slit.

The resolving power of a grating spectrometer can be expressed in terms of the angle increment $d\theta$ through which the grating must be rotated to move a spectral increment $d\nu$ across the exit slit. With reference to Bell[15] (p 21)

$$d\theta = \frac{w}{2f} \qquad \text{thus } R_G = \frac{2f}{w}\tan\theta \quad . \qquad (2.27)$$

Therefore

$$E_G = A_G\Omega_G = \frac{\ell}{f}\,\frac{A_G}{R_G}\,2\tan\theta \quad . \qquad (2.28)$$

For maximum efficiency θ is chosen near the blaze angle θ_B and for θ_B typically $\sim 30^\circ$, we have $2\tan\theta \sim 1$.

Hence we obtain

$$E_G \sim \frac{\ell}{f}\,\frac{A_G}{R_G} \quad . \qquad (2.29)$$

Assuming $A_G \sim A_m$, and that the focal length of the collimators and the resolving powers of the Michelson and the grating instrument are the same, a justifiable assumption, then

$$\frac{E_m}{E_G} \simeq 2\pi\,\frac{f}{\ell} \quad . \qquad (2.30)$$

Even in the best grating spectrometer, ℓ/f does not exceed 1/30 thus the étendue of the Michelson is nearly 200 times better than that of the grating spectrometer, a factor attributable to the cylindrical symmetry of the interferometer.

It is important that the design of the interferometer allows the detector to accept the whole available solid angle from the instrument to make the best use of this throughput advantage.

(c) Instrumental Line Shape and Apodization

The effect of truncating the interferogram as defined by (2.2) and (2.3), within the limits ±L has already been demonstrated for the case of a purely monochromatic line of frequency ν_o. From (2.6) the recovered spectrum is of the form

$$P(\nu) = P_o L \frac{\sin 2\pi(\nu-\nu_o)L}{2\pi(\nu-\nu_o)L} \quad , \qquad (2.31)$$

that is, we obtain a sinc function as an approximation to the monochromatic beam. From (2.31) we define the Instrumental Line Shape (ILS) or spectral window as

$$W(\nu) = L \operatorname{sinc} \{ 2\pi(\nu-\nu_o)L \} \quad . \qquad (2.32)$$

Besides a central peak of finite width which we can tolerate as an approximation to the monochromatic line within the resolution limits imposed by the truncation, the sinc function also possesses sharp sidelobes or "feet" (see Fig 2.1). These undesirable features are symmetrically placed either side of the central peak and in practice they could be mistaken for real spectral features. This situation is improved by a mathematical procedure known as "apodization" from the Greek word apodal meaning "removal of the feet".

The feet arise from the sharp cut-off at x = ±L and the process of apodization arranges for the interferogram to be smoothly and progressively reduced to zero at these points. In consequence a greatly improved spectral profile is obtained though a sacrifice of some of the resolution accompanies the procedure.

The apodization process can of course be applied to the case of a polychromatic source which can be considered as a linear superposition of Dirac δ functions or monochromatic lines.

The apodizing function $f(x)$ is introduced into (2.3) to give the computed apodized spectrum

$$P(\nu) = \int_{-L}^{L} f(x)\, I(x)\, \cos 2\pi\nu x\, dx \tag{2.33}$$

a closer approximation to the true spectrum than the unapodized

$$P(\nu) = \int_{-L}^{L} I(x)\, \cos 2\pi\nu x\, dx \quad . \tag{2.34}$$

In order that both positive and negative x values may be scanned the chosen $f(x)$ should be an even function. In addition, to avoid phase errors for the two-sided interferograms the peak of $f(x)$ should fall at the experimental origin, the position of zero path difference.

Three widely used apodizing functions are

$$\begin{aligned} f(x) &= 1 - |x|/L \\ f(x) &= 1 - (x/L)^2 \\ f(x) &= \cos \pi x/2L \quad . \end{aligned} \tag{2.35}$$

As an example let us apply apodization in the form of the "triangular" function $f(x) = 1 - |x|/L$ to the case of the monochromatic line. Thus using (2.6)

$$\begin{aligned} P(\nu) &= \int_{-L}^{L} P_o \left| 1 - |x|/L \right| \cos 2\pi\nu_o x\, \cos 2\pi\nu x\, dx \\ &= P_o \int_{o}^{L} \left| 1 - |x|/L \right| \cos 2\pi(\nu - \nu_o)x\, dx \quad , \end{aligned} \tag{2.36}$$

where we have dropped the $\cos 2\pi(\nu+\nu_o)x$ term as its contribution to the integral is very small.

Hence

$$P(\nu) = \frac{P_o}{L} \left| \frac{1 - \cos 2\pi(\nu-\nu_o)x}{[2\pi(\nu-\nu_o)]^2} \right|$$

and by use of the identity $\cos 2\theta = 1 - 2\sin^2\theta$ we obtain

$$P(\nu) = P_o \frac{L}{2} \frac{\sin^2\pi(\nu-\nu_o)L}{[\pi(\nu-\nu_o)L]^2}$$

$$\text{ie} \quad P(\nu) = P_o \frac{L}{2} \operatorname{sinc}^2 \{\pi(\nu-\nu_o)L\} \quad . \qquad (2.37)$$

This result is illustrated in Fig 2.1 along with the unapodized spectrum given by (2.31). The effect of the apodization can easily be seen. The sidelobes are greatly reduced in height and the negative intensity values disappear. The width has slightly increased, hence the resolution has been slightly degraded but not seriously. The resultant apodized spectrum is now a spectroscopically acceptable approximation to the pure monochromatic line.

(d) Discrete Sampling and the Phenomenon of Aliasing

In a real experiment the problem arises of how to record the interferogram in a form that can be fed into the computer for Fourier analysis. In practice the interferogram is sampled at equal intervals of path difference Δx. This is often achieved as in our case by mounting the movable mirror on a micrometer which is moved in discrete steps of length $x' = \Delta x/2$ thus giving a "there and back" path difference increment of Δx in the arm of the interferometer.

One benefit of adopting this procedure is that use may be made of the Fast Fourier "Cooley Tukey" algorithm in the Fourier analysis, which

greatly reduces the computation time, for this method requires the data to be recorded in equal increments.

The sampled interferogram $I_s(x)$ obtained in this way is not the continuous interferogram $I_c(x)$ as given by (2.2), for the integration has now been replaced by a summation. The two interferograms are related by

$$I_s(x) = \text{Ш}\left(\frac{x}{\Delta x}\right) I_c(x) \tag{2.38}$$

where $\text{Ш}\left(\frac{x}{\Delta x}\right)$ is the Shah "Comb" function defined mathematically in terms of the Dirac δ function

$$\text{Ш}(x) = \sum_{n=-\infty}^{\infty} \delta(x-n) \tag{2.39}$$

where n is an integer.

Therefore in (2.38) the Shah function allows for $I_s(x)$ to have only those values for which $x = 0, \pm\Delta x, \pm 2\Delta x \ldots$.

The effect of discrete sampling on the final computed spectrum can be deduced using the convenient property of the Shah function that it is its own Fourier transform. That is

$$\text{FT}\{\text{Ш}(ax)\} = \frac{1}{|a|}\text{Ш}(\nu/a) \quad . \tag{2.40}$$

This follows from the definition of the Dirac δ function and a change of variable relation.

And from (2.2) and (2.3)

$$\begin{aligned} P_s(\nu) &= \text{FT}\{I_s(x)\} \\ P_c(\nu) &= \text{FT}\{I_c(x)\} \quad . \end{aligned} \tag{2.41}$$

Use must now be made of the convolution theorem which states that

if $h(x) = \int f(y)g(x-y)dy \equiv f(x)*g(x)$, ie the convolution of f(x) and g(x)

then $H(K) = F(K)G(K)$ where $H(K) = FT\{h(x)\}$ etc.

Hence from (2.38)

$$P_s(\nu) = FT\{ \text{Ш} (\tfrac{x}{\Delta x})\} * P_c(\nu) \quad , \tag{2.42}$$

and using (2.40) one may write

$$P_s(\nu) = \Delta x \ \text{Ш}(\nu\Delta x) * P_c(\nu)$$

leading to

$$FT\{I_s(x)\} = P_s(\nu) = \sum_{n=-\infty}^{\infty} P_c(\nu - n\Delta'\nu) \tag{2.43}$$

where $\Delta'\nu = 1/\Delta x$ and the definitions of the Shah function, the convolution integral and the Dirac δ function were employed. Note that $\Delta'\nu$ is not the same as the resolution $\Delta\nu$ discussed previously.

The complete spectrum $P_c(\nu)$ is then obtained for $\nu = n\Delta'\nu$ for all n, leading to duplicate spectra starting at $n\Delta'\nu$. Overlapping or aliasing of these spectra may occur depending on the magnitude of $\Delta'\nu$. This aliasing must be avoided by separating the repeated spectra in order to determine the true spectrum. Fig 2.3 shows a spectrum where the problem of aliasing arises. A double-sided continuous interferogram $I_c(x)$ gives both positive and negative frequency values for $P_c(\nu)$ which thus extends from $-\nu_{MAX}$ to $+\nu_{MAX}$, a width of $2\nu_{MAX}$. In Fig 2.3(a) the full lines represent the positive spectra and the dashed lines the negative spectra as computed from a sampled interferogram. Fig 2.3(b) shows the resultant spectrum which would thus be computed, the sum of the components of (a). The negative mirrored spectrum from $-\nu_{MAX}$ to zero is ordinarily ignored leaving the required positive spectrum from zero to ν_{MAX}. But of course, as illustrated by Fig 2.3, the separation of repeated spectra can only be assured by setting

$$\Delta'\nu \geq 2\nu_{MAX}$$

$$\text{or} \quad \Delta x \leq 1/2\nu_{MAX} \qquad . \qquad (2.44)$$

The stepping increment $x' = \Delta x/2$ must therefore be chosen carefully to avoid aliasing. As the true spectral information is restricted to the range $0 \rightarrow \nu_{MAX}$ we define the cut-off or aliasing frequency

$$\bar{K} = \nu_{MAX} = \frac{1}{2\Delta x} = \frac{1}{4x'} \qquad . \qquad (2.45)$$

The micrometer of the polarising interferometer was rotated using a stepping motor with a maximum of 200 steps per revolution, equivalent to 0.5 mm of micrometer travel. Thus the smallest stepping increment was 2.5 μm corresponding to a cut-off frequency $\bar{K} = 1000\ cm^{-1}$.

2.4 DISPERSIVE FOURIER TRANSFORM SPECTROSCOPY

The technique of DFTS, where the phase spectrum is measured directly by placing the sample in one arm of the interferometer, was developed to remove some of the limitations that arose in conventional power FTS. There, the phase must be constructed from the power reflectivity $P(\nu)$ using the Kramers-Krönig (KK) analysis which is, in practice, an approximation procedure, for the experimental data is generally incomplete since it is recorded over a restricted spectral range. Details of the KK procedure are given in chapter 3. In this section, the basic integral for DFTS is derived and shown to be valid also for the power FTS case.

First we must again assume that the law of superposition holds and also that the electric fields are real functions. In addition we now attribute different reflectivities to the two reflectors in the two arms of

the interferometer.

The essential expression for the electric field as a function of position z is

$$E(z) = \int_{-\infty}^{\infty} g(\nu) \exp[2\pi i\nu z] d\nu \quad . \tag{2.46}$$

Here we are concerned with electric field amplitudes and the corresponding reflectivity is the complex reflection coefficient defined as

$$\rho(\nu) = |\rho(\nu)| \exp i\phi(\nu) \tag{2.47}$$

where $|\rho(\nu)|$ is the modulus or amplitude and $\phi(\nu)$ the phase. For a plane mirror, for example, $|\rho(\nu)| = 1$ and $\phi(\nu) = \pi$, thus $\rho(\nu) = \exp i\pi = -1$.

The power reflectivity or reflectance, the ratio of reflected to incident power is given by

$$R(\nu) = \rho(\nu)\rho^*(\nu) \tag{2.48}$$

where the * denotes the complex conjugate.

The field from the sample arm is

$$E_1(z) = \int_{-\infty}^{\infty} \rho(\nu)g(\nu) \exp(2\pi i\nu z) d\nu \tag{2.49}$$

and from the moving mirror arm

$$E_2(z) = \int_{-\infty}^{\infty} \exp(i\pi)\ g(\nu) \exp(2\pi i\nu[z+x]) d\nu \tag{2.50}$$

where x is the path difference between the two arms and $\rho(\nu)$ the true complex reflection coefficient of the sample.

Invoking the principle of linear superposition the resultant recombined amplitude is

$$\mathcal{E}_R(x,\nu) = g(\nu)\ [\rho(\nu) + \exp i(2\pi\nu x+\pi)] \quad , \tag{2.51}$$

and the resulting flux

$$P(x,\nu) = g_R(x,\nu)\, g_R^*(x,\nu)$$

$$= g^2(\nu)\{1+R(\nu)+|\rho(\nu)|[\exp i(2\pi\nu x+\pi-\phi(\nu))+\exp -i(2\pi\nu x+\pi-\phi(\nu))]\} \quad (2.52)$$

Hence the interferogram

$$I(x) = \int_{-\infty}^{\infty} g^2(\nu)\{1+R(\nu) + 2|\rho(\nu)|\cos[2\pi\nu x+\pi-\phi(\nu)]\}d\nu \quad (2.53)$$

The information on the spectrum is, however, provided by the varying part of the interference function ie the cosine term, the other terms merely contributing to a charge in the overall level. Thus essentially

$$I(x) = 2\int_{-\infty}^{\infty} |\rho(\nu)|\, g^2(\nu)\cos[2\pi\nu x+\pi-\phi(\nu)]\, d\nu \quad . \quad (2.54)$$

Now multiplying both sides by $\exp(-2\pi i\nu' x)$, expressing the cosine as a sum of complex exponentials and integrating we obtain

$$\int_{-\infty}^{\infty} \exp(-2\pi i\nu' x)\, I(x)d\nu = \int_{-\infty}^{\infty} |\rho(\nu)|g^2(\nu)\{\int_{-\infty}^{\infty}(\exp i[2\pi(\nu-\nu')x+\pi-\phi(\nu)]$$

$$+ \exp -i[2\pi(\nu+\nu')x+\pi-\phi(\nu)])dx\}\, d\nu \quad . \quad (2.55)$$

Using the integral result

$$\int_{-\infty}^{\infty} \exp(iKx)\, dx = 2\pi\delta(K)$$

where $\delta(K)$ is the Dirac delta function defined such that

$$\int_{-\infty}^{\infty} \delta(x-a)\, f(x)\, dx = f(a)$$

and ignoring the negative wave number part of the solution and any multiplying constants we obtain the result

$$|\rho(\nu')|g^2(\nu')\exp\, i[\pi-\phi(\nu')] \;=\; \int_{-\infty}^{\infty} I(x)\, \exp(-2\pi i\nu' x)dx \quad . \quad (2.56)$$

Since $P(\nu) = g^2(\nu)$ is the spectrum, (2.56) yields the basic complex Fourier transform integral for FTS

$$-P(\nu)\, \rho^*(\nu) \;=\; \int_{-\infty}^{\infty} I(x)\, \exp[-2\pi i\nu x]\, dx \quad . \quad (2.57)$$

Hence for the case where a sample replaces one of the interferometer mirrors we require the complex FT (2.57) and not the cosine FT (2.3). The complex FT yields $\rho(\nu)P(\nu)$ rather than just $P(\nu)$ where $\rho(\nu)$ is the complex reflection coefficient of the sample.

For conventional power FTS where the sample is placed in the recombined beams and the interferometer contains perfect mirrors in each of the two arms, we have $\rho(\nu) = -1$. Thus (2.57), the complex transform, may be used for this case as well as for the dispersive case. Even if the two mirrors are not perfect, this factor cancels when ratioing results obtained with the sample in against those with the sample out.

Returning to the dispersive situation described by (2.57), $P(\nu)$ is easily obtained by replacing the sample with a perfect plane mirror

$$[\; |\rho(\nu)| = 1, \quad \rho(\nu) = \exp i\pi = -1 \;] \; .$$

Hence

$$P(\nu) \;=\; \int_{-\infty}^{\infty} I(x)_{\text{MIRROR}}\, \exp[-2\pi i\nu x]dx \quad . \quad (2.58)$$

Ratioing this with the complex FT of the sample interferogram gives

$$\rho^*(\nu) \;=\; |\rho(\nu)|\exp -i\phi(\nu) \;=\; -\frac{\text{FT}\{I(x)_{\text{SAMPLE}}\}}{\text{FT}\{I(x)_{\text{MIRROR}}\}} \quad . \quad (2.59)$$

Thus both the amplitude $\rho(\nu)$ and the phase $\phi(\nu)$ reflection spectra are

obtained by direct measurement. The optical constants [n and k] and the related dielectric functions [ε' and ε''] may then be calculated using the Fresnel relations which are derived in the following chapter.

Besides providing a direct measurement of $\phi(\nu)$ another advantage of DFTS is that extremely small values of power reflection or transmission may be determined on squaring the measured amplitudes. For example, a measured transmission amplitude of 1% yields a power transmission of 0.01%, a figure beyond the limits of a power FTS experiment.

2.5 PHASE ERRORS DUE TO MISMATCHING OF RATIOED INTERFEROGRAMS

It has been shown that to obtain the phase spectrum $\phi(\nu)$ in DFTS we may ratio the interferogram obtained with the sample in the fixed arm against that obtained with the mirror in the same arm. To avoid phase errors it is important that the reflecting plane of the sample coincides exactly with that of the mirror it replaces and that the recording of the two interferograms commences at the same point. This is to ensure that the experimental origins coincide. A technique for achieving this exact replacement experimentally will be discussed later in chapter 4.

We will now consider the effect on the measured phase spectrum of a mismatch of the two interferograms.

For the sample, using (2.57)

$$-P(\nu)\ \rho^*(\nu) \;=\; \int_{-\infty}^{\infty} I_{SAMPLE}(x)\ \exp[-2\pi i\nu x]dx \quad . \qquad (2.60)$$

Suppose the mirror interferogram is mismatched at every step by a distance δ; ie the experimental origin of the interferogram is displaced a distance δ from that of the sample interferogram. We can express the mirror spectrum as

$$B(\nu) \;=\; \int_{-\infty}^{\infty} I(x-\delta)_{MIRROR}\ \exp[-2\pi i\nu x]dx \quad . \qquad (2.61)$$

On ratioing we obtained

$$\rho'^*(\nu) = \frac{P(\nu)}{B(\nu)} \rho^*(\nu) \qquad (2.62)$$

and not the required $\rho^*(\nu)$ as for (2.59).

However, use of the Shift rule for Fourier transforms gives

$$B(\nu) = \exp[-2\pi i\nu\delta] \int_{-\infty}^{\infty} I(x)_{MIRROR} \exp[-2\pi i\nu x]dx \; . \qquad (2.63)$$

Thus

$$B(\nu) = \exp[-2\pi i\nu\delta] \; . \; P(\nu) \qquad (2.64)$$

and

$$\rho'^*(\nu) = \exp[2\pi i\nu\delta] \; \rho^*(\nu)$$

$$= |\rho(\nu)| \exp - i[\phi(\nu) - 2\pi\nu\delta] \quad . \qquad (2.65)$$

Thus the true phase spectrum is shifted by a factor which is linear in wave number ν.

If, for example, we mismatch by one sampling step, ie $\delta = \Delta x$, then the phase error is

$$\Delta\phi = 2\pi\nu\Delta x \quad . \qquad (2.66)$$

At the cut-off or aliasing frequency $\nu = \bar{K} = \frac{1}{2\Delta x}$ (see 2.45),

the phase error $\Delta\phi = \pi$.

Hence a one sampling step mismatch between the ratioed interferograms leads to a phase error of π at the cut-off or aliasing frequency.

FIG 2.1

PLOTS OF

① $\text{sinc}\, z' = \frac{\sin z'}{z'}$ versus z'

② $\text{sinc}^2 z'/2$ versus z'

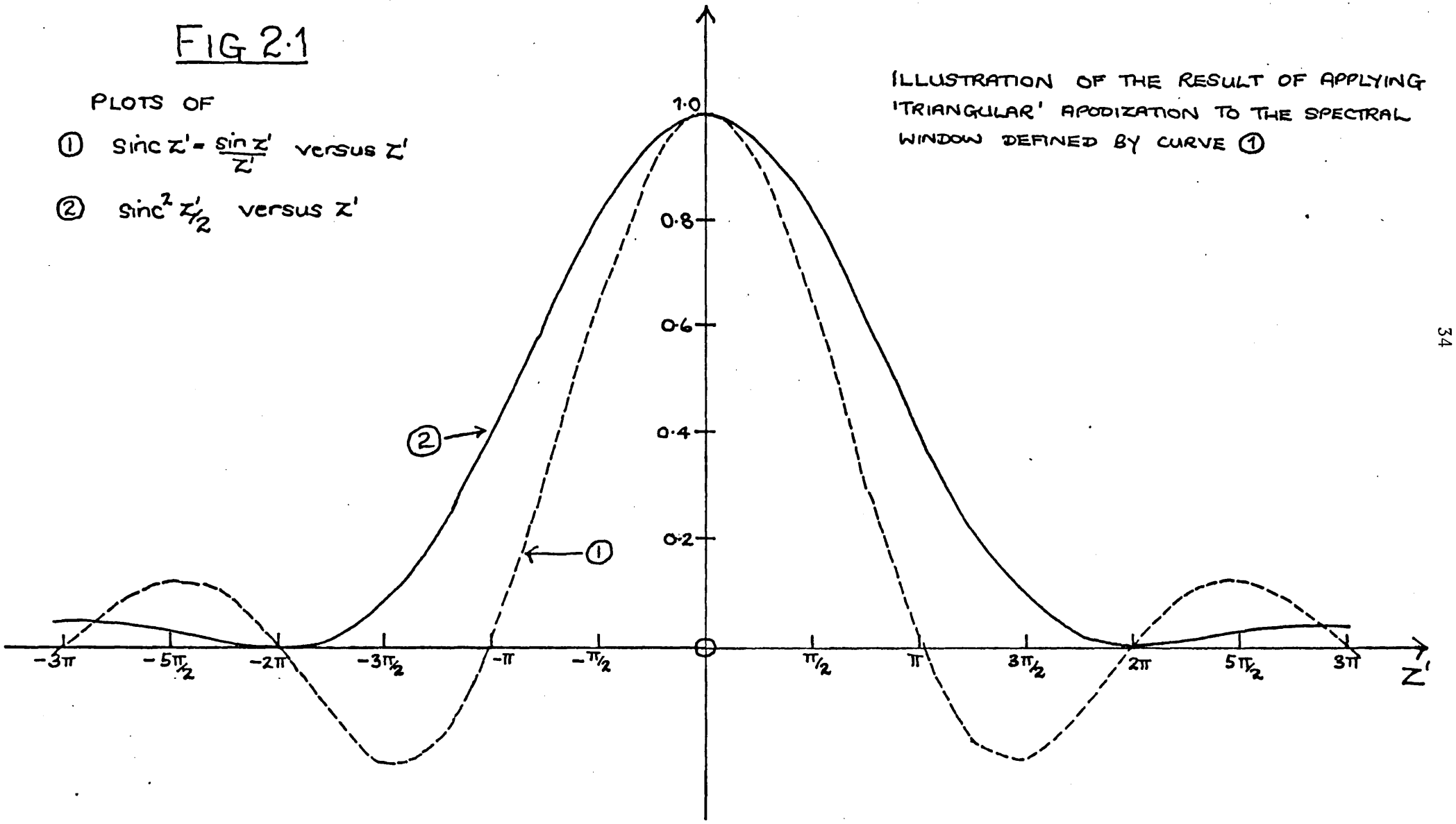

ILLUSTRATION OF THE RESULT OF APPLYING 'TRIANGULAR' APODIZATION TO THE SPECTRAL WINDOW DEFINED BY CURVE ①

FIG 2.2 :- PART OF THE EQUIVALENT OPTICAL DIAGRAM OF A MICHELSON INTERFEROMETER SHOWING THE TWO MIRRORS AND AN OFF-AXIS RAY

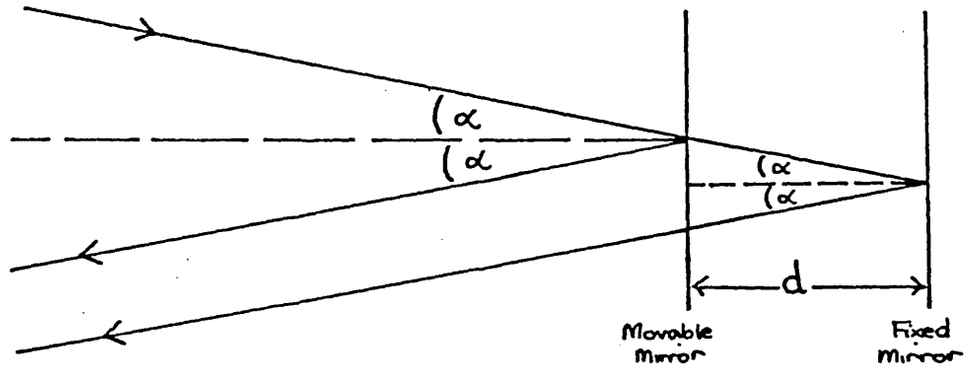

FIG 2.3 :- THE PHENOMENON OF ALIASING

(a) Computed spectral components from the sampled interferogram. The full lines represent positive $\tilde{\nu}$ spectra, the dashed lines the negative $\tilde{\nu}$ spectra

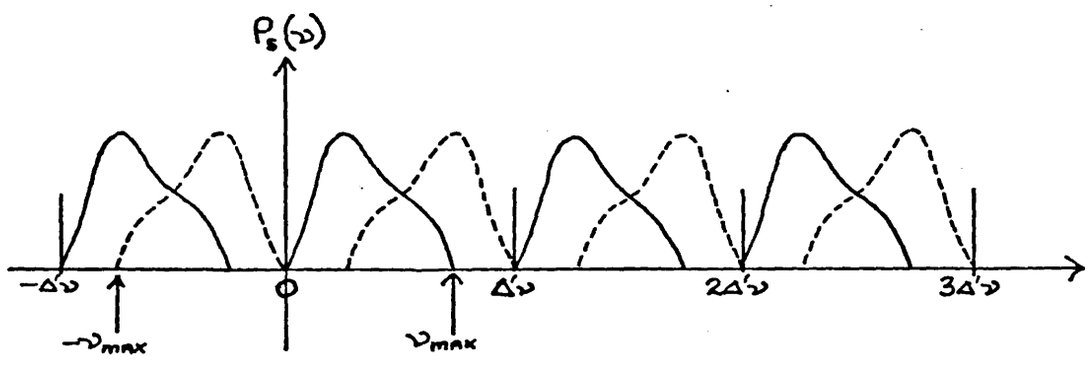

(b) The total interferogram as would be computed from the sampled interferogram. This spectrum is the sum of the spectral components of (a)

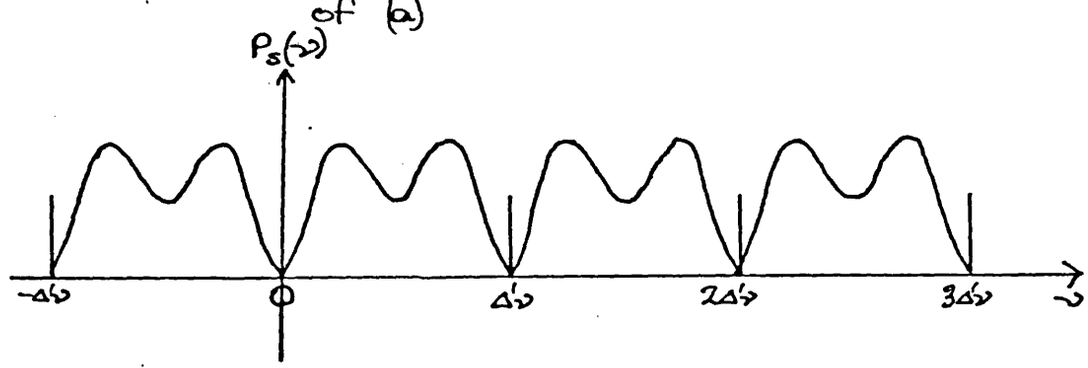

CHAPTER 3

DIELECTRIC AND OPTICAL THEORY OF CRYSTALS

3.1 INTRODUCTION

With a view to providing a background for the discussion and interpretation of experimental results, the relevant elements of the dielectric and optical theory of crystals are presented in this chapter.

It is inevitable that such an outline will commence with a statement of Maxwell's fundamental equations giving a description of an electromagnetic field. With these as a basis, the electromagnetic theory of reflection and refraction is considered leading to a derivation of the Fresnel equations, relating reflected and refracted energy to incident energy.

Then via dispersion theory the oscillator model equation for the dielectric constants ε' and ε'' is developed and certain other aspects of the theory are thereby deduced.

The chapter is concluded with a section on linear response theory and Kramers-Krönig analysis. It has already been indicated that knowledge of this procedure is required in order to obtain optical constant data from conventional power FTS measurements.

The theoretical details presented in this chapter were obtained from a number of sources which included books by Born and Wolf[17], Born and Huang[18], Turrell[19] and Nudelman and Mitra (eds)[20].

As most of the time available was spent making measurements on the ferroelectric KDP and the anti-ferroelectric ADP and fitting theoretical models to these results, a discussion of the theory of ferroelectricity and crystals such as KDP merits a chapter of its own. Hence, chapter 5 has been devoted to this topic.

3.2 ELECTROMAGNETIC BASIS

An electromagnetic field in a dielectric medium is described by four vector quantities, the electric field $\underline{E}$, the magnetic field $\underline{H}$, the electric displacement $\underline{D}$ and the magnetic induction $\underline{B}$. The macroscopic electromagnetic properties of the medium are then determined by Maxwell's equations which take the general form

$$\nabla \cdot \underline{D} = \rho \tag{3.1}$$

$$\nabla \cdot \underline{B} = 0 \tag{3.2}$$

$$\nabla \times \underline{H} = \underline{j} + \dot{\underline{D}} \tag{3.3}$$

$$\nabla \times \underline{E} = -\dot{\underline{B}} \tag{3.4}$$

where ρ is the charge density in the medium and $\underline{j}$ is the current density given by Ohm's law

$$\underline{j} = \sigma \underline{E} \tag{3.5}$$

σ being the electrical conductivity which is zero for a non-conducting dielectric medium.

It is convenient to introduce an additional variable, the polarization $\underline{P}$ which represents the electric dipole moment per unit volume defined by the relation

$$\underline{D} = \varepsilon_o \underline{E} + \underline{P} \tag{3.6}$$

where ε_o is the permittivity of a vacuum.

For an isotropic medium $\underline{D}$, $\underline{E}$ and $\underline{P}$ are parallel and for small fields $\underline{P}$ is proportional to $\underline{D}$. Thus we write

$$\underline{D} = \varepsilon \underline{E} \tag{3.7}$$

where
$$\varepsilon = \varepsilon_o + \frac{P}{E} \tag{3.8}$$

and $\varepsilon/\varepsilon_o$ is the dielectric constant or relative permittivity of the medium.

Rewriting (3.8) gives

$$\underline{P} = \underline{E}(\varepsilon - \varepsilon_o) \quad . \tag{3.9}$$

We now define the electric susceptibility or polarizability χ by the equation

$$\underline{P} = \chi \varepsilon_o \underline{E} \quad . \tag{3.10}$$

Hence

$$\chi = \frac{\varepsilon}{\varepsilon_o} - 1 \tag{3.11}$$

which is usually split into electronic and atomic contributions. For an isotropic crystal

$$\frac{\varepsilon}{\varepsilon_o} = 1 + \chi_{elec} + \chi_{ion} \tag{3.12}$$

where χ_{elec} is due to distortion of the electron distribution by the electric field, and χ_{ion} arises from ionic displacements during lattice vibrations. At frequencies which are high compared to molecular and ionic vibrational frequencies a high-frequency or optical dielectric constant may be defined as

$$\frac{\varepsilon_\infty}{\varepsilon_o} = 1 + \chi_{elec} \quad . \tag{3.13}$$

At lower frequencies ε_∞ is essentially constant and the variation of ε is due to the χ_{ion} term in (3.12).

Considering the magnetic properties of the medium, $\underline{H}$ is defined by

$$\mu_o \underline{H} = \underline{B} - \mu_o \underline{M} \tag{3.14}$$

where $\underline{M}$ is the magnetic polarization for unit volume. Similar considerations as those used for the electric properties lead to

$$\mu \underline{H} = \underline{B} \tag{3.15}$$

where μ/μ_o is the relative permeability of the medium.

Furthermore, for a homogeneous electrically neutral medium there is

no net charge, ie $\rho = 0$. We may thus rewrite equations (3.1) to (3.4) as

$$\nabla \cdot \underline{D} = \varepsilon \nabla \cdot \underline{E} = 0 \tag{3.16}$$

$$\nabla \cdot \underline{H} = 0 \tag{3.17}$$

$$\nabla \times \underline{H} = \sigma \underline{E} + \varepsilon \dot{\underline{E}} = \sigma \underline{E} + \varepsilon_0 \dot{\underline{E}} + \dot{\underline{P}} \tag{3.18}$$

$$\nabla \times \underline{E} = -\mu \dot{\underline{H}} \quad . \tag{3.19}$$

By taking the curl of (3.19) and using (3.18) we obtain the differential equation for the electric field in a homogeneous, neutral medium, as

$$\nabla^2 \underline{E} = \mu\varepsilon \ddot{\underline{E}} + \mu\sigma \dot{\underline{E}} \quad . \tag{3.20}$$

The final term in (3.20) essentially describes the damping of the field by the medium. For a non-conducting, lossless, dielectric medium the conductivity $\sigma = 0$. However, for real crystals losses are present, ie radiation is absorbed by the medium, in the infrared region of the spectrum and hence σ cannot be set equal to zero. This requires both the refractive index and the dielectric constant of the medium to be complex.

3.3 GENERAL CONSIDERATIONS AND DEFINITIONS

Plane wave solutions of (3.20) are of the form

$$\underline{E} = \underline{E}_0 \exp i[\underline{K} \cdot \underline{r} - \omega t] \tag{3.21}$$

where K is the propagation constant and is in general complex for a lossy medium; ie $K = \beta + i\alpha$.

Taking the simple example of a wave travelling in the positive z direction, ie

$$E = E_0 \exp i[Kz - \omega t] \tag{3.21b}$$

then substitution into (3.20) which now has the form

$$\frac{\partial^2 E}{\partial z^2} = \mu\varepsilon \frac{\partial^2 E}{\partial t^2} + \mu\sigma \frac{\partial E}{\partial t} \tag{3.22}$$

yields

$$K^2 = \omega^2\mu(\varepsilon + \frac{i\sigma}{\omega}) \quad . \tag{3.23}$$

This corresponds to the situation for non-conducting media ($\sigma = 0$) where the dielectric constant is real if a complex dielectric constant $\hat{\varepsilon}$ is introduced as

$$\hat{\varepsilon} = \varepsilon + \frac{i\sigma}{\omega} \quad . \tag{3.24}$$

Hence

$$K = \omega\sqrt{\mu\hat{\varepsilon}} = \omega/v \quad , \tag{3.25}$$

where $v = (\mu\hat{\varepsilon})^{-\frac{1}{2}}$ is the complex phase velocity at which $\underline{E}$ is propagated in the medium.

Following from the general definition of refractive index we may introduce a complex refractive index

$$N = \frac{C}{v} = \frac{C}{\omega}K = \frac{K}{\omega\sqrt{\mu_o\varepsilon_o}} \quad . \tag{3.26}$$

Thus

$$N(\omega) = \left(\frac{\mu}{\mu_o\varepsilon_o}\left[\varepsilon + \frac{i\sigma}{\omega}\right]\right)^{\frac{1}{2}} = n + ik \tag{3.27}$$

where n and k are the optical constants of the absorbing medium, n is the real refractive index and k/n is known as the extinction coefficient or attenuation index.

Now the magnetic equivalent of (3.11) is

$$\chi_m = \mu/\mu_o - 1 \tag{3.28}$$

where χ_m is the magnetic susceptibility which is zero in our case for we are not concerned with magnetic phenomena.

Therefore (3.28) gives $\mu = \mu_o$. Using this result and equating real and imaginary parts of (3.27)

$$n^2 - k^2 = \varepsilon/\varepsilon_o \quad , \tag{3.29}$$

and

$$2nk = \sigma/\varepsilon_o\omega. \tag{3.30}$$

From (3.24) and (3.27) we may write

$$\hat{\varepsilon} = \varepsilon_o[n + ik]^2 = \varepsilon' + i\varepsilon'' \tag{3.31}$$

leading to

$$\varepsilon'/\varepsilon_o = n^2 - k^2 \tag{3.32}$$

$$\varepsilon''/\varepsilon_o = 2nk \quad . \tag{3.33}$$

Henceforth the symbol ε will be used to designate the complex dielectric constant given by

$$N^2(\omega) = \frac{\varepsilon(\omega)}{\varepsilon_o} = \frac{\varepsilon' + i\varepsilon''}{\varepsilon_o} \tag{3.34}$$

and not the real part of the dielectric constant as in (3.24).

A relative refractive index for two media 1 and 2 may be defined as

$$N_{21} = \frac{N_1}{N_2} = \frac{K_1}{K_2} = \frac{v_2}{v_1} = \sqrt{\frac{\varepsilon_1}{\varepsilon_2}} \quad . \tag{3.35}$$

The effect of absorption due to the medium through which the wave propagates can be determined by substitution of (3.26) and (3.27) into the equation for the plane wave (3.21).

Consequently,

$$\underline{E} = \underline{E}_o \exp\left(-\frac{k\omega}{C}\,\hat{\underline{K}}\cdot\underline{r}\right) \exp i\omega[n/C\ \hat{\underline{K}}\cdot\underline{r} - \omega t] \tag{3.36}$$

where $\hat{\underline{K}}$ is the unit vector in the direction of propagation.

This represents a plane wave with velocity C/n which is exponentially

damped by the term

$$\exp(-\frac{k\omega}{c}\hat{\underline{K}}\circ\underline{r}).$$

The power flux I is proportional to the square of the modulus of the complex amplitude, hence

$$\frac{I}{I_o} = \frac{\underline{E}\circ\underline{E}^*}{\underline{E}_o^2} = \exp\left[-\frac{2k\omega}{c}\hat{\underline{K}}\circ\underline{r}\right] \qquad (3.37)$$

or

$$I = I_o \exp -\alpha(\hat{\underline{K}}\circ\underline{r}) \qquad (3.38)$$

which is usually referred to as Lambert's Law.

$$\alpha = \frac{2k\omega}{c} = \frac{4\pi k}{\lambda} \qquad (3.39)$$

is the power absorption coefficient per unit length within the medium, λ being the wavelength in vacuum.

3.4 REFLECTION AND REFRACTION OF RADIATION - THE FRESNEL RELATIONS

Now consider the case of a plane wave as given by (3.21) incident onto a plane boundary separating two media 1 and 2, with medium 2 more dense, ie $k_2 > k_1$.

The situation is illustrated in Fig 3.1 where the relevant $\underline{E}$ and $\underline{H}$ vectors, the propagation vectors $\underline{n}_i$ and the required angles are drawn. The problem is treated in two separate cases for $\underline{E}_o$ perpendicular and $\underline{E}_o$ parallel to the plane of incidence.

The boundary plane is designated by

$$\underline{n}\circ\underline{r} = 0 \quad . \qquad (3.40)$$

The wave vectors are:

$$\begin{aligned} &\text{For the incident wave} && \underline{K}_o = K_o \underline{n}_o = K_1 \underline{n}_o \\ &\text{For the reflected wave} && \underline{K}_1 = K_1 \underline{n}_1 \\ &\text{For the transmitted wave} && \underline{K}_2 = K_2 \underline{n}_2 \end{aligned} \tag{3.41}$$

where K_i is given by (3.23).

To relate the $\underline{E}$ and $\underline{H}$ vectors, assume they are of the form given by (3.21b) and substitute into (3.19), one of Maxwell's equations.

Therefore

$$\underline{n} \times \frac{\partial \underline{E}}{\partial z} = -\mu \dot{\underline{H}} = i\omega\mu \underline{H} \tag{3.42}$$

or

$$\{ iK(\underline{n} \times \underline{E}_o) - i\omega\mu \underline{H}_o \} \exp i[Kz - \omega t] = 0$$

$$\text{ie } \underline{H}_o = \frac{K}{\omega\mu} (\underline{n} \times \underline{E}_o) \quad . \tag{3.43}$$

Since $\underline{E}_o \cdot \underline{n} \times \underline{E}_o = 0$,

then $$\underline{E}_o \cdot \underline{H}_o = 0. \tag{3.44}$$

Therefore $\underline{E}_o$ and $\underline{H}_o$ are mutually perpendicular and both are perpendicular to $\underline{n}$, the propagation direction. These three vectors form a positive right-handed triad.

We may now write the wave equations as:

Incident plane wave

$$\begin{aligned} \underline{E}_i &= \underline{E}_o \exp i[K_1 \underline{n}_o \cdot \underline{r} - \omega t] \\ \underline{H}_i &= \frac{K_1}{\omega\mu_1} \underline{n}_o \times \underline{E}_i \end{aligned} \tag{3.45}$$

Reflected wave (assume plane)

$$\begin{aligned} \underline{E}_r &= \underline{E}_1 \exp i[K_1 \underline{n}_1 \cdot \underline{r} - \omega t] \\ \underline{H}_r &= \frac{K_1}{\omega\mu_1} \underline{n}_1 \times \underline{E}_r \end{aligned} \tag{3.46}$$

Transmitted wave (assume plane)

$$\underline{E}_t = \underline{E}_2 \exp i[K_2 \underline{n}_2 \cdot \underline{r} - \omega t]$$
$$\underline{H}_t = \frac{K_2}{\omega \mu_2} \underline{n}_2 \times \underline{E}_t \qquad (3.47)$$

The boundary conditions of the problem demand that the tangential components of $\underline{E}$ and $\underline{H}$ be continuous across the boundary plane $\underline{n} \cdot \underline{r} = 0$. Consequently the arguments of the exponentials in the three cases are identical and this condition requires that the frequencies be the same for the three waves. We may rewrite the boundary condition using the expression

$$\underline{n} \times (\underline{n} \times \underline{r}) = \underline{n}(\underline{n} \cdot \underline{r}) - \underline{r}(\underline{n} \cdot \underline{n}) \quad . \qquad (3.48)$$

The first term on the right-hand side is zero at the boundary and $(\underline{n} \cdot \underline{n}) = 1$. Thus

$$-r = \underline{n} \times (\underline{n} \times \underline{r}) = \underline{n} \times \underline{h} \qquad (3.49)$$

where $\underline{h} = \underline{n} \times \underline{r}$ must lie in the boundary plane.

Substitution for $\underline{r}$ in (3.45) → (3.47) and using the boundary condition yields

$$\underline{K}_o \cdot (\underline{n} \times \underline{h}) = \underline{K}_1 \cdot (\underline{n} \times \underline{h}) = \underline{K}_2 \cdot (\underline{n} \times \underline{h}) \qquad (3.50)$$

or $$(\underline{K}_o \times \underline{n}) \cdot \underline{h} = (\underline{K}_1 \times \underline{n}) \cdot \underline{h} = \underline{K}_2 \cdot (\underline{n} \times \underline{h}) \qquad (3.51)$$

Hence $$(\underline{K}_o - \underline{K}_1) \times \underline{n} \cdot \underline{h} = 0 \qquad (3.52)$$

$$(\underline{K}_1 - \underline{K}_2) \times \underline{n} \cdot \underline{h} = 0 \quad . \qquad (3.53)$$

As the plane of incidence is defined by $\underline{K}_o$ and $\underline{n}$ then $\underline{K}_1$ and $\underline{K}_2$ also lie in this plane, a statement of the Coplanar Law.

Furthermore, from Fig 3.1

$$|\underline{K}_o \times \underline{n}| = K_1 \sin\theta_o ; \; |\underline{K}_1 \times \underline{n}| = K_1 \sin\theta_1 ; \; |\underline{K}_2 \times \underline{n}| = K_2 \sin\theta_2 \; .$$

(3.54)

So using (3.52)

$$\sin\theta_o = \sin\theta_1 \tag{3.55}$$

and $$K_1\sin\theta_o = K_2\sin\theta_2 \quad ; \tag{3.56}$$

respectively, the law of Reflection and Snell's law of Refraction.

For $\underline{E}$ and $\underline{H}$ to be continuous across the boundary

$$\underline{n} \times (\underline{E}_o+\underline{E}_1) = \underline{n} \times \underline{E}_2 \tag{3.57}$$

and $$\underline{n} \times (\underline{H}_o+\underline{H}_1) = \underline{n} \times \underline{H}_2 \tag{3.58}$$

or rewriting (3.58) using (3.43)

$$\underline{n} \times (\underline{n}_o \times \underline{E}_o + \underline{n}_1 \times \underline{E}_1) \frac{K_1}{\omega\mu_1} = \underline{n} \times (\underline{n}_2 \times \underline{E}_2) \frac{K_2}{\omega\mu_2} \quad . \tag{3.59}$$

Expanding, we have typically

$$\underline{n} \times (\underline{n}_o \times \underline{E}_o) = \underline{n}_o(\underline{n}\cdot\underline{E}_o) - \underline{E}_o(\underline{n}\cdot\underline{n}_o) \quad . \tag{3.60}$$

We now resolve $\underline{E}_o$ into components perpendicular and parallel to the plane of incidence and treat the two cases independently.

CASE 1: $\underline{E}_o$ perpendicular ($\perp$) to the plane of incidence

Consequently we have

$$\underline{n}\cdot\underline{E}_{o\perp} = \underline{n}_o\cdot\underline{E}_{o\perp} = \underline{n}\cdot\underline{E}_{1\perp} = \underline{n}\cdot\underline{E}_{2\perp} = 0 \tag{3.61}$$

for in this case $E_{o\perp}$, $E_{1\perp}$ and $E_{2\perp}$ are parallel.

Now $\underline{n}\cdot\underline{n}_o = \cos\theta_o$; $\underline{n}\cdot\underline{n}_1 = \cos(\pi-\theta_1) = -\cos\theta_1$; $\underline{n}\cdot\underline{n}_2 = \cos\theta_2$, (3.62)

so from (3.57) and (3.58) and putting $\mu_o = \mu_1 = \mu_2$ as before,

$$E_{o\perp} + E_{1\perp} = E_{2\perp} \tag{3.63}$$

and $$[- E_{o\perp}(\underline{n}\cdot\underline{n}_o) - E_{1\perp}(\underline{n}\cdot\underline{n}_1)] K_1 = - E_{2\perp}(\underline{n}\cdot\underline{n}_2) K_2 \quad . \tag{3.64}$$

Thus

$$E_{o\perp}\cos\theta_o - E_{1\perp}\cos\theta_1 = E_2\cos\theta_2\frac{K_2}{K_1} \tag{3.65}$$

so solving (3.63) and (3.65) for $E_{1\perp}$ and $E_{2\perp}$.

The reflected wave is given by

$$E_{1\perp} = \frac{K_1\cos\theta_o - K_2\cos\theta_2}{K_1\cos\theta_1 + K_2\cos\theta_2}\cdot E_{o\perp} \tag{3.66}$$

and the transmitted wave is given by

$$E_{2\perp} = \frac{K_1(\cos\theta_o + \cos\theta_1)}{K_1\cos\theta_1 + K_2\cos\theta_2} \quad . \tag{3.67}$$

CASE 2: $\underline{E}_o$ parallel ($\|$) to the plane of incidence.

As $\underline{E}$ and $\underline{H}$ are perpendicular, then for this case, the $\underline{H}$ vectors are perpendicular to the plane of incidence, and also $\underline{n}_o\cdot\underline{E}_o = 0$ since E_o is transverse.

From (3.43) $\underline{H}_o = \frac{K_1}{\omega\mu_1}\underline{n}_o\times\underline{E}_o$.

Thus

$$\underline{n}_o\times\underline{H}_o = \frac{K_1}{\omega\mu_1}[\underline{n}_o(\underline{n}_o\cdot\underline{E}_o) - \underline{E}\cdot(\underline{n}_o\cdot\underline{n}_o)]$$

and hence

$$E_{o\|} = -\frac{\omega\mu_1}{K_1}(\underline{n}_o\times H_{o\perp}) \quad . \tag{3.68}$$

Similarly

$$E_{1\|} = -\frac{\omega\mu_1}{K_1}(\underline{n}_1\times H_{1\perp}) \; ; \; E_{2\|} = -\frac{\omega\mu_2}{K_2}(\underline{n}_2\times H_{2\perp}) \; . \tag{3.69}$$

Typically,

$$\frac{K_1}{\omega\mu_1}(\underline{n}\times E_{o\|}) = -\underline{n}\times(\underline{n}_o\times H_{o\perp}) = -\underline{n}_o(\underline{n}\cdot H_{o\perp}) + H_{o\perp}(\underline{n}\cdot\underline{n}_o)$$

$$= H_{o\perp}\cos\theta_o \; , \tag{3.70}$$

since $\underline{n}\cdot\underline{H}_{o\perp} = 0$, and so from (3.57)

$$[H_{o\perp}\cos\theta_o - H_{1\perp}\cos\theta_1]\frac{\mu_1}{K_1} = H_{2\perp}\cos\theta_2\frac{\mu_2}{K_2} \tag{3.71}$$

and using (3.58)

$$H_{o\perp} + H_{1\perp} = H_{2\perp} \quad . \tag{3.72}$$

Solving (3.71) and (3.72) for $H_{1\perp}$ and $H_{2\perp}$, and putting $\mu_o = \mu_1 = \mu_2$, gives for the reflected wave

$$H_{1\perp} = \frac{K_2\cos\theta_o - K_1\cos\theta_2}{K_2\cos\theta_1 + K_1\cos\theta_2} H_{o\perp} \tag{3.73}$$

and the transmitted wave is given by

$$H_{2\perp} = \frac{K_2(\cos\theta_o + \cos\theta_1)}{K_2\cos\theta_1 + K_1\cos\theta_2} H_{o\perp} \quad . \tag{3.74}$$

Using (3.35), the Law of Reflection (3.55) and Snell's Law of Refraction (3.56), the complex refractive index

$$N_{12} = \frac{K_2}{K_1} = \frac{\sin\theta_1}{\sin\theta_2} \tag{3.75}$$

and we may rewrite (3.66), (3.67), (3.73) and (3.74) as

$$E_{1\perp} = -\frac{\sin(\theta_1-\theta_2)}{\sin(\theta_1+\theta_2)} E_{o\perp} \tag{3.76}$$

$$E_{2\perp} = \frac{2\sin\theta_2\cos\theta_1}{\sin(\theta_1+\theta_2)} E_{o\perp} \tag{3.77}$$

$$H_{1\perp} = \frac{\tan(\theta_1-\theta_2)}{\tan(\theta_1+\theta_2)} H_{o\perp} \tag{3.78}$$

$$H_{2\perp} = \frac{2\sin2\theta_1}{\sin2\theta_1+\sin2\theta_2} H_{o\perp} \quad . \tag{3.79}$$

The equations (3.78) and (3.79) for the $\underline{H}$ vectors may be expressed in terms

of the $\underline{E}$ vectors remembering from (3.43) that

$$|E_{1\parallel}| = \frac{\omega\mu_1}{K_1} |H_{1\perp}| \tag{3.80}$$

giving

$$E_{1\parallel} = \frac{\tan(\theta_1-\theta_2)}{\tan(\theta_1+\theta_2)} E_{o\parallel} \tag{3.81}$$

$$E_{2\parallel} = \frac{2\sin\theta_2\cos\theta_1}{\sin(\theta_1+\theta_2)\cos(\theta_1-\theta_2)} \quad . \tag{3.82}$$

The four equations for the $\underline{E}$ vectors form the well-known Fresnel relations, derived in slightly less general form by Fresnel in 1823, on the basis of his elastic theory of light.

For normal incidence, $\theta_1 = 0$ and consequently $\theta_2 = 0$ and so the Fresnel relations reduce to

$$E_{1\perp} = - E_{o\perp} \frac{N_{12} - 1}{N_{12} + 1} \tag{3.83}$$

$$E_{2\perp} = E_{o\perp} \frac{2}{N_{12} + 1} \tag{3.84}$$

$$E_{1\parallel} = E_{o\parallel} \frac{N_{12} - 1}{N_{12} + 1} \tag{3.85}$$

$$E_{2\parallel} = E_{o\parallel} \frac{2}{N_{12} + 1} \quad . \tag{3.86}$$

The distinction between perpendicular components now disappears and the concept of a plane of incidence becomes inapplicable.

3.5 REFLECTION AT NORMAL AND OBLIQUE INCIDENCE

The reflecting power R_o is defined to be the ratio of the reflected to the incident energy for normal incidence. Thus, from (3.83) and (3.85) we have

$$R_o = \frac{E_{1\perp} \cdot E^*_{1\perp}}{E^2_{o\perp}} = \frac{E_{1\parallel} \cdot E^*_{1\parallel}}{E^2_{o\parallel}} = \frac{N-1}{N+1} \cdot \frac{N^*-1}{N^*+1} \tag{3.87}$$

and with $N = n + ik$,

$$R_o = \frac{(n-1)^2 + k^2}{(n+1)^2 + k^2} \quad . \tag{3.88}$$

For regions of the spectrum where the conductivity σ and hence losses are low, $k^2 << n^2$, hence (3.88) may be modified to assume the form for a non-conducting medium ($N = n$ is real), by neglecting k^2. This leads to

$$R_o\Big|_{\sigma=0} = R'_o = \frac{(n-1)^2}{(n+1)^2} \tag{3.89}$$

$$\text{or} \quad n = \frac{1 + \sqrt{R'_o}}{1 - \sqrt{R'_o}} \quad . \tag{3.90}$$

For the case of oblique incidence we have from (3.76) and (3.81)

$$\frac{E_{1\perp}}{E_{o\perp}} = \rho_s = -\frac{\sin(\theta_1-\theta_2)}{\sin(\theta_1+\theta_2)} \tag{3.91}$$

$$\frac{E_{1\parallel}}{E_{o\parallel}} = \rho_p = \frac{\tan(\theta_1-\theta_2)}{\tan(\theta_1+\theta_2)} \tag{3.92}$$

$$\text{where, via Snell's Law,} \quad \cos\theta_2 = \frac{1}{N}(N^2 - \sin^2\theta_1)^{\frac{1}{2}} \quad . \tag{3.93}$$

Expressing $(N^2 - \sin^2\theta_1)^{\frac{1}{2}} = a + ib$, then

$$a^2 - b^2 = n^2 - k^2 - \sin^2\theta_1; \quad ab = nk \tag{3.94}$$

and with these new variables we may conveniently write (3.93) as

$$\cos\theta_2 = \frac{a+ib}{N} \quad . \tag{3.95}$$

(Ref. Roessler[21])

Thus

$$\rho_s = -\left[\frac{(a+ib) - \cos\theta_1}{(a+ib) + \cos\theta_1}\right] \tag{3.96}$$

and

$$\frac{\rho_p}{\rho_s} = -\left[\frac{(a+ib) - \sin\theta_1\tan\theta_1}{(a+ib) + \sin\theta_1\tan\theta_1}\right] \quad . \tag{3.97}$$

The corresponding power reflectivities are hence

$$R_s = |\rho_s|^2 = \frac{(a-\cos\theta_1)^2 + b^2}{(a+\cos\theta_1)^2 + b^2} \tag{3.98}$$

$$\frac{R_p}{R_s} = \left|\frac{\rho_p}{\rho_s}\right|^2 = \frac{(a-\sin\theta_1\tan\theta_1)^2 + b^2}{(a+\sin\theta_1\tan\theta_1)^2 + b^2} \quad . \tag{3.99}$$

The phase change (ϕ) on reflection at the boundary for normal incidence can be found using (3.83) or (3.85).

The complex reflected amplitude

$$\frac{E_{1\|}}{E_{o\|}} = \tilde{\rho}_o = |\tilde{\rho}_o| \exp i\phi = \frac{n+ik-1}{n+ik+1} \quad , \tag{3.100}$$

$$\text{ie} \quad |\tilde{\rho}_o| \{\cos\phi + i\sin\phi\} = \frac{(n^2-1)+k^2+2ik}{(n+1)^2 + k^2} \quad . \tag{3.101}$$

Comparison of real and imaginary parts yields

$$|\tilde{\rho}_o| \cos\phi = \frac{n^2-1 + k^2}{(n+1)^2+k^2} \quad ; \quad |\tilde{\rho}_o| \sin\phi = \frac{2k}{(n+1)^2+k^2}$$

$$\text{or } \tan\phi = \frac{2k}{n^2-1+k^2} \quad . \tag{3.102}$$

However, from (3.33)

$$\frac{\varepsilon''}{\varepsilon_o} = 2nk;$$

thus

$$\phi = \tan^{-1} \frac{\varepsilon''/\varepsilon_o}{n(n^2-1)+nk^2} \quad . \tag{3.103}$$

For the limiting case $n^2 >> k^2$, we obtain

$$\phi = \tan^{-1} \frac{\varepsilon''/\varepsilon_o}{n(n^2-1)} \quad . \tag{3.104}$$

3.6 INFRARED DISPERSION BY IONIC CRYSTALS

There now follows an outline of the dispersion of infrared radiation by cubic diatomic ionic crystals which possess optical isotropy. This category includes the common alkali halides such as NaCl. The analysis of lattice vibrations in such crystals has been dealt with in depth by various authors (Born and Huang[18]; Donovan and Angress[22]) requiring the sclution of an eigenvalue equation relating a dynamical matrix D to the frequencies $\omega_i(q)$.

In general, for a crystal with n atoms per unit cell, the angular frequency ω has 3n branches. Three of these branches are the so-called acoustic modes identified by the fact that $\omega_i(q) \to 0$ as $q \to 0$. The remaining 3n-3 branches are termed the optic modes and have non-zero values of $\omega_i(q)$ as $q \to 0$. A diatomic crystal thus has six branches, three acoustic and

three optic.

In the long wavelength limit the optical vibrations of a diatomic lattice correspond to atoms of one type moving as a body in anti-phase to atoms of the other kind. The resultant strong electric moment will interact directly with an electric field due to incident electromagnetic radiation. The infrared active frequency branches are modified by the incident radiation and the resulting waves that propagate through the crystal are due to a combination of the EM and mechanical vibrations.

A rigorous treatment of the diatomic dispersion problem must account for this electro-mechanical combination in order that both the lattice vibrations and the optical (radiative) waves, which together form the infrared dispersion, are accounted for.

If $\underline{u}$ represents the displacement of the positive ions relative to the negative ions, a reduced vector $\underline{\omega}$ may be expressed as $\underline{\omega} = \underline{u}/\bar{m}$ where $\bar{m}$ is the reduced mass of the positive and negative ions. The macroscopic equations describing the polar motions are then (Huang[23])

$$\begin{aligned} \ddot{\underline{\omega}} &= b_{11}\underline{\omega} + b_{12}\underline{E} \\ \text{and} \quad \underline{P} &= b_{21}\underline{\omega} + b_{22}\underline{E} \end{aligned} \tag{3.105}$$

where $\underline{E}$ the macroscopic electric field and $\underline{P}$ the dielectric polarisation are related by (3.8). The b coefficients are scalar constants which are characteristic of the solid and furthermore the principle of conservation of energy gives

$$b_{12} = b_{21} \tag{3.106}$$

for the cubic diatomic lattice.

The linearity of the equations of motion implies that anharmonic, higher order terms in the electric moment have been neglected.

A purely electrostatic treatment of the problem, which assumes a Coulomb-type interaction between the ions, fails to take into account the retardation of the interaction forces due to the finite velocity of light. The full electro-mechanical analysis recognises the retardation by solving the two equations of motion simultaneously with the four Maxwell equations (3.16) → (3.19). (Born and Huang[18])

The short range isotropic forces are represented by the coefficient b_{11} whilst the long range forces are represented by an EM field which satisfies Maxwell's equations.

Trial solutions of the form

$$(\underline{\omega},\underline{P},\underline{E}) = (\underline{\omega}_o,\underline{P}_o,\underline{E}_o) \exp i(\underline{K}\cdot\underline{x} - \omega t) \qquad (3.107)$$

are used.

Elimination of $\underline{\omega}$ from the equations of motion (3.105) yields

$$\underline{P} = \{b_{22} + \frac{b_{12}b_{21}}{-b_{11}-\omega^2}\}\underline{E} \qquad (3.108)$$

and comparison with (3.9) gives the dielectric constant

$$\epsilon = \epsilon_o + b_{22} + \frac{b_{12}b_{21}}{-b_{11}-\omega^2} . \qquad (3.109)$$

This dispersion formula is more generally written

$$\epsilon = \epsilon_\infty + \frac{\epsilon_o-\epsilon_\infty}{1 - (\omega/\omega_o)^2} \qquad (3.110)$$

where ω_o is the infrared dispersion frequency, the frequency at which the dielectric constant and refractive index become infinitely large.

Comparison of (3.109) and (3.110) enables us to express the b coefficients in terms of measurable quantities,

$$b_{11} = -\omega_o^2; \quad b_{12} = b_{21} = (\epsilon_o-\epsilon_\infty)^{\frac{1}{2}}\omega_o; \quad b_{22} = \epsilon_\infty-\epsilon_o \quad . \qquad (3.111)$$

Substitution of solutions of the form (3.107) into the system of six simultaneous equations and recognising that $\underline{E}$ cannot vanish as this gives the trivial case $\underline{E} = \underline{H} = \underline{P} = \underline{\omega} = 0$, leads to two alternative possibilities (Born and Huang[18]):

(i) $\underline{\omega}$, $\underline{P}$, $\underline{E}$ and $\underline{K}$ are all parallel and the resulting longitudinal frequencies are given by solution of

$$\omega^2 = -b_{11} + \frac{b_{12}b_{21}}{\varepsilon_o + b_{22}} = \omega_\ell^2 \qquad (3.112)$$

which is a constant independent of $\underline{K}$.

Use of the identities (3.111) leads to the well-known Lyddane-Sachs-Teller (LST) relation

$$\omega_\ell = \left(\frac{\varepsilon_o}{\varepsilon_\infty}\right)^{\frac{1}{2}} \omega_o \quad , \qquad (3.113)$$

or

(ii) $\underline{\omega}$, $\underline{P}$ and $\underline{E}$ are parallel but are perpendicular to $\underline{K}$. The resulting transverse modes are given by

$$\left(\frac{K}{\omega}\right)^2 = \varepsilon_o + b_{22} + \frac{b_{12}b_{21}}{-b_{11}-\omega^2} = \varepsilon_\infty + \frac{(\varepsilon_o - \varepsilon_\infty)}{1-(\omega/\omega_o)^2} \quad . \qquad (3.114)$$

For a given K (3.114) gives two solutions. However, there also exist two alternative orientations of $\underline{K}$ with respect to $\underline{E}$ which maintain their mutual orthogonality. Thus there are two doubly degenerate frequencies and hence four independent transverse vibrational modes. These modes which arise as a result of the long range polarisation of the crystal by the ionic motion are termed polarisation modes. The excitations are neither those of pure phonons or pure photons and the term polariton has come to be used for such a coupled excitation.

Using the dispersion relation (3.110) we may formulate the corresponding reflection spectra from (3.87) the expression for the

reflecting power at normal incidence R_o and remembering that $N^2 = \frac{\epsilon(\omega)}{\epsilon_o}$ from (3.34).

As ω increases, N increases steadily and when ω reaches the dispersion frequency ω_o, $\epsilon(\omega)$ and hence N become infinite and R = 1, ie the crystal becomes a perfect reflector. Past this point $\epsilon(\omega)$ is negative until becoming zero again for a frequency satisfying

$$0 = \epsilon_\infty + \frac{\omega_o^2(\epsilon_o - \epsilon_\infty)}{\omega_o^2 - \omega^2} \qquad (3.115)$$

$$\text{or} \quad \omega = \left(\frac{\epsilon_o}{\epsilon_\infty}\right)^{\frac{1}{2}} \omega_o = \omega_\ell \qquad (3.116)$$

the longitudinal optic (LO) frequency of equation (3.112). Thus between the frequency values ω_o and ω_ℓ the refractive index N is imaginary and there exists a band of perfect reflection. This is known as the Reststrahlen phenomenon.

In real diatomic cubic crystals the observed reflectivities in this region, the characteristic reststrahlen bands, do not agree quantitatively with the above case of an ideal crystal. This is because the dispersion relation (3.110) is incapable of representing the dispersion of a real crystal in the region $\omega \sim \omega_o$. Anharmonic, higher order electric moment terms must be included in the equations of motion to account for energy dissipation.

A more realistic dispersion relation may be obtained by the inclusion of a damping term in the first equation of motion which now becomes

$$\ddot{\underline{w}} = b_{11}\underline{w} - \gamma\dot{\underline{w}} + b_{12}\underline{E} \qquad (3.117)$$

leading to the following relation which includes the effect of absorption in the vicinity of ω_o :

$$\varepsilon(\omega) = \varepsilon_\infty + \frac{\omega_o^2(\varepsilon_o-\varepsilon_\infty)}{\omega_o^2-\omega^2-i\gamma\omega} \quad . \qquad (3.118)$$

However, in reality the damping (γ) may be frequency dependent giving rise to additional structure in the observed spectrum. For most alkali halides γ varies considerably in the LO frequency region and the theory must be modified to account for this.

Two important effects, which are features of real crystals, arise from the inclusion of anharmonic terms in the equation of motion. First, thermal expansion is allowed, and secondly, the anharmonicity leads to interactions between the normal modes. The temperature dependent changes of the normal mode frequencies, ie the phonon energy shifts, of an anharmonic crystal can thus be divided into two parts. The thermal expansion causes changes in the distances and hence the forces between the ions resulting in a temperature dependent change in the harmonic normal mode frequencies. The other contribution arises from the anharmonic interactions between phonons causing a further temperature dependent shift in the normal mode frequencies and this is present even if the crystal is held at a constant volume.

To account for anharmonicity, Maradudin and Fein[24] and Cowley[25] proposed that the dielectric function may be fitted to an oscillator model according to

$$\varepsilon(\omega) = \varepsilon'+i\varepsilon'' = \varepsilon_\infty + \frac{\omega_o^2(\varepsilon_o-\varepsilon_\infty)}{\omega_o^2-\omega^2+2\omega_o(\Delta(\omega)-i\Gamma(\omega))} \qquad (3.119)$$

where the real and imaginary parts $\Delta(\omega)$ and $\Gamma(\omega)$ are, respectively, the frequency dependent self-energy and mode damping functions.

The phonon self-energy shift $\Delta(\omega)$ has two components, Δ^E which is frequency independent and arises from thermal expansion, and $\Delta^A(\omega)$ which

arises purely from the anharmonic interactions. The experimental determination of $\Gamma(\omega)$ and the components of $\Delta(\omega)$ is discussed in chapter 6.

3.7 THE KRAMERS-KRÖNIG DISPERSION RELATIONS

To obtain information on the optical properties of a material from measurements of its power reflectivity spectrum $P(\nu)$, use must be made of Kramers-Krönig (KK) analysis (Kramers[26] and Krönig[27]). A dispersion relation must first be employed to calculate the phase $\phi(\nu)$ from $P(\nu)$. In order to do this with confidence, $P(\nu)$ must be known over a wide frequency range. In practice this is achieved by a combination of measurement and extrapolation. Then from $P(\nu)$ and $\phi(\nu)$, the optical constants, n, k and the related dielectric functions $\varepsilon'(\nu)$ and $\varepsilon''(\nu)$ can be calculated.

However, the method of KK, although successful in many aspects, is an approximation procedure when applied to a truncated spectrum and its use is very precarious; small errors in $P(\nu)$ can lead to very large errors in the final optical property data.

It is principally for this reason that the method of DFTS was developed. Here, the phase is measured directly avoiding the need for extrapolations, wide frequency range measurements and the approximating KK analysis. Since this thesis is chiefly concerned with the method of DFTS, only the basics of the KK analysis are outlined. This section is, however, relevant to the power transmission measurements performed on thin crystals of KDP which are described in chapter 7.

The behaviour of a dielectric under the influence of an electric field is one example of various physical phenomena which can be treated using linear response theory. In general, a system is linear if its

response to the sum of a number of independent applied signals is equal to the sum of its responses to each signal. The linear response may be related to the stimulus or cause by a set of dispersion relations.

For a linear response, we may write

$$g(\omega) = A(\omega)f(\omega) \tag{3.120}$$

where $f(\omega)$ and $g(\omega)$ are generalised input and output functions, and $A(\omega)$ is the generalised response function. The time dependent stimulus $F(t)$ and the response $G(t)$ are then given by the Fourier transforms

$$f(\omega) = \frac{1}{\sqrt{2\pi}} \int_{-\infty}^{\infty} F(t) \exp i\omega t \, dt \tag{3.121}$$

$$g(\omega) = \frac{1}{\sqrt{2\pi}} \int_{-\infty}^{\infty} G(t) \exp i\omega t \, dt \quad .$$

Let us now consider the response $T(t-t')$ produced at time t by a δ-function pulse applied at time t'. The response produced by $F(t)$ is then

$$G(t) = \frac{1}{\sqrt{2\pi}} \int_{-\infty}^{\infty} T(t-t') \, F(t') \, dt' \, . \tag{3.122}$$

The principle of causality implies $T(t-t') = 0$ for $t < t'$ as there can be no response to the pulse until the pulse (or cause) is applied.

To relate the above to the measurements obtained by FTS, we introduce the power reflectivity $R(\omega)$ via the expression for the complex reflection coefficient (2.44)

$$\rho(\omega) = |\rho(\omega)| \exp i\phi(\omega) = \sqrt{R(\omega)} \exp i\phi(\omega) \, . \tag{3.123}$$

For normal incidence reflection at a vacuum/medium interface, $\rho(\omega)$ is given by (3.100) and is an analytic function of the complex valued ω, having no poles in the upper half plane.

A further and obvious condition is that for a finite input signal, the conservation of energy requires that the output signal be less than or equal to the input.

The response function $A(\omega)$ of (3.120), analytic in the upper half plane, may be expressed by the contour integral

$$P\int_{-\infty}^{\infty} \frac{A(\omega_r)}{\omega_r-\omega_o}\, d\omega_r + \lim_{r\to 0} \int_{\gamma} \frac{A(\omega)}{\omega-\omega_o}\, d\omega + \lim_{R\to\infty} \int_{\Gamma} \frac{A(\omega)}{\omega-\omega_o}\, d\omega = 0 \quad . \tag{3.124}$$

The first term is the Cauchy principal integral, denoted by P, along the real $\omega=\omega_r$ axis. The second term is the integral along the contour γ of radius r about the singularity ω_o on the real axis, and the third term is the contribution of contour Γ of radius R as $R\to\infty$.

Evaluation of the integrals leads to

$$P\int_{-\infty}^{\infty} \frac{A(\omega_r)}{\omega_r-\omega_o}\, d\omega_r - i\pi(A(\omega_o) - A(\infty)) = 0 \quad . \tag{3.125}$$

Now we relate the function $A(\omega)$ to the reflectivity via the definition

$$A(\omega) = \ln \rho(\omega) = \ln |\rho(\omega)| + i\phi(\omega) \quad . \tag{3.126}$$

Equating real and imaginary parts of (3.125) and (3.126) leads to

$$\phi(\omega_o) = -\frac{1}{\pi} P\int_{-\infty}^{\infty} \frac{\ln|\rho(\omega_r)|}{\omega_r-\omega_o}\, d\omega_r + \phi(\infty) \tag{3.127}$$

$$\ln |\rho(\omega_o)| = \frac{1}{\pi} P \int_{-\infty}^{\infty} \frac{\phi(\omega_r)}{\omega_r-\omega_o}\, d\omega_r + \log|\rho(\infty)| \quad . \tag{3.128}$$

For real response functions $\rho(-\omega) = \rho^*(\omega)$ and by the choice of phase $\phi(\infty) = 0$, the phase shift dispersion relation of (3.127) may be rewritten

$$\phi(\omega_o) = -\frac{2\omega_o}{\pi} P\int_o^\infty \frac{\ell n|\rho(\omega_r)|}{\omega_r^2-\omega_o^2}\, d\omega_r \quad . \qquad (3.129)$$

The optical constants and the dielectric functions may then be calculated from an expression such as (3.100) which leads to

$$\left[\frac{\varepsilon'(\omega)+i\varepsilon''(\omega)}{\varepsilon_o}\right]^{\frac{1}{2}} = n(\omega) + ik(\omega) = \frac{1+|\rho(\omega)|\exp i\phi(\omega)}{1-|\rho(\omega)|\exp i\phi(\omega)} \, . \qquad (3.130)$$

The KK dispersion relation (3.129) is the relevant one for the power FTS measurements covered in this thesis. Details of the KK analysis and other dispersion relations may be found in a number of books including a conference review edited by Nudelman and Mitra[20].

FIG. 3·1

TYPICAL CONFIGERATION OF $\underline{E}$ AND $\underline{H}$ VECTORS FOR THE CASE OF A PLANE WAVE INCIDENT ON A PLANE BOUNDARY SEPARATING TWO MEDIA 1 AND 2 WITH MEDIUM 2 MORE DENSE IE. $k_2 > k_1$

CASE 1:- $\underline{E}_0$ PERPENDICULAR TO THE PLANE OF INCIDENCE

NOTE REVERSAL OF $\underline{E}$ VECTOR ON REFLECTION, PHASE CHANGE OF π FOR ALL θ_0

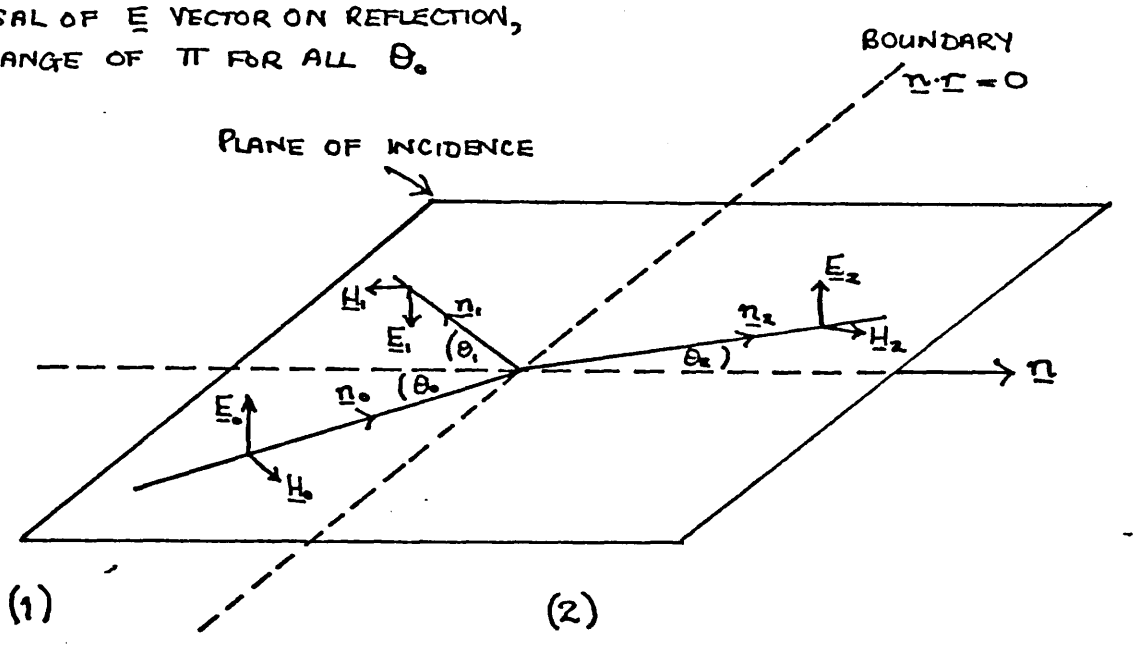

CASE 2:- $\underline{E}_0$ PARALLEL TO PLANE OF INCIDENCE

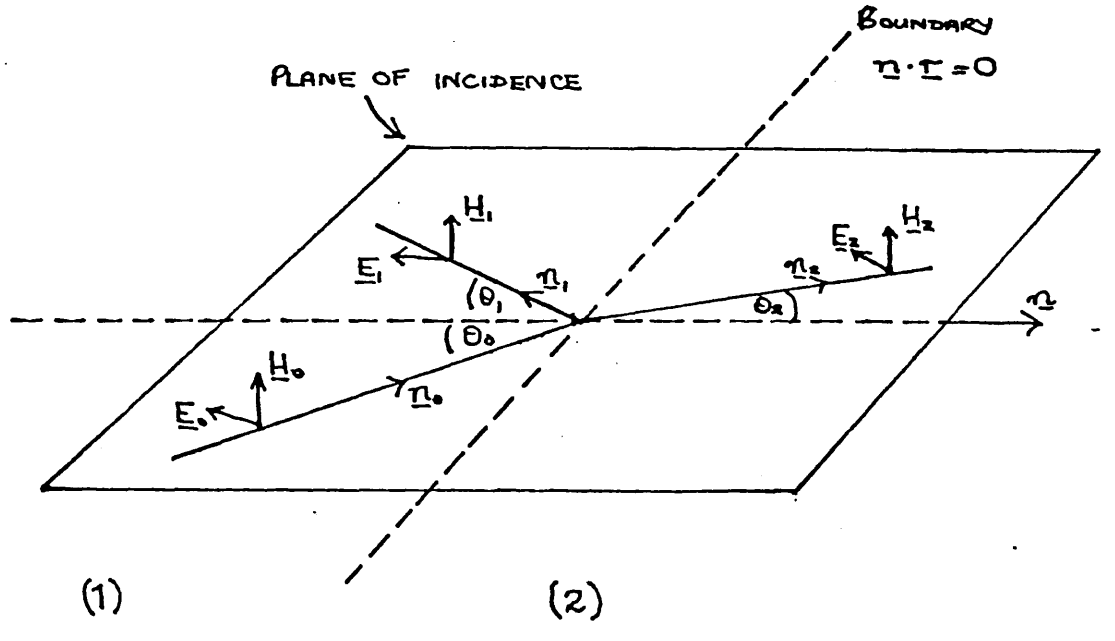

AGAIN, NOTE REVERSAL OF $\underline{E}$ VECTOR ON REFLECTION

CHAPTER 4

THE EXPERIMENTAL APPARATUS

4.1 INTRODUCTION

Two different interferometers were used during the course of the experimental work. The great majority of the time available was spent building and developing the polarising instrument for low frequency measurement. However, the versatility of a conventional power FTS interferometer was exploited in order to obtain the transmission results for thin crystals of KDP.

The chapter commences with a description of this basic power instrument together with a discussion of the limitations one encounters when long wavelength spectral measurement below $\sim 30\ cm^{-1}$ is being considered. There is then a natural progression to a description of the development of the polarising interferometer for DFTS, with emphasis on the way the limitations of the power instrument are overcome in this design.

Various experimental problems that arose are then discussed together with their solutions and the dispersive spectroscopic method of division of the field of view is introduced (Parker et al[10]). The chapter is concluded with a short description of the mode of operation of the recording electronics.

4.2 THE BASIC INTERFEROMETER FOR POWER FTS

The design of both interferometers is based upon the modular units developed by the National Physical Laboratory with the cooperation of Grubb Parsons and Co Ltd (Chantry[28]), and follows very closely that of the original interferometer conceived by Michelson. In addition a large

number of supplementary units which are not commercially available have been designed and built here at Westfield and their compatibility with the basic units enables the interferometer designs to be extended to allow specialised work to be performed.

A typical configuration of the instrument used for general power measurements is illustrated in Fig 4.1. The hub of the design is the central cube which contains the mylar beam divider held vertically along the cube diagonal. The ports in the four vertical faces of the cube allow four extension arms to be bolted on. Essentially these arms house the source, the moving mirror, the fixed mirror and the detector.

The source is a quartz encapsulated mercury lamp which generates broad band submillimetre radiation by thermal emission. The lamp is located in a water-cooled housing and to approximate a point source, the aperture is limited using a cylinder of copper positioned around the lamp with a hole of diameter $\sim \frac{3}{8}$" centred on the optical axis of the instrument. The radiation emerging from this aperture is collimated and caused to be incident upon the beam divider by the joint influence of a parabolic and a plane mirror (M_1 and M_2 in Fig 4.1), which together form the collimator unit.

At the divider the radiation is partially transmitted and partially reflected into the two mirror arms. The movable plane mirror in one arm is mounted on the non-rotating spindle of a micrometer which has a maximum travel of 25 mm and which is driven by a stepping motor. The motor and its associated electronics allow the mirror to move in either direction in steps of length 2.5, 5, 7.5 or 10 μm corresponding to cut-off or aliasing frequencies of 1000, 500, 333 and 250 cm^{-1} respectively. (Ref equation 2.45). For power measurements the mirror in the fixed arm is clamped, but a facility for aligning it to give a maximum throughput signal is provided by a system of three aligning screws.

Following reflection by the two mirrors, the two beams are incident back onto the beam divider where they recombine and interfere according to the difference in the optical paths in the two mirror arms. The recombined beam then passes through a specimen chamber where the optical system focusses it down to be either reflected or transmitted by the sample under investigation. It is then finally refocussed by a Pfund-type all-reflecting condensing system onto the window of a Golay detector.

The Pfund system consists of a plain mirror and a spherical concave mirror (M_3 and M_4 in Fig 4.1), and replaces the pair of polythene lenses which are normally used and which absorb a large proportion of the energy that would otherwise be incident on the Golay nose. Use of the Pfund system in place of the lenses increases the throughput energy of the instrument by more than 100%.

Two important precautionary measures to improve the performance of the apparatus were adopted and were also incorporated into the design of the polarising interferometer.

A temperature stabilising system was installed on the interferometers to reduce thermal expansion or contraction due to ambient temperature changes. Water circulates through pipes attached to the outside of the interferometer and then passes through a radiator and is kept at a temperature of a few degrees above room temperature by a thermostatic heater incorporated in the circulator. Thermal stability is maintained to better than 0.25° C over periods of many hours. This is particularly important for a dispersive instrument such as the polarising one when changes in the overall temperature and differential expansion of the two mirror arms can cause significant errors in the directly measured phase spectra.

The second precaution taken is that the interferometer is evacuated to eliminate water vapour which heavily absorbs the radiation in the far

infrared and which would, if not removed, seriously degrade sample spectra recorded in this region of the spectrum. A water vapour spectrum is included amongst the results (Fig 6.2) and the strong absorption at certain wavelengths is clearly visible. For room temperature work reduction of the pressure tc 10^{-1} Torr is sufficient to remove the absorption effect of the vapour and such pressures are easily obtained with a rotary vacuum pump. However, when low temperature data is being recorded pressures as low as 10^{-5} Torr are required to prevent or at least delay icing-up of the sample surface due to the small amounts of water vapour present even in such a vacuum. This icing-up can have a serious effect on the phase spectrum measured by DFTS especially in the case of alkali halides. A diffusion pump is employed to obtain these low pressures and is situated immediately below the central cube. The modular components have either male or female flanges and an 'O' ring is carried on the male flange. This provides a vacuum tight seal when the male flange is mated and bolted tightly to the female flange.

4.3 FACTORS LIMITING THE PERFORMANCE OF THE CONVENTIONAL INTERFEROMETER

A number of factors exist which limit the working range of the conventional instrument described above.

As previously indicated the detector in standard use is a Golay cell. Amongst its advantages are its convenient size, its ease of operation and the fact that its performance is perfectly adequate for most IR applications. A choice of window materials enables different regions of the IR spectrum to be investigated, the two most commonly used for interferometric studies being diamond and quartz. The diamond Golay has no upper frequency cut-off in the IR, being transparent up to and beyond 10,000 cm^{-1}, apart from an

absorption region between about 1500 and 3000 cm^{-1}. The cheaper quartz Golay has a high frequency cut-off at $\sim$ 250 cm^{-1}.

Below about 30 cm^{-1} the output from the mercury lamp is extremely weak and for accurate spectroscopy below this point the Golay cell must be exchanged for a liquid helium cooled detector. The performance of any detector is characterised by the radiating power "equivalent to the noise of the receiver", a factor termed the Noise Equivalent Power (NEP). This is the average power of sinusoidal modulated radiation which would give a signal equal to the average quadratic value of the detector noise. When defining the NEP, the experimental conditions such as the time constant, the modulation frequency, the temperature and the solid angle employed must be stated. The inverse of the NEP is termed the detectivity, a measure of the quality of the detector (Hadni[29]). The NEP for a typical liquid helium cooled detector is of the order of 1000 times better than that of a Golay, under similar experimental conditions, with a corresponding superior detectivity. Consequently such detectors perform well in this energy starved region. The helium cooled detector used in the laboratory is an Antimony (Sb) doped Germanium (Ge) thermal bolometer manufactured by QMC Industrial Research Limited. This detector has a working range of 2 to 250 cm^{-1}. Other types of liquid helium cooled detector are also available, in particular an Indium Antimonide (InSb) photodetector with a range of 1 to 50 cm^{-1}. Helium cooled detectors are normally only used for special applications, when the performance of a Golay is inadequate, because of the need for cryogenic facilities.

To discriminate against noise inherent in the interferometer, such as lamp fluctuations, the radiation is modulated before reaching the detector and the recording electronics only measures the signal which lies within a small bandwidth around the modulation frequency. This procedure

is discussed in more detail in section 4.8 where the mode of operation of the recording electronics is described. A significant amount of far IR radiation is emitted by the warm walls of the interferometer and by other points in the field of view in addition to the lamp source. Due to the large acceptance angle of the Golay nose (60°), modulation must be performed far enough back along the optical path in the interferometer in order that any stray rays produced by these extraneous sources, that may enter the nose, are unmodulated and thus do not contribute to the measured signal.

Several methods of modulating the radiation may be used. The first and most obvious is amplitude modulation (AM) or chopping, usually performed in the Grubb Parsons system by installing a cylindrical chopper around the lamp. This however has the unfortunate result that a large DC load is carried at the detector as a background to the required signal. The resultant noise and drift of the mean level of the interferogram is often an embarrassment when accurate spectroscopy is required. This DC load may be reduced by chopping in one of the mirror arms though this presents practical problems, in particular microphony effects at the detector due to the vibrations caused by the rotating chopper. Furthermore, by its very nature, AM has the disadvantage that 50% of the lamp energy, or more for a non-ideal chopping system, is immediately extinguished. Its great advantage is that it is frequency independent, and does not impose any envelope or cut-off on the throughput spectrum.

The second form of modulation that has found favour in the last few years after initial development problems, is that of phase modulation (PM). Here the path difference is modulated by a small periodic displacement of one of the interferometer mirrors.

If the modulation function has the form

$$j(ft) = a \sin 2\pi ft \ , \qquad (4.1)$$

where 'a' is the maximum amplitude of vibration of the mirror, then the time dependent signal from the detector is a modified form of (2.2)

$$V(x,t) \sim P(\nu) \cos\{ 2\pi\nu (x + a \sin 2\pi ft)\} \quad . \qquad (4.2)$$

The time dependent parts of this function are complicated and the coefficients of their Fourier components are Bessel functions. The pass band of the electronics may be arranged so as to include only the first order and the resulting interferogram adopts the form (Chantry[28], Chamberlain[30])

$$I(x) \sim \int_0^\infty P(\nu)\, J_1(2\pi\nu a) \sin 2\pi\nu x \, d\nu \quad . \qquad (4.3)$$

Thus the effect of sinusoidal PM on the throughput spectrum is to impose on it a Bessel function envelope. The Bessel function $J_1(2\pi\nu a)$ has its first zero at $\nu = 0$ and next zeroes at a frequency given by $2\pi\nu a = 3.84$ (Chamberlain[30]). Use of PM thus impairs the low frequency side of the throughput spectrum, although it does have a number of distinct advantages over AM.

In the region of the primary maximum of the Bessel function the modulation approaches 100%, a vast improvement on AM. Furthermore, the DC contribution to the signal is unmodulated so drift problems are eliminated and the noise due to source fluctuations is greatly reduced. The vibrational problems associated with the chopper in AM do not occur and finally the frequency dependent nature of the Bessel function provides a non-absorptive method of limiting the frequency range of the instrument. For good quality spectroscopy it is usually an advantage to limit the throughput profile to the spectral range of interest. Since the Bessel function maximises and zeroes at frequencies dictated by 'a' the amplitude of vibration of the mirror, then changing 'a' by altering the power provided by the oscillator drive unit enables the response in a particular frequency region to be

optimised. Thus, for instance, improved low frequency performance may be obtained by increasing the vibrational amplitude to shift the primary maximum and hence the peak of the measured energy spectrum to lower wave numbers. The pass band however is consequently progressively reduced in width and the resultant lack of "high" frequency modulated energy required for aligning purposes can be a great handicap when DFTS measurements are performed as the quality of the optical alignment is dependent on the highest frequency present.

It is of interest at this stage to compare the interferograms obtained using AM and PM. The two situations are illustrated in Fig 4.2. The AM interferogram is symmetrical about the position of zero-path difference (ZPD) and has a mean background level of ideally half the value of the central maximum. The PM interferogram of (4.3) is, however, antisymmetrical about ZPD and has a mean level of zero as there is no DC contribution to the signal. The interferogram of (4.3) involves sine rather than cosine terms, but it is just as readily Fourier transformed using the complex transform of equation (2.57).

Apart from the use of Golay detectors and phase modulation, a third limitation on the working range of the conventional interferometer is caused by the use of dielectric beam dividers. These are usually made of mylar (polyethylene terepthalate) and are stretched taut on a metal frame which locates into a slot cut across the diagonal of the central cube.

Since the divider is parallel sided the phenomenon of multiple internal reflection occurs. Hence, not only the primary reflected and transmitted beams must be considered but all the other beams produced by internal reflection as well. It is obviously necessary to determine which, if any, of the secondary and higher order beams are of sufficient magnitude to be important. Bell[15] has shown that for an unpolarised beam of radiation incident at 45° upon a mylar beam divider, the primary

transmitted beam contains about 83% of the incident flux whereas the secondary transmitted beam contributes a mere 0.7%, a negligible amount. The primary, secondary and third order reflected beams respectively contain 8.9, 7.4 and 0.07% of the incident intensity. Hence, only the two primary beams and the secondary reflected beam are significant. For these calculations the refractive index of the mylar was taken to be 1.85 and the divider was assumed to be non-absorbing whereas in practice, absorption occurs.

As the magnitudes of the two reflected beams are nearly equal and a definite phase relationship exists between them, these two components interfere. This interference occurs upon each reflection by the divider.

For external and internal reflection by the divider the phase shifts are π and zero respectively. If d is the thickness of the mylar and n the refractive index, then the condition for interference between the two reflected components is (Bell[15])

$$m\lambda = 2d\,(n^2-\tfrac{1}{2})^{\frac{1}{2}} \qquad (4.4)$$

where for destructuve interference m = 0, 1, 2, 3 ....
and for constructive interference m = $\frac{1}{2}$, 3/2, 5/2 ... .

Equation (4.4) essentially governs the efficiency of the beam divider. The efficiency at $\nu = 1/\lambda = 0$ is zero as one reflected component has a phase shift of π with respect to the other and they thus interfere destructively. The other minima are predicted by (4.4) with m = 1,2 etc. The first order interference fringes, ie those lying between m = 0 and m = 1, for a number of different thicknesses (d) of mylar are illustrated in Fig 4.3. Clearly, when measurements are performed using an interferometer equipped with a mylar or similar dielectric beam divider, the thickness d must be chosen so as to optimise the throughput energy in the spectral region under

investigation. By the use of thicker and thicker mylar, the low frequency performance of the instrument may be improved although as Fig 4.3 shows, the instrumental bandwidth dictated by the first order interference fringe progressively narrows. Consequently, such dielectric beam dividers are far from ideal for long wavelength measurements below $\sim$ 20 cm^{-1}.

Some other properties of dielectric beam dividers are worth mentioning at this stage prior to discussing possible solutions to the problems they cause.

The beams in the two arms of a conventional interferometer each undergo one transmission and one reflection before reaching the detector. Assuming unit incident intensity and that the non-absorbing beam divider has power transmission and reflection coefficients T_o and R_o respectively, then the intensity falling on the detector is $2R_oT_o$ and that lost back to the source is $R_o^2 + T_o^2$. The maximum of $2R_oT_o$ occurs for $R_o = T_o = 0.50$ and hence the maximum efficiency of even a perfect Michelson is only 50%.

The reflected and transmitted powers are given by the Fresnel relations (section 3.4) and are dependent on the angle of incidence. Hence, if a beam of unpolarised radiation is incident upon a dielectric divider, the reflected and transmitted beams are partially polarised. For mylar, the well-known Brewster angle θ_p (given by $\tan\theta_p = n$, where n is the refractive index), the angle for which the reflected radiation is 100% perpendicularly polarised, is approximately 60^o. So with beam dividers used in practice at the convenient angle of 45^o to the incident beam, a considerable degree of polarisation occurs in the emerging recombined beam. The experimental polarising ratio of the parallel and perpendicular components in the beam at the detector for the power instrument with a 12.5 μm mylar divider is shown in Fig 4.4. The most extreme ratio is $\sim$ 2:1 in favour of the vertical component, ie the

component perpendicular to the plane of incidence.

To summarise this section, the main problems that restrict the range of the conventional instrument and in particular impair its performance at the important low frequency end of the IR are the following. First, the high NEP of the Golay detector which severely limits its use at frequencies < 30 cm^{-1}, due to the extremely low lamp energy in this region. This may be overcome by the use of a liquid helium cooled detector with its vastly superior detectivity. Secondly, the use of phase modulation which imposes an envelope function on the throughput spectrum. PM may, however, be "tuned" to the low frequency region provided the resultant narrow bandwidth can be tolerated. Otherwise, frequency independent AM may be used as long as the associated noise levels and drift can be adequately suppressed. Finally, due to multiple internal reflection in the dielectric beam divider, the divider efficiency and consequently the throughput of the instrument is extremely frequency dependent. It is zero at zero frequency and has additional minima at frequencies inversely proportional to the beam divider thickness (4.4).

This last problem has been surmounted by the use of polarising interferometers, several configurations of which have been recently developed, eg Martin[13]. These employ one or more wire grid polarisers as beam dividers, resulting in greatly improved low frequency throughput. The following sections describe the layout and mode of action of the polarising interferometer developed by the author at Westfield College.

4.4 THE POLARISING INTERFEROMETER

The fundamental design of the polarising interferometer developed was formulated by Chamberlain at the National Physical Labotatory (see

for example Chamberlain et al[6]). Its principal advantages over other types of polarising interferometer are first that the radiation is incident normally on the specimen, and secondly its relative simplicity. As a result, few modifications are required to the dispersive "mylar" interferometer developed by Parker which has been successfully employed to obtain a variety of DFTS results in the range 30 to 500 cm^{-1} [9,11].

The layout of the polarising instrument is illustrated in Fig 4.5 and the photograph Fig 4.6 which shows an updated form of an earlier version[31]. Many of the modular components are identical to those previously described for the power instrument. The major difference is the use of two "central cube" units each containing a wire grid polariser.

The Pfund type "all-reflecting" condensing optics was designed to replace the polythene lenses used in the earlier version[31]. Since, as will be shown in the following section, the grid polarisers themselves act as low pass filters, none of the usual polythene filters to suppress the near IR and protect the Golay from overload, are required. Thus, removal of the lenses eliminates all absorbing material from the path of the radiation from source to the detector window excepting, of course, the sample under investigation, and consequently troublesome polythene absorption lines do not appear in the measured spectra. The Pfund system was designed to be compact since pressures as low as 10^{-6} Torr were required and so it was desirable that the volume of the instrument to be pumped was kept to a minimum. A compromise had to be made between the compactness and the need for space to arrange the optics so as to minimise off-axis aberrations. This was achieved by choosing a concave mirror (M_1 in Fig 4.5) with $f = 10$ cm and $r = 2.5$ cm.

Phase modulation was originally provided by mounting the moving mirror on the cone of a loudspeaker. This arrangement, which worked within the

tolerances required of the quality of the oscillations, is shown in Fig 4.7. The loudspeaker is bolted to an adjustable jig mounted on the micrometer spindle and the plane of the mirror was aligned normal to the axis of the spindle by spinning the complete assembly slowly on a lathe.

The proposed use of a liquid helium cooled detector initiated a change in the PM arrangement. The noise which occurs in the recording electronics is not "white" but varies inversely with the frequency of modulation. It is thus desirable to use as high a chopping frequency as possible to avoid excessive noise though this frequency is limited by the response time of the detector. For the Golay, a frequency of $\sim$ 16 Hz is used and cannot be greatly exceeded. However, the response time of a typical helium cooled detector is much faster ($\sim$ 1 μs) and hence much higher modulation frequencies (up to $\sim$ 800 Hz with some detectors) may be used, with a corresponding decrease in noise. The performance of the loudspeaker at such high frequencies over long periods of time was suspect and so a more robust commercial vibrator was used. This necessitated a change in the design of the moving mirror arm. The vibrator could not be attached to the micrometer spindle but was housed in a right-angled unit half-way along the arm and vibrated a plane mirror at 45° to the propagation direction. This angle could be adjusted using a system of aligning screws.

The temperature of the interferometer was stabilised to within $0.25^{\circ}C$ using a thermostatically controlled water supply circulating through tubes attached to the arms, cubes and lamp housing, a system similar to that used on the power instrument. The interferometer could be evacuated to $\sim 10^{-6}$ Torr using a diffusion pump. This pump was situated beneath the cube to which the two arms were attached so as to be as near the sample as possible.

The arm that contained the fixed mirror or sample was designed so that the DFTS technique of "Division of the field of view" developed by

Parker et al[10] could be adopted.

The fixed reflector was held in a copper mount (Fig 4.8). This was attached by means of thermally isolating nylon bolts to a sensitive micrometer alignment mechanism in the specimen chamber (Fig 4.10) and could be aligned in vacuum by the use of feedthrough adjusters in the chamber lid. Using this arrangement the fixed reflector could be accurately aligned with a precision of better than 0.15 μm at any temperature between 90 and 300K. Changing the reflector was a simple task and it could also be rotated through any angle without first being removed from the mount, a great advantage when studying the different axes of ferroelectric crystals.

The direct measurement of phase by DFTS requires replacement of the fixed mirror by the sample, between recording calibration and sample interferograms, to a high degree of accuracy. The phase error due to a misplacement was calculated in section (2.5), from which it follows that typically replacement to within 0.2 μm (ie ±0.1 μm) results in a phase accuracy of $\sim \pm 1.5^{\circ}$ at 100 cm^{-1}.

DFTS measurements have been undertaken by a number of workers using the obvious method of accurately replacing the fixed mirror by the sample. Birch et al[7] have designed a counter-balancing support system for the fixed reflector which enables replacement to be made to better than 0.1 μm and allows this replacement to be performed inside the evacuated interferometer. There are, however, two major problems: the sinkage of soft specimens on the reference supports and the fact that since the crystal must remain "free", it is not possible to perform low temperature measurements requiring good thermal linkage between the sample and a liquid nitrogen dewar. Other workers have tried similar methods and met the same problems and more besides.

Although when using the copper mount, the reflectors in the fixed

arm could not be replaced to within the limits set by the desired phase accuracy, use of the division of the field of view technique developed by Parker et al[10] gave reproducibility of phase measurements to within $\pm 1^{\circ}$. It also solved the problems met by other workers.

Low temperature results were obtained by connecting the back of the mount to the base of a nitrogen "cold finger" dewar using a thick piece of copper braid (Fig 4.8). A feedback system comprising a 40 W thermostat heater mounted on the back of the sample mount and controlled by a cryogenic temperature unit, and two copper-constantan thermocouples held the sample at the required temperature. Stability to $\sim$ 0.1K could be obtained in practice anywhere between 90 and 300K. This was achieved within 5 minutes for small temperature steps $\sim$ 25K and took up to 30 minutes for changes of $\sim$ 150K.

4.5 THE TECHNIQUE OF DIVISION OF THE FIELD OF VIEW

The division of the field of view technique was utilised in the following way. With reference to Fig 4.9, the outer ring X of the optically flat sample was aluminised in an evaporator using a mask to cover the inner circle Y which thus remained as exposed sample surface. By an arrangement of opaque screens located in a screen unit between the wire grid and the specimen chamber (Fig 4.11) which could be slid into position from outside the interferometer when it was evacuated, each of the areas X and Y could in turn be used as the fixed reflector. The geometry of the screens is illustrated in Fig 4.9 and was such that the possibility of cross-talk between the areas X and Y was eliminated.

A set of data was recorded in the following manner. First, with the fixed mirror installed in the mount, the outer area X was used to align

its surface perpendicular to the incident beam. This was achieved by maximising the detector signal at the grand maximum of the PM interferogram near the zero path position with the moving mirror at a sampling point. Having a large radius the area X provides a very reproducible alignment. Interferograms were then recorded from part X and by moving the screens, part Y. The interferograms were Fourier transformed and the resulting amplitude and phase spectra (r_X,ϕ_X and r_Y,ϕ_Y) ratioed to give a complex calibration spectrum (r_Y/r_X and $\phi_Y-\phi_X$). The experiment was then repeated using the sample in place of the mirror. The sample was again aligned on the aluminised outer ring X and two more interferograms recorded from area X and area Y, the exposed sample surface. These interferograms were also Fourier transformed and the ensuing complex spectra (r'_X, $'_X$ and r_S,ϕ_S) were ratioed to give the complex reflection spectrum of the sample (r_S/r'_X and $\phi_S-\phi'_X$). Then, systematic errors caused by asymmetry between the areas X and Y and differences in the two arms were reduced by re-ratioing against the calibration spectrum. Thus the corrected amplitude and phase sample spectra are

$$r = \frac{r_S/r'_X}{r_Y/r_X} \quad \text{and} \quad \phi = (\phi_S-\phi'_X) - (\phi_Y-\phi_X) \,. \qquad (4.5)$$

In this way the sample phase spectrum was measured directly though a correction had to be made (see section 2.5) to allow for the thickness of the aluminising film. The thickness of the film introduces an undesirable problem. Typically films laid down by the evaporator have a thickness $\sim$ 0.2 μm. However, at 300K the skin depth (d) for aluminium at 100 cm^{-1} is $\sim$ 0.05 μm and at 10 cm^{-1} increases to $\sim$ 0.165 μm[32]. Thus the use of films $\sim$ 0.2 μm thick could lead to significant errors in the measured amplitude particularly at low frequencies ($d \propto \sqrt{\lambda/\sigma}$ where σ is the conductivity). For example, with a deposition which corresponds to 2d for a wavelength λ, the reflectivity from the aluminium which should be 100% to

match that from the mirror is low by an amount $(1/e)^2 \sim 13\%$ at that point in the spectrum. Increasing the thickness to 4d reduces the error to less than 2%, a figure comparable to the reproducibility of repeated amplitude spectral measurements. Hence, for measurements below 100 cm^{-1} the film thickness should be at least ~ 0.5 μm thus requiring a large phase correction ($\sim 3.6^{\circ}$ at 100 cm^{-1}). When the specimen is cooled for low temperature measurements, the situation improves since the conductivity σ increases leading to a reduction in the skin depth.

Thus the division of field technique eliminates the need for exact replacement of the fixed mirror by the sample.

Certain precautions were taken to minimise other systematic errors. Backlash errors due to the micrometer were minimised by scanning each interferogram in the same direction. Also, each interferogram commenced at the same sampling point which could thus be used as the phase reference. A manual single step trigger in the stepping motor drive circuit enabled the starting point to be chosen conveniently. The method itself reduces the effects of any systematic changes in the lamp intensity between the mirror and sample runs. However, the effects of fluctuations in the lamp output during the time taken to record a pair of runs from areas X and Y contributed to noise in the usual way.

The method does, however, have drawbacks. Firstly, a series of four interferograms is required, each of which is in practice recorded a number of times and averaged to reduce the noise. Also, the measured reflector areas are reduced by the use of the screens. The excessive cost and general unavailability of some of the crystals measured necessitated using small samples. The crystals used were either 1" diameter or 1" square and were aluminised so as to leave a 0.6" diameter exposed area of the sample surface at the centre. However, despite the small reflector areas,

the phase reproducibility appeared to be limited, not by lack of energy, but by flatness of the specimen surface, typically $\sim \pm 0.2$ μm, and by the flatness of the wire grids, a problem discussed in the following section.

In addition to the division of field technique, a simpler method which did not require four different interferograms was employed. Interferograms were recorded from the whole unaluminised sample surface which was then replaced by the fixed mirror from which interferograms were also recorded for calibration purposes; no screens were used at all. When the spectra obtained by Fourier transform from these sample and mirror interferograms were ratioed, a true measurement of the sample amplitude reflection spectrum was obtained. This was providing the lamp intensity and various other experimental factors did not change significantly between the sample and mirror measurements. However, as the sample surface had not been, indeed could not be, replaced exactly by the mirror surface, the phase spectrum obtained had to be corrected for the error in the zero path. Knowledge of the exact phase at a particular point obtained from spectra measured using the division of field technique enabled this correction to be made.

The advantages of this method were that, unlike in the division of field technique where about 50% of the sample surface was covered by the aluminising layer, the whole of this surface could be utilised for the recording of sample data, thus giving a large increase in the reflected energy. In addition, only two different interferograms were required to achieve a final result, though prior knowledge of certain phase points was required. The two techniques thus go hand-in-hand.

4.6 WIRE GRID POLARISERS AND THE MODE OF ACTION OF THE POLARISING INTERFEROMETER

Some of the earliest experiments with wire grids were performed by Hertz at the turn of the century using short wavelength radio waves ($\lambda \sim$ 1 cm). If d is the distance between the centres of adjacent wires of the grid, Hertz demonstrated that for $\lambda \leq d$ the transmitted radiation is partially polarised whilst for $\lambda \geq d$, it is completely polarised with the electric vector E perpendicular to the wires. The reflected radiation is always completely polarised with E parallel to the wire direction. In practice the polarisation is never 100%; however, in general it is typically of the order of 95%, enough to justify ignoring the minor component.

The electromagnetic theory of the polarising action of such grids has been discussed by a number of authors by analogy with a transmission line problem. The theory explains why the E vector parallel to the wires is reflected and that perpendicular is transmitted with constant efficiency up to a frequency $\sim 1/d$, in fact in practice $\sim 1/2d$. The expressions for the transmittances of the polarising grid for radiation with E perpendicular and parallel to the grid lines have been derived by Marcuvitz[33] and tested experimentally by Auton[34]. The grids and the more complex meshes have been used in various aspects of IR spectroscopy for a number of years (Vogel and Genzel[35], Martin and Puplett[13]).

The polarising interferometer employs two grid dividers, one in each central cube unit, a configuration similar to that first used by Chamberlain et al[6]. The grids are constructed of 10 μm tungsten wire wound with a spacing of 25 μm using a technique developed at the National Physical Laboratory[36]. Hence the interferometer has a constant transmissivity up to frequencies in excess of 200 cm^{-1} eliminating the internal reflection problem associated with dielectric dividers which

leads to a frequency dependent transmissivity in this range.

For use in the polarising interferometer, one grid is wound with the wires vertical (grid A in Fig 4.5), and the other (grid B) so that its wires lie at 45° with respect to the wires in grid A. As the grid frames are held across the cube diagonals, grid B must be wound at an angle $\tan^{-1}\frac{1}{\sqrt{2}} = 35^{\circ}\ 16'$ on the divider frame in order that the incident radiation "sees" the wires at an effective angle of 45°. Improved "high" frequency performance is obtained by winding grid A vertically as opposed to horizontally since, as it lies across the cube diagonal, the effective spacing "seen" by the incident radiation is a factor $\frac{1}{\sqrt{2}}$ times the real spacing.

The grids are wound concurrently onto frames which are a slightly modified form of those used for the dielectric beam dividers. One half of each of the frames is clamped at the appropriate angle to either side of a winding jig which is slowly rotated on a lathe. The tungsten wire is held in a tensioned bobbin which traverses the length of the jig such that the wire winds around the jig and frames with the desired spacing. On completion of the winding across the whole frame aperture of 4" diameter, the other two halves of the frames are carefully bolted to the halves lying on the jig, the wires being held in position by an 'O' ring contained in the top half frame. A solution of "Durofix" adhesive and acetone is then dripped onto the wires around the outside of the frames to ensure they are firmly secured and then the wire is cut so that the complete grids may be lifted away from the jig. A grid wound in this manner is shown in Fig 4.12.

To maintain plane wavefronts upon reflection and thus minimise errors in the directly measured phase spectra, it is obviously important for the grids to be as flat as possible. This was found to be a critical

factor in the performance of the instrument along with the flatness of the reflecting surface of the specimen.

To improve the flatness of the grid across the important central area a simple tensioning system was installed on the grid frames. This system consisted of a brass annular ring of 2.5" diameter, one side of which was lapped and pressed gently against the grid wires by means of three copper spring strips. The arrangement, which may clearly be seen in the photograph of Fig 4.12, markedly improved the reproducibility of the alignment of the specimen and consequently the accuracy of the measured phase spectra.

The polarising action of the interferometer can be briefly summarised as follows. With reference to Fig 4.5, having emerged from the collimator, the unpolarised radiation is incident upon the grid A which reflects a plane polarised beam towards grid B, the wires of which are at 45° to the plane of polarisation of the incident radiation. The component of this radiation with its E-vector perpendicular to the grid wires is transmitted into the moving mirror arm, whilst the parallel component is reflected into the fixed arm. Following reflection from the moving mirror and fixed reflector, the beams follow the same transmission and reflection laws on their return to B and pass on to grid A which now acts as an analyser. The components of each beam with their E-vectors perpendicular to the wires of A are transmitted by A and interfere according to the difference in the optical paths of the two beams in the instrument. Thus an interferogram is obtained in the usual way by displacing the moving mirror about the position of zero path difference. An advantage of this arrangement is that the radiation in the fixed reflector arm is plane polarised and so no additional polariser is required when single axis measurements on certain samples are performed.

A more detailed analysis of this polarising action is presented with the aid of the vector diagrams illustrated in Fig 4.13. This clearly shows

why the interference function has a dark fringe, ie a minimum, at the position of zero path difference when amplitude modulation is used.

Empirical curves illustrating the performance of wire grids similar to the type used in the polarising interferometer may be found in a paper by Costley et al[36].

4.7 ADDITIONAL EXPERIMENTAL METHODS AND PROBLEMS

The importance of the temperature stability of the instrument for DFTS measurements has already been stressed. Differential expansion between the two arms can cause severe errors in the measured phase spectra. The water circulation system stabilised the temperature of the overall interferometer to better than $\pm 0.25^{\circ}C$ over a period of many hours. For low temperature measurement the sample temperature could be held to $\sim$ 0.1K anywhere between 90K and 300K. To check the stability of the apparatus the detector signal at a sampling point near the position of ZPD was monitored over a period of time. As the chosen point lay between the grand maximum and the grand minimum of the phase modulated interferogram it was extremely sensitive to instability. In practice, fluctuation and drift of the signal were negligible provided the apparatus had been allowed sufficient time to stabilise. The time allowed was generally $\sim$ 12 hours after having turned on the apparatus which, during a course of measurements, was probably not turned off again for a few weeks.

Another possible source of significant phase errors was the flatness of the mirrors and samples used in the interferometer. All the mirrors used were flat to better than ± 0.1 μm. Simple geometrical considerations show that finer tolerances are required of the flatness of the 45° vibrating mirror in the moving mirror arm and so it is particularly important that this mirror is as flat, if not flatter, than the other interferometer mirrors.

The samples could often not be polished commercially to better than ±0.2 μm and thus the accuracy of phase measurement was determined by sample flatness and the aforementioned flatness of the wire grids.

To prevent warping, both the samples and the mirrors used were $\geq$ 5 mm thick to ensure that the carefully prepared surface flatness was maintained. Care had to be taken when performing measurements on the alkali halide CsI because of its hygroscopic nature. To avoid deterioration of the reflecting surface prolonged exposure of the crystal to the air was avoided.

Any parallel-sided piece of material in the optical path of the interferometer with an optical thickness (t) less than that corresponding to the distance scanned by the moving mirror gives rise to spurious signals or "signatures" at positions ±t either side of the zero path on the recorded interferogram, due to multiple reflection. These signatures can have a harmful effect on spectra, being difficult to ratio out between mirror and sample runs. In many interferometers the cause of the trouble can lie with thin filters but no filters were used in the polarising instrument though signatures were present at a distance ±1.2 mm from the zero path. At first the quartz envelope of the lamp was suspected and so a dimpled lamp was fitted but the problem still existed. It was finally traced to multiple reflections in the quartz window of the Golay detector. To avoid signatures or the need for extreme care to ratio them out, the interferograms were recorded within the limits imposed by the signatures giving a maximum resolution $\sim$ 5 cm^{-1}, sufficient for most measurements undertaken. However, for higher resolution a Golay with a wedged nose window (4°) was available. The water vapour spectrum of Fig 6.2 resolved to better than 1 cm^{-1} clearly shows the ability of the interferometer to attain such resolutions when the signatures on the interferograms are carefully ratioed out.

A particular advantage of the design of this polarising interferometer

is that by replacing grid A by a mirror, an aluminised mylar beam divider being used in practice, and grid B by a mylar beam divider, transferring the Golay to the vacant part of the other cube converts the instrument to the more conventional dispersive Michelson[11]. Thus changing the thickness of the mylar beam divider enables a new range of frequencies in excess of the 240 cm^{-1} attainable with the grids, to be studied.

4.8 THE RECORDING ELECTRONICS

The recording electronics used for both the power and the polarising interferometers was basically identical, though different sampling techniques could be employed leading to improved results in certain circumstances.

The signal due to the modulated radiation falling on the detector passes on to be rectified by a phase sensitive detector (PSD). In order to operate the PSD, a reference voltage which is coherent with the signal to be measured, is required. This reference is derived from the power oscillator which drives the phase modulated mirror and is passed through a phase-shifter where it is phase-matched to the signal. The resultant output comprises a DC voltage proportional to the required component of the signal and also AC components due to noise which are filtered using a low pass RC filter of variable time constant. These AC noise components are not coherent with the reference and the response of the electronics to the noise depends on the time constant τ of the PSD, which acts as a selective rectifier of bandwidth $1/\tau$. If τ is chosen to be long, to make the bandwidth narrow, the spectrum must be recorded slowly in order that sharp features are properly observed. There is usually an optimum time constant, a compromise between noise reduction and the time taken to record the whole interferogram.

The PSD also responds to frequencies corresponding to odd harmonics of the reference, and noise bands centred on these frequencies are recorded but with reduced sensitivity. This extra noise is usually negligible but can be eliminated by altering the frequency response of the electronics.

The output from the PSD, which has acted as a Fourier analyser, is passed to both a digital voltmeter (DVM) and a chart recorder. The sampling sequence is dictated by an electronic triggering unit. First, the moving mirror is stepped; there then follows a short delay during which time the signal to the PSD rises exponentially under the action of the RC filter. After this set delay which may be varied but is held accurately constant for a series of measurements, the signal on the DVM is read and recorded on paper tape for analysis by computer. There then follows a further short delay before the mirror is stepped again and the cycle is repeated.

The electronic trigger units, the paper tape punch drive and the stepping drive were all built in the Electronics Workshop at Westfield.

The stepping time interval and the PSD time constant are inter-related and both are chosen to give an adequate signal to noise ratio for the spectrum recorded with the required resolution, whilst not allowing the total scan time to be prohibitive.

The electronic recording system used is shown in the block diagram of Fig 4.14. A slightly different recording system was available in the laboratory and was sometimes employed. The analogue signal from the PSD is converted to a square wave of frequency proportional to the analogue signal which passes to a frequency counter to which an oscillator is connected. After a short delay from the time the mirror steps, the PSD integrates the signal for a certain "integration" time which can be varied, whilst the frequency counter, triggered by the oscillator counts the pulses proportional to the input signal over this time period. The result is then punched onto the paper tape and the sequence repeated until the scan is complete.

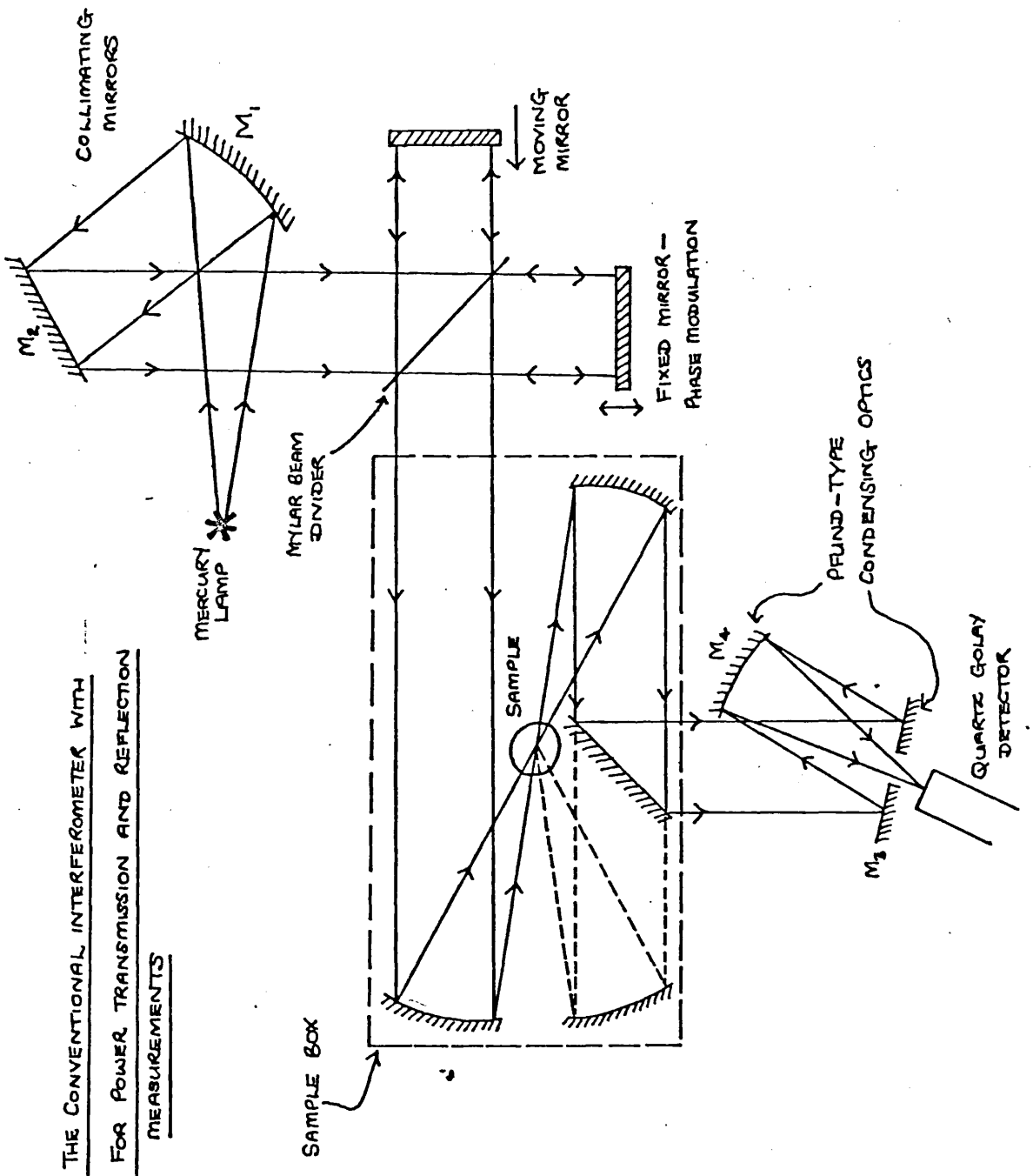

FIG. 4.1 THE CONVENTIONAL INTERFEROMETER WITH SAMPLE BOX FOR POWER TRANSMISSION AND REFLECTION MEASUREMENTS

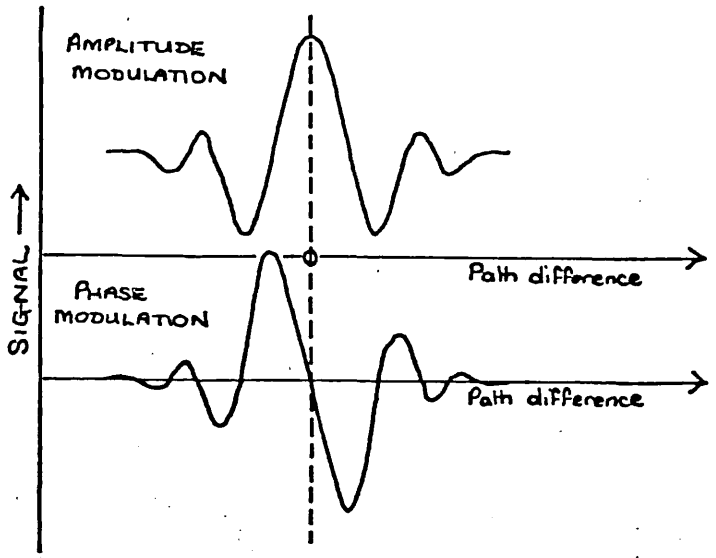

FIG. 4.2 TYPICAL AMPLITUDE AND PHASE MODULATED INTEREROGRAMS NEAR THE POSITION OF ZERO PATH DIFFERENCE

FIG 4.3.

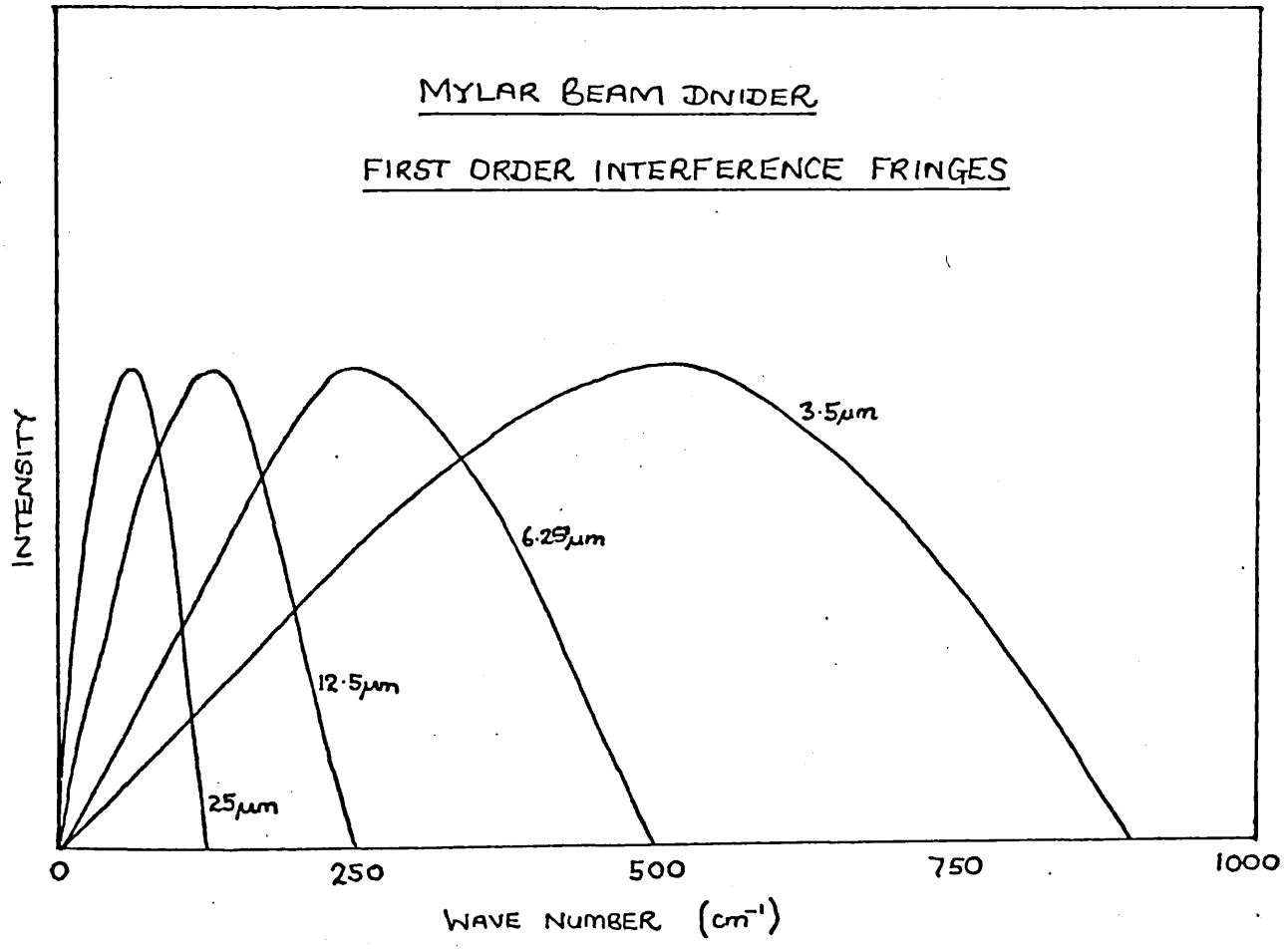

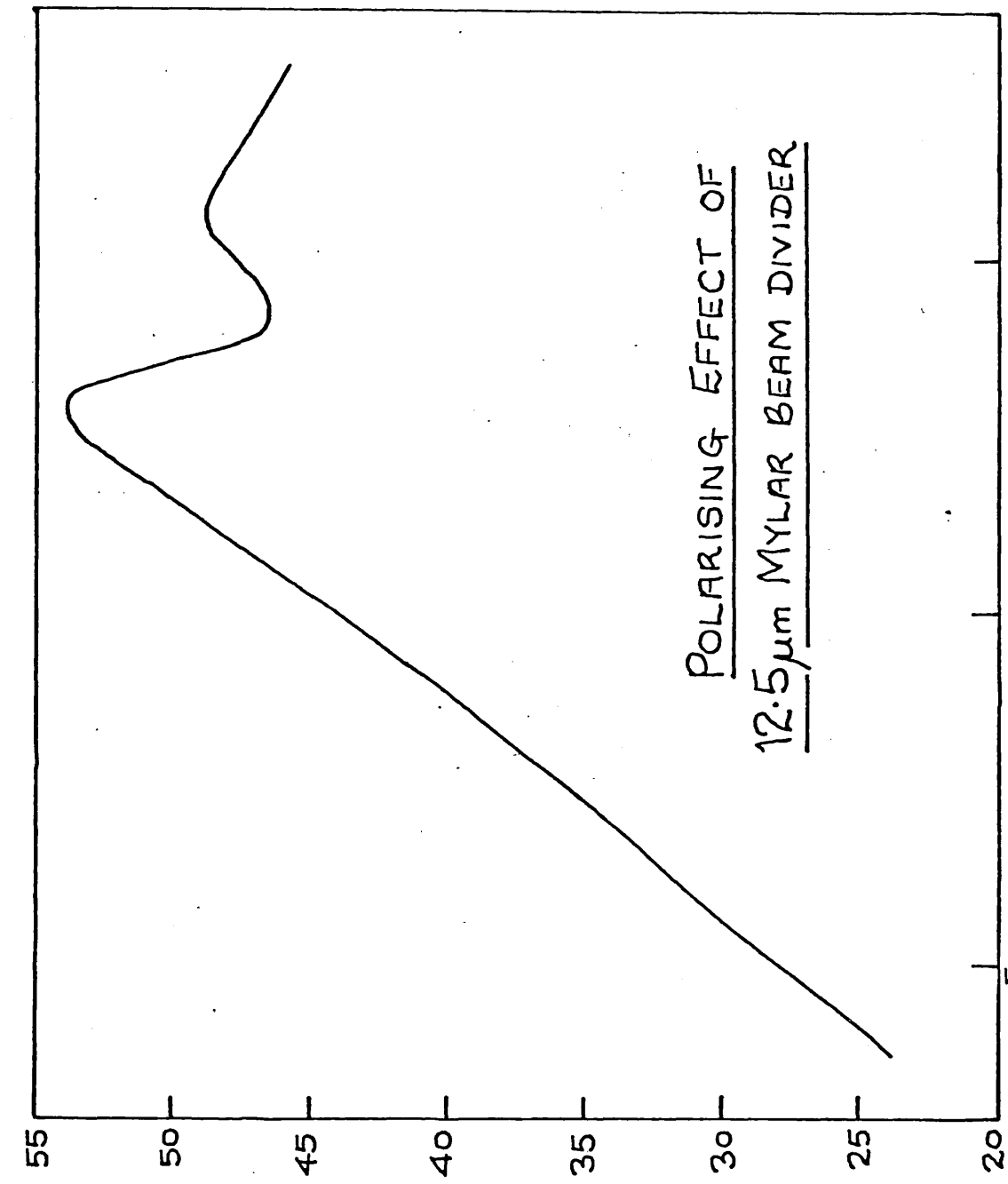
POLARISING EFFECT OF
12·5μm MYLAR BEAM DIVIDER
RATIO
E HORIZ. / E VERT.
(%)
55
50
45
40
35
30
25
20
50
100
150
WAVE NUMBER (cm⁻¹)

FIG 4.4

FIG 4.5. SCHEMATIC DIAGRAM OF THE POLARISING INTERFEROMETER

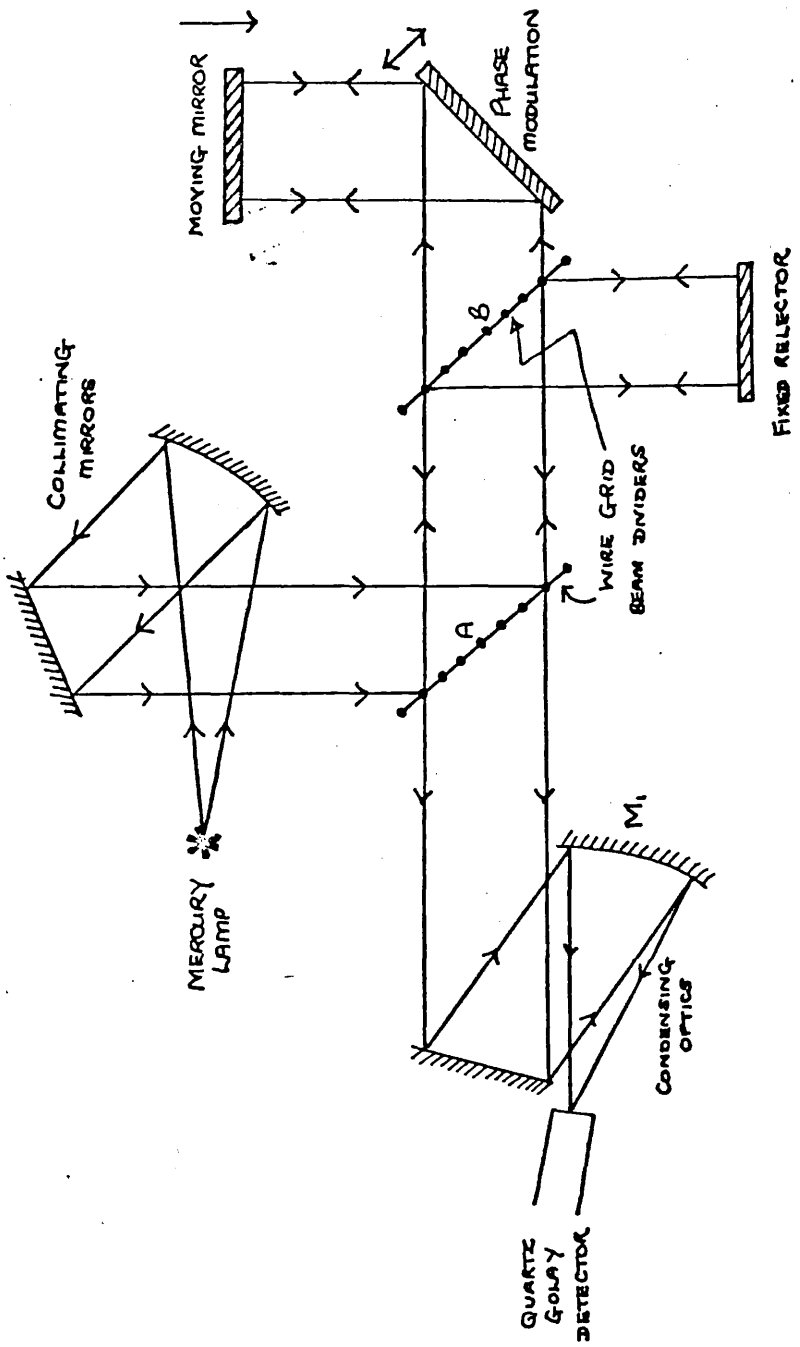

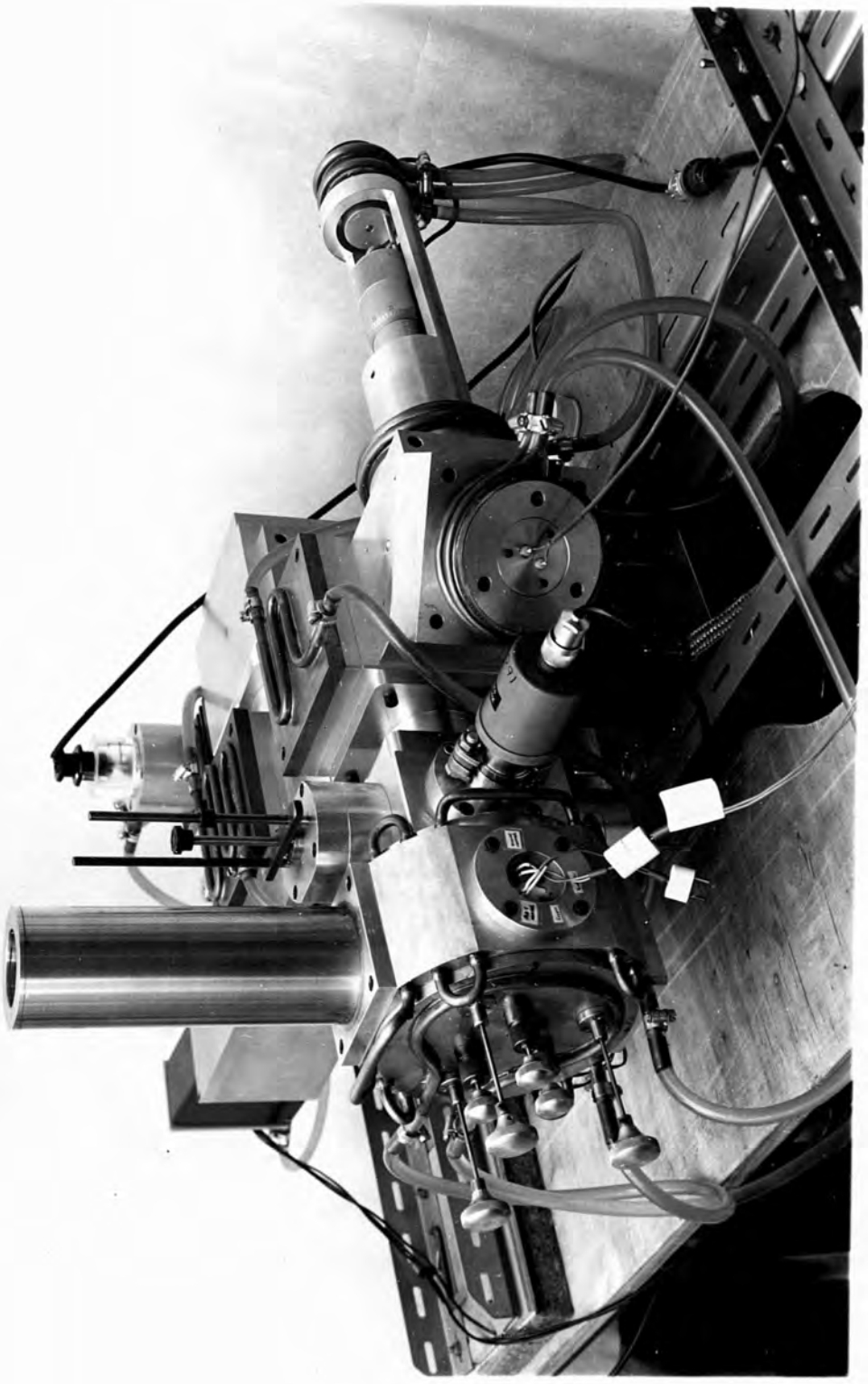

FIG 4.6: THE POLARISING INTERFEROMETER

FIG 4.7: THE EARLIER VERSION OF THE PHASE MODULATION SYSTEM – the mirror is attached to the cone of a loudspeaker which is held in an adjustable jig mounted on the micrometer spindle

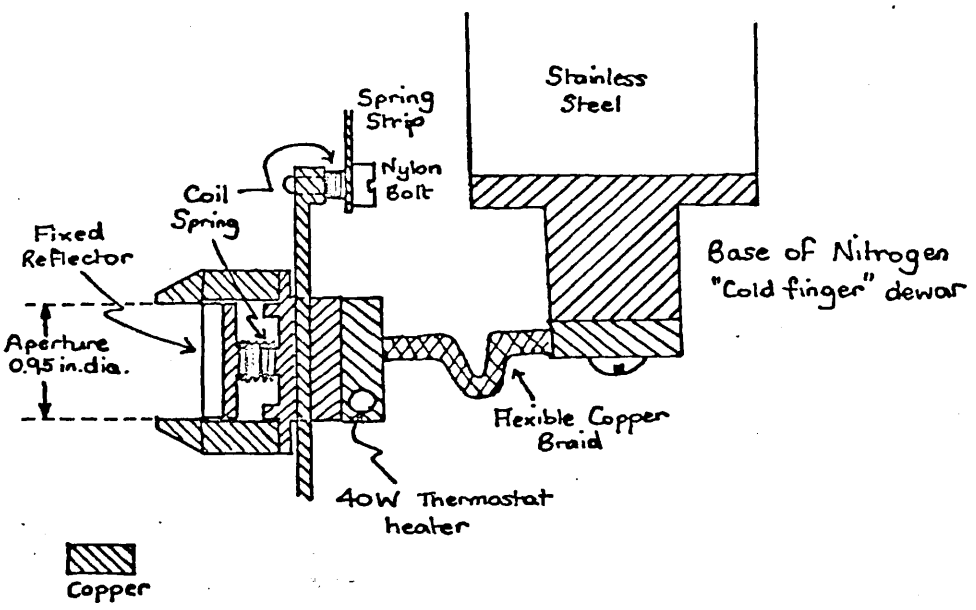

FIG. 4.8 THE FIXED REFLECTOR MOUNT AND "COLD FINGER" CONNECTIONS

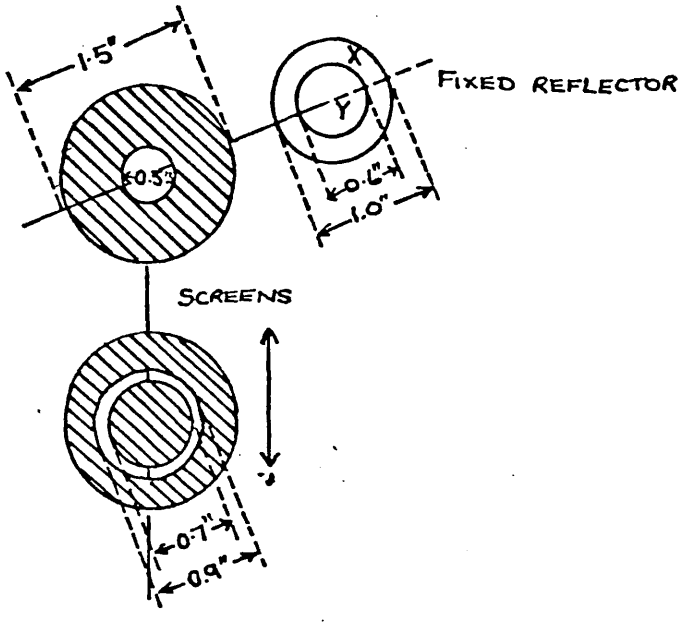

FIG. 4.9 THE GEOMETRY OF THE SCREENS AND THE DIVISION OF THE FIELD OF VIEW AT THE FIXED REFLECTOR

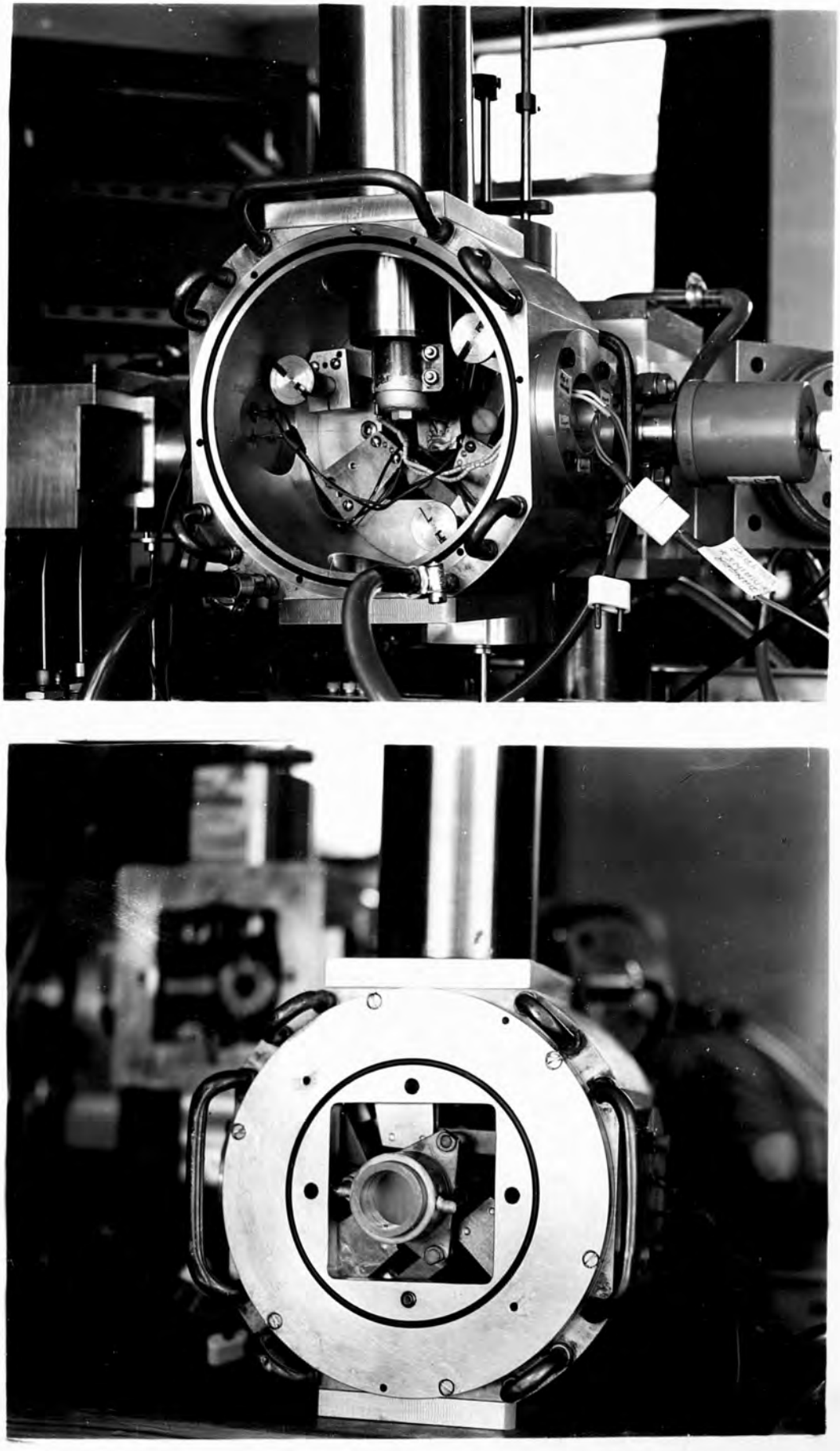

FIG 4.10 : TWO VIEWS OF THE SPECIMEN CHAMBER OF THE POLARISING INTERFEROMETER

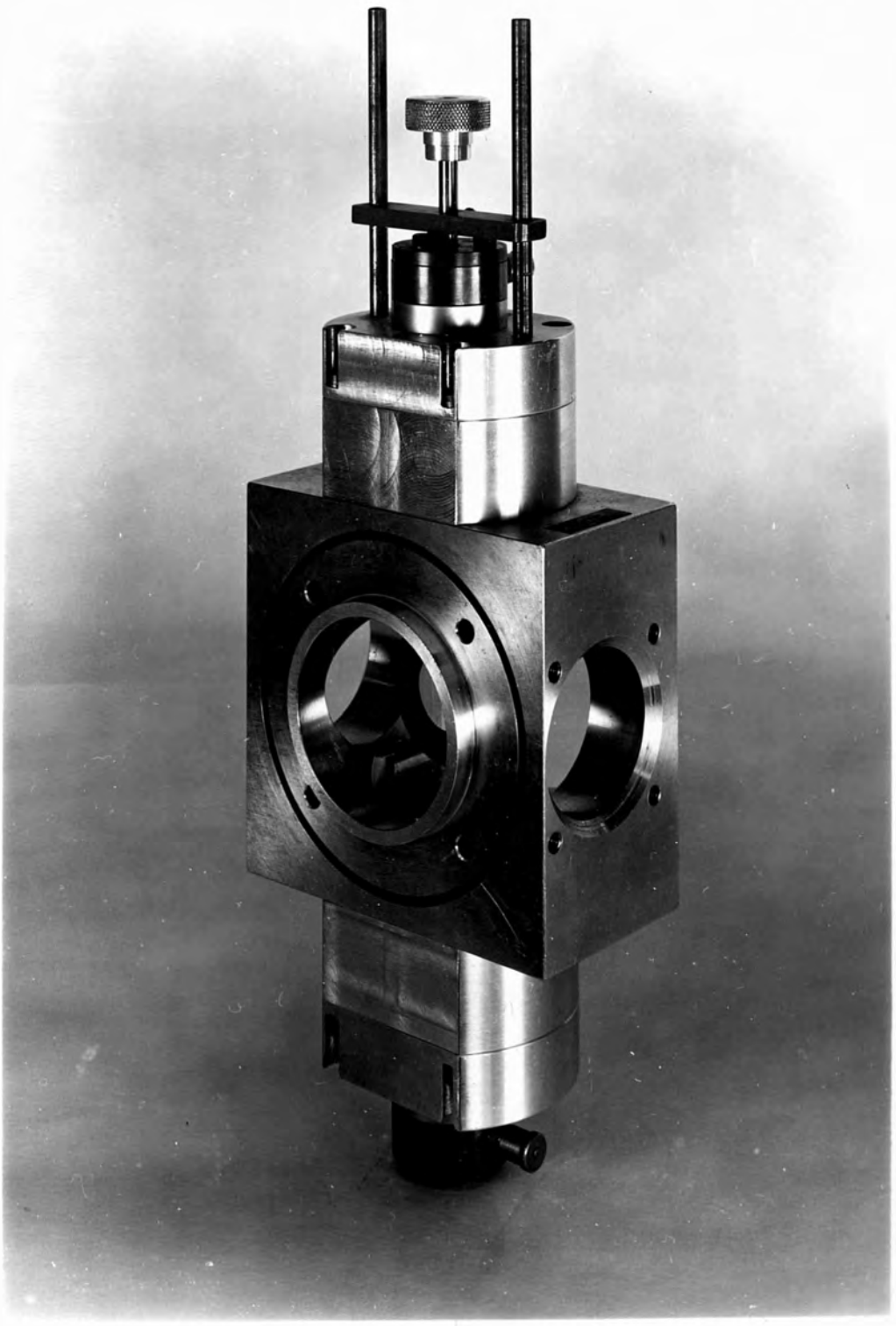

FIG 4.11 : A SCREEN UNIT AS USED IN THE POLARISING INTERFEROMETER

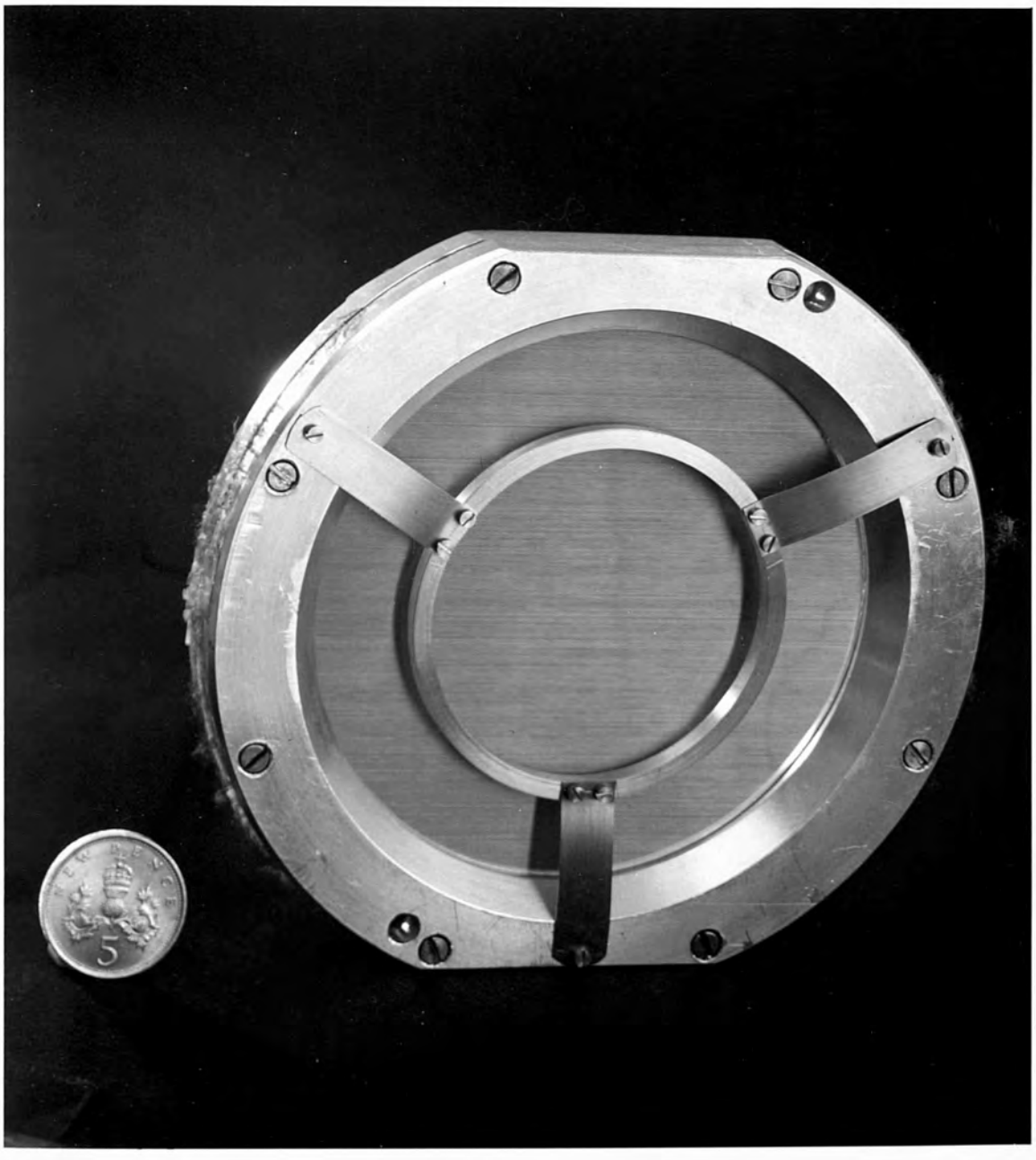

FIG 4.12 : A WIRE GRID BEAM DIVIDER

FIG 4.13(a) THE ACTION OF THE POLARISING INTERFEROMETER

For simplicity the action is described for a single frequency component ν and for the situation where the two interferometer arms have the same physical length, defined as the position of zero path difference (ZPD). The horizontal and vertical axes with respect to the instrument are shown. The grids are assumed to be lossless. For an unpolarised beam, the component of the radiation perpendicular to the wires is 100% transmitted and the component parallel to the wires, assumed to have the same amplitude as the perpendicular component, is 100% reflected. It is also assumed that the reflecting areas in the two arms are equal.

1. AT GRID 'A'

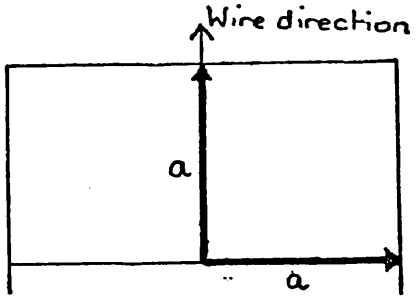

Unpolarised radiation is incident from the source via the collimator onto grid 'A', the wires of which are vertical. A vertically polarised beam is thus reflected into the instrument towards grid 'B'. The horizontal component is transmitted and lost.

2. AT GRID 'B'

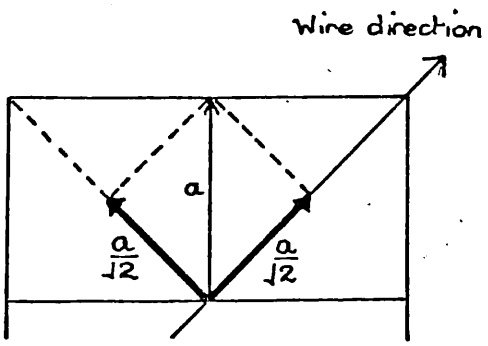

The plane polarised beam from 'A' is split into two components parallel and perpendicular to the wires of 'B'. The parallel component is reflected into the fixed reflector arm whilst the perpendicular component is transmitted into the moving mirror arm.

FIG 4.13(b)

3. AT GRID 'B' FOLLOWING REFLECTION IN THE TWO ARMS

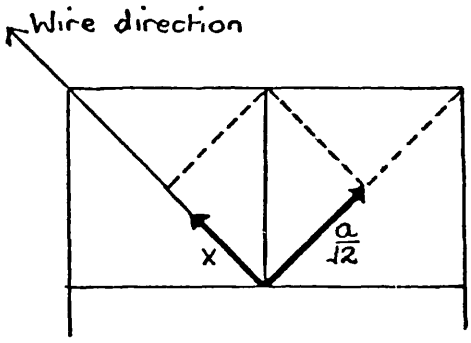

Assume the mirror is a perfect reflector and that the reflectivity of the fixed reflector is $\rho(\nu) = |\rho(\nu)|\exp i\phi$ with $0 \leq |\rho(\nu)| \leq 1$. Thus the length X of the vector which represents the radiation from the fixed reflector is dependent on both the amplitude and phase reflectivities of the reflector, neither of which is completely determined by the value of the other at this frequency. The vector length

$$X = |\rho(\nu)| \frac{a}{\sqrt{2}} \cos\phi$$

represents the projection of the reflected amplitude $|\rho(\nu)|a/\sqrt{2}$ along the wire direction. No interference is observed at this stage as the two components are orthogonal.

4. ON RETURN TO GRID 'A'

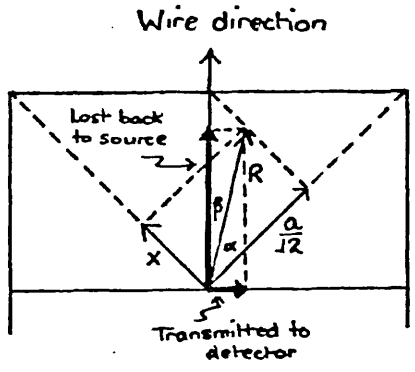

Resultant of two components from 'B'

$$R = \left(\frac{a^2}{2} + X^2\right)^{1/2} = \frac{a}{\sqrt{2}}\left(1 + |\rho(\nu)|^2\cos^2\phi\right)^{1/2}$$

'A' now acts as the analyser, causing the interference of the two components from 'B' to be observable. The signal transmitted through to the detector is $R\sin\beta$ with R as given.

For the non-dispersive case when $|\rho(\nu)| = 1$ and $\phi = 0$ for all ν, $X = a/\sqrt{2}$, and $\beta = 0$ and thus no signal reaches the detector, ie a dark fringe occurs at the position of ZPD.

However, in the dispersive situation when $|\rho(\nu)| < 1$ and $\phi \neq 0$, then $\beta \neq 0$, but is given by

$$\alpha = 45° - \beta = \tan^{-1}\frac{X}{a/\sqrt{2}} = \tan^{-1}\{\,|\rho(\nu)|\cos\phi\,\} \quad .$$

The signal transmitted to the detector, $R\sin\beta$ is therefore a function of $|\rho(\nu)|\cos\phi$ and thus information on both $|\rho(\nu)|$, the amplitude reflectivity and $\phi(\nu)$ the phase reflectivity may be obtained.

At the frequency ν, the position of equal optical path lengths, as opposed to physical path length, is found by displacing the moving mirror out a distance $\frac{1}{2}(\phi/2\pi\nu)$ from the position of ZPD. Thus the positions of optical ZPD for different frequencies are dispersively distributed on the phase delayed side of the position of ZPD.

FIG 4.14 BLOCK DIAGRAM OF THE RECORDING ELECTRONICS ARRANGEMENT

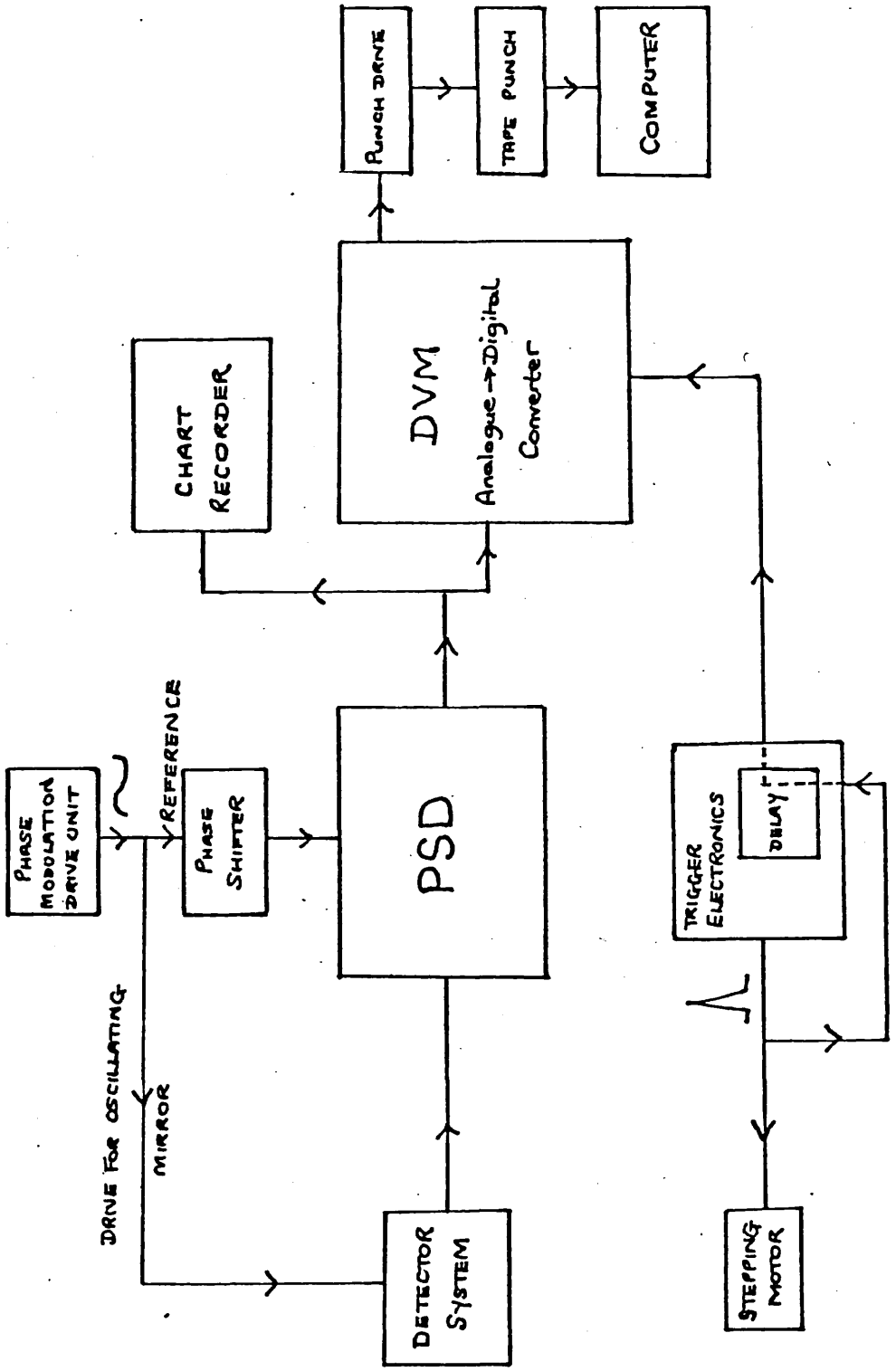

CHAPTER 5

ASPECTS OF FERROELECTRIC THEORY

5.1 INTRODUCTION

The dielectrics considered in Chapter 3 had a linear relation between polarisation and applied electric field (3.9). However, a class of dielectrics exists for which this relationship exhibits hysteresis effects. Their dielectric behaviour, by analogy to the magnetic behaviour of ferromagnetic materials leads to their name, ferroelectrics. Such materials possess a degree of polarisation in the absence of an external field, termed spontaneous polarisation P_s. The direction of the spontaneous polarisation may be altered by application of an electric field.

In general, a macroscopic ferroelectric crystal consists of a number of domains which form to reduce the electrostatic self-energy of the crystal. Within each domain the polarisation has a specific direction which varies from one domain to another. The existence of domains, confirmed by X-ray studies, explains the possibility for a crystal in its ferroelectric phase to have a zero or very small overall polarisation. When an electric field is applied to such a crystal, the number and size of domains polarised in the field direction may be increased. Reversal of the field leads to the phenomenon of switching and is accompanied by the hysteresis observed in the P versus E curves, giving rise to dielectric losses. The domains can often be seen very easily with an optical microscope as a direct result of the birefringence of the crystal.

A necessary requirement for a solid to be a ferroelectric is that its crystal structure lacks a centre of symmetry. No centro-symmetric crystal can possess a finite polarisation, for inversion of the polarisation vector by the symmetry operation leads to a recognisable change, contradicting the

symmetry requirements. This is an example of Neumann's Principle which states that the symmetry elements of any physical property of a crystal must include the symmetry elements of the crystal point group.

Of the 32 crystal classes, 21 lack a centre of symmetry and of these, 20 are termed piezoelectric. The polarisation of such crystals may be altered by external stress. Ten of the piezoelectric classes form the subgroup of pyroelectric crystals which are spontaneously polarised, possessing a finite polarisation even for zero external fields and stresses. The polarisation changes when the crystal temperature is altered. Ferroelectrics are a further subgroup of these spontaneously polarised pyroelectrics having the additional property that the polarisation may be reversed or switched by an applied electric field.

A permanent electrical polarisation would arise in a crystal if, having started with an unpolarised ionic crystal, the whole structure of positive ions were displaced with respect to the structure of negative ions, a situation of the type which seems to exist in ferroelectric materials where X-ray evidence shows actual displacements of ions in the polarised state.

The ferroelectric properties of most ferroelectric crystals disappear above a critical transition temperature T_o. The magnitude of the spontaneous polarisation decreases as the temperature rises until at T_o it disappears. Above T_o the crystal is non-polar and the dielectric constant frequently obeys the Curie Weiss Law

$$\varepsilon = \frac{C}{T-T_c} + \varepsilon_o \qquad (5.1)$$

where T_c is the characteristic Curie temperature which sometimes coincides with, but more often lies a few degrees below, the transition temperature T_o. At the transition temperature, a change in crystal structure

accompanies the change in phase, the ferroelectric structure being a distortion of the non-polar structure which exists above T_o, with correspondingly lower symmetry. Anomalies in certain physical properties of the crystal can occur at this transition.

Ferroelectricity was first discovered by Valasek in 1921 in the sodium-potassium salt of tartaric acid ($NaKC_4H_4O_6 \cdot 4H_2O$) known as Rochelle salt. This salt was first prepared by Seignette in 1672 at La Rochelle and has led to ferroelectrics being alternatively termed Seignette-electrics.

In 1935, potassium dihydrogen phosphate (KH_2PO_4), well-known by the initials KDP, was found to exhibit ferroelectric properties by Busch and Scherrer[37]. It is typical of a group of ferroelectrics consisting of dihydrogen phosphates and arsenates of the alkali metals.

In 1942 came the observation of anomalous dielectric properties in barium titanate ($BaTiO_3$), an important member of the Perovskite group of ferroelectrics with a general formula ABO_3. The independent discovery of $BaTiO_3$ in several laboratories during World War II prompted renewed theoretical interest in the mechanisms of the crystallographic distortions accompanying the phase transitions and much experimental work was performed to try to produce practical technological devices such as piezoelectric transducers, from the new ferroelectric materials, to aid the war effort. This experimental work was primarily on $BaTiO_3$ and the hydrogen bonded ferroelectrics discovered earlier, in particular triglycine sulphate (TGS) and KDP.

Since the war a large number of materials have been shown to exhibit ferroelectric properties and the vast amount of research on ferroelectrics done in recent years ensures that this list continues to grow.

Numerous books and articles have been written in recent years on ferroelectric materials, their properties and the various theories

derived to explain ferroelectric behaviour. This Chapter only touches upon a few of the general aspects of ferroelectric theory that are pertinent to the studies performed using the polarising and power interferometers. For further details consultation of the referenced literature is required, in particular the excellent review of the experimental studies of structural phase transitions by Scott[38].

Two further definitions deserve a mention at this stage, those of an antiferroelectric and the order of a transition. Early definitions of anti-ferroelectricity were based on the model of dipoles occupying lattice sites in a simple cubic structure with alternate arrays of the dipoles orientated in opposite directions leading to zero overall polarisation. Calculations show that this anti-ferroelectric configuration is the stable arrangement for such a two-dimensional system of dipoles, as opposed to the metastable ferroelectric arrangement of parallel dipoles all with the same orientation.

Later definitions of anti-ferroelectrics were based on the behaviour of the dielectric constant in which a small peak is generally observed at the transition temperature between the anti-ferroelectric and the higher temperature paraelectric phases. Scott however points out that according to this definition a crystal without a phase transition cannot be defined as anti-ferroelectric and neither can the highest temperature phase of any crystal. He proposes a definition analogous to the one he puts forward for a ferroelectric. Ammonium dihydrogen phosphate ($NH_4H_2PO_4$), otherwise known as ADP, is an example of a crystal that has been termed anti-ferroelectric.

A common feature of any phase transition, whether it is ferroelectric or of another nature, is the existence of a displacement or order parameter which is a measure of the ordering which takes place at the

transition temperature (see for example Burfoot[39]). In ferroelectrics the order parameter is the spontaneous polarisation P_s which has the temperature dependence

$$P_s \sim (T_o - T)^{\beta} \text{ for } T < T_o \text{ and } P_s = 0 \text{ for } T > T_o \qquad (5.2)$$

where β has the value of $\frac{1}{2}$ in some theories.

A 'first order' transition, and use of the word order here is not to be confused with its use above, is one where the displacement parameter changes discontinuously at $T = T_o$. By second order we designate those transitions in which the displacement parameter decreases continuously to zero as T_o is approached from above and below. Hence ferroelectric transitions are graded according to the continuous or discontinuous behaviour of the spontaneous polarisation at $T = T_o$. However, it is usually not possible to obtain a clear-cut distinction between a first or second order transition from measurement of P_s with temperature as, even for a second order transition, the rise of P_s just below T_o is rapid. They may, however, be distinguished by the so-called "double hysteresis loop" experiment (Dekker[40]).

It is perhaps worth noting in passing that a class of ferroelectrics exists where P_s is not the phase transition displacement parameter, and such materials are termed 'improper ferroelectrics'. The observed spontaneous polarisation and the dielectric anomalies are here not the primary critical characteristics but are secondary effects linked to the primary lattice anomaly, a crystallographic quantity usually being the order parameter.

5.2 THEORIES OF THE FERROELECTRIC TRANSITION

A comprehensive discussion of the ferroelectric phenomenon and the phase transition has been given by Slater[41] who employs the analogy of the mechanical problem of a particle held in a double potential well, two minima with a maximum between. The maximum, a position of unstable equilibrium, corresponds to the unpolarised state and the particle can be pushed in either of two opposite directions into a lower, stable, potential minimum corresponding to a permanent polarisation P_s. P_s is the product of ion displacement and ion charge, the displacement in this simple model being the maximum to minimum separation. Thus the decrease to zero at $T = T_o$ of the magnitude of P_s as the temperature is raised, corresponds to the two minima becoming shallower, moving together and finally coalescing at the critical transition temperature T_o. This treatment leads to the proposed existence of a vibrational mode with a frequency of the form

$$\omega^2(T) \sim C(T-T_o) \qquad (5.3)$$

which thus vanishes at $T = T_o$ and becomes unstable for $T < T_o$ leading to the onset of spontaneous polarisation. The existence of such a mode was earlier predicted by the free energy theories of Landau[42] and Devonshire[43] the lattice dynamical theory of Cochran[44] and the microscopic, anharmonic theory of Cowley[25].

An earlier dipole theory (Dekker[40] p 192), analogous to the Langevin-Weiss theory of ferromagnetism, assumed that in ferroelectrics a degree of "cooperation" was present. The existence of spontaneous polarisation requires that the dipole moments of the different unit cells in the crystal are orientated in the same direction, the cooperation being the tendency for a unit cell to have its dipole direction parallel to that of its neighbours. An expression for the internal field which orientates

a given dipole

$$E_i = E + \gamma P \qquad (5.4)$$

where E is the external field, P the polarisation and γ the internal field constant, illustrates the cooperation between the dipoles. The larger the value of P, the larger E_i and the stronger the tendency for the dipole to align itself in the direction of the polarisation of its surroundings. The field of (5.4) leads to the Curie-Weiss law for the dielectric constant for $T > T_o$ and also an expression for the saturation polarisation corresponding to complete alignment of dipoles.

The free energy theories assume the free energy F near T_o may be expanded in a power series of the displacement parameter, the spontaneous polarisation in the case of a ferroelectric. By requiring F to be a minimum, the condition for stability, then the signs of the remaining coefficients of the expansion describe both the onset of the transition and its order. This leads to the prediction that the order parameter η obeys

$$\eta = \eta_o(T_o - T)^{\frac{1}{2}} \quad . \qquad (5.5)$$

From the simple single harmonic oscillator equation with linear response

$$m\omega^2 = \frac{\partial^2 F}{\partial \eta^2} \qquad (5.6)$$

it follows that there exists a phonon frequency

$$\omega = \omega_o(T - T_o)^{\frac{1}{2}} \quad . \qquad (5.7)$$

Hence the free energy model, which assumes infinitely long range forces, leads to an equation of the form (5.3).

This same equation was obtained by both Cowley and Cochran via their particular theories. In general, Cochran proposed that for most transitions

in which the crystal possesses periodic transitional symmetry (ie is ordered) in both the phases, above and below T_o, the structural distortions are characterised by an unstable optical phonon, whose frequency decreases substantially as the transition temperature is approached from above or below. The stability of a crystal lattice is dependent upon the elastic coefficients which must satisfy certain conditions conveniently summarised by the requirement that

$$\omega_i > 0$$

for all i, where ω_i is the i^{th} normal mode frequency. Thus $\omega_i \to 0$ is equivalent to some generalised elastic coefficient becoming small. The crystal's restoring force against some shear deformations is consequently weak and the crystal literally softens. This equivalence of ω_i with a generalised elastic coefficient is thus responsible for the term "soft mode" applied to the normal mode for which $\omega(T) \to 0$.

The basic concept of such a soft mode was first put forward after measurements on quartz by Raman and Nedungadi[45] in 1940. Following Cochran's theory, the existence of such a mode in the vibrational spectrum of strontium titanate ($SrTiO_3$) was shown experimentally by Cowley[46] using neutron scattering techniques, the mode becoming unstable for $T < T_o$ resulting in the onset of spontaneous polarisation.

The soft mode concept can be readily extended to anti-ferroelectric materials as discussed by Cochran. However, here the transition is usually characterised by a soft mode at the Brillouin zone boundary, not at the zone centre as in ferroelectrics.

Objections have been raised to various aspects of the theories outlined above, but they form a background to the vast amount of work, both experimental and theoretical, that has been performed in recent years on ferroelectric materials and soft modes.

5.3 POTASSIUM DIHYDROGEN PHOSPHATE (KH_2PO_4)

The bulk of theoretical and experimental studies on ferroelectrics belonging to the hydrogen-bonded group have concerned KDP and its isomorphs. Such materials have been known for a long time in comparison to other ferroelectrics and work in the early days of ferroelectricity was largely limited to these crystals.

KDP has one ferroelectric transition temperature, T_o = 122K. It is perhaps worth mentioning at this stage that some crystals have more than one such transition temperature. Rochelle salt, for example, has the peculiar property of being ferroelectric only in the region between 255K and 296K, thus it has two transition temperatures.

KDP is piezoelectric in both phases. In its non-polar paraelectric phase above 122K the crystal symmetry is tetragonal with the point group $\bar{4}2m$ (D_{2d}). In the ferroelectric phase the crystal is orthorhombic belonging to the group mm2 (C_{2v}). In both cases, the primitive cell contains two KH_2PO_4 units. In the paraelectric phase, there are three mutually perpendicular axes a, a and c. Thus above T_o the dielectric properties of KDP are described by two complex dielectric constants, one for radiation polarised parallel to the 'c' axis and one for radiation polarised along an 'a' axis. Below T_o, the three mutually perpendicular axes are a, b and c, corresponding to the orthorhombic symmetry.

The crystal structure is built up in the following manner (Agrawal[47]). Each phosphorus atom is surrounded by four oxygens at the corners of a near regular tetrahedron. Every [PO_4] group of this kind is linked to four others by hydrogen bonds. These bonds are between the upper oxygen of one [PO_4] group and a lower oxygen of a neighbouring group, and hence each adopt a form O-H-O. Each hydrogen bond of this type lies almost perpendicular to the 'c' axis and thus perpendicular to the ferroelectric

axis, for this axis, the direction along which the spontaneous polarisation occurs, lies parallel to the 'c' axis of the tetragonal phase.

The important role played by these hydrogen bonds in the polarisation of the crystal is clear from the large effect deuteration has been shown to have on the transition temperature. Replacement of the hydrogen by deuterium in KDP, leading to KD_2PO_4, raises the transition temperature from 122K to 213K.

Above T_o, neutron and X-ray studies have revealed that the protons are randomly distributed on either side of the O-H-O bond and are not centred exactly between the oxygens. They can thus be considered as disordered. In passing through the transition from above, the lengths of the hydrogen bonds do not change significantly but below T_o, the protons are all near the upper oxygens or near lower oxygens depending on polarity, resulting in an ordered arrangement. Reversal of the polarity by means of an electric field, for example, produces a shift of the hydrogen atoms along the O-H-O bonds from one ordered system to another.

The ferroelectric transition in KDP is thus of the order - disorder type. Whilst the protons undergo the order-disorder transition at T_o, the metal ions undergo a displacive transition from one ordered arrangement to another.

The ordering of the protons below T_o results in changed forces on the other ions which result in a distortion of the crystal as a whole, there being a small though significant shift of the other ions from their equilibrium positions in the tetragonal phase. Since the proton shifts at T_o are nearly perpendicular to the 'c' axis, the axis along which the spontaneous polarisation occurs, then the 'c' axis component of such a displacement is far too small to account for the total polarisation which develops at T_o. It is far more likely that the spontaneous polarisation

arises from the aforementioned displacement of the potassium and phosphorus ions along the 'c' axis caused by complex coupling between the protons and these heavy ions. Indeed it has been shown by Bacon and Pease[48] that the polarisation calculated in this way agrees well with experimental values.

Following his double potential well model developed to explain the occurrence of the ferroelectric transition in generalised terms (section 5.2), Slater[49] suggested that the protons in KDP occupy such double wells corresponding to the O-H-O hydrogen bond arrangement. He produced a statistical theory based on this model showing that the proton ordering was the origin of the ferroelectric transition.

In 1968 Kobayashi[50] published a theory which assumed a tunnelling motion of individual protons between the two Slater potential minima in the presence of direct proton-proton interaction. The two positions of the proton in the hydrogen bond well are treated like a spin system described by ficticious spin $+\frac{1}{2}$ and $-\frac{1}{2}$ states. He incorporated into his theory the strong proton-lattice interaction, the coupling of the tunnelling frequency of the protons to the lattice vibrations of the heavy potassium and phosphorus ions. This strong coupling results in a pair of optic-lattice-vibration modes ω_+ and ω_-. Kobayashi identified the low frequency member ω_- as the ferroelectric mode which follows the soft behaviour predicted by Cochran, the higher frequency transverse optic mode ω_+ remaining unshifted as the temperature is lowered towards T_o.

Since, for KDP, the transition order parameter is given by the proton tunnelling, whereas the polarisation is determined by a transverse optic mode of the K-P-O system, the material has been considered by some to be an improper ferroelectric, although its properties are typical of those of a ferroelectric. However, the strong proton-lattice interaction leads to a coupling between P_s and the proton ordering which, furthermore,

is linear. They thus have the same temperature dependence whereas in a typical improper ferroelectric the coupling is not linear. Hence KDP is a ferroelectric in which we are dealing with a mixed, coupled mode system and not just with a simple soft mode. An analysis of the coupled mode problem is given in the following section.

Until recently all evidence indicated that the transition in KDP was of second order, that is, the spontaneous polarisation P_s rises continuously from zero at T_o. However, Benepe and Reese[51] in 1971 found that P_s actually rises discontinuously at the transition indicating a first order type transition. A double hysteresis loop in the P versus E relation has been observed, by a number of workers, just above T_o by use of an external field of ultra-low frequency.

5.4 THE COUPLED MODE ANALYSIS

It was described in the previous section how the onset of ferroelectricity in KDP involves both proton displacements (tunnelling) and some optical-phonon instability involving the heavier ions. This section deals with the experimental work performed on KDP in recent years, and its interpretation in terms of a coupled mode formalism which has led to a better understanding of the transition.

In 1962 Barker and Tinkham[52] found a low frequency highly overdamped band peaking at $\sim 50\ cm^{-1}$ in the room temperature reflectivity spectrum of the KDP 'c' axis. By means of its strength and temperature dependence, they deduced that it was the mode responsible for the interesting ferroelectric and electro-optic properties of the crystal. They could not, however, give a precise description of it in terms of classical oscillator parameters.

Quantitative measurements of the temperature dependence of this low frequency mode were first made by Kaminow and Damen[53] using the technique of Raman scattering. Their measurements revealed a broad low frequency ferroelectric mode which they represented by a simple damped harmonic oscillator function in the following manner.

The classical equation for force- damped harmonic motion may be written as

$$\ddot{x} + \Gamma\dot{x} + kx = eE(\omega) \qquad (5.8)$$

where x is the displacement parameter, Γ is the damping, k represents the restoring forces and e is the effective charge. The mass m of the particle is included in these definitions.

Assuming harmonic solutions E, x $\sim$ exp $i\omega t$ then (5.8) leads to

$$(-\omega^2 + i\Gamma\omega + k)x = eE \quad . \qquad (5.9)$$

The polarisation P = ex, the product of charge and displacement, is also given by (3.9) which thus allows for the substitution for x in (5.9) yielding

$$\varepsilon(\omega) = \varepsilon_o + \frac{e^2}{\omega_o^2 - \omega^2 + i\Gamma\omega} \qquad (5.10)$$

where the restoring force parameter has been written in the form $k = m\omega_o^2$.

The Raman (Stokes) scattering intensity $S(\omega)$ measured by Kaminow and Damen is related to the imaginary part of the susceptibility $\chi''(\omega)$ by means of the fluctuation-dissipation theorem

$$S(\omega) = R[n(\omega+1)]\chi''(\omega) \qquad (5.11)$$

where

$$n(\omega) = \left[\exp\frac{\hbar\omega}{kT} - 1\right]^{-1} \qquad (5.12)$$

and R is a normalisation constant.

The electrical susceptibility $\chi(\omega)$ and the dielectric function $\varepsilon(\omega)$ are related by (3.11) and comparison with (5.10) yields

$$\chi(\omega) = \frac{1}{\varepsilon_o} \frac{e^2}{(\omega_o^2-\omega^2+i\Gamma\omega)} \quad . \tag{5.13}$$

Simplification may be achieved via the limit $\omega \to 0$ which gives

$$\chi(0) = \frac{e^2}{\varepsilon_o \omega_o^2} \quad . \tag{5.14}$$

Hence we may write

$$\chi(\omega) = \frac{\omega_o^2 \chi(0)}{\omega_o^2-\omega^2+i\Gamma\omega} \quad , \tag{5.15}$$

the imaginary part of which is

$$\chi''(\omega) = \frac{\omega_o^2 \chi(0) \Gamma\omega}{(\omega_o^2-\omega^2)^2+\Gamma^2\omega^2} \tag{5.16}$$

enabling us to relate to the measured scattering intensities via (5.11).

On fitting their experimental intensity curves using the oscillator function of (5.15), Kaminow and Damen made the following observations.

To a good accuracy

$$\chi(0) = \frac{C}{T-T_c^*} \tag{5.17}$$

with $T_c^* = 117K$ and C an undetermined Curie constant. The damping constant Γ was large and temperature independent to within the experimental accuracy and the characteristic frequency ω_o tended tc zero as $T \to T_o$ and approached a constant value for $T >> T_o$.

To obtain a function fitting this temperature dependence they employed an elementary single oscillator model of a ferroelectric and assumed certain temperature dependences for the microscopic parameters

which would lead to the observed dependence of (5.17).

They thereby obtained an ω_o^2 temperature dependence of the form

$$\omega_o^2 = \left[C \frac{k}{m}\right] / \chi(0)I = \left[\frac{k}{m}\right] \left[\frac{T-T_c^*}{T}\right] \qquad (5.18)$$

where for the best fit to their experimental data, the high temperature value of ω_o^2, $k/m = 99\ cm^{-1}$. This fit was achieved to within the experimental uncertainty over the range $10 \rightarrow 140\ cm^{-1}$.

However, by use of only a single oscillator model, Kaminow and Damen had neglected the strong coupling between the ferroelectric mode and the optic phonon mode of the same symmetry lying near $180\ cm^{-1}$, the proton-phonon interaction proposed by Kobayashi.

This was later pointed out by Katiyar et al[54] and She et al[55], who realised that only when this coupling was properly accounted for could the correct temperature dependence of the uncoupled soft mode parameter ω_o be found.

Barker and Hopfield[14] formulated such a coupled-optical-phonon mode theory in 1964 in order to explain an interference effect in the IR dispersion of $BaTiO_3$ and other high dielectric constant materials. They found such an analysis gave greatly improved fits to their data which could not be fitted by any choice of parameters using uncoupled oscillators.

Their analysis took the following form. Consider a system of two particles with effective charges e_1 and e_2 coupled mutually by a spring of constant k_{12} and to fixed points by springs of constants k_1 and k_2 respectively. The equations of motion of the two particles coupled reactively in this way may be written

$$\begin{aligned} \ddot{y}_1 + \Gamma\dot{y}_1 + k_1 y_1 &= e_1 E + k_{12}(y_2 - y_1) \\ \ddot{y}_2 + \Gamma\dot{y}_2 + k_2 y_2 &= e_2 E + k_{12}(y_1 - y_2) \ , \end{aligned} \qquad (5.19)$$

with polarisation $P = y_1 e_1 + y_2 e_2$. (5.20)

Here E is the applied electric field, y_1 and y_2 are the displacements of particles 1 and 2 and the Γ_i are damping constants. The model for two independent oscillators is identical but with $k_{12} = 0$.

As shown by Barker and Hopfield these equations of motion can be written in an equivalent way to describe two particles with resistive "dashpot" coupling:

$$\begin{aligned} \ddot{x}_1 + \gamma_1 \dot{x}_1 + \omega_1^2 x_1 &= z_1 E + \gamma_{12} (\dot{x}_2 - \dot{x}_1) \\ \ddot{x}_2 + \gamma_2 \dot{x}_2 + \omega_2^2 x_2 &= z_2 E + \gamma_{12} (\dot{x}_1 - \dot{x}_2) \end{aligned} \qquad (5.21)$$

with polarisation $P = x_1 z_1 + x_2 z_2$. (5.22)

The equivalence is given by a 2x2 orthogonal (ie a real unitary) transformation (u) which diagonalises the force constant matrix, with

$$u \equiv \begin{pmatrix} \cos\theta & \sin\theta \\ -\sin\theta & \cos\theta \end{pmatrix} \qquad (5.23)$$

$$\begin{pmatrix} x_1 \\ x_2 \end{pmatrix} = u \begin{pmatrix} y_1 \\ y_2 \end{pmatrix} , \qquad \begin{pmatrix} z_1 \\ z_2 \end{pmatrix} = u \begin{pmatrix} e_1 \\ e_2 \end{pmatrix} \qquad (5.24)$$

$$\begin{pmatrix} \gamma_1+\gamma_{12} & \gamma_{12} \\ \gamma_{12} & \gamma_2+\gamma_{12} \end{pmatrix} = u \begin{pmatrix} \Gamma_1 & 0 \\ 0 & \Gamma_2 \end{pmatrix} u^{-1} \qquad (5.25)$$

and $$\begin{pmatrix} \omega_1^2 & 0 \\ 0 & \omega_2^2 \end{pmatrix} = u \begin{pmatrix} k_1+k_{12} & k_{12} \\ k_{12} & k_2+k_{12} \end{pmatrix} u^{-1} \quad . \qquad (5.26)$$

Multiplying out equation (5.26) leads to the following expression for θ,

$$\cot^2\theta + \{(k_2-k_1)/k_{12}\} \cot\theta - 1 = 0 \quad . \qquad (5.27)$$

The mechanical analogue of (5.21) is illustrated in Fig 5.1. The three "resistive" dashpots γ_1, γ_2 and γ_{12} contribute to losses by providing velocity dependent damping for driving fields of nearly any frequency. If the two particles have opposite charges there exists a frequency, between the resonant frequencies of each of the particles, which causes them to move together resulting in the γ_{12} dashpot becoming inactive, and hence, a reduction in the losses.

If we assume harmonic soluctions E, x_1, $x_2 \sim \exp i\omega t$, then from (5.21)

$$x_1 = \frac{z_1 E + \dfrac{i\omega\gamma_{12} z_2 E}{\omega_2^2-\omega^2+i\omega(\gamma_2+\gamma_{12})}}{\omega_1^2-\omega^2+i\omega(\gamma_1+\gamma_{12}) + \dfrac{\omega^2\gamma_{12}^2}{\omega_2^2-\omega^2+i\omega(\gamma_2+\gamma_{12})}} \qquad (5.28)$$

$$x_2 = \frac{z_2 E + \dfrac{i\omega\gamma_{12} z_1 E}{\omega_1^2-\omega^2+i\omega(\gamma_1+\gamma_{12})}}{\omega_2^2-\omega^2+i\omega(\gamma_2+\gamma_{12}) + \dfrac{\omega^2\gamma_{12}^2}{\omega_1^2-\omega^2+i\omega(\gamma_1+\gamma_{12})}} \quad .$$

The dielectric constant ε is the sum of the contributions due to each oscillator plus the background term ε_∞ due to any higher frequency modes {(3.8) → (3.13)}

$$\text{ie} \qquad \varepsilon(\omega) = \varepsilon_\infty + \frac{P}{E} = \varepsilon_\infty + \varepsilon_1 + \varepsilon_2 \qquad (5.29)$$

$$\text{where} \qquad \varepsilon_1 = z_1 x_1/E; \qquad E_2 = z_2 x_z/E \quad . \qquad (5.30)$$

Thus substitution yields:

$$\varepsilon_1 = \frac{z_1^2+i\omega\gamma_{12}z_1z_2/[\omega_2^2-\omega^2+i\omega(\gamma_2+\gamma_{12})]}{\omega_1^2-\omega^2+i\omega(\gamma_1+\gamma_{12})+\omega^2\gamma_{12}^2/[\omega_2^2-\omega^2+i\omega(\gamma_2+\gamma_{12})]} \qquad (5.31)$$

$$\varepsilon_2 = \frac{z_2^2+i\omega\gamma_{12}z_1z_2/[\omega_1^2-\omega^2+i\omega(\gamma_1+\gamma_{12})]}{\omega_2^2-\omega^2+i\omega(\gamma_2+\gamma_{12})+\omega^2\gamma_{12}^2/[\omega_1^2-\omega^2+i\omega(\gamma_1+\gamma_{12})]} \qquad (5.32)$$

and hence from (5.29)

$$\varepsilon(\omega)-\varepsilon_\infty = \frac{P}{E} = \frac{z_1^2G_1+z_2^2G_2+2z_1z_2i\omega\gamma_{12}G_1G_2}{1+\omega^2\gamma_{12}^2G_1G_2} \qquad (5.33)$$

where

$$G_j = \frac{1}{\omega_j^2-\omega^2+i\omega(\gamma_j+\gamma_{12})} \qquad (j = 1,2) \qquad (5.34)$$

is the response function of the uncoupled mode.

Alternatively, from the equations of motion for the spring coupling model (5.19) we may obtain

$$\varepsilon(\omega)-\varepsilon_\infty = \frac{P}{E} = \frac{e_1^2G_1'+e_2^2G_2'+2e_1e_2k_{12}G_1'G_2'}{1-k_{12}^2G_1'G_2'} \qquad (5.35)$$

where

$$G_j' = \frac{1}{[k_j+k_{12}-\omega^2+i\omega\Gamma_j]} \qquad (j = 1,2) \quad . \qquad (5.36)$$

The models of (5.33) and (5.35) each have seven parameters.

There are in fact an infinite number of mathematically correct models to describe a coupled mode system, each with its corresponding set of seven parameters. The "spring" and "dashpot" couplings are two particular

choices. These additional solutions are intermediate forms involving both kinds of coupling and are obtained by use of unitary transformations (u) which diagonalise neither the force constant matrix nor the damping matrix. Each model gives the same fit to data since they are equivalent to within the unitary transformation. However, the different models may be used to give insights into the physics of the vibrating system.

One consequence of the coupled mode analysis may be noted from (5.33) where it may be seen that $\varepsilon(\omega)$ depends on the signs of the effective charges of the two interacting modes, via the last term in the numerator. The independent mode formula, however, obtained by putting $\gamma_{12} = 0$ is insensitive to the sign of the charges as only z_1^2 and z_2^2 appear.

Barker and Hopfield found that fits obtained using interaction damping for $BaTiO_3$ and other perovskite materials were a great improvement in the region that could not be fitted by any choice of parameters using uncoupled oscillators. A third classical independent mode was added in each case as these perovskite structure materials all have three optically active modes.

$$\text{Thus} \quad \varepsilon(\omega) = \varepsilon_\infty + \varepsilon_1 + \varepsilon_2 + \varepsilon_3 \tag{5.37}$$

where ε_1 and ε_2 are given by (5.31) and (5.32) and

$$\varepsilon_3 = \frac{z_3^2}{\omega_3^2 - \omega^2 + i\omega\gamma_3} \quad . \tag{5.38}$$

It was this coupled mode formalism of Barker and Hopfield that was adopted by She et al[55] to explain their KDP 'c' axis Raman spectra in terms of the proton-phonon coupling. This resulted in a more complete treatment of the problem than that which had been performed by Kaminow and Damen, who neglected this interaction. Katiyar et al[54] also applied

this analysis to treat similar coupling in CsH_2AsO_4 (CsDA) and KH_2AsO_4 (KDA).

In these and other cases where coupled mode fits were made to Raman spectra, a Green's function formalism of the problem was employed.

Following Katiyar, the complex susceptibility $\chi(\omega)$ for the coupled modes may be written in terms of the Green's functions $G_{ij}(\omega)$ and the mode strengths P_i, P_j as

$$\chi(\omega) = \sum_{ij} P_i P_j \, G_{ij}(\omega) \tag{5.39}$$

where the $G_{ij}(\omega)$ may be expressed in terms of the response functions of the uncoupled modes

$$G_i = \frac{1}{\omega_i^2-\omega^2+i\omega\Gamma_i} \tag{5.40}$$

from (5.39)

$$\chi''(\omega) = \mathrm{Im} \sum_{ij} P_i P_j \, G_{ij}(\omega) \tag{5.41}$$

which may be related to the scattered Raman intensity $S(\omega)$ by means of the fluctuation-dissipation theorem (5.11).

For the case of coupling between the ferroelectric mode and the higher frequency optic mode, let $G_a = [\omega_a^2-\omega^2+i\omega\Gamma_a]^{-1}$ and $G_b = [\omega_b^2-\omega^2+i\omega\Gamma_b]^{-1}$ be the response function of the uncoupled ferroelectric and optic modes, respectively.

The coupled mode equation may then be written as

$$\begin{bmatrix} G_a^{-1} & \Delta^2+i\omega\Gamma_{ab} \\ \Delta^2+i\omega\Gamma_{ab} & G_b^{-1} \end{bmatrix} \begin{bmatrix} G_{11} & G_{12} \\ G_{12} & G_{22} \end{bmatrix} = \begin{bmatrix} 1 & 0 \\ 0 & 1 \end{bmatrix} , \tag{5.42}$$

where the coupling is described by $\Delta^2+i\omega\Gamma_{ab}$. Δ^2 is the force constant of a "spring" connecting the two oscillators having unperturbed frequencies ω_a and ω_b and Γ_{ab} is the damping constant of a "dashpot" connecting the two modes.

Thus, solving (5.42)

$$\begin{bmatrix} \frac{G_{11}}{G_a} + G_{12}\,[\Delta^2+i\omega\Gamma_{ab}] & \frac{G_{12}}{G_a} + G_{22}\,[\Delta^2+i\omega\Gamma_{ab}] \\ G_{11}\,[\Delta^2+i\omega\Gamma_{ab}] + \frac{G_{12}}{G_b} & G_{12}\,[\Delta^2+i\omega\Gamma_{ab}] + \frac{G_{22}}{G_b} \end{bmatrix} = \begin{bmatrix} 1 & 0 \\ 0 & 1 \end{bmatrix} . \tag{5.43}$$

Comparison of coefficients yields

$$\begin{aligned} \frac{G_{11}}{G_a} + G_{12}[\Delta^2+i\omega\Gamma_{ab}] &= 1 \qquad \text{(i)} \\ \frac{G_{12}}{G_a} + G_{22}[\Delta^2+i\omega\Gamma_{ab}] &= 0 \qquad \text{(ii)} \\ G_{11}[\Delta^2+i\omega\Gamma_{ab}] + \frac{G_{12}}{G_b} &= 0 \qquad \text{(iii)} \\ G_{12}[\Delta^2+i\omega\Gamma_{ab}] + \frac{G_{22}}{G_b} &= 1 \qquad \text{(iv)} \quad . \end{aligned} \tag{5.44}$$

From (ii) and (iv), elimination of G_{22} yields

$$\frac{G_{12}}{G_a} + (\Delta^2+i\omega\Gamma_{ab})\{\,1 - G_{12}(\Delta^2+i\omega\Gamma_{ab})\}G_b = 0 \quad . \tag{5.45}$$

Thus

$$G_{12} = \frac{(\Delta^2+i\omega\Gamma_{ab})\; G_a G_b}{(\Delta^2+i\omega\Gamma_{ab})^2 G_a G_b - 1} \quad , \tag{5.46}$$

and from (i) and (iii) elimination of G_{12} leads to

$$\frac{G_{11}}{G_a} - (\Delta^2+i\omega\Gamma_{ab})^2 G_{11} G_b = 1 \quad . \tag{5.47}$$

Hence

$$G_{11} = \frac{G_a}{1-(\Delta^2+i\omega\Gamma_{ab})^2 G_a G_b} \quad . \tag{5.48}$$

Likewise from (ii) and (iv)

$$G_{22} = \frac{G_b}{1-(\Delta^2+i\omega\Gamma_{ab})^2 G_a G_b} \quad . \tag{5.49}$$

Expansion of (5.39) gives

$$\chi(\omega) = P_1^2 G_{11} + P_2^2 G_{22} + 2P_1 P_2 G_{12} \tag{5.50}$$

and substituting for the G_{ij}

$$\chi(\omega) = \frac{P_1^2 G_a + P_2^2 G_b - 2P_1 P_2(\Delta^2+i\omega\Gamma_{ab})G_a G_b}{1 - (\Delta^2+i\omega\Gamma_{ab})^2 G_a G_b} \quad . \tag{5.51}$$

As described previously, Barker and Hopfield pointed out that the equations of motion of the oscillators coupled by a spring ($\Gamma_{ab} = 0$) may be transformed to describe oscillators coupled by a dashpot ($\Delta = 0$) since they are connected by a unitary transformation. Thus the choice of real or imaginary coupling is arbitrary; both will give the same fits to spectra. Katiyar et al[54] and She et al[55] both chose real coupling ($\Gamma_{ab} = 0$) as they found only this produced simple temperature dependences for the parameters.

The expression of (5.51) may be compared with (5.33) and (5.35) by use of (3.8) → (3.13) which gives

$$\frac{\varepsilon(\omega)-\varepsilon_\infty}{\varepsilon_o} = \chi(\omega) = \frac{P_1^2 G_a + P_2^2 G_b - 2P_1P_2(\Delta^2+i\omega\Gamma_{ab})G_aG_b}{1-(\Delta^2+i\omega\Gamma_{ab})^2 G_aG_b} \quad . \quad (5.52)$$

Thus, putting $\Delta^2 = 0$ leads to (5.33) and putting $\Gamma_{ab} = 0$ leads to (5.35). It should be noted that the effective charges of (5.33) and (5.35) ie e_1, e_2 and z_1, z_2 are both pairs of opposite sign charges. To indicate this, a minus is attached to e_2 and z_2 when performing parameter fits (see Chapter 6). This accounts for the difference in sign of the third term in the numerator of (5.51) compared to (5.33) and (5.35).

5.5 FURTHER ASPECTS OF THE COUPLED MODE THEORY

The choice of real or imaginary coupling has an effect on the temperature at which the uncoupled soft mode frequency ω_a extrapolates to zero. The choice of real ($\Gamma_{ab} = 0$) coupling, as used by She et al, causes this temperature to be necessarily lower than T_c^*, theclamped Curie temperature which occurs when $\chi(0) \to \infty$ or $1/\chi(0) \to 0$.

ie from (5.51)

$$[1 - \Delta^4 G_a(0)G_b(0)]_{T=T_c^*} = 0 \quad . \quad (5.53)$$

This occurs above the temperature at which $G_a(0) = \frac{1}{\omega_a^2} \to \infty$; ie $\omega_a^2 \to 0$.

The appearance of this finite temperature gap resulting from an analysis with real coupling is a consequence of the proton-phonon coupling. The divergence of $\chi(0)$ at T_c^* is a property of the coupled modes and not of the ferroelectric mode alone.

From Kobayashi[50] the coupled mode frequency ω_-, with damping neglected, is given by

$$\omega_-^2 = \frac{1}{2}(\omega_a^2+\omega_b^2) - \{\frac{1}{2}(\omega_a^2-\omega_b^2)^2 + \Delta^4\}^{\frac{1}{2}} . \qquad (5.54)$$

Now, the results of She et al may be summarised analytically as

$$1/\chi(0) \propto (T - 116) \qquad (5.55)$$

and $$\omega_a^2 = 67.7\ (T - 30) \quad cm^{-1} \qquad (5.56)$$

from which it is clear that ω_a^2, the square of the uncoupled soft mode frequency, is linear with temperature and extrapolates to zero at 30K. This dependence differs from that obtained by Kaminow and Damen using a single oscillator fit, (5.17). When they plotted ω_-^2, given by (5.54), as a function of temperature, a linear plot was again obtained which extrapolated to zero at the same temperature as $1/\chi(0)$, ie 116K. The temperature gap, they explained, was attributable to the level repulsion of the strong proton-phonon coupling which forces the coupled mode to become soft ($\omega_-^2 \to 0$) long before the extrapolated transition temperature of the uncoupled soft mode is reached at 30K.

If, on the other hand, the coupling is chosen to be imaginary ($\Delta = 0$) then from (5.51)

$$\chi(0) = P_1^2 G_a(0) + P_2^2 G_b(0) \qquad (5.57)$$

and thus $\chi(0)$ and $G_a(0)$ must diverge at the same temperature T_c^*, or in other words, $1/\chi(0)$ and ω_a^2 ($= 1/G_a(0)$) extrapolate to the same temperature, T_c^*.

The difference between the extrapolated temperature of 116K obtained by She et al and the true phase transition in KDP at 122K, may be explained in terms of further coupling between the ferroelectric soft mode and a soft transverse acoustic mode. This coupling was described by Brody and Cummins, [56], and later by Reese, Fritz and Cummins[57]. They extended the theory of Kobayashi to include the piezoelectric coupling between the ferro-

electric soft mode and the x-y shear acoustic mode. As $T \to T_o$, the soft ferroelectric mode frequency approaches that of the acoustic mode and the piezoelectric interaction forces the acoustic mode frequency down until it reaches zero. As the transition is approached from above, the phase transition occurs when this soft acoustic mode reaches zero at T_o, a few degrees above T_c^*. Thus, the acoustic mode becomes unstable before the optic mode has an opportunity to do so.

The difference in the transition temperatures for the acoustic and optic modes is a manifestation of a similar measured difference for high and low frequency (clamped and free) dielectric constants. This has been shown by Lagakos and Cummins[58]. In order to describe the coupling of the ferroelectric mode to both the x-y transverse acoustic mode and the optic mode they extended the coupled mode formalism of Barker and Hopfield to a three oscillator model. The response function of the acoustic mode was taken to be of the form

$$G_c = [\omega_c^2 - \omega^2 + i\omega\Gamma_c]^{-1} \tag{5.58}$$

and direct coupling between the optic mode and the acoustic mode was excluded as it was considered unimportant. The coupling of the ferroelectric mode to the optic mode was chosen as imaginary ($\Delta = 0$) and that between the ferrcelectric and acoustic modes was taken to be real ($\Gamma_{ac} = 0$). By solving the coupled mode equation of the form (5.42) which now of course includes 3x3 matrices, the static susceptibility is given by

$$\chi(0) = \frac{P_1^2 G_a + P_3^2 G_c + P_2^2 G_b (1 - \Delta_{ac}^4 G_a G_c) - 2P_1 P_3 \Delta_{ac}^2 G_a G_c}{1 - \Delta_{ac}^4 G_a G_c} . \tag{5.59}$$

If the crystal is clamped, then $G_c = 0$ and $\chi(0)$ is again given by (5.57) demonstrating that $G_c(0)$ should diverge at the clamped Curie

temperature T_c^*, ascribed the value of 117.7K by Lagakos and Cummins. For a free crystal, the transition will occur at the free Curie temperature T_o determined by

$$[1 - \Delta_{ac}^4 G_a(0)G_c(0)]_{T=T_o} = 0 \quad . \tag{5.60}$$

For KDP the free Curie temperature T_o = 122K, 4.3K above the clamped Curie temperature.

Some workers reported improved fits to their KDP data by assuming a Debye relaxation form for the soft mode response when using the two oscillator coupled model. Such a Debye response has the form

$$\chi(\omega) = \frac{\chi(0)}{1 - i\omega\tau} \tag{5.61}$$

when the relaxation time

$$\tau(T) = \Gamma_a(T)/\omega_a^2(T) \quad . \tag{5.62}$$

However, the work of Peercy[59] who obtained an underdamped soft mode in KDP by applying hydrostatic pressure showed that the mode can only be described by a damped harmonic oscillator and not by a Debye relaxation.

5.6 A SUMMARY OF OTHER WORK ON KDP-TYPE CRYSTALS

Though much of the coupled mode theory of KDP discussed to date in this chapter followed from Raman scattering experiments the techniques of FTS and grating spectroscopy have also proved useful in the investigation. The earliest work of this type was that of Barker and Tinkham[52] in 1962 who used an IR monochromator with a wire grid polariser. It was they who first found the overdamped ferroelectric mode band in the 'c' axis of

paraelectric KDP.

Other work was later performed by Onyango et al[60] who used the combination of a power interferometer and a grating spectrometer to obtain reflection spectra of the 'a' and 'c' axes of KDP at 290K and of the 'a' axis at 125K over the range 10 - 700 cm^{-1}. Furthermore, they obtained transmission data from thin polycrystalline films of KDP and correlated these results with the dielectric functions obtained from a Kramers-Krönig analysis of the reflection spectra. Similar power reflection measurements have been performed by Agrawal[47] on KDP, KD^*P (KD_2PO_4) and ADP, to supplement results he obtained using Raman techniques. Reflection measurements have also been made on KDP by Kawamura et al[61] and Sugawara and Nakamura[62] using far IR grating spectrometers.

The technique of DFTS has been used to investigate KDP by Gauss et al[8] who measured the 'c' axis complex reflection spectrum at 300K with an asymmetric interferometer. The spectrum was fitted with a coupled oscillator model of the form (5.52) using the choice of imaginary coupling, ($\Delta = 0$). They also measured the complex reflection coefficient for both 'a' and 'c' axes at $\omega = 4.62$ cm^{-1} between 100 and 295K using a Michelson and a laser radiation source. Hence they were able to deduce the temperature dependence of the complex dielectric constants of both axes. They concluded that the temperature dependence of ω_1^2 (where ω_1 is the uncoupled soft mode frequency associated with the 'c' axis) was not linear in the range between T_c and room temperature but was best fitted with a formula of the type

$$\omega_1^2 = \frac{15911\ (T - 117.7)}{T + 155} \quad cm^{-2} \quad ,$$

thereby disagreeing with the linear fits obtained by other workers.

Gauss also measured the 'a' axis complex reflection spectrum at room

temperature in the range 10 to 80 cm^{-1} and found evidence of a shoulder on the ε'' curve. This had also been found by Onyango et al[60] during the course of their power interferometric studies. This low frequency structure could be fitted by a heavily damped oscillator and was identified as the protonic mode of E symmetry which has been discussed in a recent publication by Havlin et al[63] using a theoretical pseudospin model. These authors found the frequency of this mode to be nearly temperature independent for $T > T_c$ but strongly temperature dependent for $T < T_c$. They concluded that the pseudospin formalism which predicts anomalous behaviour for the ferroelectric soft mode (a protonic mode of B_2 symmetry), necessarily predicts an anomalous behaviour of the protonic E mode. Quantitative temperature dependence measurements of this E mode have yet to be performed.

A number of workers have investigated, both experimentally and theoretically, the behaviour of KDP in its ferroelectric phase (ie T < 122K) where the crystal has orthorhombic symmetry. Amongst their power reflectivity results, Sugawara and Nakamura[62] included a spectrum for the electric vector parallel to the 'c' axis recorded at a temperature of 83K.

Raman scattering was used to investigate KDP below its transition by Shigenari and Takagi[64] in 1971. They found evidence of a satellite mode appearing on the high frequency side of the ferroelectric mode. This extra mode appeared on cooling the crystal below 140K, as a shoulder at $\sim$ 130 cm^{-1} which was hidden under the broad ferroelectric mode at room temperature. On cooling further to below the transition, the mode width narrowed and its frequency increased. Lavrencic et al[65,66] analysed this underdamped spectral feature and concluded that it was also a soft mode with a frequency proportional to the spontaneous polarisation. Their theoretical spectra calculated from a pseudospin analysis with damping included, were in excellent agreement with the experimental results of Shigenari and Takagi[64].

This chapter summarises the theoretical and experimental work on ferroelectrics which is relevant to the measurements that have been performed with the power and polarising interferometers. Various other important but less relevant aspects of ferroelectric theory have been omitted but may readily be found described in recent literature. They include the recently theoretically predicted central modes, a peak at $\omega \sim 0$ which grows in intensity as $T \rightarrow T_o$. The existence of such modes has been confirmed by various Raman experiments including the work of Lagakos and Cummins[58].

FIG. 5.1. THE MECHANICAL MODEL OF TWO OPTIC MODE OSCILLATORS WITH DASHPOT COUPLING

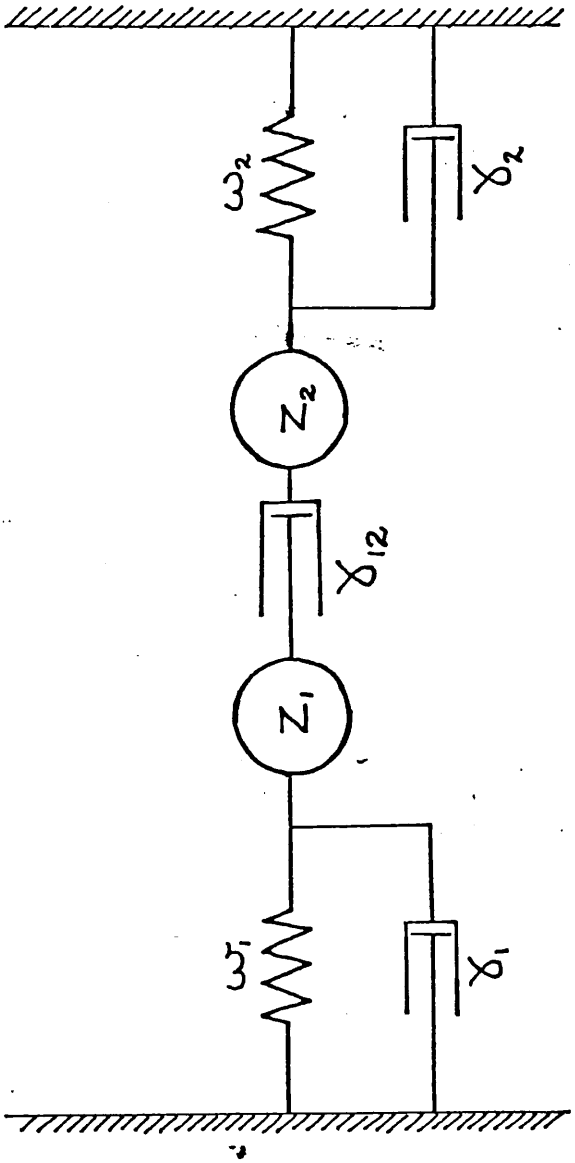

The dashpots $\gamma_1, \gamma_2, \gamma_{12}$ provide damping forces proportional to velocity

CHAPTER 6

A DISCUSSION OF THE RESULTS OBTAINED WITH THE POLARISING INTERFEROMETER

6.1 INTRODUCTION

The performance of the polarising interferometer was rigorously assessed at each stage in its development to detect any defects in the various components. Primarily the testing consisted of performing repeated ratioed run pairs, area Y divided by area X (section 4.5), with the two mirrors in the two arms to check the reproducibility of the complex calibration spectra. This provided an insight into the limitations due to various instrumental factors such as micrometer backlash, instrumental alignment, the flatness of the mirrors and wire grids, and the quality of motion of the phase modulated mirror.

The high frequency cut-off of the wire grid beam dividers was near 250 cm^{-1} and so to avoid aliasing effects a stepping increment (x') of 5 μm was used corresponding to an aliasing frequency $\bar{K}$ = 500 cm^{-1} (2.45). This micrometer step length was twice the smallest that could be achieved with the stepping motor used. No spectral information was lost by 'double' rather than 'single' stepping ($\bar{K}$ = 1000 cm^{-1}) and the time taken to record each data run was halved.

Fig 6.1 illustrates three throughput 'amplitude' spectra $|\rho(\nu)|$ obtained with mirrors in the two arms of the evacuated polarising interferometer and using a quartz window Golay detector. Each of the three spectra corresponds to a different vibrational amplitude of the phase modulated mirror achieved by altering the power (v) supplied by the oscillator driving the mirror vibrator. As discussed in the previous

chapter, this has the effect of shifting the peak of $|\rho(\nu)|$ within the spectral range, an effect clearly shown by Fig 6.1. Curve 'a' was obtained by optimising the power delivered by the oscillator (v = 9.5 mV) to give the largest possible Golay signal from the aligned interferometer at the grand maximum of the interferogram. Curves 'b' and 'c' were obtained by respectively 'underblowing' (v = 5 mV) and 'overblowing' (v = 25 mV) the phase modulation. In the case of curve 'c', the effect of the envelope Bessel function imposed by the phase modulation is clearly recognisable.

For the majority of studies undertaken a resolution of ~ 5 cm^{-1} was adequate. This was achieved by recording double-sided interferograms each of 400 double (5 μm) steps (2.10). The resolving power of the instrument could be conveniently assessed by recording a water vapour spectrum. Published results show a large number of narrow absorption lines in the far IR. The spectrum is easily measured by ratioing the mirror calibration spectrum obtained with air in the interferometer against that obtained from the evacuated interferometer. A spectrum obtained in this manner is illustrated in Fig 6.2. The lines indicated are listed in a reference of wavelength standards in the IR[67]. The spectrum was computed from a 'single side' interferogram scan whereby the moving mirror traversed 200 steps up to the position of ZPD and continued beyond for a further 2000 steps. This corresponds to a resolution of 0.5 cm^{-1} which is slightly degraded in the final computed spectrum by the apodisation process. The leading 200 points were required by the 'single side scan' computer program to detect and computationally relocate the position of zero path difference at an actual sampling point. The water vapour interferogram, recorded from the unevacuated interferometer in the manner just described is shown in Fig 6.3.

6.2 ALKALI HALIDE STUDIES

Alkali halides are a good subject for spectroscopic studies in the far IR because of their distinctive reststrahlen region. Previous DFTS work has been done mainly on KBr[11,12]; however, for studies using the polarising interferometer, CsBr and CsI were chosen, for the reststrahlen band of each lies comfortably within the working range of the instrument.

The major problems encountered during these studies were in preparing the samples for measurement in the interferometer. Both the Cs salts investigated are hygroscopic, and so prolonged exposure of the crystals to the air had to be avoided. The crystals were polished flat to $\sim$ 0.2 μm (ie $\sim$ ±0.1 μm) across the reflecting surface of 1" diameter. It was soon discovered that the flatness of these samples deteriorated with time. The deterioration was hastened by repeated cooling to low temperatures. The surface flatness was thus checked after each set of measurements and if necessary, the crystal was repolished.

After polishing, the crystals were aluminised in an evaporator. A mask was used in order that a 0.6" diameter area of exposed crystal surface remained at the centre of the crystal. The thickness of the aluminium film exceeded 0.3 μm, thus the problems due to skin-depth, discussed in section 4.5, were overcome. Any errors in the amplitude spectra due to this cause that were still present were smaller than those in the reproducibility of repeated amplitude measurements.

Upon installing the sample in the interferometer, the screens were carefully aligned to eliminate crosstalk between the aluminised and exposed crystal areas. Care was also taken to ensure that the exposed area was free of specks of aluminium. The effect of these specks, crosstalk or sample flatness outside the required tolerances was particularly apparent

at the point in the crystal spectrum where the amplitude reflectivity drops to a minimum on the high frequency side of the reststrahlen resonance. In the region of this minimum, which is characteristic of an alkali halide, excess noise has a marked effect on the phase spectrum and must therefore be avoided in order that accurate dielectric function values can be obtained.

The complex reflectivity spectra of CsBr and CsI, measured using the polarising interferometer, are shown in Figs 6.4 and 6.5, and the ensuing dielectric functions are illustrated in Figs 6.6 and 6.7. The TO and LO frequencies are given and may be compared to those of Lowndes and Martin[68].

Assuming these functions can be fitted by an oscillator model according to (3.119) then $\Delta(\omega)$ and $\Gamma(\omega)$ the self-energy and damping functions respectively can be derived and are shown in Figs 6.8 and 6.9. The self-energy calculated in this manner by fits to the dielectric functions is the sum of two components, Δ^E which is frequency independent and arises from thermal expansion and $\Delta^A(\omega)$ arising purely from anharmonic interactions. In order to isolate the anharmonic contribution $\Delta^A(\omega)$, knowledge of Δ^E must be acquired. Lowndes[69] has obtained such information for RbI, CsI and TlCl using high pressure far IR studies.

6.3 INITIAL AMBIENT TEMPERATURE STUDIES OF KDP AND ADP

Ferroelectric KDP was first investigated, along with anti-ferroelectric ADP, at ambient temperature using an early version of the polarising interferometer[31]. In this early form, the phase modulation was provided by the loudspeaker arrangement shown in Fig 4.7 and the output focussing was performed by polythene lenses rather than the all-reflecting output optics system adopted later.

Both the 'a' and 'c' axis spectra were obtained for KDP and ADP. The

results over the range 40 - 210 cm^{-1} are illustrated in Figs 6.10 to 6.15. They are in good agreement with previous published data including that of Birch et al[7] in which the first direct measurements of the complex reflectivities of both axes of KDP and the 'a' axis of ADP are reported, and with earlier work involving Kramers-Krönig determinations[52,60,61].

The ε'' curve for the KDP 'c' axis should exhibit a maximum in the region of 50 cm^{-1}, associated with the ferroelectric transition, but in these initial measurements this was not resolved.

The sensitivity of the dielectric functions of both KDP and ADP to small changes in the phase spectra is illustrated by the dotted and dashed curves in Figs 6.11, 6.12, 6.14 and 6.15. These curves show the effect of errors of ±0.1 of a sampling step (ie ±0.5 μm), on the computed dielectric functions. The dotted and dashed curves correspond, respectively, to shifts which increase and decrease the phase of the computed reflectivity, by an amount linearly proportional to the frequency. This has little effect on the positions of the various features in the spectrum but changes the magnitudes of the features quite markedly in some cases.

6.4 TEMPERATURE DEPENDENT INVESTIGATIONS OF THE KDP FERROELECTRIC 'c' AXIS

In order to improve upon the results presented in section 6.3, certain modifications described in Chapter 4 were made to the polarising interferometer. These included changes in the phase modulation system and the use of all-reflecting output optics. This later version of the polarising interferometer was used for temperature dependent studies of the KDP 'c' axis[70].

The complex reflectivity spectra of the 'c' axis of KDP at 300, 200,

175 and 150K are shown in Fig 6.16 and the resulting dielectric functions are displayed in Fig 6.17. The results were obtained from two crystals purchased from different sources and no significant difference was observed in the spectra obtained from them.

The overdamped band, found by Barker and Tinkham[52], in the 300K ε'' curve which peaks at about 50 cm^{-1} has been resolved.

To account for the coupling in the KDP 'c' axis spectrum between the soft mode and the higher frequency optic mode lying near 180 cm^{-1}, the results were fitted using the coupled mode formalism of Barker and Hopfield[14] discussed in Chapter 6.

Both resistive 'dashpot' and reactive 'spring' coupling fits were performed to the KDP spectra using equations (5.33) and (5.35) respectively. In each case, j = 1 was taken to designate the ferroelectric soft mode and j = 2, the optic mode. Each model has seven parameters, the set ω_1^2, ω_2^2, $(\gamma_1+\gamma_{12})$, $(\gamma_2+\gamma_{12})$, γ_{12}, $z_1, -z_2$ was used for resistive coupling and the set (k_1+k_{12}), (k_2+k_{12}), k_{12}, Γ_1, Γ_2, e_1, $-e_2$ was used for reactive coupling following Barker and Hopfield. The effective charges are of opposite sign and to indicate this a minus sign is attached to e_2 and z_2.

The parameters obtained via the fits are listed in Tables 1 and 2. For both sets of parameters the value $\varepsilon_\infty = 3.2$ was used[8,52], and only the results above 40 cm^{-1} were employed in the fits. Also included in these tables is the equivalent notation for the parameters as used by other workers who employed the same coupling model.

The use of the Barker and Hopfield notation clearly illustrates the problem that arises when the resistive coupling model is employed. This problem, encountered by Barker and Hopfield, has since become obscured by the different notation adopted by other workers[8,58]. It is immediately

TABLE 1

Parameters obtained from theoretical fits to the experimental data using the resistive "dashpot" coupling model

Barker and Hopfield analysis parameters	z_1 (cm^{-1})	z_2 (cm^{-1})	ω_1^2 (cm^{-2})	ω_2^2 (cm^{-2})	$\gamma_1+\gamma_{12}$ (cm^{-1})	$\gamma_2+\gamma_{12}$ (cm^{-1})	γ_{12} (cm^{-1})
Equivalent notation of Gauss et al (8)	M_1	M_2	ω_1^2	ω_2^2	γ_1	γ_2	$\Gamma(\Delta=0)$
T = 300K	293	472	7300	37800	140	96	108
200K	352	507	5300	39200	143	88	110
175K	363	488	4100	37900	139	76	99
150K	388	478	2700	36300	125	59	81

TABLE 2

Parameters obtained from theoretical fits to the

experimental data using the reactive "spring" coupling model

Barker and Hopfield analysis parameters	e_1 (cm^{-1})	e_2 (cm^{-1})	k_1+k_{12} (cm^{-2})	k_2+k_{12} (cm^{-2})	Γ_1 (cm^{-1})	Γ_2 (cm^{-1})	k_{12} (cm^{-2})
Equivalent notation of She et al (55).	P_a	P_b	ω_a^2	ω_b^2	Γ_a	Γ_b	$\Delta^2(\Gamma_{ab}=0)$
T = 300K	526	181	19500	25600	228	7.2	15000
200K	589	182	18200	26300	229	2.3	16500
175K	581	181	15800	26200	211	4.0	16100
150K	589	181	13100	25900	180	4.1	15600

evident from Table 1 that $(\gamma_2+\gamma_{12}) < \gamma_{12}$ in all cases hence $\gamma_2 < 0$ and so we have the unphysical occurrence of a negative resistance in the high frequency mode. The resistive model should thus be treated simply as a mathematical curve fitting exercise and not as a description of the physical situation. Consequently, the author prefers to use reactive coupling as did She et al[55].

In this version, it is found that in two cases the spring constant k_1 is negative, but this simply means that the low frequency oscillator would be unstable by itself, and that the overall stability is maintained by the spring coupling to the other oscillator.

The clue to what is happening is the very small value of ε''_c at $\sim$ 135 cm^{-1} (Fig 6.17). This minimum can be described as follows. The heavily damped soft mode is not being driven here because the direct coupling to the radiation field is cancelled by the indirect coupling through the high frequency mode. The low value of ε'' caused by this "interference" requires firstly that any damping in the coupling and in the high frequency mode must be small, and secondly that the effective charges must have opposite signs, since the interference takes place below the frequency of the high frequency mode. Any attempt to describe the situation by using resistive coupling leads to the use of an unphysical compensating negative damping in the high frequency mode. The reactive mode, however, only requires a low value of Γ_2 and opposite signs for the effective charges. There may be some damping in the coupling but it cannot be very large; a recent paper by Wehner and Steigmeier[71] discusses the need for more information before the choice of one set of parameters can be physically justified.

The resistive parameters are listed so that comparison can be made with results obtained by other workers[8,58]. The main difference is that

the ω_1^2 values obtained, the square of the ferroelectric mode frequency, are consistently larger due perhaps to a lack of accurate data below 40 cm^{-1}. However, the trend in these values does exhibit the soft behaviour of this mode.

Theoretical fits to the dielectric functions using the reactive "spring" coupling model are illustrated in Fig 6.18. The parameters obtained can be compared with those of She et al[55]. Here the (k_1+k_{12}) values are higher than those of She but show the expected "softening" whereas the (k_2+k_{12}) values are temperature independent to $\sim \pm 1\%$.

Fits using the reactive model were also performed on three modified 300K spectra. These spectra were obtained by ±1% changes in the experimental ρ curve and by shifting the ϕ curve by the equivalent of -0.020 of a sampling step (ie 0.020 x 5 μm). This corresponds to a phase shift which is linearly proportional to the frequency and typically produces a change of -1° at 136 cm^{-1} in the ϕ spectrum. In this way, the effects on the parameter values of errors in the measured spectra could be observed.

The parameters changed by only $\sim$ 1% due to the modifications in the amplitude. However, the model appeared to be sensitive to shifts in the phase spectrum. The phase shift used gave the following parameter values. The figures in brackets show the difference between these values and those given in Table 2, obtained from the unmodified spectra.

$$e_1 = 551\ (+5\%) \quad ; \quad e_2 = 186\ (+3\%)$$

$$k_1+k_{12} = 21600\ (+11\%); \quad k_2+k_{12} = 26100\ (+2\%)$$

$$\Gamma_1 = 248\ (+9\%); \quad \Gamma_2 = 4.3\ (-40\%); \quad k_{12} = 15900\ (+6\%)$$

One of the important regions in the spectra is the phase minimum between the two modes. The division of field technique gave $3.2\pm0.5^\circ$ at

300K, 2.5±0.05° at 200K and 2.3±0.5° at 175K and 150K as the phase at the minimum. Simulated curves show no significant variation of the phase ϕ at this point with (k_1+k_{12}). Measurements by Gauss et al[8] at 300K show almost zero phase at this point indicating decoupling of the soft mode to the electric field.

Because of the limit on the accuracy of the phase measurements the uncorrected ϕ curves, obtained by replacement of the crystal by the mirror were "phased-up" to 3° at 300K and 2.5° at 200, 175 and 150K at the minimum.

Due to the minimum in ε'' ($\sim$ 1 at 136 cm^{-1}) and the corresponding low value for the absorption coefficient ((3.33) and (3.39)), this dip in the spectrum is particularly suited to investigations by transmission spectroscopy. Such investigations, which are far more sensitive to changes of phase than those obtained by reflection techniques, are described in Chapter 7.

The trends in the curves of Fig 6.16 and 6.17 below 40 cm^{-1} illustrate the importance of obtaining better low frequency data, for most of the effects produced by cooling manifest themselves in this region. The over-damped ε'' band associated with the ferroelectric transition, which peaks at $\sim$ 50 cm^{-1} at 300K, peaks at lower frequencies as the temperature drops towards the transition temperature. Resolution of this band at these lower temperatures necessitates the use of a liquid helium cooled detector. Such a detector is now available in the laboratory and it is hoped that its use will enable the spectra to be extended down to at least $\sim$ 5 cm^{-1} and consequently enable better theoretical fits to be made.

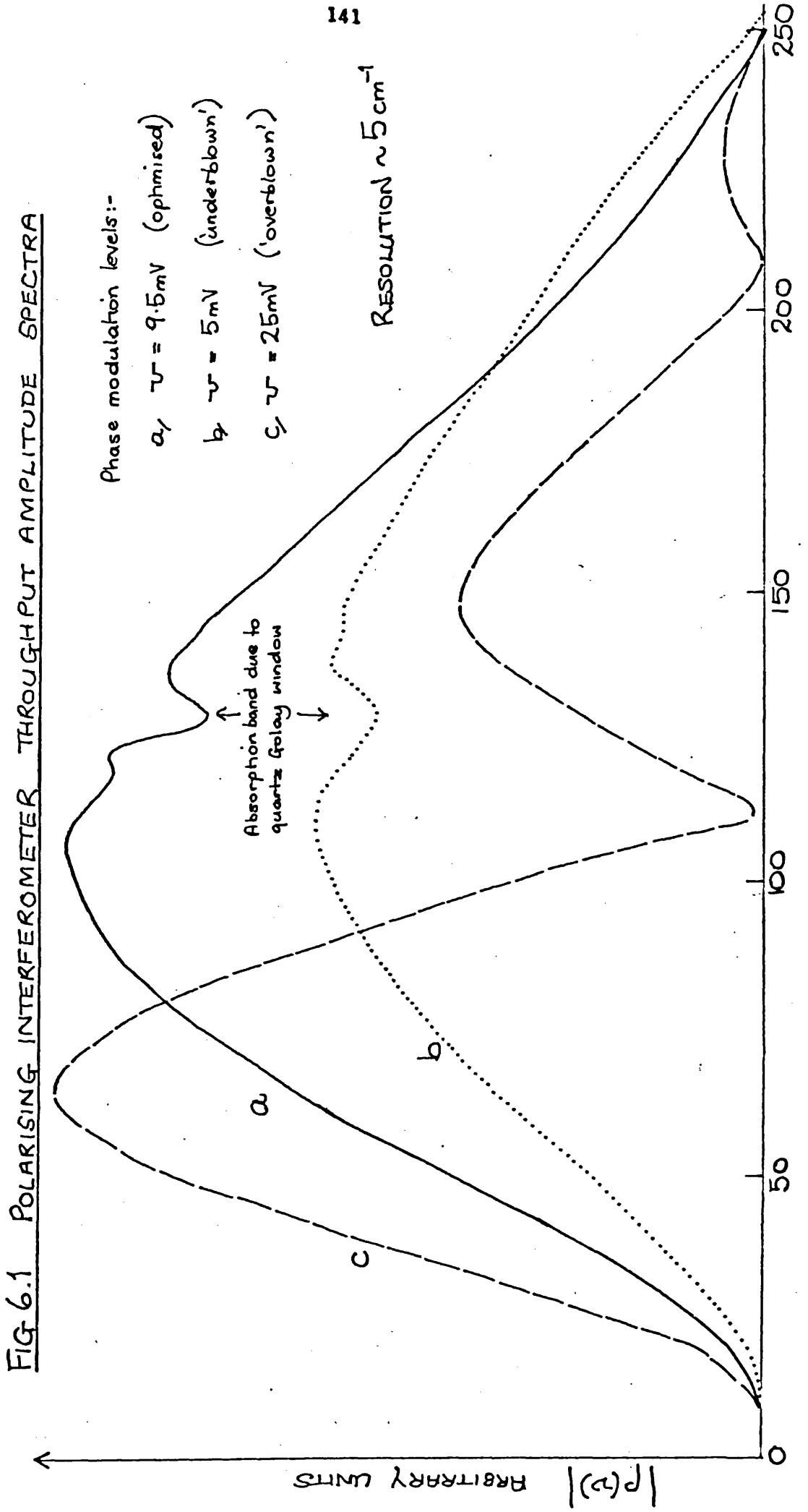

FIG 6.1 POLARISING INTERFEROMETER THROUGHPUT AMPLITUDE SPECTRA

FIG 6.2 WATER VAPOUR ABSORPTION SPECTRUM - RESOLUTION ~0.5 cm^{-1}

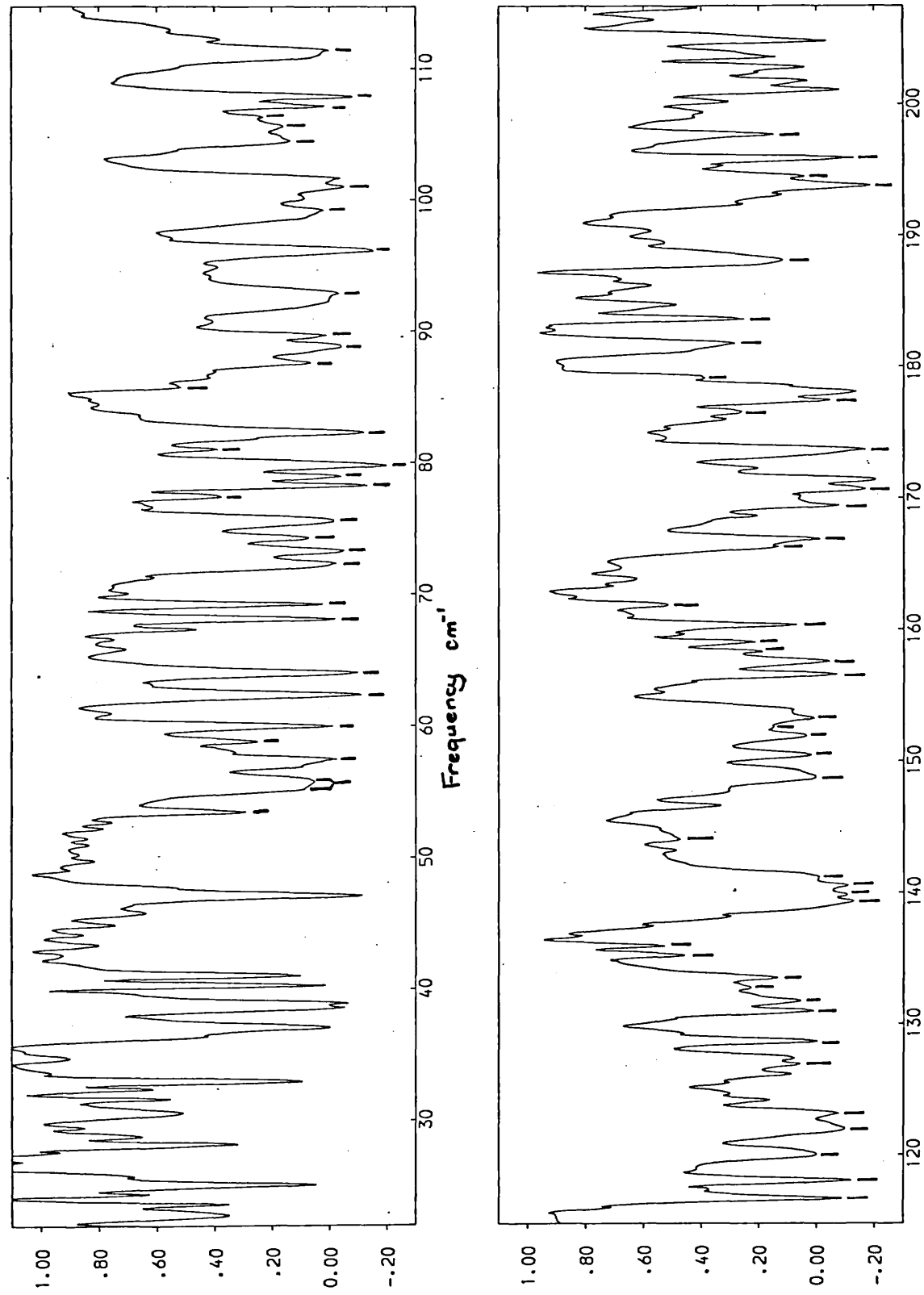

The lines listed in reference (67) are indicated

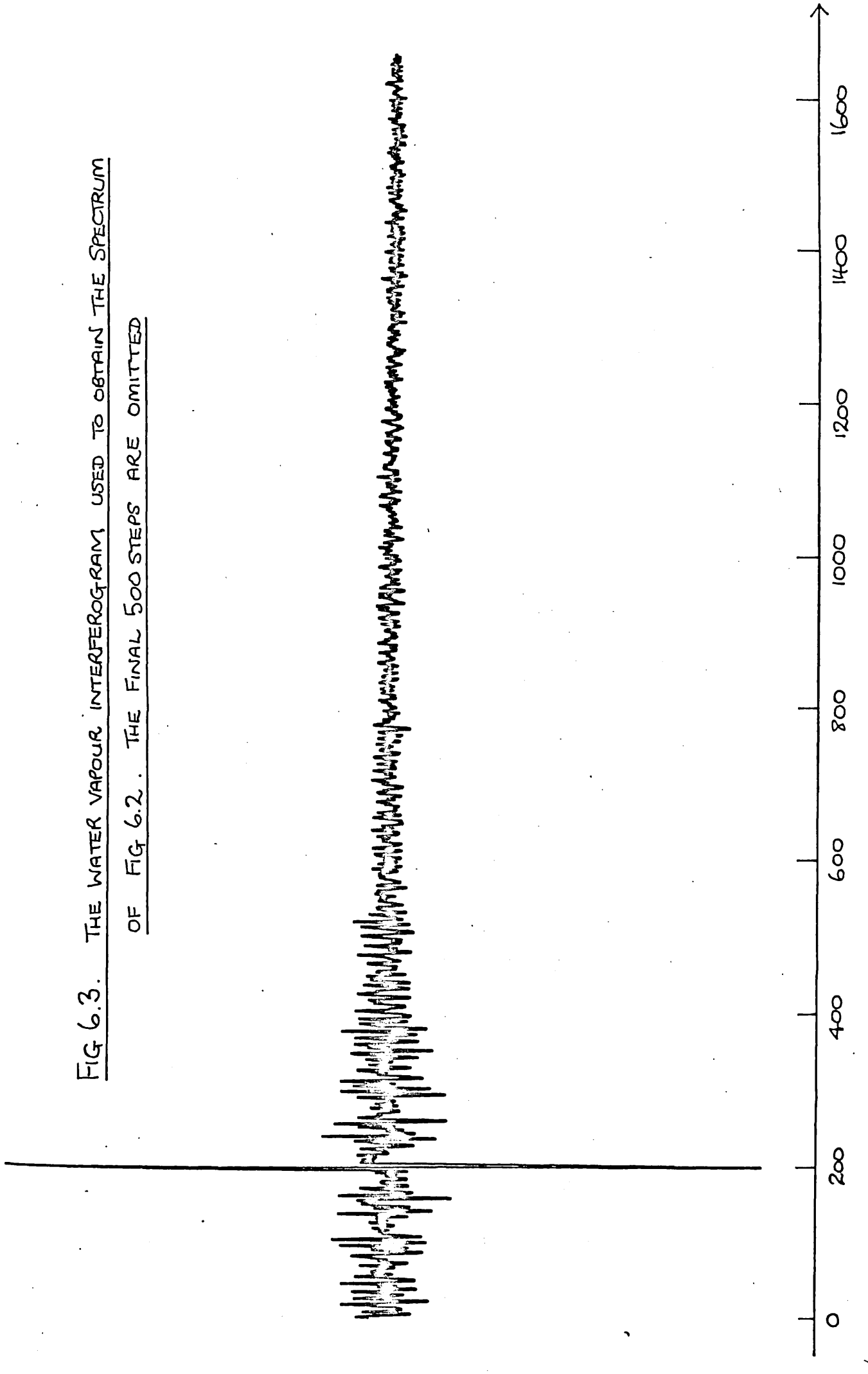

FIG 6.3. THE WATER VAPOUR INTERFEROGRAM USED TO OBTAIN THE SPECTRUM OF FIG 6.2. THE FINAL 500 STEPS ARE OMITTED

FIG 6.4: COMPLEX REFLECTIVITY OF CsBr

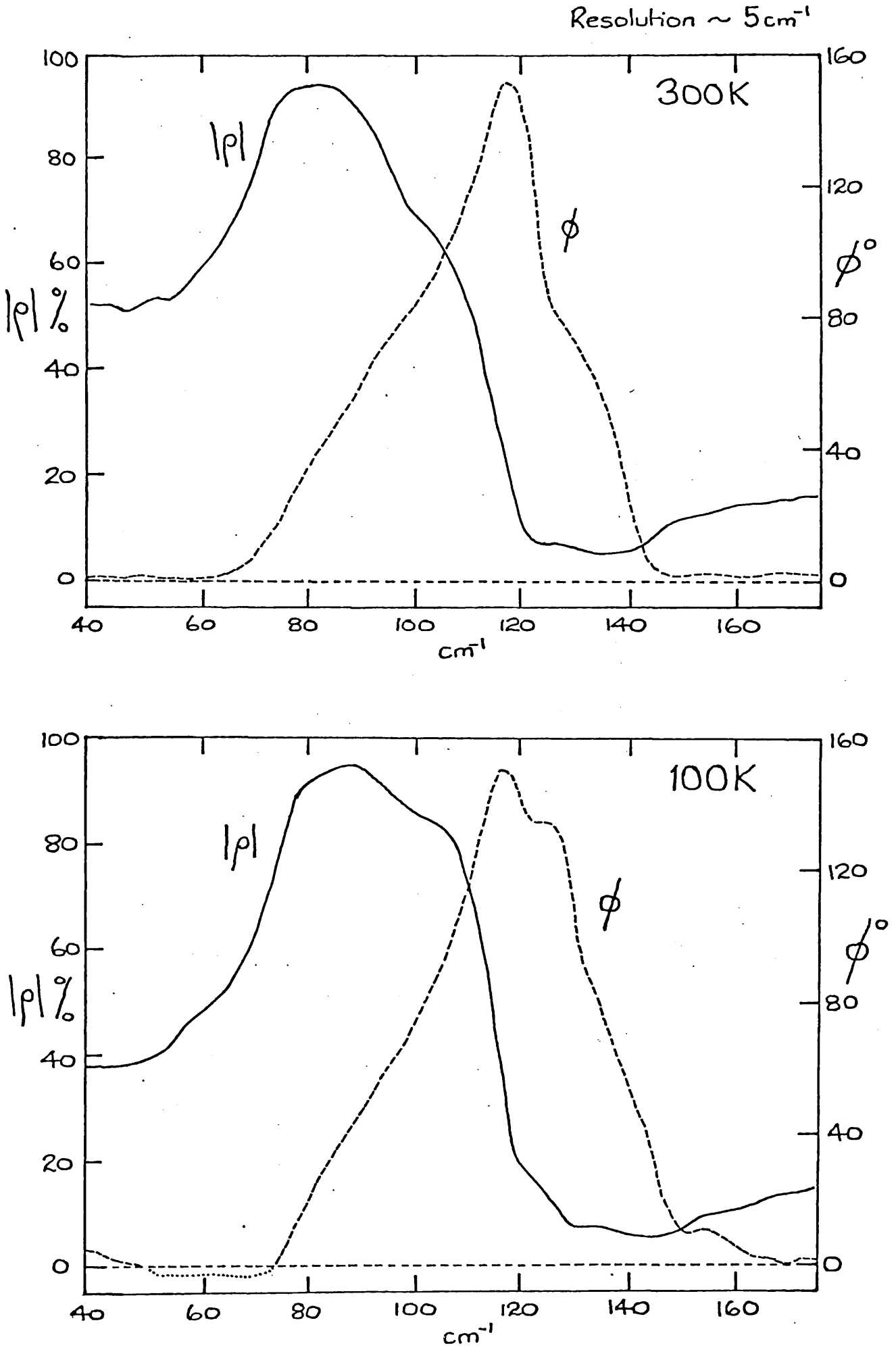

FIG 6.5 COMPLEX REFLECTIVITY OF CsI

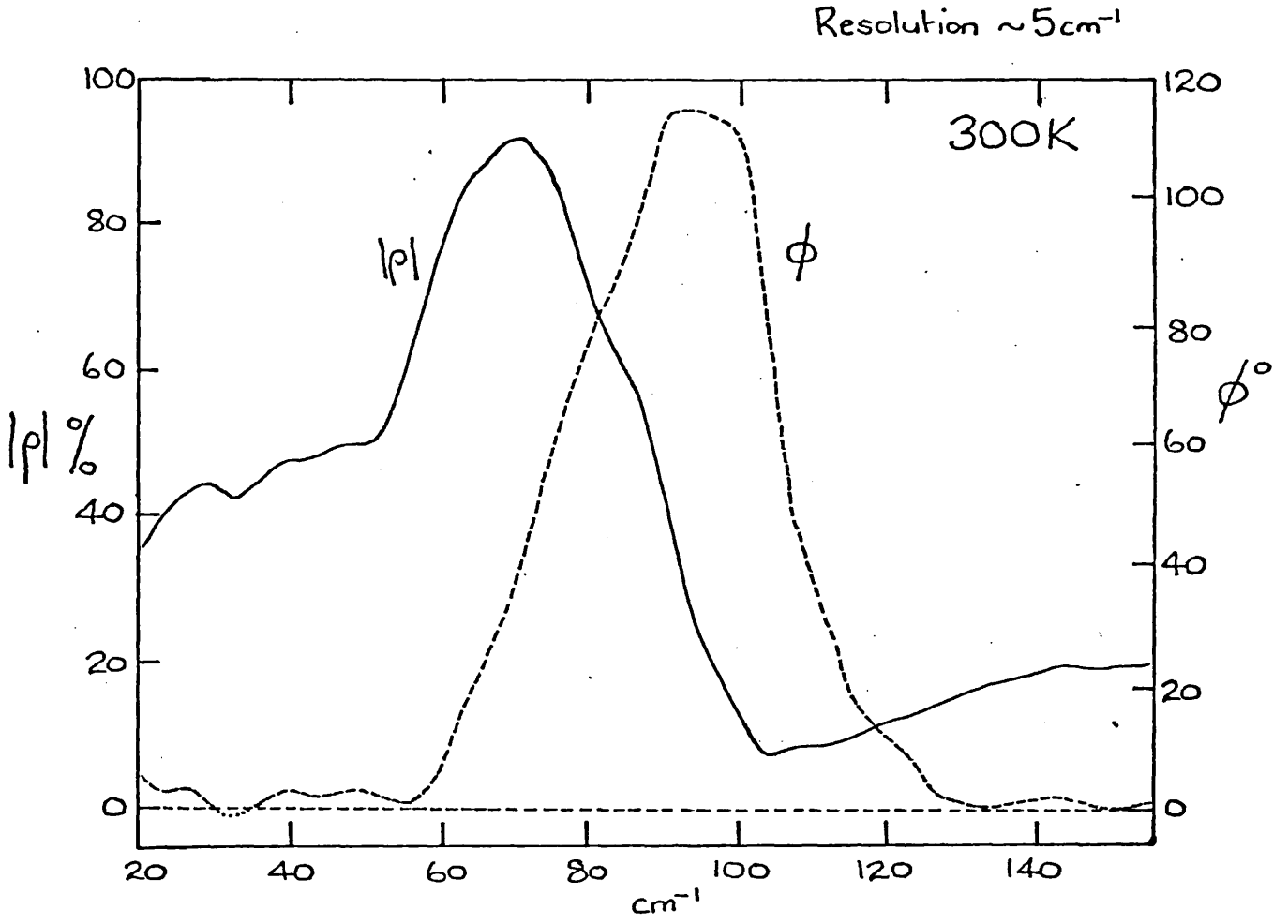

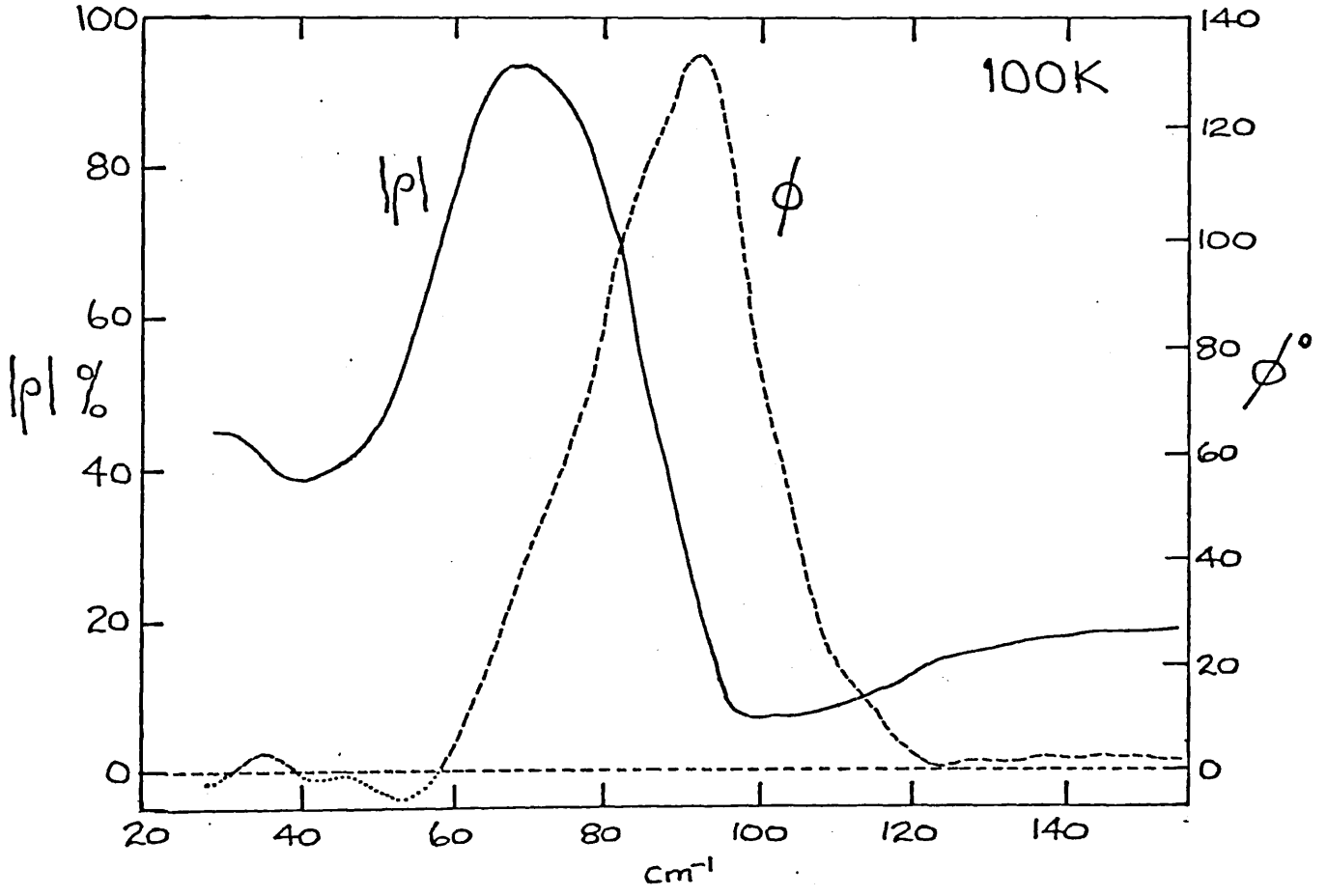

FIG 6.6 DIELECTRIC FUNCTIONS FOR CsBr

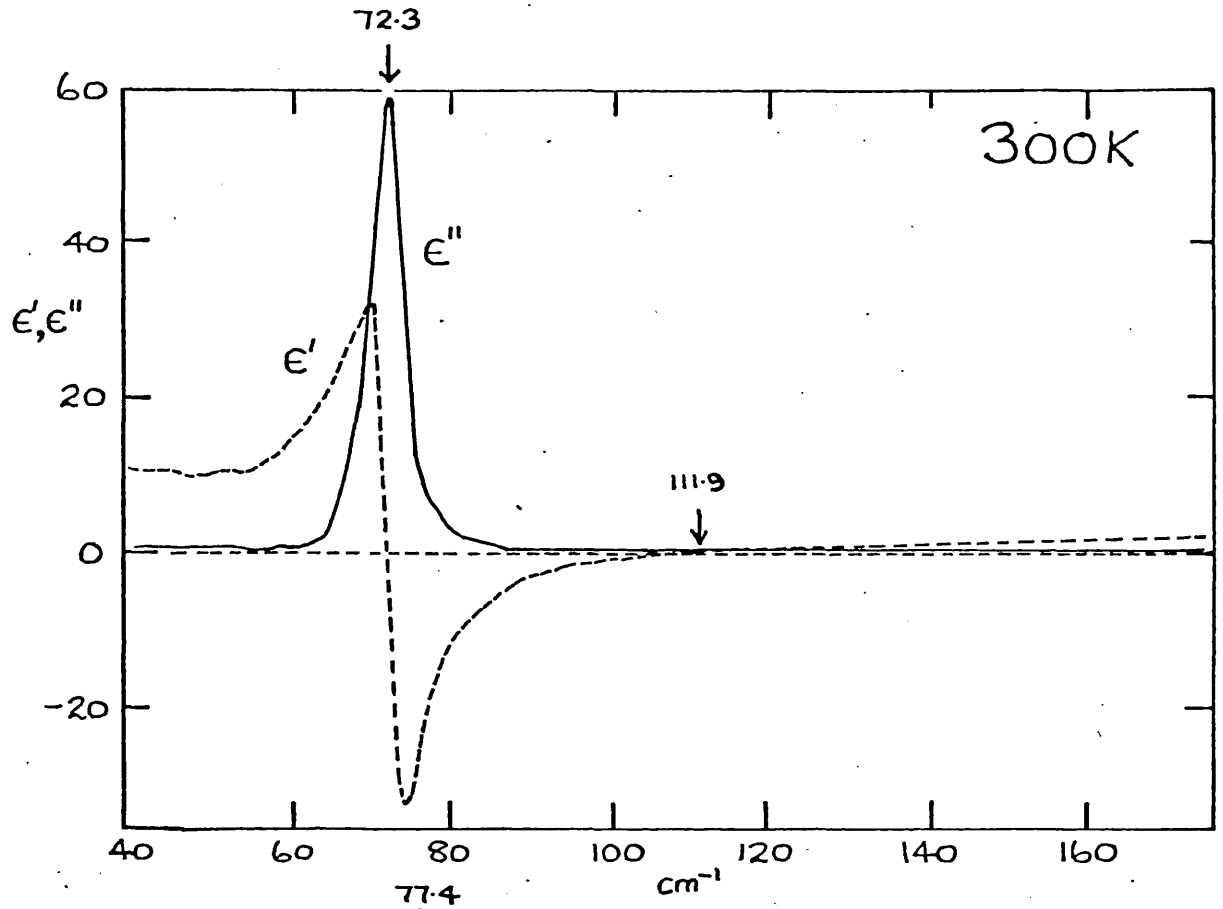

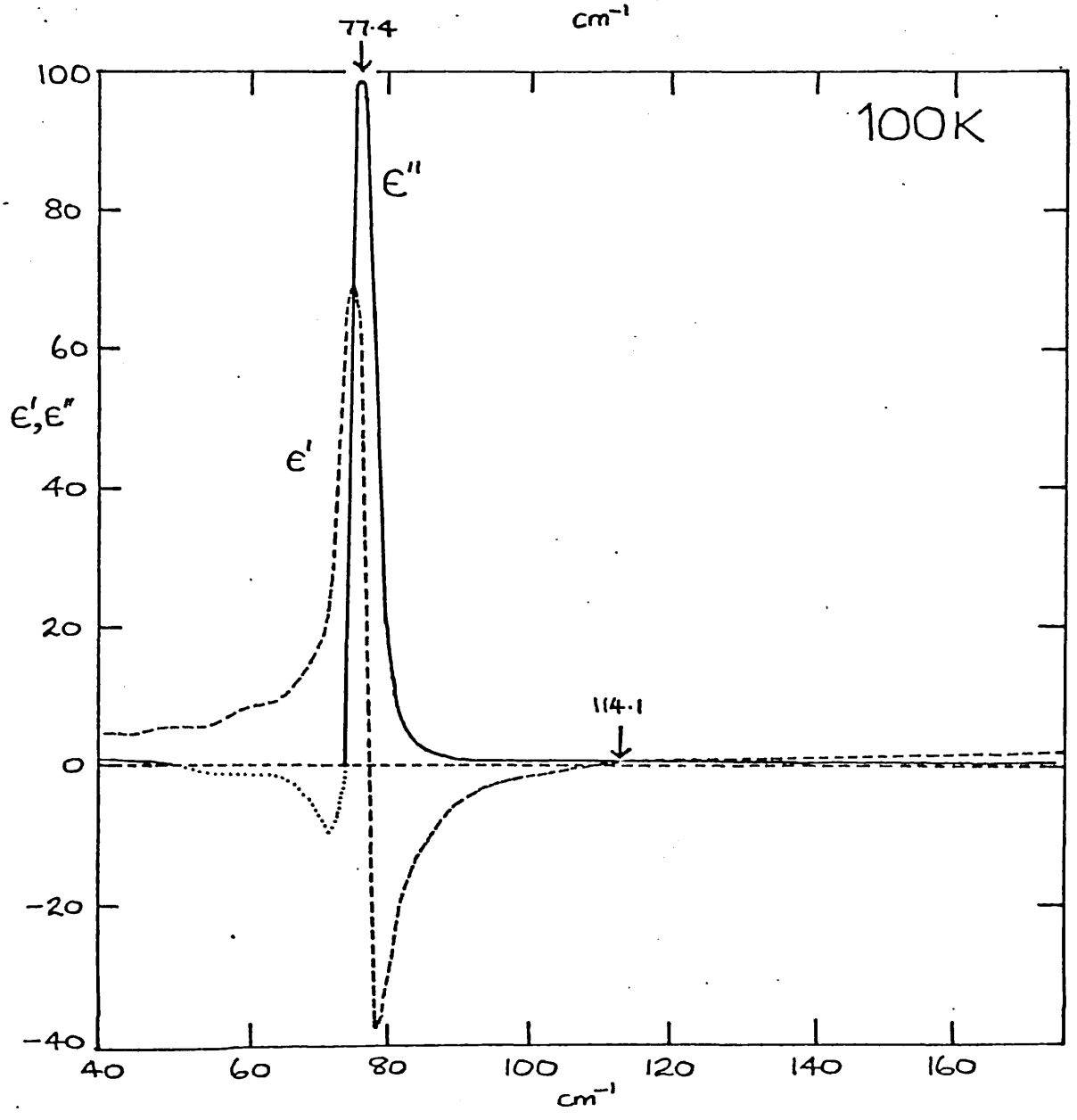

FIG 6.7 DIELECTRIC FUNCTIONS FOR CsI

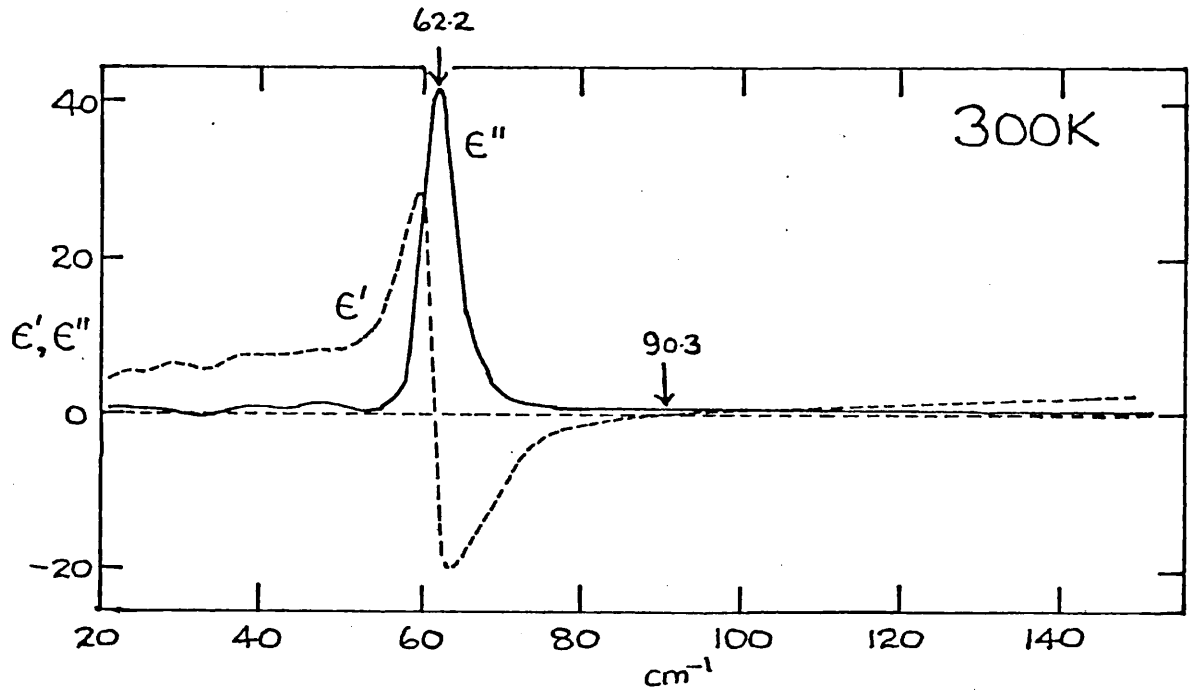

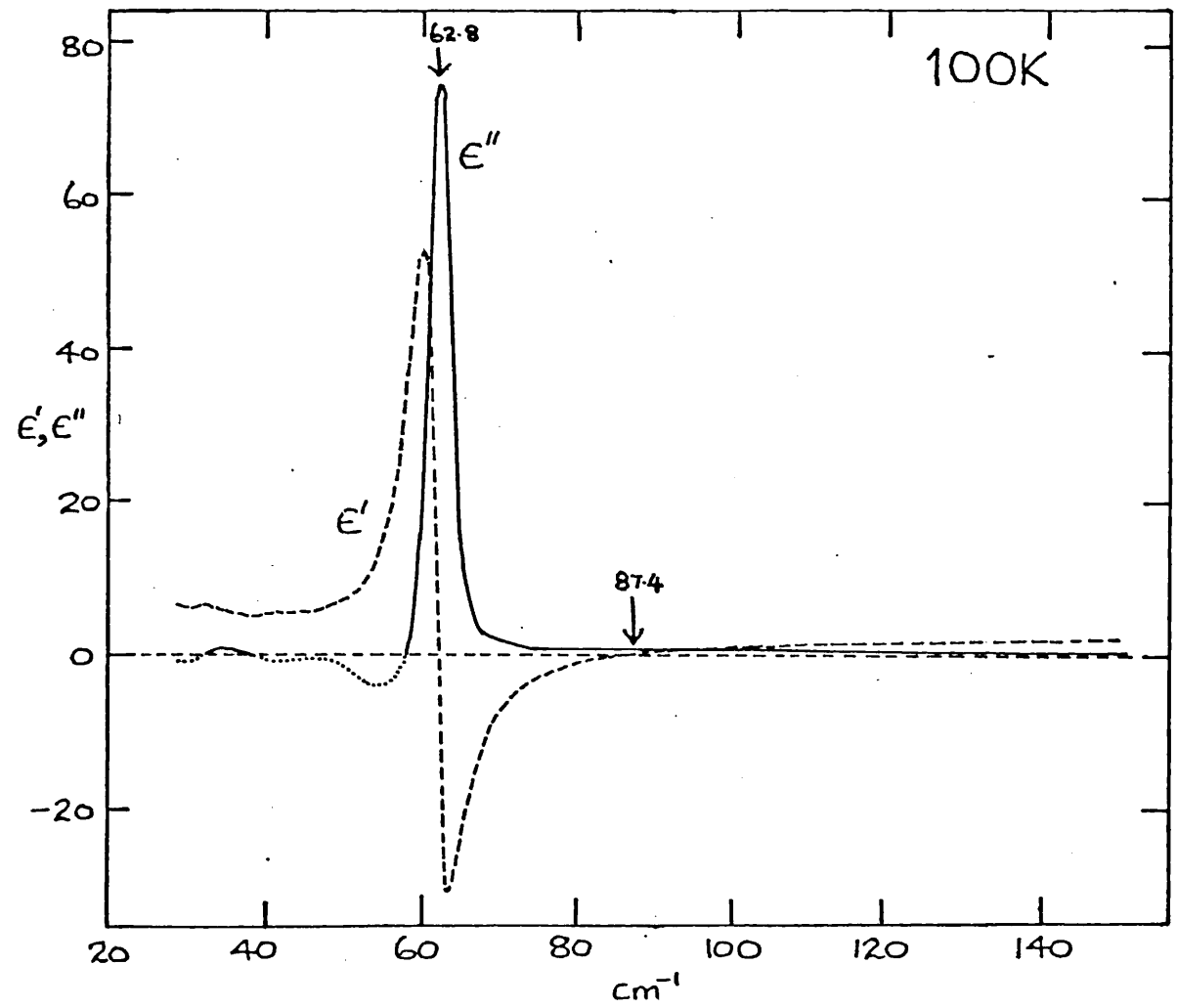

FIG 6.8 THE DAMPING AND SELF ENERGY FUNCTIONS (Γ AND Δ RESPECTIVELY) FOR CsBr AT 300K

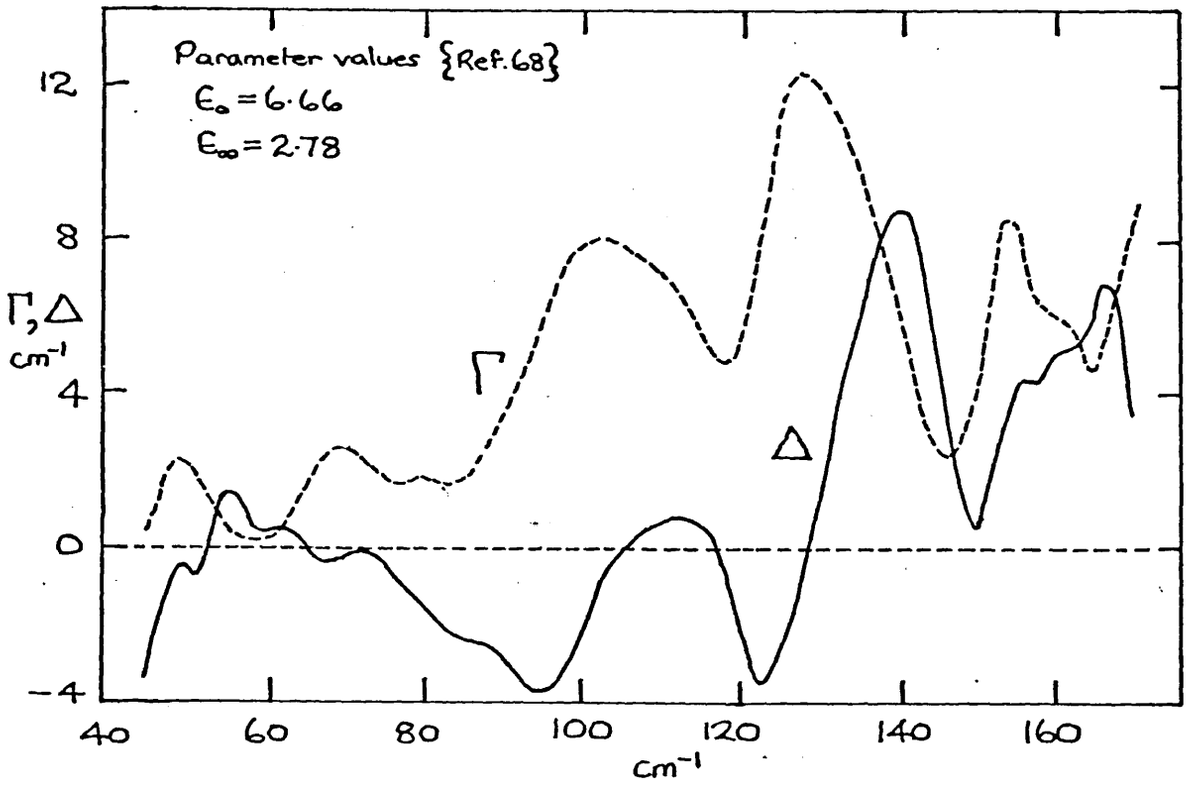

FIG 6.9 THE DAMPING AND SELF ENERGY FUNCTIONS (Γ AND Δ RESPECTIVELY) FOR CsI AT 300K

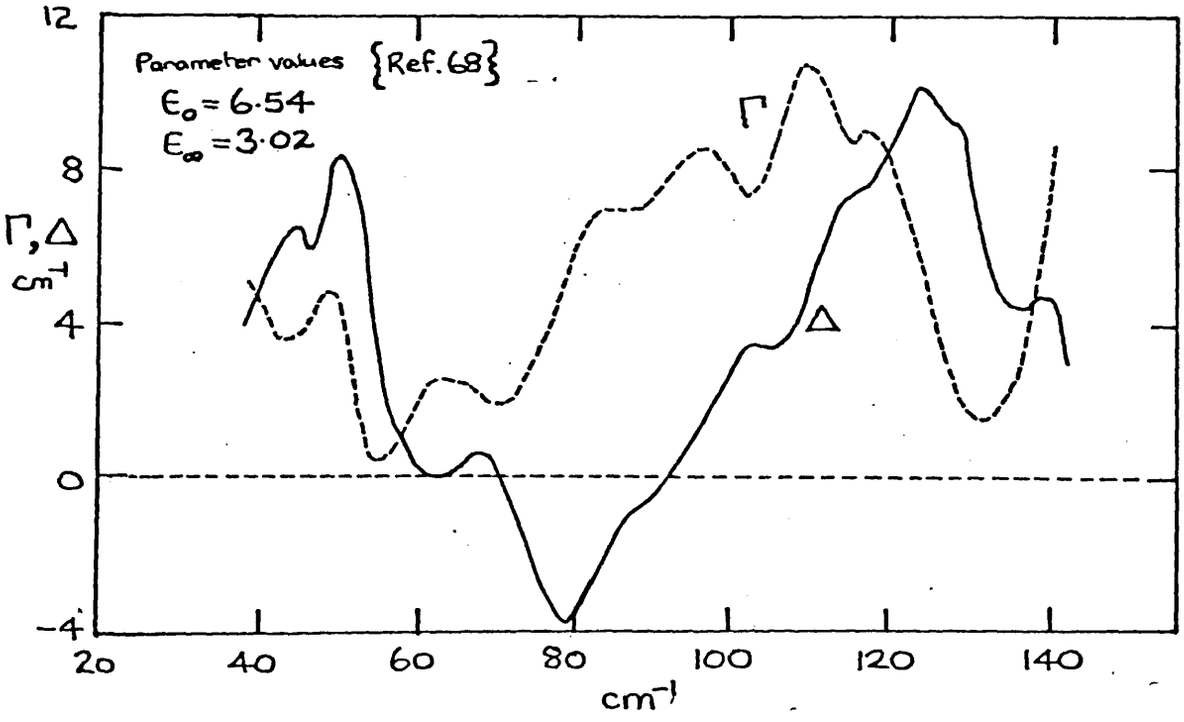

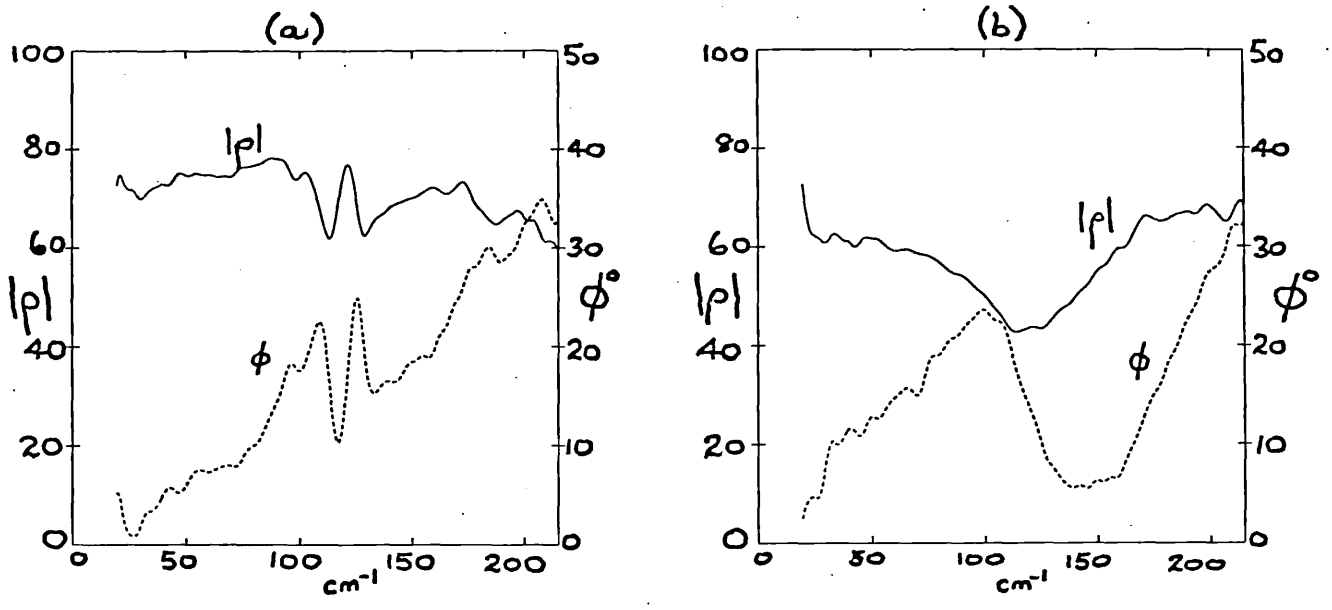

Fig 6.10 : The amplitude and phase reflection spectra of KDP at 300K for radiation polarised (a) parallel to a-axis (b) parallel to c-axis. The resolution is 5cm⁻¹.

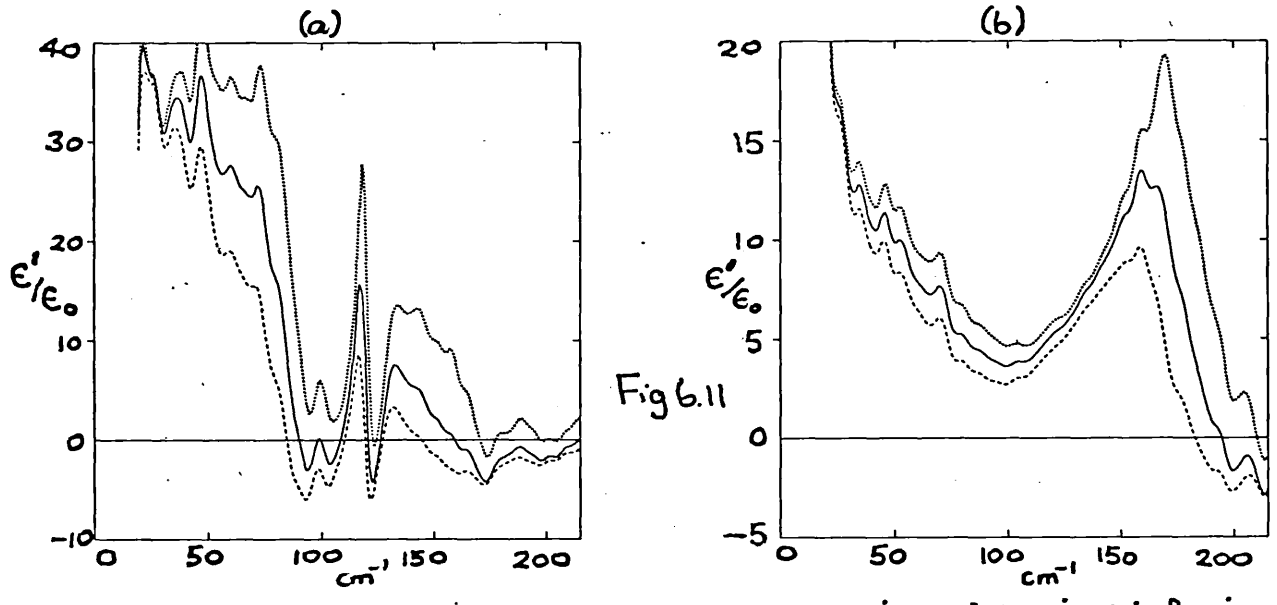

Fig 6.11

Figs 6.11 and 12. Solid Curves: The Real and Imaginary parts respectively of the dielectric functions of KDP at 300K for radiation polarised (a) parallel to a-axis (b) parallel to c-axis. Dotted and dashed curves: Effect of errors of ±0.1 of a sampling step on the calculated dielectric functions.

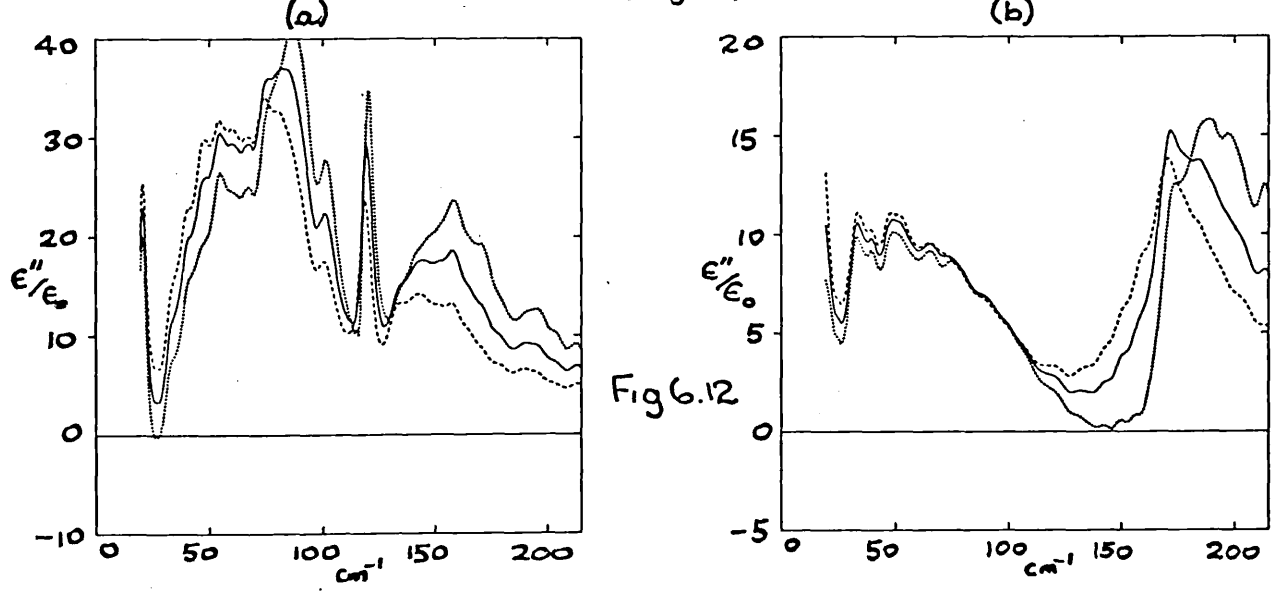

Fig 6.12

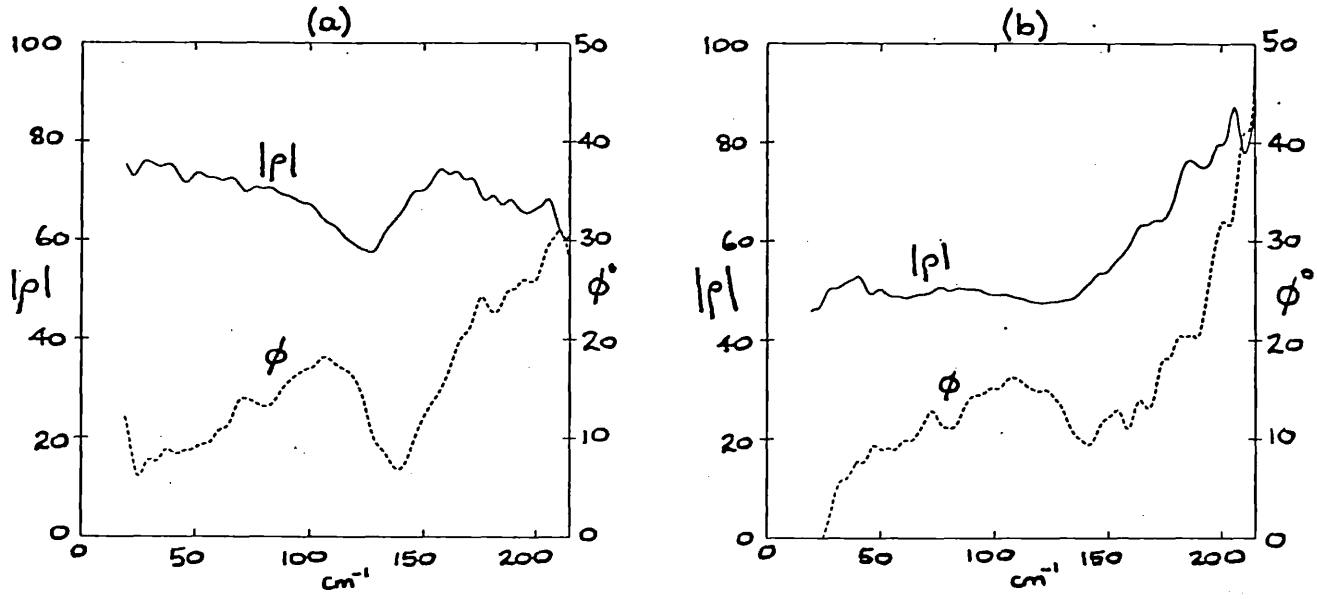

Fig 6.13: The amplitude and phase reflection spectra of ADP at 300K for radiation polarised (a) parallel to a-axis (b) parallel to c-axis. The resolution is 5 cm⁻¹.

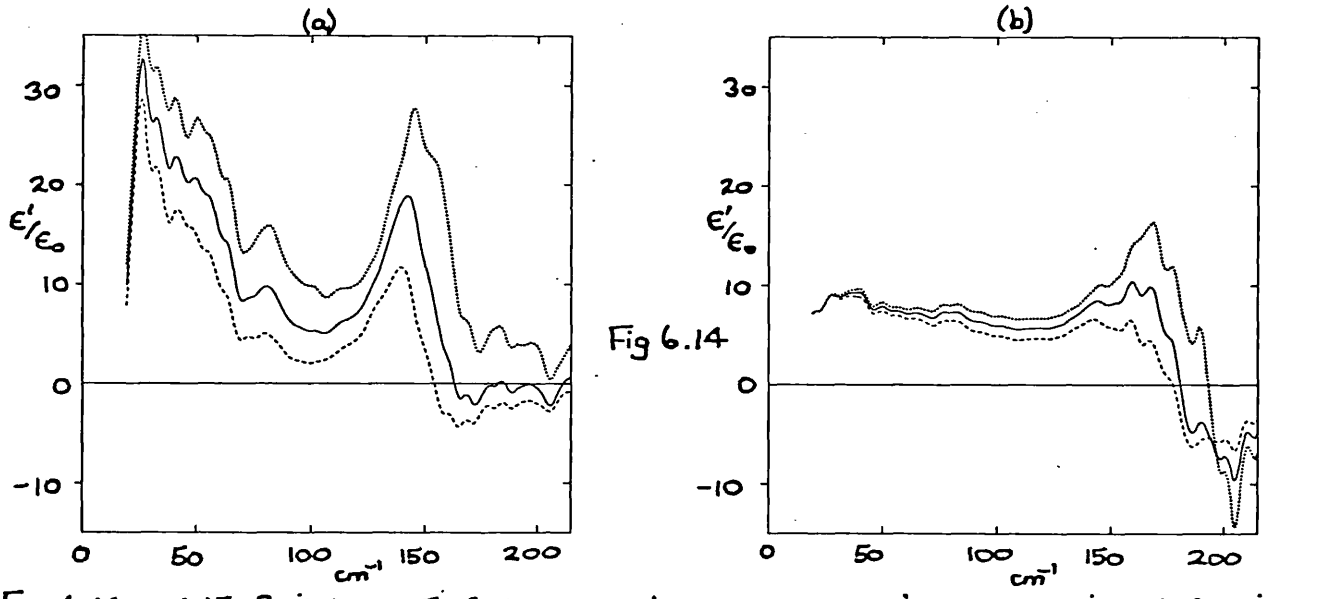

Fig 6.14

Figs 6.14 and 15: Solid Curves: The Real and Imaginary parts respectively of the dielectric functions of ADP at 300K for radiation polarised (a) parallel to a-axis (b) parallel to c-axis. Dotted and dashed curves: Effect of errors of ±0.1 of a sampling step on the calculated dielectric functions.

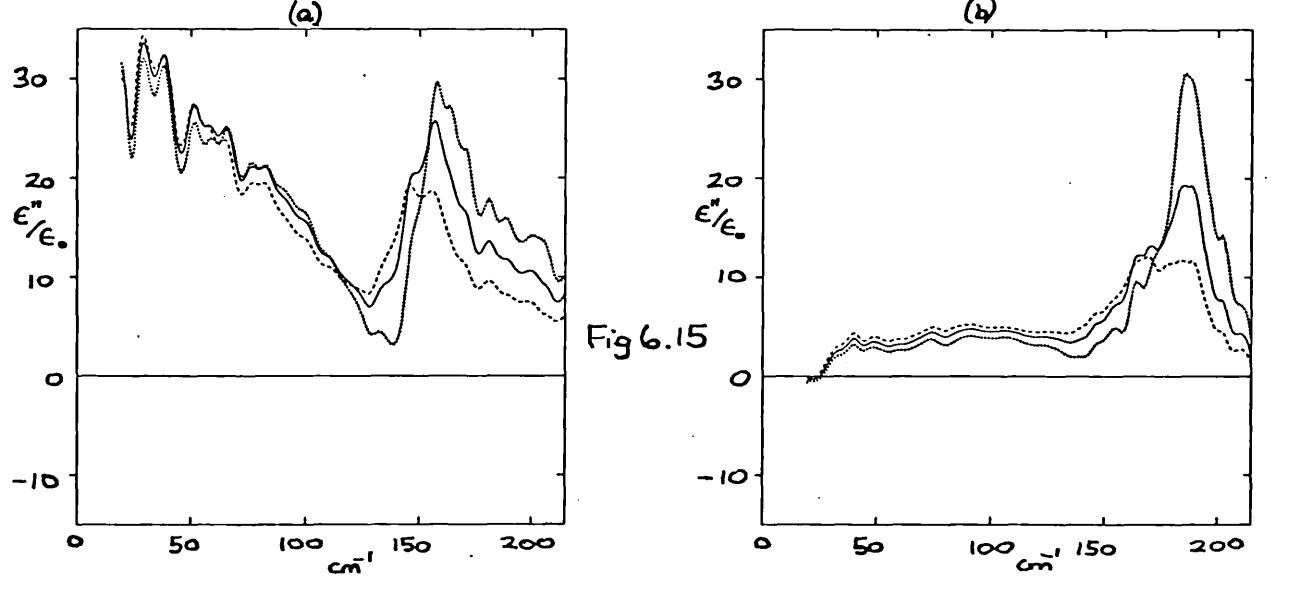

Fig 6.15

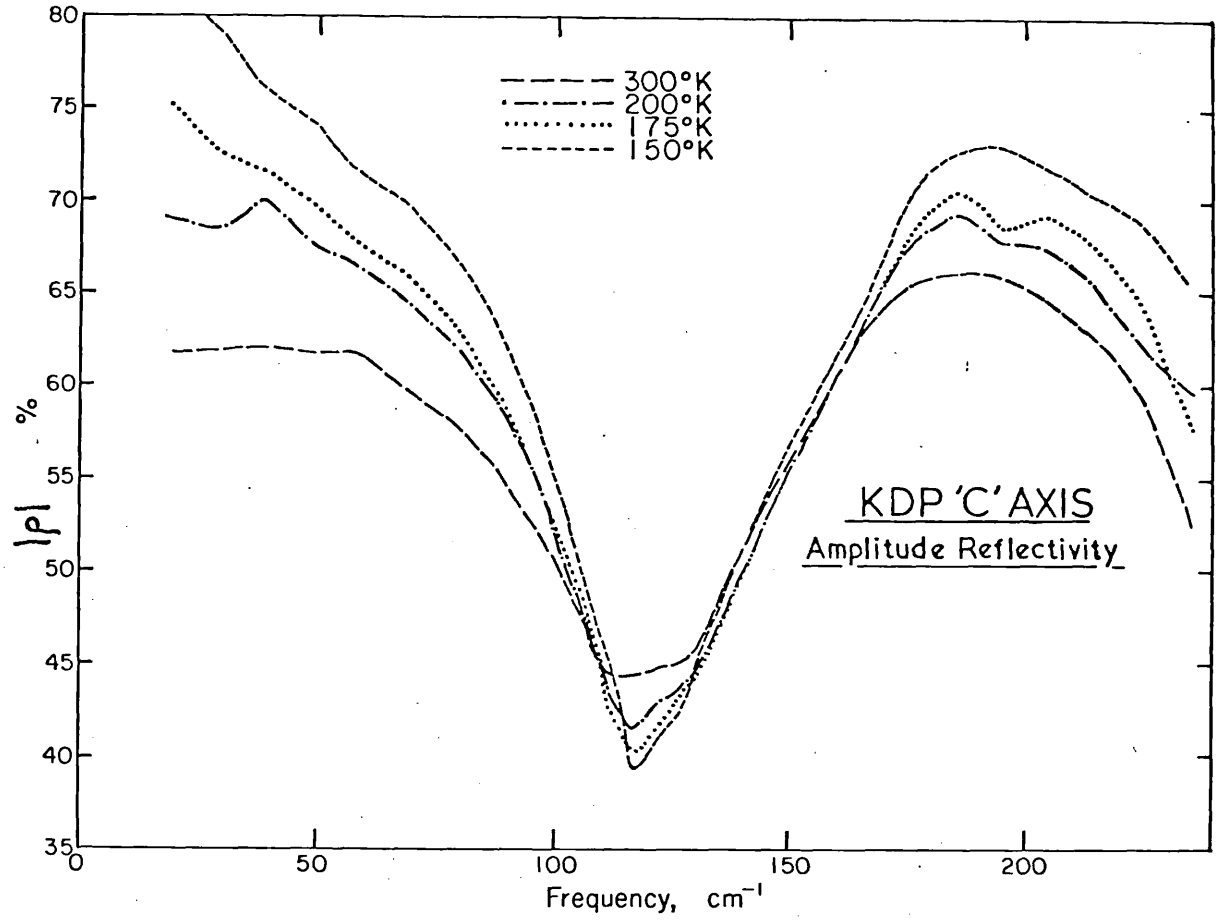

FIG 6.16: COMPLEX REFLECTIVITY SPECTRA OF KDP 'C' AXIS

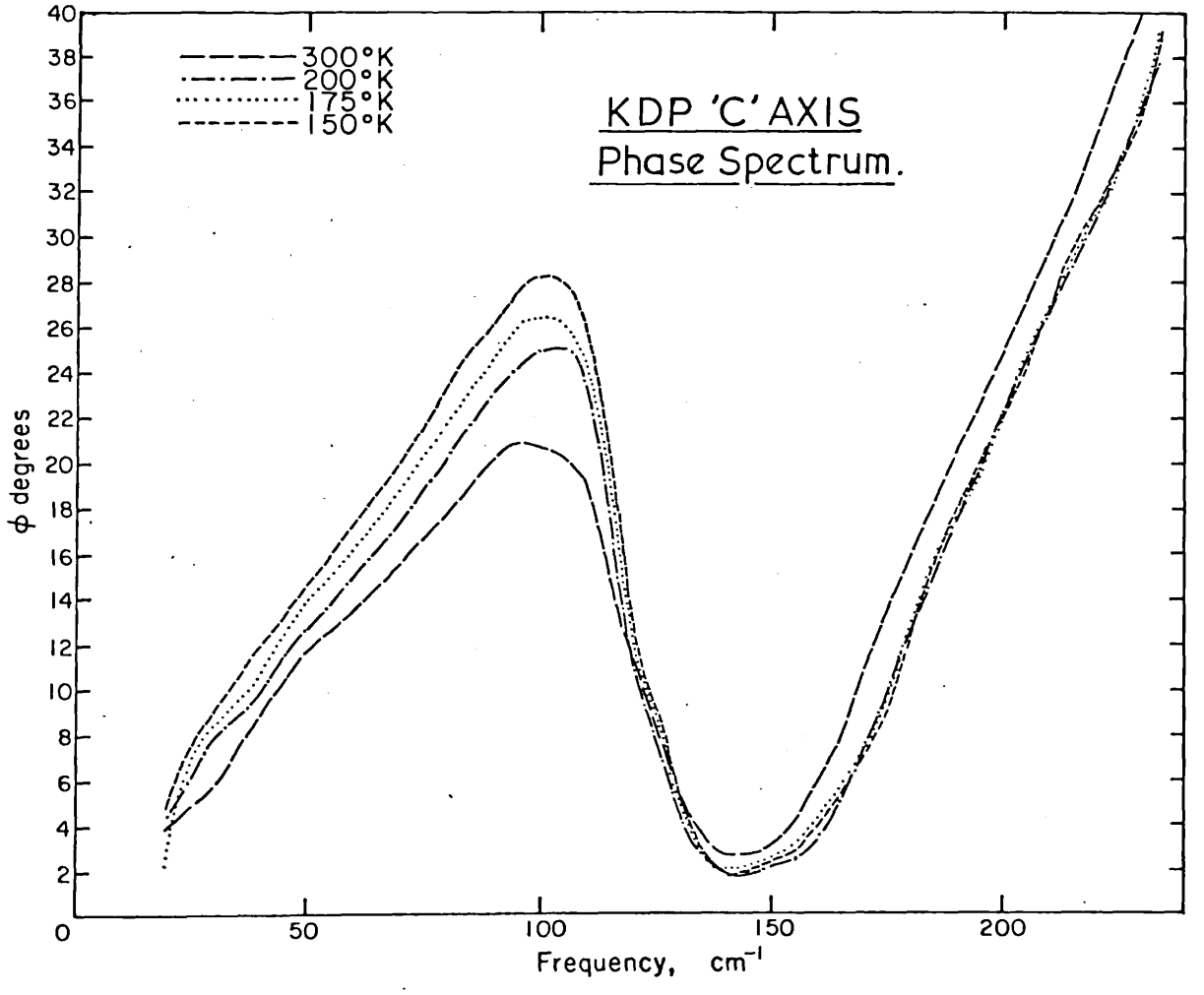

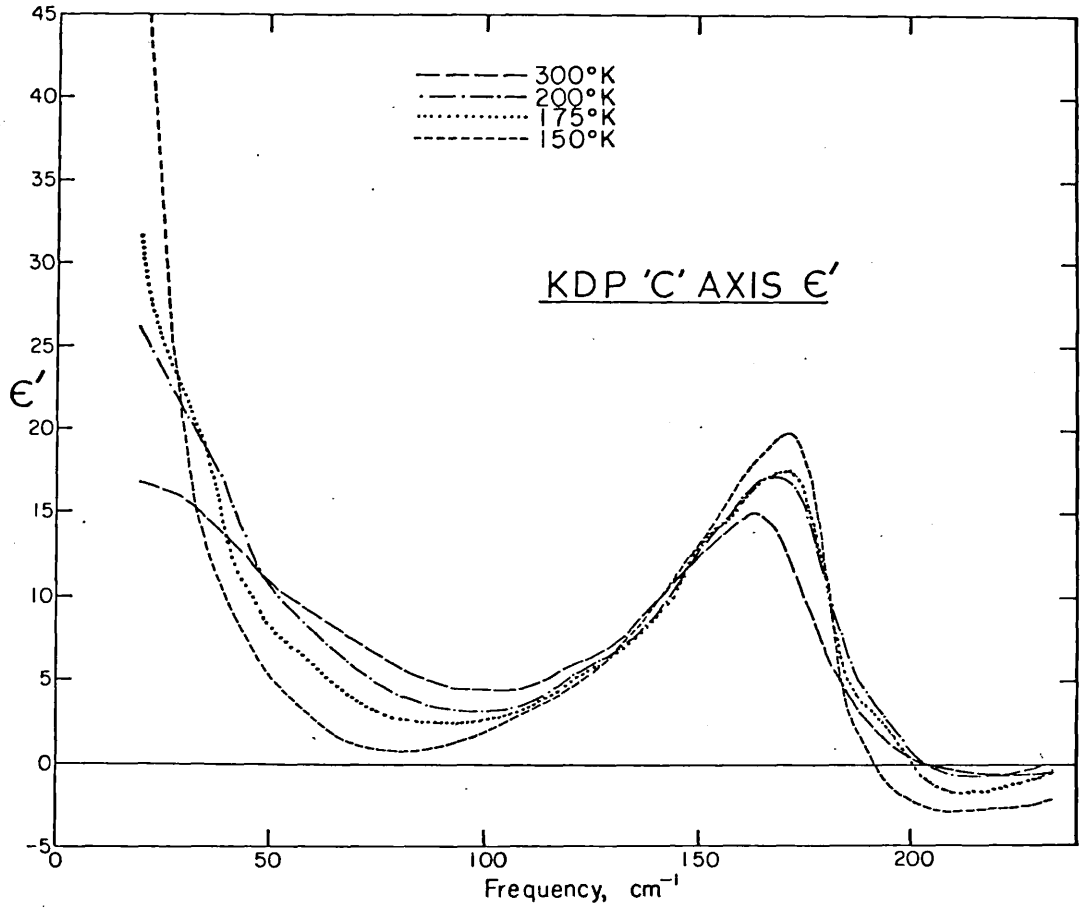

FIG 6.17: DIELECTRIC FUNCTIONS FOR KDP 'c' AXIS

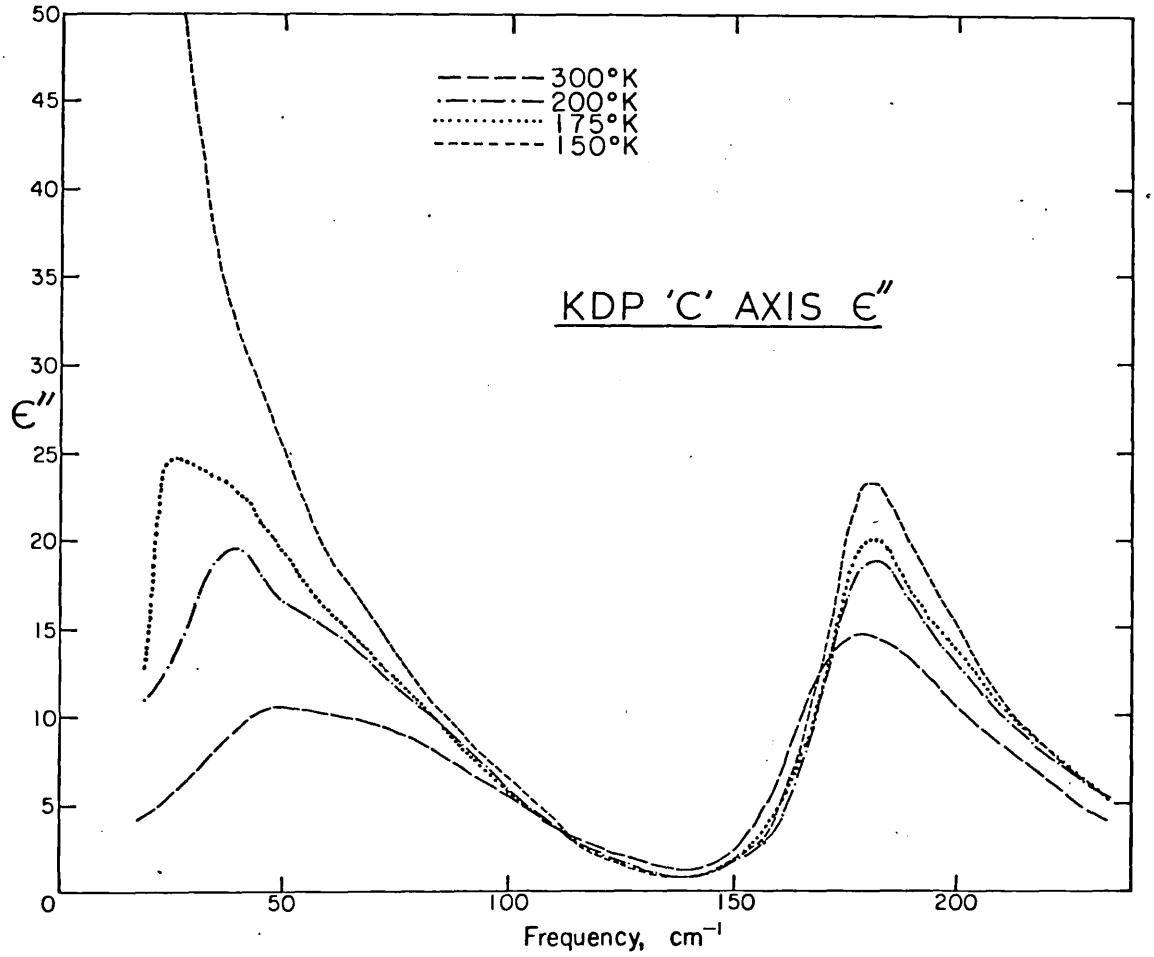

FIG 6.18 KDP 'C' AXIS

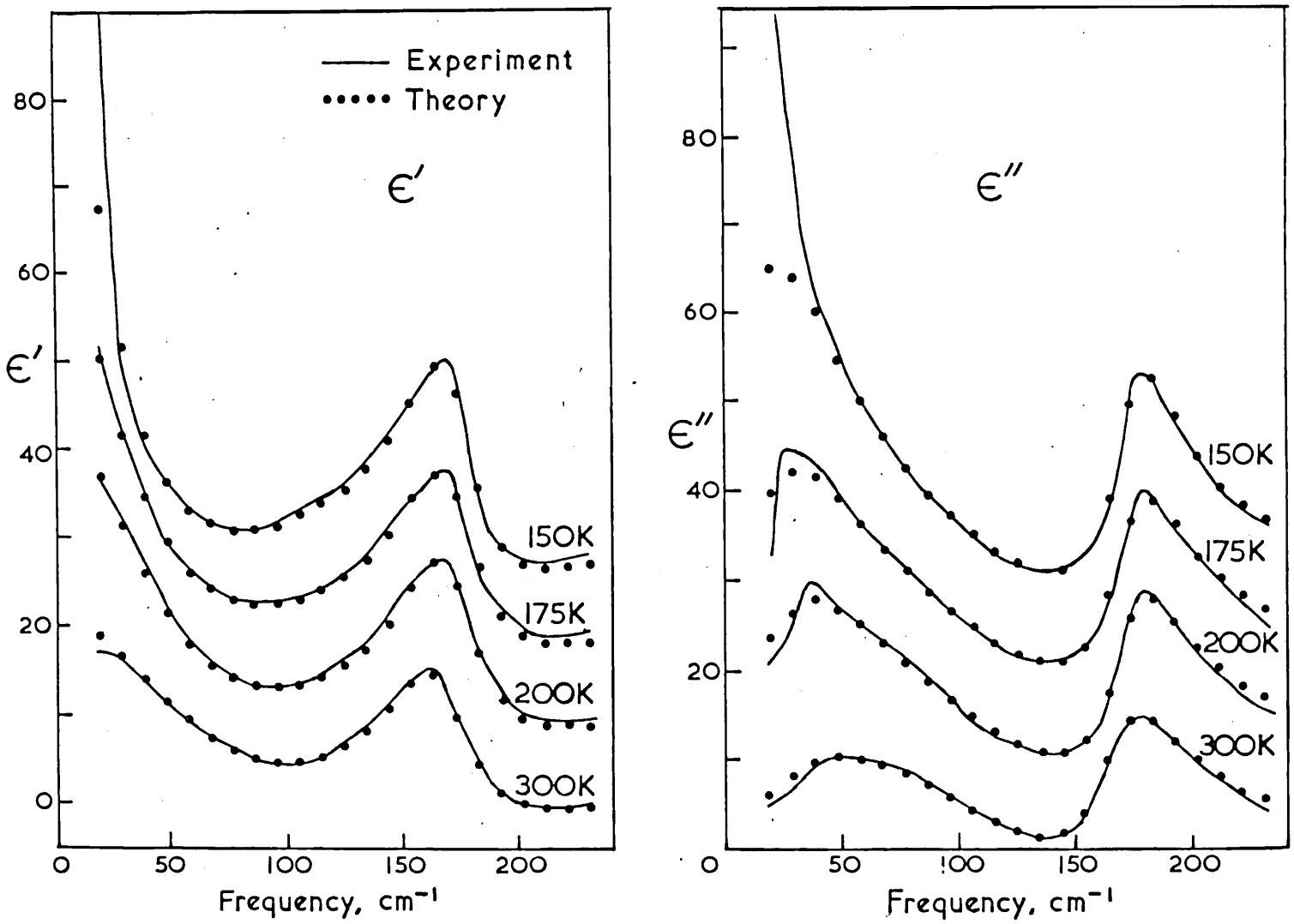

Theoretical fits to the dielectric functions (ϵ', ϵ''). The lines are the experimental curves of Fig 6.17 . The 200, 175 and 150K curves are displaced by 10, 20 and 30 units, respectively, up the ϵ axes, from the 300K curve for clarity. The dots are points from theoretical curves calculated using the parameters of Table 2 and the reactive coupling model.

CHAPTER 7

POWER FTS MEASUREMENTS ON KDP

7.1 INTRODUCTION

Transmission spectroscopy has, in certain cases, advantages over reflection studies. One such advantage is that accurate values of the phase change on reflection at a surface, the phase reflectivity, may be calculated from power transmission data. To obtain values of similar accuracy by reflection studies requires high quality dispersive measurements. Consequently, in addition to providing further information on crystal properties, the possibility arises of checking the performance of the polarising interferometer by power transmission measurements.

The main problem that arises when performing such measurements on KDP-type crystals is the high optical absorption in the spectral region of interest which necessitates the use of extremely thin single crystals. The difficulty of thinning down specimens to thicknesses at which a measurable amount of energy is transmitted has been by-passed by previous workers. Onyango et al[60] have published results obtained from polycrystalline films of KDP whilst Aref'ev et al[72] used suspensions of KDP powder in paraffin. However, their results fail to provide all the information required on the various parameters involved.

Fortunately, in KDP there exists a region in the far IR 'c' axis spectrum where the imaginary part of the dielectric constant ε''_c, which governs the optical absorption, falls sufficiently to allow crystals of thicknesses $\sim$ 150 μm to transmit radiation. The ε" curves for the KDP 'c' axis, Fig 6.17, obtained dispersively, show ε''_c falling to low values at ν 135 cm^{-1} and first indicated the possibility of transmission measurements. Following these dispersive results, the first transmission measure-

ments on a single KDP crystal were performed by Gledhill et al[73] in this laboratory. Their result displayed the 300K 'c' axis transmission as a sharp spike peaking at $\sim$ 136 cm^{-1}, with a width of $\sim$ 10 cm^{-1} and a height of 1.3% for a specimen of mean thickness 120 μm.

Furthermore, the dispersive ε_c'' curves of Fig 6.17 show that on cooling towards the transition, ε_c'' drops even lower in the region of the spectral window indicating that transmission measurements should become easier as the crystal is cooled due to the greater transmitted energy.

To supplement the dispersive results obtained with the polarising interferometer and to obtain further information on the nature of the ferroelectric transition in KDP, the room temperature measurements of Gledhill et al have been repeated and extended to low temperatures, down to and beyond the ferroelectric transition temperature.

7.2 THE THEORY OF TRANSMISSION THROUGH A THIN CRYSTAL

Fig 7.1 shows a beam of radiation of unit intensity incident normally on a parallel sided slab of crystal of thickness d. The transmitted and reflected beams up to and including the fifth multiple internal reflection are included. R and T are the normal incidence power reflection and transmission coefficients respectively, and α is the absorption coefficient of (3.39).

Allowing for multiple reflections, the power transmission (T) is given by the sum of the transmitted beams

$$T = (1-R)^2 \exp[-\alpha d].\ \{\ 1 + R^2x + R^4x^2 + \ldots\ \} \qquad (7.1)$$

where $x = \exp[-2\alpha d]$.

This is a converging series, the sum of which is

$$T = \frac{(1-R)^2 \exp[-\alpha d]}{1-R^2 \exp[-2\alpha d]} \quad . \tag{7.2}$$

It is important to consider the contribution of the multiple reflections to the transmitted energy. This may be done by investigating the ratio T_1/T where $T_1 = (1-R)^2 \exp[-\alpha d]$ is the contribution of the primary transmitted beam and T is given by (7.2).

$$\text{Thus} \quad T_1/T = 1 - R^2 \exp[-2\alpha d] \quad . \tag{7.3}$$

By considering the dispersive results obtained with the polarising interferometer an approximate value may be attached to the ratio of (7.3). The results of Gledhill et al show that the spectral region under consideration is $\sim$ 130 - 140 cm^{-1}. From Figs 6.16 and 6.17, to good approximations, $R = |\rho|^2 \sim 20\%$ and $\varepsilon''_c/\varepsilon_o \sim 1$ in this region for temperatures between 150 and 300K.

Using equations (3.33) and (3.39) we obtain

$$\alpha = \frac{2\pi}{n\lambda} \varepsilon''/\varepsilon_o \tag{7.4}$$

where λ is the wavelength of the radiation. In addition, the use of (3.90) yields

$$\alpha = \frac{2\pi}{\lambda} \frac{\varepsilon''}{\varepsilon_o} \left[\frac{1 - \sqrt{R}}{1 + \sqrt{R}}\right] . \tag{7.5}$$

By inserting the approximate values for λ, $\varepsilon''/\varepsilon_o$ and R, and assuming a crystal of thickness $d \sim 150$ μm we obtain

$$\alpha d \simeq 4.86 .$$

Hence from (7.3):

$$T_1/T \simeq 1 - (0.2)^2 \exp[-9.72] \simeq 1 - (2.4 \times 10^{-6}).$$

However, because of the exponential factor in (7.3) we should investigate the ratio T_1/T more thoroughly, particularly as Fig 6.17 indicates that ε''_c decreases as the temperature is lowered. If, for example, $\varepsilon''/\varepsilon_c$ falls by an order of magnitude to a value of 0.1, then $\alpha d \simeq 0.486$, and

$$T_1/T \simeq 1 - (0.2)^2 \exp[-0.972] \simeq 1 - 0.015.$$

Thus, even in this extreme case $T_1 \simeq T$ and hence we may justifiably ignore multiple reflections. The transmitted power is therefore

$$T = T_1 = (1-R)^2 \exp[-\alpha d] \quad . \tag{7.6}$$

Equations (7.4) and (7.6) yield

$$\frac{\varepsilon''}{\varepsilon_o} = \frac{n\lambda}{2\pi d} \log_e \frac{(1-R)^2}{T} \quad . \tag{7.7}$$

The values of $\varepsilon''/\varepsilon_o$ obtained using this expression may be used to calculate values of ϕ, the phase change on reflection at a surface, via (3.104), which was derived from the Fresnel relations and has the form

$$\phi = \tan^{-1} \left\{ \frac{\varepsilon''}{\varepsilon_o} \cdot \frac{1}{n(n^2-1)} \right\} \qquad (\text{for } n^2 \gg k^2) \ . \tag{7.8}$$

7.3 THE EXPERIMENTAL METHOD

More than twenty samples of X-cut KDP (ie 'a' and 'c' axes in the plane of incidence) of varying thicknesses between 100 μm and 250 μm were used for the low temperature transmission measurements. All the samples had an area ~ 1 cm^2. One of the great advantages of power FTS over DFTS is that sample preparation is comparatively simple. The tolerances on the sample flatness are far greater than the ±0.1 μm required for accurate

DFTS studies. Consequently the samples for FTS are much simpler and cheaper to prepare. Each specimen was obtained by polishing down a single crystal of KDP grown in this laboratory by a precipitation method. Care was taken to ensure the orientation of the 'c' axis in the final specimen was known though this could be checked by X-ray analysis.

The spectra were obtained using the power interferometer described in Chapter 4 and the temperature control system was similar to that used with the polarising interferometer giving stability to $\sim \pm 0.25$K anywhere between 90 and 300K.

It is evident from the theory (7.7) that in order to calculate values for $\varepsilon''_c/\varepsilon_o$ and hence ϕ at points in the IR spectrum from power transmission data, information on the power reflection (R) in that spectral region is required. Some of this information could be obtained from the dispersive results. However, in addition to the power transmission, power reflection measurements were performed over the same temperature range using the interferometer in the reflection mode. Once again, the samples used were cut from single crystals of KDP grown in this laboratory. After recording interferograms by reflection from the sample, the sample was then aluminised whilst still held in the sample mount which was detachable from the base of the "cold finger" dewar. Background calibration spectra were then recorded from the aluminised sample. Thus the area of the reflection surface was identical for both crystal and calibration measurements.

The reflection measurements were performed at an angle of incidence of 20°, technically necessitating the use of a correction (section 3.5) to obtain the normal incidence spectra. Figs 7.2 and 7.3 display the spectra recorded at an angle of 20° (R_{20}). The normal incidence spectra (R_o) are very similar to R_{20} in the region under investigation. However, the values

of the power reflection used to calculate ε'' and ϕ from the transmission data were corrected to the normal incidence values. Typically, R_{20} = (26.0 ± 0.5)% at 136 cm^{-1} on the 300K curve gives a corresponding value of R_o = (23.9 ± 0.5)%. This value is calculated using the optical constant values derived from the dispersive results.

For the reflection measurements it was necessary to employ a polariser placed in the beam before the sample and orientated so as to ensure the 'c' axis alone was being measured. Due to the finite width of the polarising strips, use of the polariser has the unfortunate but unavoidable result of reducing the throughput energy of the instrument by a factor in excess of three. This is not a real disadvantage for the reflection measurements as the reflected energy incident on the Golay detector is plentiful. But, for the transmission measurements where the measurable energy is already extremely small due to the high absorption of the sample, use of the polariser is highly undesirable.

Fortunately, the relatively high value of $\varepsilon_a''/\varepsilon_o$ (Fig 6.12) over the measured region, excludes the possibility of any measurable radiation being transmitted in the direction of the 'a' axis. Thus, no polariser was required when recording the crystal transmission spectra though it was used to check the results. The calibration mirror spectra against which the crystal spectra are ratioed can then either be measured using the polariser in the correct orientation or corrected to allow for its absence, taking into account the polarising effect of the mylar beam divider in the interferometer (Fig 4.4).

7.4 DISCUSSION OF RESULTS

The power reflection spectra (R_{20}) are illustrated in Figs 7.2 and 7.3. The results for $T > T_c$ compare favourably with the dispersive results of Fig 6.16 and other power reflection measurements[47,61,62]. Published results for $T < T_c$ are scarce, though a qualitative comparison may be made with the power measurement of Sugawara and Nakamura[62] performed at 83K.

The power reflection studies were primarily undertaken to obtain reflectivity measurements in the region of the transmission window, required in order to calculate phase values from the transmission measurements. However, extending the spectral range to higher frequencies by changing to a thinner mylar beam divider would yield more information on the behaviour of KDP below the transition and allow a better comparison with the result of Sugawara. Clearly there is much work that could be done in this area. If dispersive measurements are attempted below T_c, great care must be taken to ensure that the stresses that accompany the phase transition do not cause the expensive and carefully prepared samples to crack. One sample shattered in just this manner. Power reflectivity measurements below T_c have the advantage that the samples are cheap and easy to prepare and thus, to a certain degree, expendable.

The power transmission results are summarised in Table 3. The results given for each temperature are average values obtained from repeated measurements on many samples. The phase values listed are in close agreement with the corresponding results obtained dispersively (Fig 6.16) and give a good indication of the accuracy to which direct phase measurements may be made with the polarising interferometer. This accuracy appears to be well within the error of $\pm 0.5^{\circ}$, at 136 cm^{-1}, assigned in Chapter 6.

TABLE 3

A SUMMARY OF THE POWER TRANSMISSION RESULTS

SAMPLE TEMPERATURE ±2K	FREQUENCY (K) OF PEAK OF TRANSMISSION ±0.2 cm^{-1}	IMAGINARY PART OF THE DIELECTRIC CONSTANT $\varepsilon_c''/\varepsilon_o$	CALCULATED PHASE CHANGE ON REFLECTION AT K cm^{-1} ϕ^o
300	136.0	1.093±0.018	3.40±0.06
170	140.5	0.680±0.018	2.11±0.05
155	141.1	0.648±0.015	2.01±0.05
145	141.1	0.584±0.015	1.82±0.05
130	141.4	0.567±0.014	1.76±0.04
118	142.3	0.517±0.012	1.61±0.04
115	143.2	0.447±0.007	1.39±0.02
112	144.5	0.357±0.012	1.11±0.04
103	144.8	0.302±0.016	0.94±0.05
92	145.5	0.205±0.039	0.64±0.12

Two typical interferograms recorded during the course of the measurements are illustrated in Fig 7.4 and three transmission spectra, for crystals of thickness d as given, which were typical of the many obtained, are illustrated in Fig 7.5. The gain factor of the ordinate should be noted when comparing the three spectra shown, each of which was arrived at by averaging at least three interferograms for both sample and calibration spectra.

Besides providing the phase values in the window region, the power results also provide qualitative information on the ferroelectric behaviour of KDP. The transmission window indicates the position of the gap between the soft ferroelectric and the optic modes, shown in the dispersive results of Fig 6.17, where the value of ε_c'' is a minimum. The results presented in Table 3 show that on cooling towards the transition at T_c, the value of the minimum in the ε_c'' curve falls, with a corresponding increase in the transmission at this point in the spectrum. The minimum also moves to slightly higher frequencies on cooling. Such behaviour is predictable from the dispersive results and to this degree, the two sets of results correlate.

On cooling to below the transition these trends continue, the transmission increasing still further as ε_c'' drops to even lower values at the minimum which itself continues to move slowly up the frequency scale. However, as shown in Fig 7.5, when the temperature falls sufficiently, the crystal begins to become transparent in the low frequency region ≤ 80 cm^{-1}. Evidence of this first appears on reaching $\sim$ 100K. The 92K curve of Fig 7.5 shows a significant amount of radiation is transmitted in this region at this temperature. On cooling further, results indicate that the energy transmitted by this low frequency region greatly increases. When the temperature reaches $\sim$ 85K, the energy transmitted by the higher frequency window is negligible in comparison. Accurate quantitative

measurements have not yet, however, been performed at temperatures lower than 92K.

The results obtained below the transition temperature are in qualitative agreement with the Raman scattering results of Shigenari and Tagaki[64]. From their Raman intensity curves the possible occurrence of a low frequency window at temperatures below $\sim$ 100K can be predicted. In addition their results, which cover the range from 300K to 93K indicate that, as has indeed been found, the higher frequency window exists throughout this temperature range and would not be expected to shift significantly in the spectrum.

The transmission results are an aid to the understanding of KDP in its ferroelectric phase and to the determination of parameter values for models describing its behaviour, particularly when considered along with the Raman results of Shigenari. However, extensive IR reflection studies should greatly help to clarify the mode behaviour, in particular the existence of a further soft mode, below the transition.

7.5 A SHORT DISCUSSION OF EXPERIMENTAL ERRORS

As stated previously, the results in Table 3 were obtained by averaging a number of equivalent results from measurements on over 20 different samples, though no sample was measured over the whole temperature range covered in the experiment. The errors assigned to the dielectric function and phase values are the standard errors in these mean values and indicate the perhaps surprisingly good agreement of repeated results.

The most significant error in an individual result was caused by measurement of sample thickness though any systematic errors present were

minimised by the use of a number of different samples. The samples were ground down to the required thickness by hand in a fairly crude manner though the finished result was spectroscopically acceptable for power transmission measurements. The mean thickness was calculated from measurements of the sample surface area, its weight and its known density. The error in the value calculated in this manner is estimated at ±10%, a figure that should also take account of the variation in thickness across the sample. This error, when carried through the various stages in the calculations, leads typically to errors of $\sim \pm 0.3^{\circ}$ and $\pm 0.1^{\circ}$ in the phase values at 300K and 112K respectively, as calculated from a single result rather than from an average of repeated results.

The sample temperature could be stabilised to better than ±0.25K using the thermostatic control system described in Chapter 4. However, the sample temperatures quoted are estimated to be in error by $\sim$ ±2K due to problems encountered in temperature measurement during the power FTS studies. In particular, the thermocouples used could not be attached to the sample but were attached instead to the sample mount as near the sample as possible. Thus, the likely existence of a temperature gradient between the mount and the area of the sample in the radiation field would lead to incorrect sample temperatures being recorded.

FIG 7.1 TRANSMISSION OF RADIATION THROUGH A THIN CRYSTAL

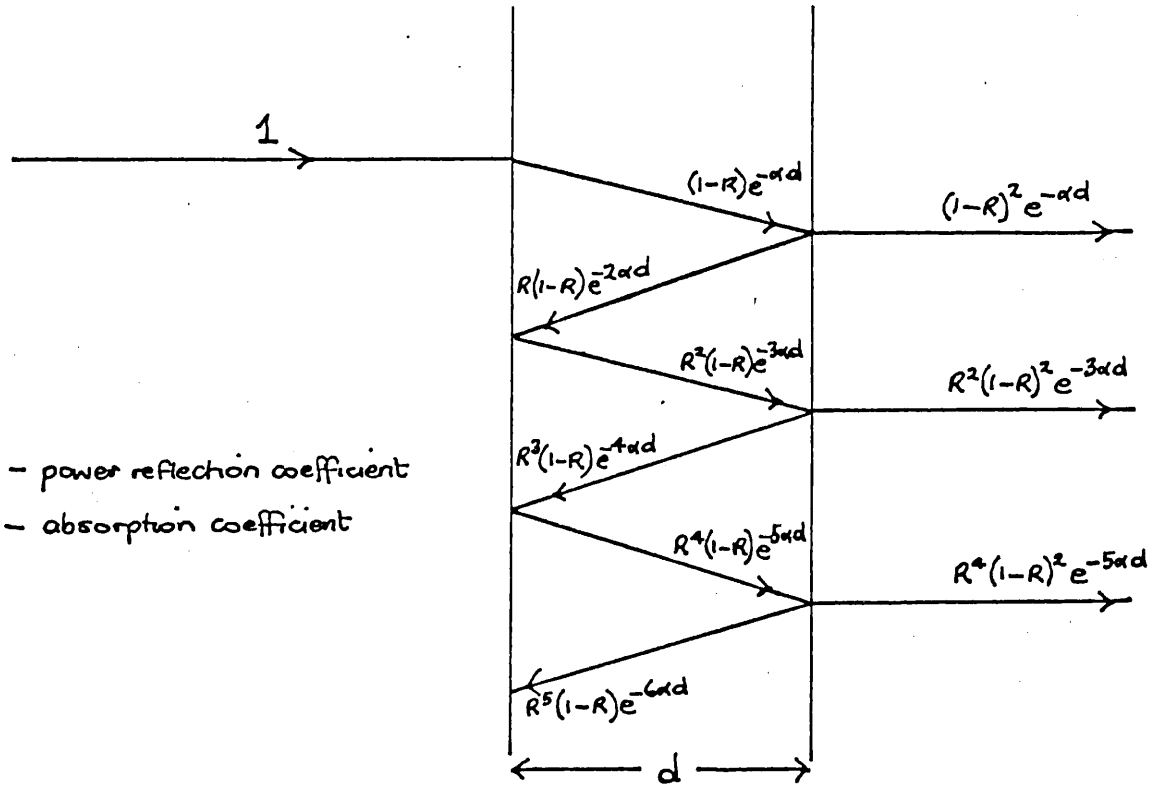

R – power reflection coefficient

α – absorption coefficient

THE SUM OF THE TRANSMITTED BEAMS

$$T = (1-R)^2e^{-\alpha d}\left[1+R^2x+R^4x^2+\text{----}\right]$$

Where $x = e^{-2\alpha d}$

THIS IS A CONVERGING SERIES OF SUM

$$T = \frac{(1-R)^2\,e^{-\alpha d}}{1-R^2e^{-2\alpha d}}$$

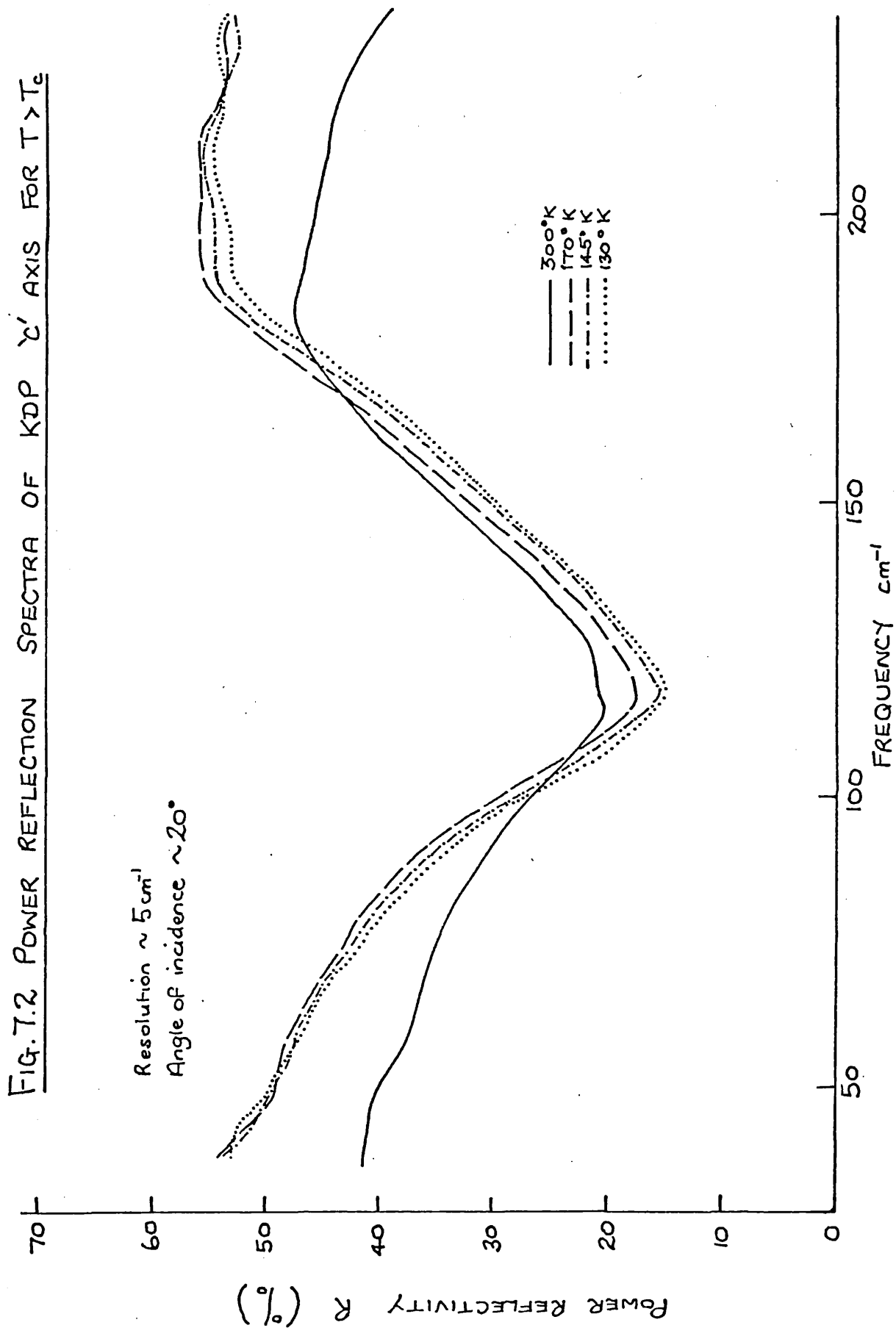

Fig. 7.2 Power reflection spectra of KDP c' axis for $T > T_c$

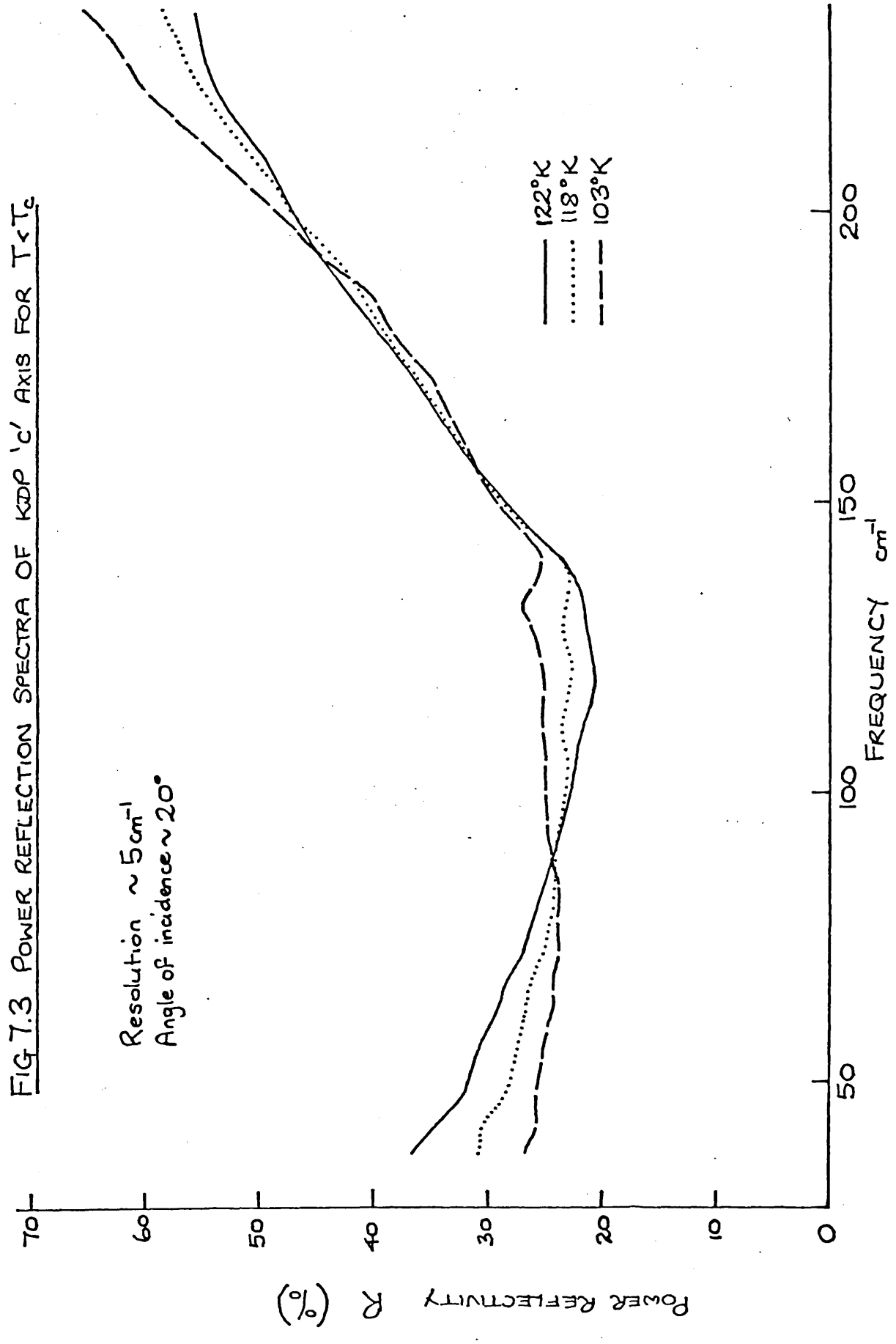

FIG 7.3 POWER REFLECTION SPECTRA OF KDP 'c' AXIS FOR $T < T_c$

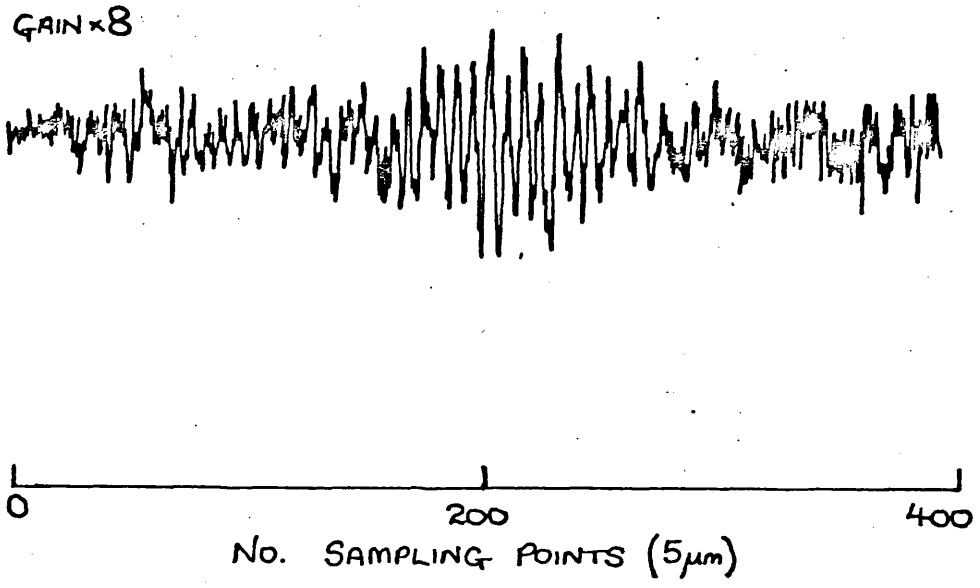

FIG 7.4 TYPICAL INTERFEROGRAMS OBTAINED DURING POWER TRANSMISSION MEASUREMENTS ON KDP 'c' AXIS

a/ 300°K b/ 87°K

FOR SAMPLE OF MEAN THICKNESS 125 μm

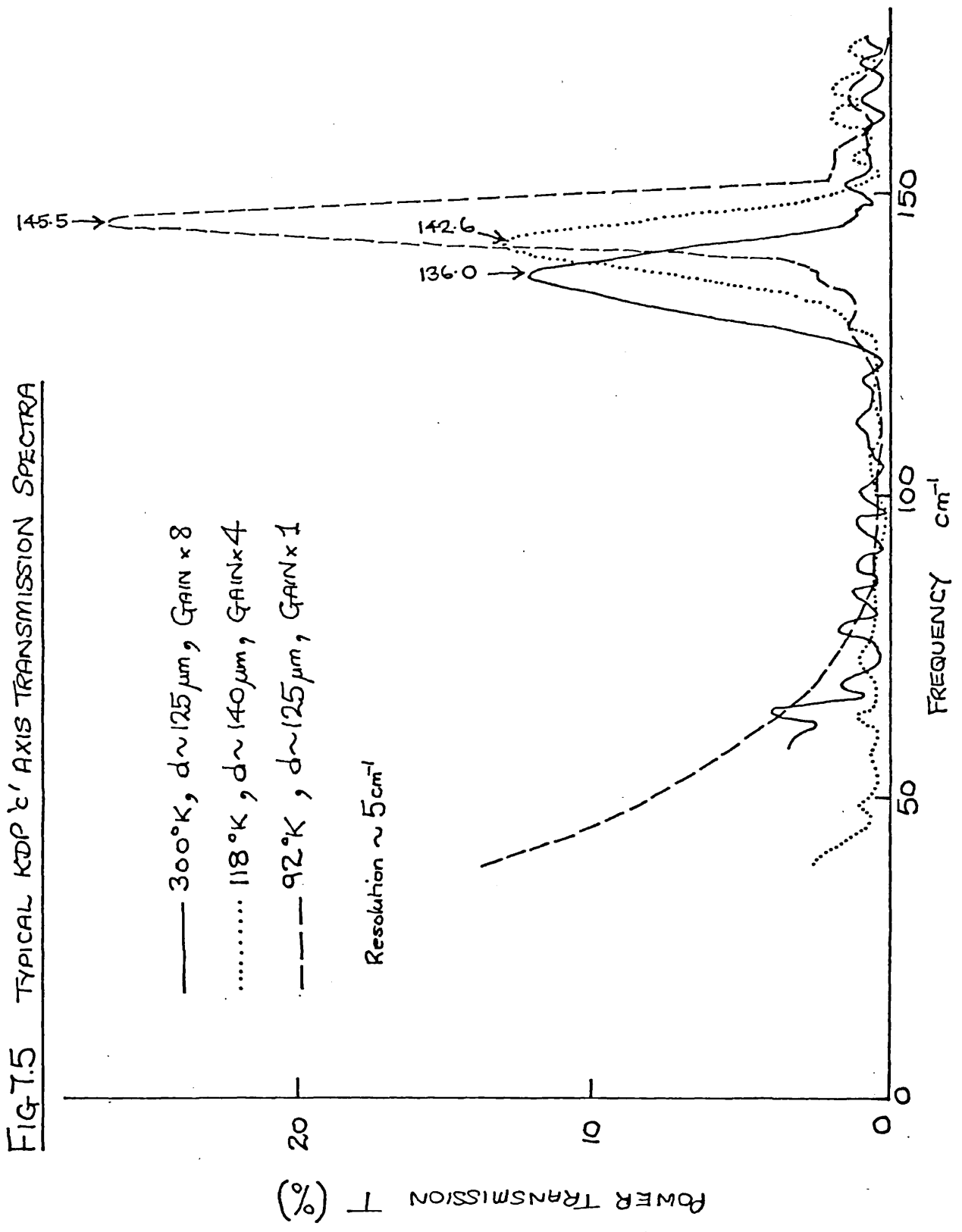

FIG 7.5 TYPICAL KDP 'c' AXIS TRANSMISSION SPECTRA

CHAPTER 8

CONCLUDING REMARKS

The direct experimental measurement of the optical constants and the dielectric response of solids in the far infrared, which provides knowledge invaluable to the understanding of the dynamics of crystal lattices, became a reality following recent advances in the technique of dispersive Fourier transform spectroscopy. This technique was firmly established by several workers including Parker et al[11,12] who have recently reported the first results of temperature dependent dispersive reflection studies on a number of different materials.

For reasons discussed in Chapter 4, extending the range of such investigations to the extreme infrared, an important spectral region in the study of many materials, notably ferroelectrics, requires the solution of a number of severe technical problems.

The design and construction of a polarising interferometer which overcomes these problems has been described in Chapter 4 and results obtained with it have been presented in Chapter 6. The instrument represents a significant advance in Fourier transform spectroscopy, allowing low frequency temperature dependent dispersive reflection studies to be performed for the first time.

The present working range of the polarising interferometer is approximately 20 - 235 cm^{-1} when used with a Golay detector. However, results in this range should be greatly improved and the range itself extended down to $\sim$ 2 cm^{-1} by the use of the liquid He cooled Ge bolometer which has recently become available in the laboratory.

An enormous amount of time and effort was put into solving numerous

experimental problems that arose during the construction of the interferometer and in evaluating the performance of the instrument at each stage in its development. A major problem lay with the fine tolerances required of the flatness of the optical components which is dictated by the accuracy required of the measured phase values. The mirrors, flat to well within the set limits, were obtained commercially, but the wire grid beam dividers were wound by the author using 10 μm diameter tungsten wire to a modified form of a design obtained from the National Physical Laboratory. The grid frames incorporated a simple tensioning system which greatly improved the flatness of the dividers and thereby removed a major source of phase errors. A possible future development would be the design of a more complex "wire-stretching" system to further improve the grid quality. The use of finer grids is planned, wound with the 5 μm diameter wire now available. The employment of these grids in the polarising interferometer would allow the high frequency cut-off to be raised towards $\sim$ 500 cm^{-1} and consequently improve the quality of the optical alignment.

At present the accuracy of phase measurement appears to be limited by the optical quality of the specimen reflecting surfaces and not by factors in the instrumental design. This was particularly apparent with the measurements on the Cs salts where the specimen surfaces appeared to deteriorate with time leading to poor reproducibility of results. The problem was much less evident with the KDP samples. The careful preparation and subsequent care of samples requires further investigation in order that the potential of the polarising interferometer be fully realised.

The KDP studies, using both the polarising interferometer and a conventional power interferometer, have provided further valuable information for the study of ferroelectric behaviour and the mechanism of the phase transition in KDP at 123K. The results obtained are discussed in detail in

Chapters 6 and 7 and are in good agreement with previously published data, where this is available. The use of the Ge bolometer detector should greatly improve the quality and extend the range of these encouraging results and lead to better correlation between experimental and theoretical studies.

REFERENCES

1. Born M and von Karman Th; Phys Z, 13, 297 (1912); 14, 15 (1913)

2. Einstein A; Ann Physik 22, 180, 800 (1906); 34, 170 (1911)

3. Debye P; Ann Physik 39, 789 (1912)

4. Bell E E; Infrared Phys 6, 57 (1966)

5. Gast J, Genzel L and Zwick U; IEEE Trans MTT-22, 1026 (1974)

6. Chamberlain J, Afsar M N, Davies G J, Hasted J B and Zafar M S; IEEE Trans MTT-22, 1028 (1974)

7. Birch J R, Price G D and Chamberlain J; Infrared Phys 16, 311 (1976)

8. Gauss K E, Happ H and Rother G; Phys Stat Sol (b) 72, 623 (1975)

9. Parker T J, Ledsham D A and Chambers W G; Infrared Phys 16, 293 (1976)

10. Parker T J, Chambers W G and Angress J F; Infrared Phys 14, 207 (1974)

11. Parker T J and Chambers W G; Infrared Phys 16, 349 (1976)

12. Parker T J and Chambers W G; IEEE Trans MTT-22, 1032 (1974)

13. Martin D H and Puplett E; Infrared Phys 10, 105 (1969)

14. Barker A S and Hopfield J J; Phys Rev 135, A1732 (1964)

15. Bell R J; "Introductory Fourier Transform Spectroscopy", Academic Press, New York and London (1972)

16. Vanasse G A, Stair Jr A T and Baker D J, eds; Proc Aspen Int Conf on Fourier Spectroscopy, Aspen, Colorado, 5 Jan 1971, Special Reports No. 114

17. Born M and Wolf E; "Principles of Optics", Pergamon Press 1970

18. Born M and Huang K; "Dynamical Theory of Crystal Lattices", Clarendon Press 1966

19. Turrell G; "Infrared and Raman Spectra of Crystals", Academic Press 1972

20. Nudelman and Mitra S S (eds); "Optical Properties of Solids", Proc Nato Adv Study Inst on Opt Props of Solids - August 1966, Freiburg, Germany, Plenum Press, New York 1969

21. Roessler D M; Brit J Appl Phys 16, 1359 (1965)

22. Donovan B and Angress J F; "Lattice Vibrations", Chapman and Hall 1971

23. Huang K; Proc Royal Soc A, 208, 352 (1951)

24. Maradudin A A and Fein A E; Phys Rev 128, 2589 (1962)

25. Cowley R A; Adv Phys 12, 421 (1963)

26. Kramers H A; Estratto dogli Atti del Congresso Internazionale de Fiscici, Como, 2, 545 (1927)

27. Krönig R de L; J Opt Soc Am, 12, 547 (1926)

28. Chantry G W; "Submillimetre Spectroscopy", Academic Press, London and New York (1971)

29. Hadni A; "Essentials of Modern Physics Applied to the Study of the IR", Pergamon Press (1967)

30. Chamberlain J; Infrared Phys 11, 25 (1971)

31. Ledsham D A, Chambers W G and Parker T J; Infrared Phys 16, 515 (1976)

32. Harvey A F; "Microwave Engineering", Academic Press 1963

33. Marcuvitz N; "Waveguide Handbook", MIT Rad Lab Ser, McGraw-Hill, New York 1951 p218

34. Auton J P; Applied Opt 6, 1023 (1967)

35. Vogel P and Genzel L; Infrared Phys 4, 257 (1964)

36. Costley A E, Hursey K H, Neill G F and Ward J W M; Contribution to 2nd Int Conf on Submillimetre Waves and Their Apps, Puerto Rico (December 1976)

37. Busch G and Scherrer P; Naturwiss 23, 737 (1935)

38. Scott J F; Reviews of Modern Physics 46, No. 1, 83 (Jan 1974)

39. Burfoot J C; "Ferroelectrics - An Introduction to the Physical Principles", Van Nostrand Co Ltd, London (1967)

40. Dekker A J; "Solid State Physics", Macmillan and Co Ltd (1970)

41. Slater J C; "Ferroelectricity", ed. Weller E F, Elsevier Pub Co (1967)

42. Landau L D; Phys Z Sowjetunion, 11, 26 (1937)

43. Devonshire A F; Phil Mag 40, 1040 (1949)

44. Cochran W; Adv Phys 9, 387 (1960); 10, 401 (1961)

45. Raman C V and Nedungadi T M K; Nature (Lond) 145, 147 (1940)

46. Cowley R A; Phys Rev A, 134, 981 (1964)

47. Agrawal D K; Ph D Thesis, Northeastern Univ, Boston, Mass, USA (June 1971)

48. Bacon G E and Pease R S; Proc Roy Soc A220, 397 (1953); A230, 359 (1955)

49. Slater J C; J Chem Phys 9, 16 (1941)

50. Kobayashi K K; J Phys Soc Jap 24, 497 (1968)

51. Benepe J W and Reese W; Phys Rev B, 3, 3032 (1971)

52. Barker A S and Tinkham M; J Chem Phys 38, 2257 (1963)

53. Kaminow I P and Damen T C; Phys Rev Lett 20, 1105 (1968)

54. Katiyar R S, Ryan J F and Scott J F; Phys Rev B4, 2635 (1971)

55. She C Y, Broberg T W, Wall L S and Edwards D F; Phys Rev B6, 1847 (1972)

56. Brody E M and Cummins H Z; Phys Rev Lett 21, 1263 (1968)

57. Reese R L, Fritz I J and Cummins H Z; Phys Rev B7, 4165 (1973)

58. Lagakos N and Cummins H Z; Phys Rev B10, 1063 (1974)

59. Peercy P S; Phys Rev Lett 31, 379 (1973)

60. Onyango F, Smith V and Angress J F; J Phys Chem Solids 36, 309 (1975)

61. Kawamura T, Mitsuishi A and Yashinaga H; J Phys Soc Japan 28, Supp. 227, (1970)

62. Sugawara F and Nakamura T; J Phys Soc Japan 28, 158 (1970)

63. Havlin S, Litov E and Sompolinsky H; Phys Lett 53A, 41 (1975)

64. Shigenari T and Takagi Y; J Phys Soc Japan 31, 312 (1971)

65. Lavrencic B, Levstek I, Blinc R and Zeks B; "Light Scattering in Solids", ed Balkanski B M, Flammarion, Paris, 424 (1971)

66. Lavrencic B, Levstek I, Zeks B and Blinc R; "Advances in Raman Spectroscopy"; ed Mathieu J P, Heyden and Sons Ltd, London, Vol 1, 157 (1972)

67. Narahari Rao K, Humphreys C J and Rank D H; "Wavelength Standards in the Infrared", Academic Press 1966

68. Lowndes R P and Martin D H; Proc Roy Soc A, 308, 473 (1969)

69. Lowndes R P; IEEE Trans MTT-22, 1076 (1974)

70. Ledsham D A, Chambers W G and Parker T J; Infrared Phys 17, 165 (1977)

71. Wehner R K and Steigmeier E F; RCA Review 36, 70 (1975)

72. Aref'ev I M, Bazhulin P A and Mikhal'tseva T V; Soviet Phys Solid State 7, 1948 (1966)

73. Gledhill G A, Angress J F, Martin R W and Chambers W G; J Phys C: Solid State Phys 9, L 01 (1976)

DISPERSIVE REFLECTION SPECTROSCOPY IN THE FAR-INFRARED

T. J. PARKER,*† D. A. LEDSHAM† and W. G. CHAMBERS‡

Westfield College, University of London, London, NW3 7ST, U.K.

(*Received* 28 *August* 1975)

Abstract—Techniques are described for making dispersive reflection measurements on solids between about 5 and 500 cm^{-1} and at temperatures above 77 K using Fourier spectrometers equipped with dielectric or wire grid beam dividers and used in the asymmetric mode. Interferograms can be recorded with a positional accuracy of $\pm 0{\cdot}1$ μm which is independent of the specimen temperature, and the performance of the instruments is illustrated with amplitude reflection measurements on crystals of NaCl and CsI at room temperature. The ensuing dielectric response functions are also given and the TO and LO mode frequencies taken from these are in good agreement with published data. In the case of NaCl the self-energy and damping functions are also computed from the data and the results are in reasonable agreement with theoretical calculations by Hisano *et al.*

INTRODUCTION

During the past few years important advances have been made in the use of dispersive Fourier transform spectroscopy for the determination of refractive index spectra in the far infrared from transmission measurements,[1–3] and for obtaining the optical constants or dielectric functions directly from measurements of amplitude and phase reflection spectra.[4–6]

Although it is well known that there are advantages in certain circumstances in obtaining the phase spectrum directly from dispersive reflection measurements rather than from a Kramers-Krönig analysis of the power reflectivity[6,7] the technique is not widely used because of the difficulty of measuring the phase with sufficient accuracy. Ideally, the phase accuracy would be limited only by the signal to noise ratio in the normal way. However, this requirement imposes severe constraints on the permissible error in the location of each interferogram on the micrometer scale. For instance, a signal to noise ratio of 100 at a frequency $\nu = 300$ cm^{-1} implies a phase accuracy $\Delta\phi = 1/100$ rad, corresponding to an absolute positional error Δx between the recorded sample and reference mirror interferograms of only $\Delta x \sim 1/4\pi\nu \times 1/100 = 0{\cdot}03$ μm, and it is the difficulty of finding a technique for comparing reference mirror and sample phase spectra with this accuracy over a wide temperature range which has been the main obstacle to further development of dispersive reflection spectroscopy.

EXPERIMENTAL

We have recently described a phase modulated Fourier spectrometer[8,9] with which dispersive measurements can be made on suitable solids by either reflection or transmission in the frequency range from 20 to 500 cm^{-1}. In this instrument, which is equipped with a dielectric beam splitter, the phase errors which usually result from the mechanical replacement of reflecting surfaces are avoided by metallising part of the specimen surface for use as a phase reference surface. The technique, which has been successfully used at room temperature and 100 K, is suitable for many applications, and the phase accuracy is independent of the specimen temperature and is illustrated in Fig. 1. The dashed line shows the mean of three phase spectra obtained with a reference mirror using a

* On leave of absence at the Department of Physics, Northeastern University, Boston, MA 02115, U.S.A.
† Department of Physics.
‡ Department of Mathematics.

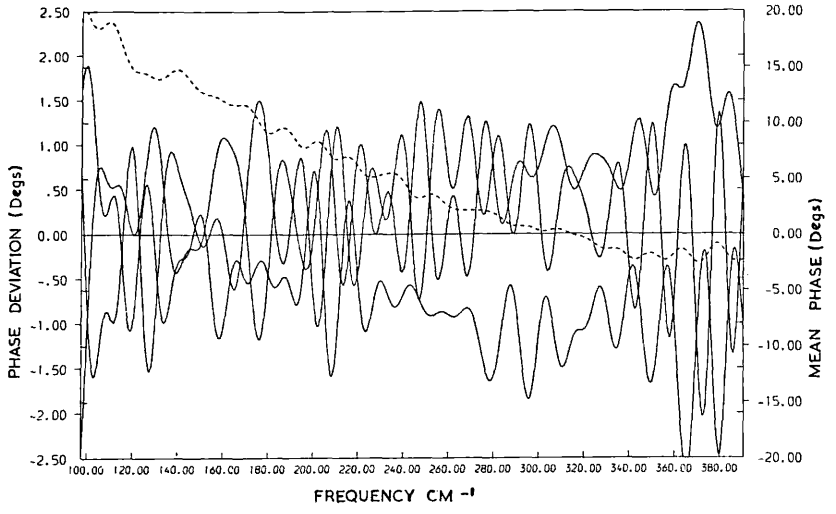

Fig. 1. Dashed curve shows the phase of the mean of three ratios of background pairs. Solid curves show the deviations of phase of each ratio from the phase of the mean.

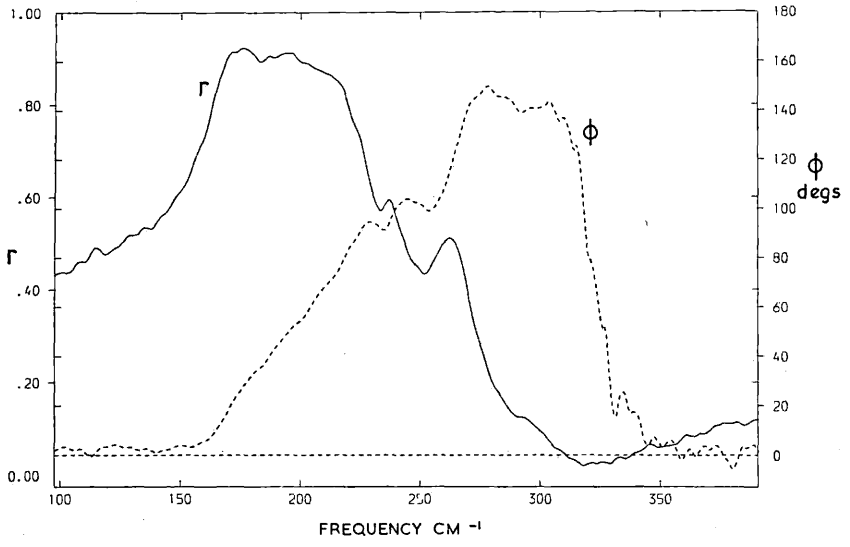

Fig. 2. Magnitude r and phase ϕ of reflectivity amplitude obtained for NaCl at 300 K. Resolution is about $2\,cm^{-1}$.

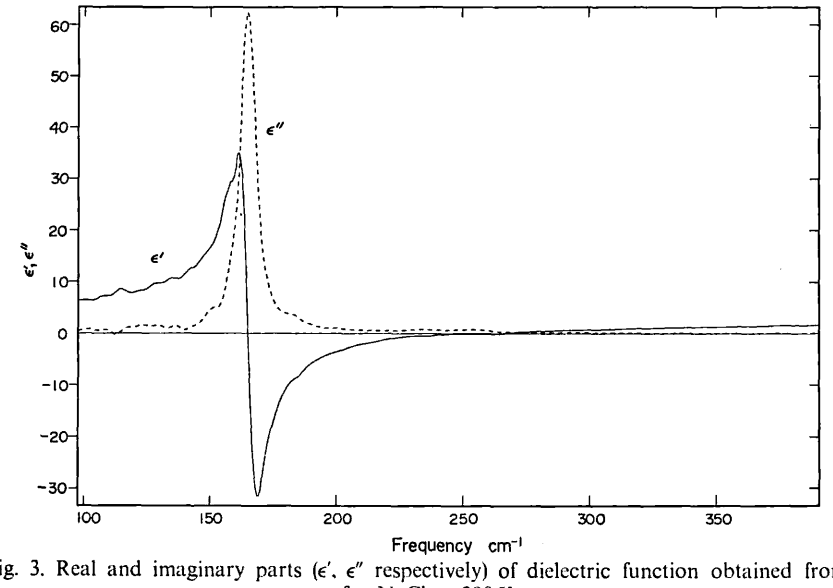

Fig. 3. Real and imaginary parts (ϵ', ϵ'' respectively) of dielectric function obtained from (1) for NaCl at 300 K.

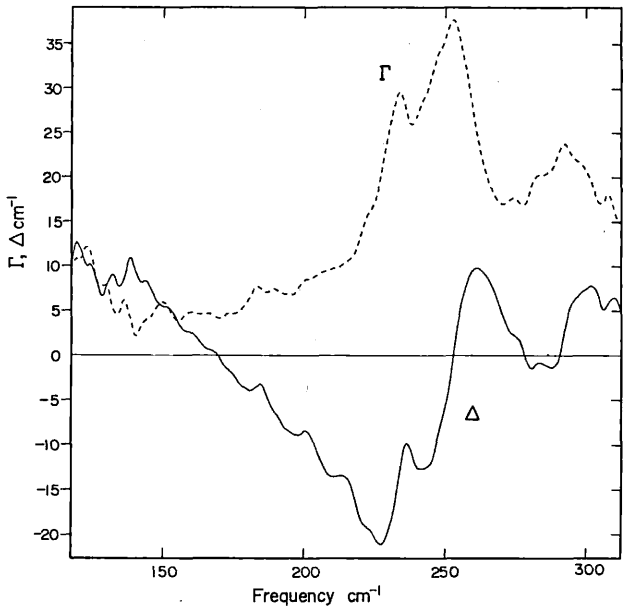

Fig. 4. Damping and self energy functions (Γ and Δ respectively) obtained from (2) for NaCl at 300 K.

6·25 μm mylar beam splitter, and the solid lines show the deviation of each phase spectrum from the mean. The interferometer was optically realigned at the position of zero path difference before each measurement so the reproducibility is limited by positional errors which arise during realignment and depend on the Golay detector noise level, as well as by positional errors due to the micrometer backlash. Errors due to the lack of flatness in the Michelson mirrors are insignificant but there may be a significant contribution from the flatness of the beam splitter. It is clear from the figure that the overall positional error does not exceed the noise level, indicating that the instrument is performing satisfactorily with a positional accuracy of better than 0·1 μm. Similar phase reproducibility is obtained with specimens of 2·5 cm dia either at room temperature or at low temperatures. However, the flatness of the specimen

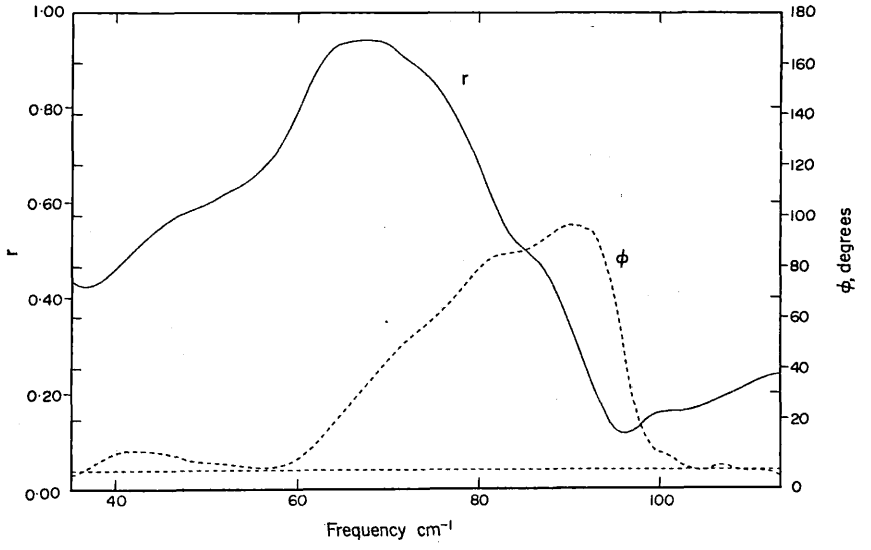

Fig. 5. Magnitude r and phase ϕ of reflectivity amplitude obtained for CsI at 300 K. Resolution is about 5 cm^{-1}.

surface becomes the limiting factor in most measurements. The lower frequency limit can be conveniently extended to about 20 cm^{-1} by changing to thicker beam splitters.

The performance of this instrument is illustrated in Fig. 2 with measurements of the amplitude and phase reflection spectra of NaCl at a temperature of 300 K, and the related dielectric functions calculated from[10]

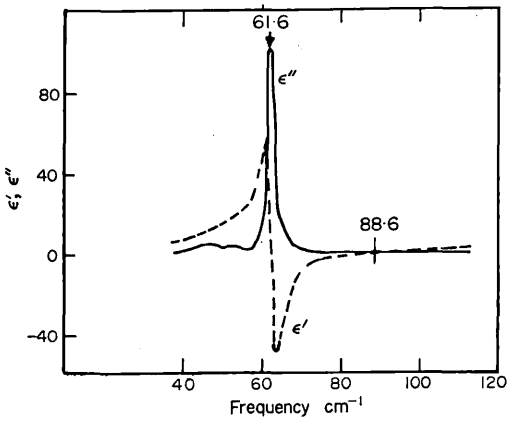

Fig. 6. Real and imaginary parts (ϵ', ϵ'' respectively) of dielectric function obtained from (1) for CsI at 300 K.

$$\epsilon' + i\epsilon'' = [(1 + re^{i\phi})/(1 - re^{i\phi})]^2 \tag{1}$$

are shown in Fig. 3. If it is assumed that the dielectric functions can be fitted by an oscillator model according to the formula[11]

$$\epsilon' + i\epsilon'' = \epsilon_\infty + \omega_0^2(\epsilon_0 - \epsilon_\infty)/[\omega_0^2 - \omega^2 + 2\omega_0(\Delta - i\Gamma)] \tag{2}$$

where ω_0 is the oscillator frequency, then $\Delta(\omega)$ and $\Gamma(\omega)$, the self energy and damping functions respectively, can be obtained from the data shown in Figs. 2 and 3 and they are shown in Fig. 4 for the limited frequency range available from these measurements. The parameters were chosen as $\epsilon_0 = 5{\cdot}90$, $\epsilon_\infty = 2{\cdot}30$ and $\omega_0 = 164\,cm^{-1}$, and the results for Γ and Δ are in reasonable agreement with the theoretical curves of Hisano *et al.*[11] with the exception of the feature at about 235 cm^{-1} which is not present in the theoretical curves.

This technique should be particularly useful in circumstances in which *KK* analysis is difficult as, for instance, in the study of soft mode behaviour in ferroelectric crystals[12], but it would be preferable if the lower frequency limit of the spectrometer could be reduced without loss of phase accuracy. This is difficult with a conventional Michelson interferometer because of the poor efficiency of dielectric beam splitters at low frequencies, combined with the disadvantage of the appearance of additional unwanted interference minima on increasing the beam splitter thickness, but these limitations are avoided in a polarising interferometer with a wire grid beam splitter.[13]

With these considerations in mind we have constructed a polarising interferometer with suitable modifications to enable dispersive measurements to be made as a function of temperature as described above. Two wire grid beam dividers constructed of 10 μm tungsten wire with 25 μm spacing are used in a configuration similar to that employed by Chamberlain *et al.*[14] This allows dispersive reflection or transmission measurements to be made at normal incidence in the frequency range from about 7 to 200 cm^{-1} using a Golay detector, and the limitation on the phase accuracy is again found to be about 0·1 μm for the same reasons as before.

The amplitude and phase reflection spectra of a CsI crystal measured at room temperature in the region of the restrahlen band with the polarising interferometer are

shown in Fig. 5, and the resulting dielectric functions calculated from the Fresnel relations[10] are shown in Fig. 6. These results are in good agreement with published data.

Acknowledgements—This work is supported in part by the Science Research Council. We also thank Mr. D. G. Moss and Mr. J. R. Birch of the National Physical Laboratory, Teddington, for sending us before publication the circuit diagram for the stabilised mercury lamp supply used in this work, and for help with the construction of wire grid beam splitters respectively.

REFERENCES

1. CHAMBERLAIN, J., J. E. GIBBS & H. A. GEBBIE, *Nature, Lond.* **198.** 874 (1963).
2. SANDERSON, R. B., *Appl. Opt.* **6,** 1527 (1967).
3. CHAMBERLAIN, J., J. E. GIBBS & H. A. GEBBIE, *Infrared Phys.* **9,** 185 (1969).
4. BELL, E. E., *Infrared Phys.* **6.** 57 (1966).
5. RUSSELL, E. E. & E. E. BELL, *Infrared Phys.* **6.** 75 (1966).
6. GAST, J., L. GENZEL & U. ZWICK, *I.E.E.E. Trans.* **MTT-22,** 1026 (1974).
7. JOHNSON, K. W. & E. E. BELL, *Phys. Rev.* **187,** 1044 (1969).
8. PARKER, T. J. & W. G. CHAMBERS, *I.E.E.E. Trans.* **MTT-22,** 1032 (1974).
9. PARKER T. J. & W. G. CHAMBERS, *Infrared Phys.* (1975).
10. BORN, M. & E. WOLF, *Principles of Optics.* p. 41, 4th Edition. Pergamon Press. Oxford (1970).
11. HISANO, K., F. PLACIDO, A. D. BRUCE & G. D. HOLAH, *J. Phys.* **C5.** 2511 (1972).
12. See, for instance, the review article by J. F. SCOTT, *Rev. Mod. Phys.* **46,** 83 (1974)..
13. MARTIN, D. H. & E. PUPLETT, *Infrared Phys.* **10.** 105 (1969).
14. CHAMBERLAIN, J., M. N. AFSAR, G. J. DAVIES, J. B. HASTED & M. S. ZAFAR, *I.E.E.E. Trans.* **MTT-22,** 1028 (1974).

Infrared Physics, 1976, Vol. 16, pp. 515–522. Pergamon Press. Printed in Great Britain

DISPERSIVE REFLECTION SPECTROSCOPY IN THE FAR INFRARED USING A POLARISING INTERFEROMETER

D. A. LEDSHAM,* W. G. CHAMBERS+ and T. J. PARKER*†

Departments of Physics* and Mathematics+, Westfield College, (University of London), Kidderpore Avenue, London, NW3 7ST

(*Received* 18 *November* 1975)

Abstract—A polarising interferometer designed for dispersive reflection measurements on solids between about 5 and 210 cm^{-1} at temperatures between 77°K and 300°K is described and its performance illustrated with measurements of the complex reflectivity spectra of CsI, KDP and ADP at 300°K in the range 40–210 cm^{-1}. The dielectric functions resulting from these spectra are given and are in good agreement with published data. In addition, the self energy and damping functions are computed for CsI. Developments for future measurements down to 77°K and 5 cm^{-1} are discussed.

INTRODUCTION

The use of dispersive Fourier transform spectroscopy (DFTS) for the determination of the optical constants or the dielectric functions directly from measurements of the amplitude and phase reflection spectra in the far infrared has been firmly established over the past few years.[1–5] This method has well-known advantages over conventional Fourier transform spectroscopy where the phase is constructed from a Kramers-Krönig analysis of the power transmission or reflection.

The advantages of a polarising interferometer over a conventional Michelson with dielectric beam splitters, for DFTS in the range 5–210 cm^{-1} have been discussed in various articles.[2,6] In the conventional instrument the poor efficiency of the dielectric beam splitters at low frequencies combined with the unwanted interference effects, leading to a strongly frequency-dependent transmissivity, make reducing the low frequency limit to 20 cm^{-1} and beyond extremely difficult. However, these problems are avoided in a polarising interferometer with wire grid beam splitters which have a constant transmissivity up to a frequency inversely proportional to the grid spacing.

In this paper we describe a polarising interferometer and initial measurements made with it on crystals of CsI, ferroelectric KH_2PO_4 (KDP) and antiferroelectric $NH_4H_2PO_4$ (ADP) at 300°K. The technique reported in previous articles[7,8] of division of the field of view in the fixed arm of the interferometer, eliminating errors due to mechanical replacement of reflecting surfaces, is used. This enables interferograms to be recorded with a positional accuracy of $\sim \pm 0.15\ \mu m$.

EXPERIMENTAL METHOD

The basic form of the instrument is illustrated in Fig. 1. The design is an extension of the conventional instrument with dielectric beam splitters.[1,7,8] Two grid beam splitters are used in a configuration similar to that employed by Chamberlain *et al.*[9] and are constructed of 10 μm tungsten wire with a spacing of 25 μm, using a technique developed by them at the National Physical Laboratory, Teddington, Middlesex. Having emerged from the collimator, the unpolarised radiation is incident upon the grid *A* which reflects a plane polarised beam towards grid *B*, the wires of which are at 45° to the plane of polarisation of the incident radiation. The component of this radiation with its *E*-vector perpendicular to the grid wires is transmitted into the moving mirror arm, whilst the parallel component is reflected into the fixed arm. Following reflection

† On leave of absence at the Department of Physics, Northeastern University, Boston, Mass. 02115, USA, until September 1976.

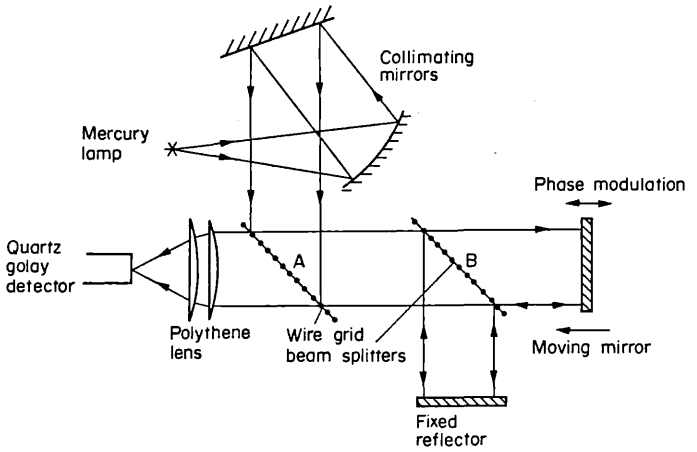

Fig. 1. Schematic diagram of the polarising interferometer.

from the moving mirror and the fixed mirror (or sample) the beams follow the same transmission and reflection laws on their return to grid B, and pass onto grid A, which now acts as an analyser. The components of each beam with their E-vectors perpendicular to the wires of A are transmitted by A and interfere according to the difference in the optical paths of the two beams in the instrument. Thus, an interferogram is obtained in the usual way by displacing the moving mirror about the position of zero path difference.

Other modifications include the use of phase modulation, described in a previous article,[1] achieved by mounting the moving mirror on the cone of a loudspeaker, and the design of a new mounting arrangement for the fixed reflector, based on one that has been successfully employed before.[8] Using this arrangement (Fig. 2) the fixed reflector could be accurately aligned with a precision of 0.15 μm at any temperature between 77 and 300°K. Changing the reflector was a simple task, and it could also be rotated through any angle without first being removed from the mount, a great advantage when studying the different axes of ferroelectric crystals.

With the temperature of the interferometer stabilised to within 0.25°C using a temperature controlled water supply circulating through cooling tubes attached to the arms, cubes and lamp housing, it was found that within one hour of installing the mount and evacuating the instrument to the working pressure of 10^{-1} Torr, movement of the fixed reflector surface due to thermal instability was negligible.

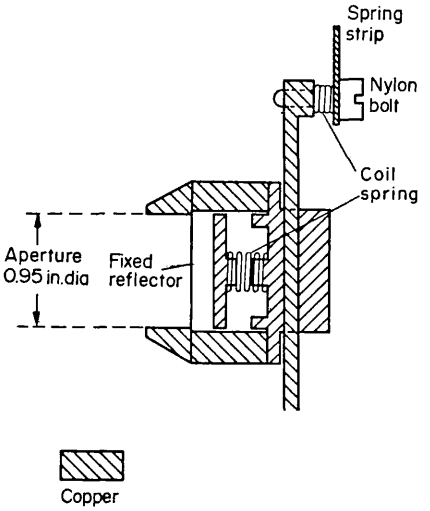

Fig. 2. The fixed reflector mount.

Although using this mount, replacement of reflectors in the fixed arm could not be achieved to within 0.15 μm, use of the division of the field of view technique gave phase reproducibility to within $\pm 1°$. This technique has been fully described before,[7,8] however, the geometry of the screens has been modified (Fig. 3) and is such that the possibility of cross-talk between the areas X and Y has been eliminated.

Four interferograms are again required. Firstly, with the fixed gold mirror installed and aligned on the outer ring X, interferograms are recorded from parts X and Y. These are Fourier transformed and the resulting spectra ratioed to give a calibration spectrum. Then, with the crystal installed and again aligned on the outer ring X which has been metallised with gold, two more interferograms are recorded, from part X and from part Y, the exposed specimen surface. On ratioing the resulting spectra,

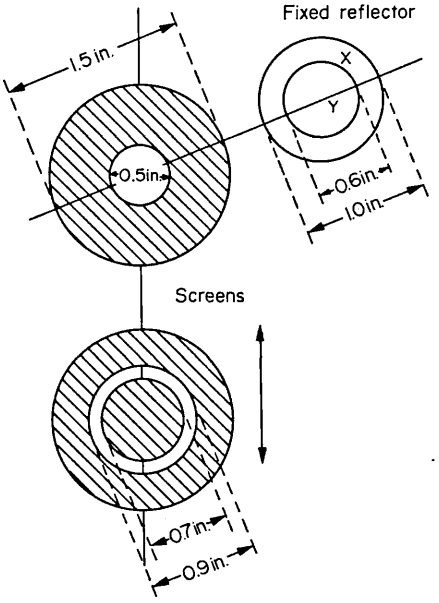

Fig. 3. The geometry of the screens and the division of the field of view at the fixed reflector.

the complex reflection spectrum of the specimen is obtained and then, systematic errors, caused by asymmetry between the areas X and Y and differences in the two arms, are reduced by re-ratioing against the calibration spectrum.

The crystals used were either 1 in. dia or 1 in. square and were metallised so as to leave a 0.6 in. dia exposed area of the specimen surface at the centre. Previous measurements[1,8] used 2.5 in. dia specimens with exposed surfaces of approximately 1 in. dia. However, the excessive cost and general unavailability of suitable ferroelectric crystals of this size necessitated adapting the technique for use on smaller crystals without loss of phase accuracy due to the reduction in the energy reflected from the smaller specimens. This has been achieved to the extent that the phase reproducibility now appears to be limited, not by lack of energy, but by the flatness of the specimen surface.

DISCUSSION OF RESULTS

To improve the signal to noise ratio which, for an individual crystal measurement was of the order of 100:1, each pair of interferograms was recorded at least four times. An average pair of interferograms was then obtained which were Fourier transformed in the usual way. Before each pair was recorded, the interferometer was optically realigned at the position of zero path difference. Thus, the reproducibility of successive pairs from the same fixed reflector is limited by positional errors due to realignment, dependent on the Golay detector noise level, and micrometer backlash. Reproducibility

to $\pm 1°$ was obtainable in practice, thus with a sampling step length of 5 μm, giving a 500 cm^{-1} cut-off,[10] this implies a positional accuracy $\Delta x \sim 0.15\,\mu m$ at 150 cm^{-1}.

Below about 40 cm^{-1}, the reproducibility of the results is impaired by lack of energy, due in particular to the low frequency cut-off imposed by the use of phase modulation. The ferroelectric spectra are shown with faint lines in this region, as further measurements are required before the spectral features can be published with any confidence.

This, of course, is the region of interest when ferroelectrics such as KDP are being studied, for it is here that the soft modes lie. The use of amplitude modulation which, although noisier than phase modulation, has no low frequency cut-off, and other modifications are at present being investigated to improve the performance of the instrument below 40 cm^{-1}. The results will be published in a later article. Ultimately for results below about 7 cm^{-1}, the Golay cell will have to be changed for a liquid Helium cooled detector.

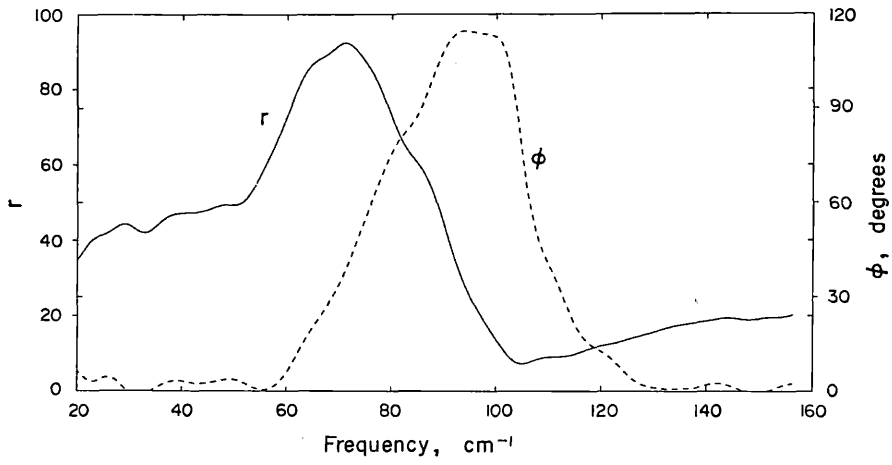

Fig. 4. The magnitude and phase reflection spectra of CsI at 300°K. The resolution is 5 cm^{-1}.

(i) CsI *Results*

Alkali halides are a good subject for spectroscopic studies in the far infrared because of their distinctive restrahlen region. Previous work has been done mainly on KBr,[1,8,11] however, for this work, CsI was chosen as its restrahlen band, along with that of CsBr, are the only two of the common alkali halides to lie comfortably within the working range of the instrument. Unfortunately, the hygroscopic nature of CsI introduced unwanted problems into the measurements and care had to be taken to avoid prolonged exposure of the crystal to the air.

The reflection spectra of CsI at 300°K are shown in Fig. 4 and the related dielectric functions calculated from

$$\epsilon' + i\epsilon'' = [(1 + re^{i\phi})/(1 - re^{i\phi})]^2 \tag{1}$$

are shown in Fig. 5. The values $\omega_{TO} = 62.2\,cm^{-1}$ and $\omega_{LO} = 90.3\,cm^{-1}$ obtained from these functions are in good agreement with published data,[12] and are more accurate than those published previously.[2] Assuming these functions can be fitted by an oscillator model according to

$$\epsilon' + i\epsilon'' = \epsilon_\infty + \omega_{TO}^2(\epsilon_0 - \epsilon_\infty)\,[\omega_{TO}^2 - \omega^2 + 2\,\omega_{TO}(\Delta - i\Gamma)]^{-1} \tag{2}$$

then $\Delta(\omega)$ and $\Gamma(\omega)$ the self energy and damping functions respectively, can be obtained and are shown in Fig. 6. The parameters were chosen as $\epsilon_0 = 6.54$ and $\epsilon_\infty = 3.02$.[12]

(ii) *The KDP and ADP results*

Both the 'a' and 'c' axis spectra were obtained for KDP and ADP. The results,

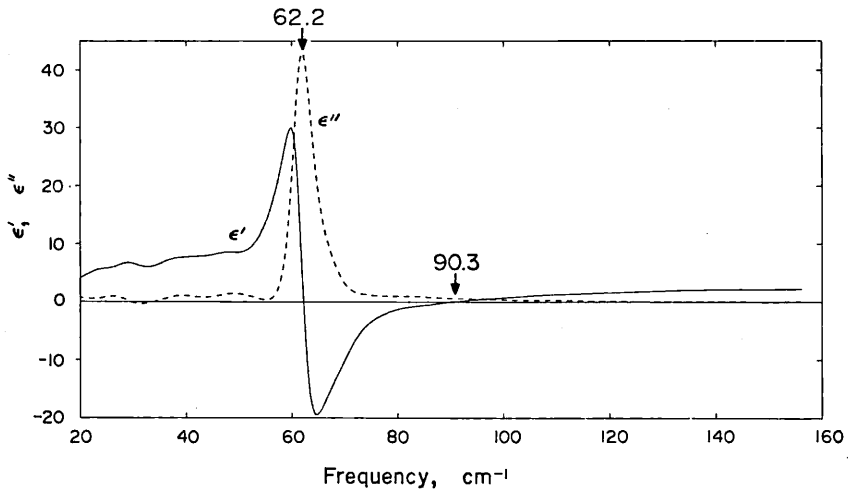

Fig. 5. The real and imaginary parts (ϵ',ϵ'' respectively) of the dielectric functions for CsI at 300°K.

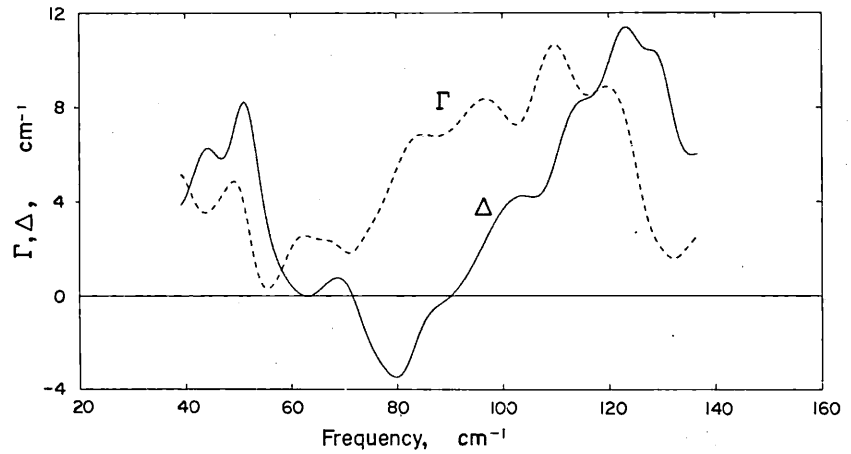

Fig. 6. The damping and self energy functions (Γ and Δ respectively) for CsI at 300°K.

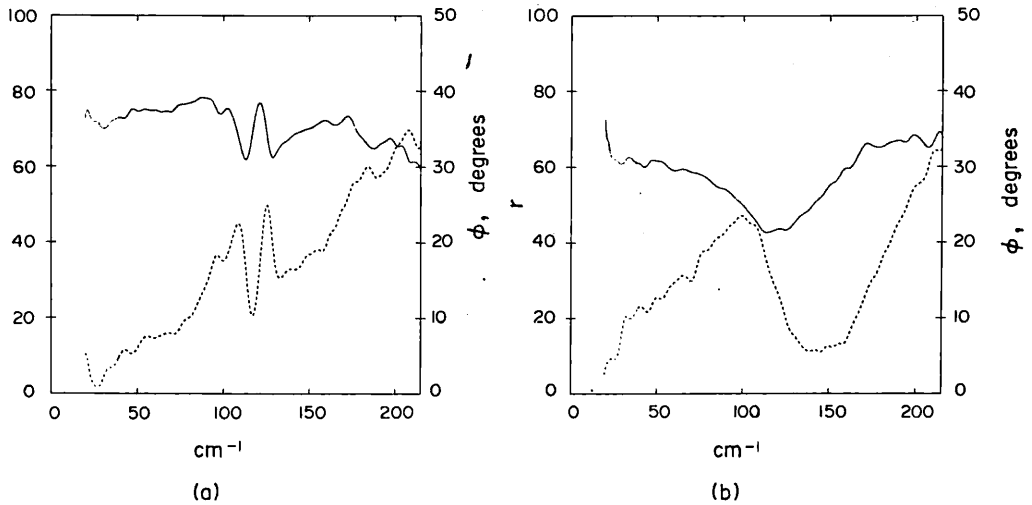

Fig. 7. The magnitude and phase reflection spectre of KDP at 300°K for radiation polarised (a) parallel to a-axis, (b) parallel to c-axis. The resolution is 5 cm^{-1}.

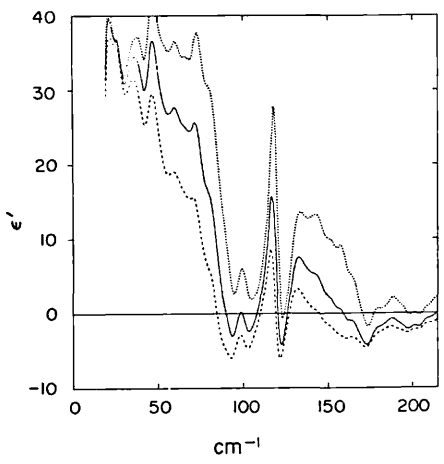

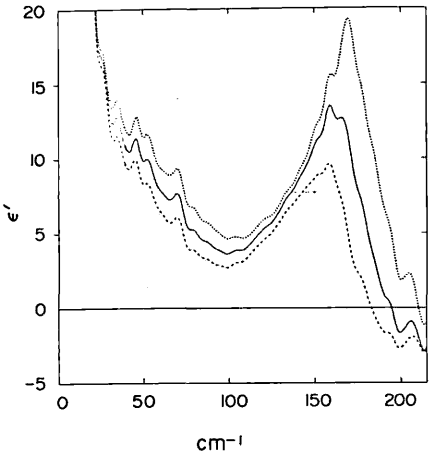

Fig. 8.

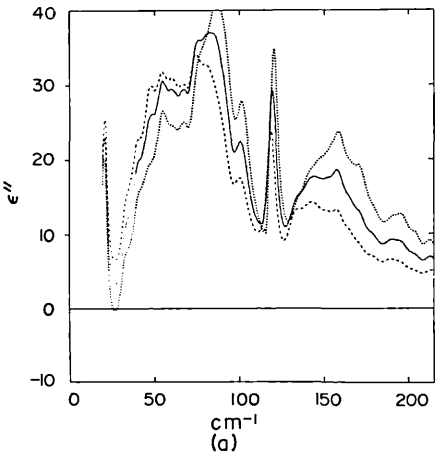

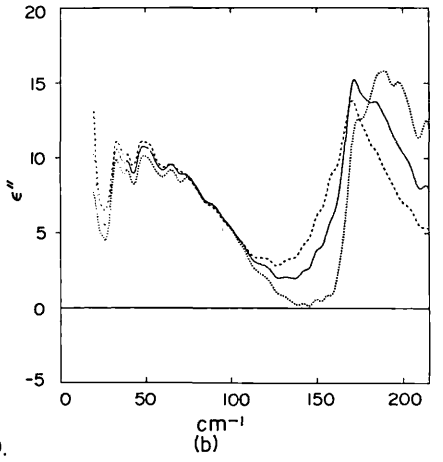

Fig. 9.

Figs. 8 and 9. Solid curves: The real and imaginary parts respectively of the dielectric functions of KDP at 300°K for radiation polarised. (a) parallel to a-axis, (b) parallel to c-axis. Dotted and dashed curves: Effect of errors of ± 0.1 of a sampling step on the calculated dielectric functions.

Figs. 7–12, over the range 40–210 cm^{-1} are in good agreement with previous published data including that by Birch *et al.*[13] in which the first direct measurements of the complex reflectivities of both axes of KDP and the 'a' axis of ADP are reported, and earlier work involving Kramers–Krönig determinations.[14–16]

The ϵ'' curve for the KDP 'c' axis should exhibit a maximum in the region of 50 cm^{-1}, associated with the ferroelectric transition but this has not been resolved. However, the improvements in the performance of the instrument below 40 cm^{-1}, mentioned earlier, should solve this problem.

The sensitivity of the dielectric functions, of both KDP and ADP, to small changes in the phase spectra is illustrated by the dotted and dashed curves in Figs. 8, 9, 11, 12. These curves show the effect of errors of ± 0.1 of a sampling step (ie $\pm 0.5\,\mu m$) on the computed dielectric functions. The dotted and dashed curves correspond, respectively, to shifts which increase and decrease the phase of the computed reflectivity, by an amount linearly proportional to the frequency. This has little effect on the positions of the various features in the spectrum but changes the magnitudes of the features quite markedly in some cases.

CONCLUDING REMARKS

Besides the use of amplitude modulation to improve the low frequency performance of the instrument, other developments are being investigated.

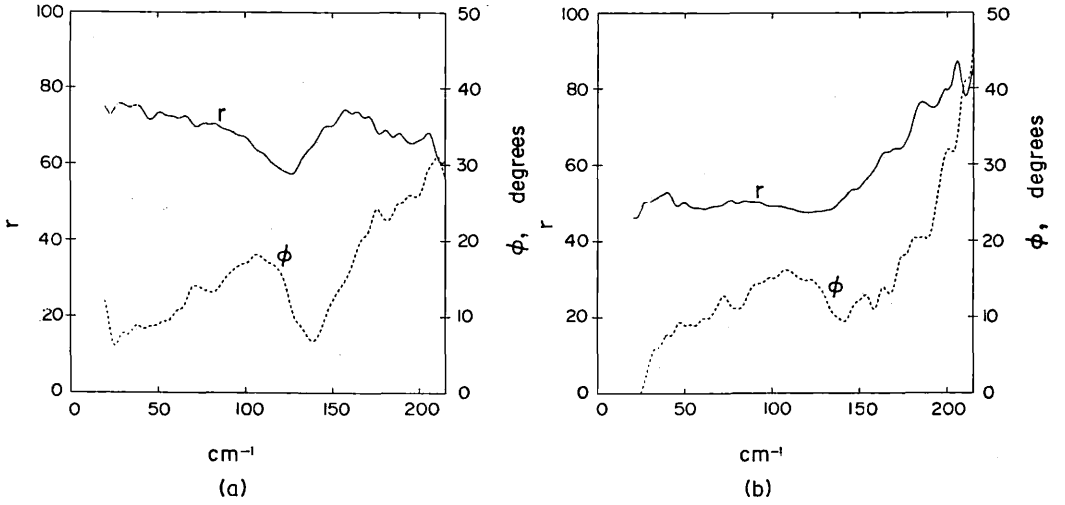

Fig. 10.

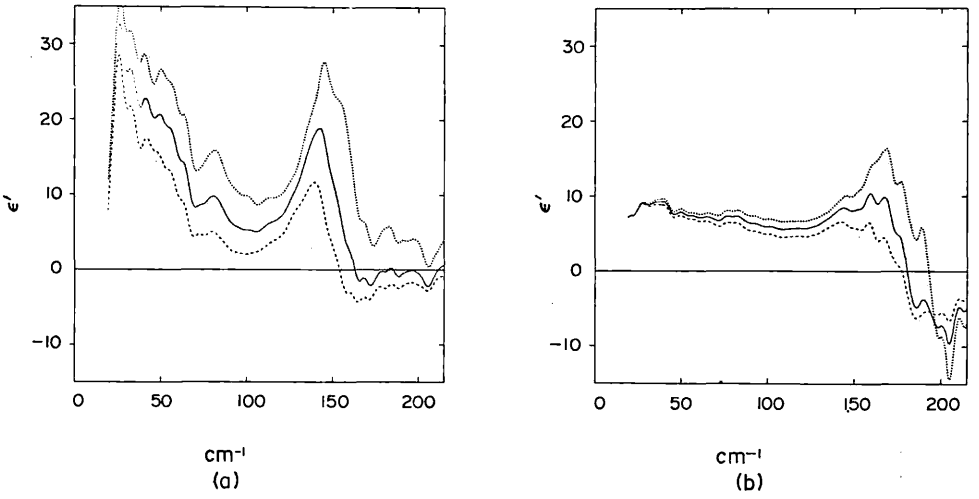

Fig. 11.

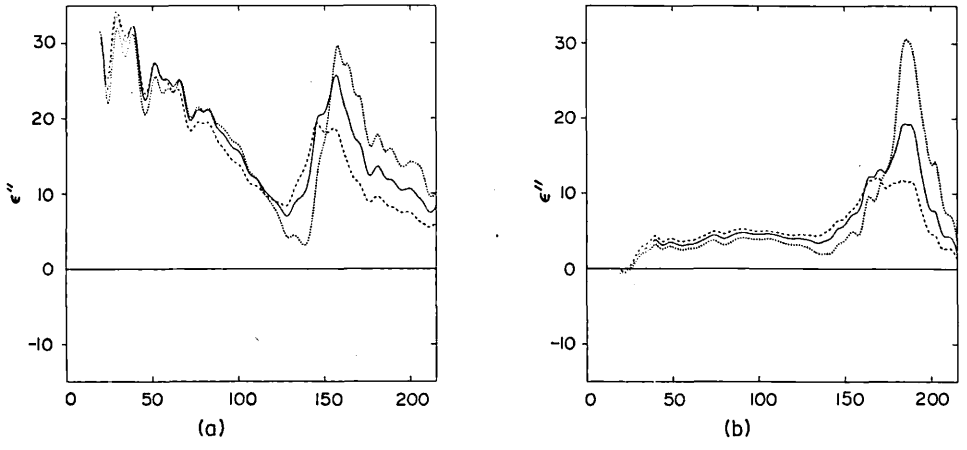

Fig. 12.

Figs. 10, 11, 12. As Figs. 7–9 but for ADP.

The stability of the instrument has already been tested at low temperatures. It is now possible to control the temperature of the crystal to within ~ 0.25°C anywhere between 90°K and 300°K using a cryogenic temperature controller and a system of thermocouples and heaters in conjunction with a dewar of liquid nitrogen. Improving the working pressure from ~ 10^{-5} Torr to better than 10^{-6} Torr should eliminate or delay the "icing-up" of the crystal surface caused by water vapour inside the instrument condensing on it. At present this gradual "icing-up" process doesn't allow sufficient time for repeated measurements on the cooled crystal after allowing time for the temperature, and then the output at that temperature, to stabilise.

Use of "all-reflecting" output optics to replace the polythene lenses is also being considered as the lenses absorb a large proportion of the energy that would otherwise be incident on the Golay nose. Since the grids themselves act as low pass filters, none of the usual black polythene filters are required and so removal of the lenses would eliminate all absorbing material from the path of the radiation from source to detector, excepting, of course, the crystal.

With these developments and the use of a liquid Helium cooled detector, the measurement of spectra down to about 5 cm^{-1} and 77°K should be possible to the required accuracy, allowing plots of the soft mode frequency of various ferroelectrics, such as KDP, vs temperature, to be obtained down to their ferroelectric transition temperature.

A particular advantage of the design of this polarising interferometer is that by replacing grid A by a mirror, an aluminised mylar beam splitter is used in practice, and grid B by a mylar beam splitter, transferring the Golay to the vacant port of the other cube converts the instrument to the more conventional Michelson.[1] Thus, changing the thickness of the mylar beam splitter enables a new range of frequencies, greater than 210 cm^{-1}, to be studied.

Acknowledgements—This work is supported in part by the Science Research Council. The authors also wish to thank the technical staff of the Physics Department and Computer Unit for their valuable assistance, and Mr J R Birch and others at the National Physical Laboratory, Teddington, for teaching us the grid winding technique and for the loan of equipment.

REFERENCES

1. PARKER, T. J. & W. G. CHAMBERS, *Infrared Phys.* **16,** 349 (1976).
2. PARKER, T. J., D. A. LEDSHAM & W. G. CHAMBERS, *Proc. CIRP*, Zurich (1975).
3. BELL, E. E., *Infrared Phys.* **6,** 57 (1966).
4. RUSSELL, E. E. & E. E. BELL, *Infrared Phys.* **6,** 75 (1966).
5. GAST, J., L. GENZEL & U. ZWICK, *IEEE Trans.* **MTT-22,** 1026 (1974).
6. AFSAR, M. N., J. R. BIRCH & J. CHAMBERLAIN, *Conference on Dielectric Materials, Measured and Applications.* Cambridge, England, July 1975. IEE Conference Publications 129.
7. PARKER, T. J., W. G. CHAMBERS, & J. F. ANGRESS, *Infrared Phys.* **14,** 207 (1974).
8. PARKER, T. J. & W. G. CHAMBERS, *IEEE Trans.* **MTT-22,** 1032 (1974).
9. CHAMBERLAIN, J., M. N. AFSAR, G. J. DAVIES, J. B. HASTED & M. S. ZAFAR, *IEEE Trans.* **MTT-22,** 1028 (1974).
10. CHANTRY, G. W. *Submillimetre Spectroscopy*, p. 58. Academic Press, New York (1971).
11. CHAMBERLAIN, J., M. N. AFSAR, D. K. MURRAY, G. D. PRICE & M. S. ZAFAR, *IEEE Trans.* **IM-23,** 483 (1974).
12. LOWNDES R. P. & D. H. MARTIN, *Proc. Roy. Soc. (Lond.)* **A308,** 473 (1969).
13. BIRCH, J. R., G. D. PRICE & J. CHAMBERLAIN, *Proc. CIRP.* Zurich (1975).
14. ONYANGO, F., W. SMITH & J. F. ANGRESS, *J. Phys. Chem. Solids.* **36,** 309 (1975).
15. BARKER, A. S. & M. TINKHAM, *J. Chem. Phys.* **38,** 2257 (1963).
16. KAWAMURA, T., A. MITSUISHI & H. YASHINAGA, *J. Phys. Soc. Japan* **28,** Suppl. 227 (1970).

Infrared Physics, 1977, Vol. 17, pp. 165–172. Pergamon Press. Printed in Great Britain.

FAR INFRARED MEASUREMENTS ON KH_2PO_4 USING DISPERSIVE REFLECTION SPECTROSCOPY

D. A. LEDSHAM*, W. G. CHAMBERS† and T. J. PARKER*

Departments of Physics* and Mathematics,† Westfield College, University of London, Kidderpore Avenue, London, NW3 7ST, U.K.

(*Received* 23 *July* 1976)

Abstract—Dispersive measurements of the *c* axis complex reflectivity spectra of KH_2PO_4 in the range 20–235 cm^{-1}, from 300 down to 150°K, obtained using a polarising interferometer are presented. The resulting dielectric functions are calculated and the results are analysed in terms of coupled mode theory. The model parameters obtained by curve-fitting, using both reactive "spring" coupling and resistive "dashpot" coupling, are listed and comparison made with those obtained by other workers. For both models, the "soft" frequency values are higher than those of other authors, probably because of the lack of reliable low frequency data.

INTRODUCTION

Recent advances in the technique of dispersive Fourier transform spectroscopy (DFTS) have led to far infrared measurements of the complex reflectivity spectra of various alkali halides, particularly KBr, at 300°K and 100°K[1,2] and of certain ferroelectrics at room temperature.[3–5] The development of a polarising interferometer and initial results obtained with it for the reflection spectra of CsI, ferroelectric KH_2PO_4 (KDP) and antiferroelectric $NH_4H_2PO_4$ (ADP) at 300°K have been described in a previous article.[3]

Due to the considerable interest, both experimental and theoretical, shown in KDP and similar ferroelectrics, Raman scattering [6–9] and power spectroscopic measurements[10–12] have been performed on such materials down to and beyond their ferroelectric transition temperatures. Through this work, which began with measurements by Barker and Tinkham,[13] a coupled-mode picture of the infrared spectra of KDP type ferroelectrics has been formulated.

In this paper we describe dispersive reflection measurements performed on the *c* axis of KDP, with the polarising interferometer, from 300 down to 150°K. The results are discussed in terms of the coupled-mode formalism.

EXPERIMENTAL METHOD

Descriptions of the polarising instrument, which employs two wire-grid beam dividers, and of the measuring technique, have been given in detail previously,[3,14] though certain modifications have brought improvements and simplifications to both.

An all-reflecting output optics system has been developed to replace the polythene lenses. This increases the through-put energy of the instrument by more than 100%, since the lenses absorbed a large proportion of the infrared radiation. Since the grids themselves act as low pass filters, none of the usual polythene filters are used and the polythene absorption lines in the measured spectra have been eliminated.

Phase modulation is produced by vibrating a mirror, at 45° to the propagation direction, mounted in a right-angled unit halfway along the moving mirror arm. This arrangement is similar to that used by Birch *et al.*[4] The vibrator used, makes this arrangement capable of a far wider range of modulation frequencies with far larger amplitudes than were possible with the system previously employed,[3] and gives improved stability. These aspects are especially important as the use of a liquid Helium detector is being considered for low frequency measurements below $\sim 30\,cm^{-1}$.

Although the wire grids, which cut-off above 250 cm^{-1}, and the Golay detector, the efficiency of which falls off rapidly below about 30 cm^{-1}, limit the working range of the instrument, the profile of the through-put spectrum could be altered within this range by changing the amplitude of the phase modulation. This has the effect of shifting the peak of the energy spectrum, thus enabling more accurate results to be obtained by concentrating the energy in different regions of the range.

The working pressure for the low temperature measurements has been reduced to $< 10^{-5}$ Torr and no significant "icing-up" of the crystal surface occurred during low temperature experimental runs. These runs had a duration of up to 5 h.

The measuring technique was simplified in the following way. The division of the field of view method[3,14] was again used. Partly aluminised crystal surfaces and screens enable the phase to be measured directly after a correction has been made to allow for the thickness of the aluminising film ($\simeq 0.1\ \mu m$). This method eliminates the need for exact replacement of the crystal by the fixed mirror, though a series of four interferograms is required.

However, in addition, interferograms were recorded from the whole unaluminised crystal surface which was then replaced by the fixed mirror from which an interferogram was also recorded for calibration purposes; no screens were used at all. When the spectra obtained by Fourier transform from these crystal and mirror interferograms were ratioed, a true measurement of the crystal amplitude reflection spectrum was obtained. This was providing the lamp intensity and various other experimental factors did not change significantly between the crystal and mirror measurements. However, as the crystal surface had not, indeed could not, be replaced exactly by the mirror surface, the phase spectrum obtained had to be corrected for the error in the zero path. Knowledge of the exact phase at a particular point obtained from spectra measured using the division of field technique, together with a knowledge of the theory, enabled this correction to be made.

The advantages of this method were that unlike the division of field technique where about 50% of the crystal surface was covered by the aluminising layer, the whole of this surface could be utilised for the recording of crystal data, thus giving a large increase in the reflected energy. In addition, only two different interferograms were required to achieve a final result though prior knowledge of certain phase points is required. The two techniques thus go hand-in-hand and gave a series of spectra which were averaged to give the results presented in this paper.

The low temperature measurements were obtained using a liquid nitrogen dewar fixed to the sample chamber of the interferometer and in good thermal contact with the crystal mount. A feedback system comprising of a 40 W thermostat heater, controlled by a cryogenic temperature unit, and two thermocouples, held the crystal mount at the required temperature. Stability to ~ 0.1°K could be obtained in practice anywhere between 90° and 300°K. This was achieved within 5 min for small temperature steps ~ 25°K and took up to about 30 min for changes of ~ 150°K.

RESULTS AND CURVE FITTING

The amplitude and phase reflection spectra for the c axis of KDP at 300, 200, 175 and 150°K are shown in Figs. 1(a) and (b) and the resulting dielectric functions are displayed in Figs. 2(a) and (b). It should be noted that the results were obtained from two crystals purchased from different sources and no significant difference was observed in the spectra obtained from them.

The overdamped band in the 300°K ϵ'' curve which peaks at about 50 cm^{-1} and is associated with the ferroelectric transition has been resolved. This feature was found by Barker and Tinkham in 1962.[13] Quantitative measurements of the temperature dependence of this low frequency mode were first made by Kaminov and Damen,[8] using Raman scattering, who fitted their data to a simple damped harmonic oscillator function.

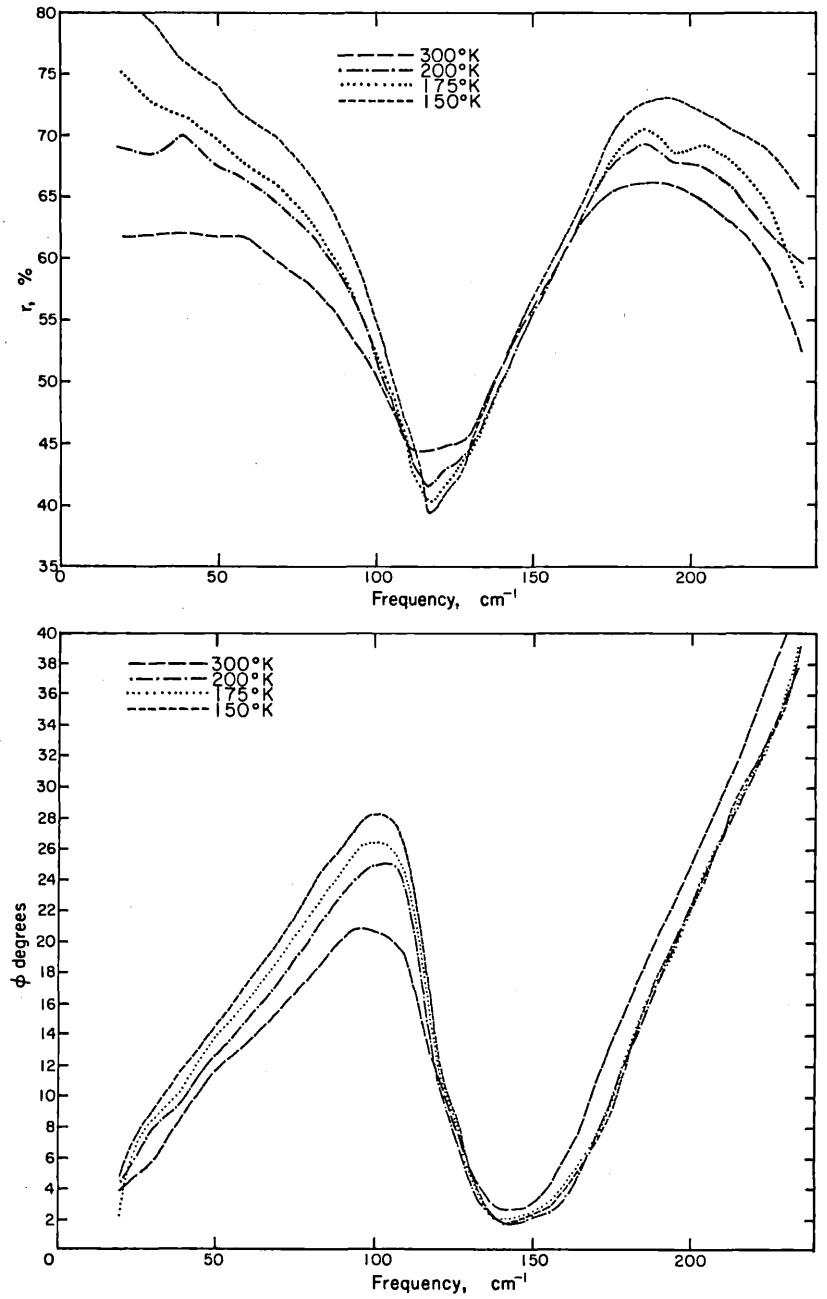

Figs. 1(a) and (b). The amplitude (r) and phase (ϕ) reflection spectra, respectively, of the c axis of KDP. The resolution is $5\,cm^{-1}$.

More recent Raman experiments[6,9] have revealed that the ferroelectric soft mode is strongly coupled to an optic phonon mode of the same symmetry lying near $180\,cm^{-1}$. Barker and Hopfield[15] formulated a coupled-optical–phonon mode theory in 1964 in order to explain the i.r. dispersion of $BaTiO_3$ and other high dielectric constant materials. They found such an analysis gave greatly improved fits to their data which could not be fitted by any choice of parameters using uncoupled oscillators.

This coupled mode theory has been used to analyse the spectra of KDP and similar materials[5–7,9] where, once again, spectra could not be interpreted by superposition of independent oscillators, and will be used in the discussion of our present data.*

* This theory has been further developed recently, for the ferroelectric soft mode is also coupled piezoelectrically to a soft acoustic mode.[16,17] Thus, a three-mode formalism has been put forward[6] which has been used to explain the occurrence of a finite temperature gap between the ferroelectric transition temperature and the temperature at which the frequency of the ferroelectric soft mode goes to zero.

Following Barker and Hopfield[15] we consider two particles of unit mass with effective charges e_1 and e_2, coupled mutually by a spring of spring constant k_{12} and to fixed points by springs of constants k_1 and k_2 respectively. The equations of motion for the two particles are:

$$\begin{aligned} \ddot{y}_1 + \Gamma_1\dot{y}_1 + \mathrm{k}_1 y_1 &= e_1 E + k_{12}(y_2 - y_1) \\ \ddot{y}_2 + \Gamma_2\dot{y}_2 + k_2 y_2 &= e_2 E + k_{12}(y_1 - y_2) \end{aligned} \qquad (1)$$

with polarisation $P = y_1 e_1 + y_2 e_2$.

Here E is the applied electric field, y_1 and y_2 are the displacements of particles 1 and 2, and the Γ_i are damping constants.

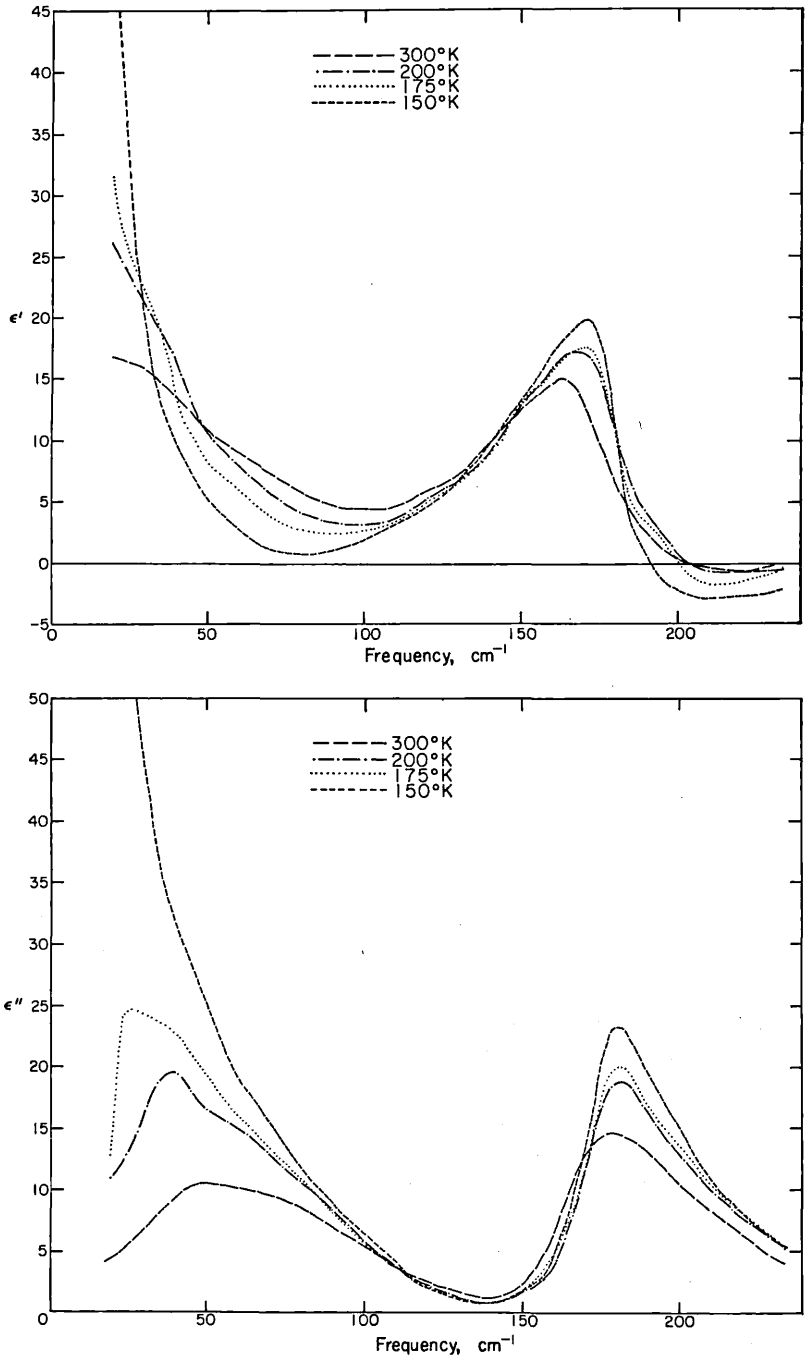

Figs. 2(a) and (b). The real (ϵ') and imaginary part, (ϵ'') respectively, of the dielectric functions of the c axis of KDP.

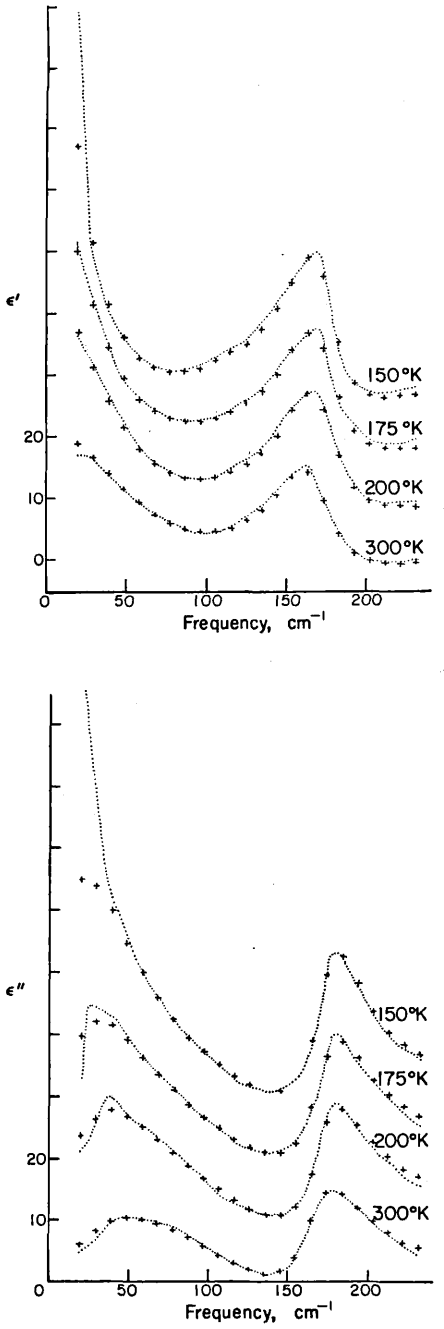

Figs. 3(a) and (b). Theoretical fits to the dielectric functions (ϵ', ϵ''). The dotted lines are the experimental curves of Figs. 2(a) and (b). The 200, 175 and 150°K curves are displaced by 10, 20 and 30 units, respectively, up the ϵ axes, from the 300°K curve, for clarity. The crosses are points from theoretical curves calculated using the parameters of Table 1 and the reactive coupling model.

As shown by Barker and Hopfield, these equations of motion can be written in an equivalent way to describe two particles with resistive "dashpot" coupling. The equivalence is given by a 2 × 2 orthogonal transformation which diagonalizes the force constant matrix to give:

$$\begin{aligned} \ddot{x}_1 + \gamma_1 \dot{x}_1 + w_1^2 x_1 &= z_1 E + \gamma_{12} (\dot{x}_2 - \dot{x}_1) \\ \ddot{x}_2 + \gamma_2 \dot{x}_2 + w_2^2 x_2 &= z_2 E + \gamma_{12} (\dot{x}_1 - \dot{x}_2) \end{aligned} \tag{2}$$

$$\text{with the polarisation } P = x_1 z_1 + x_2 z_2.$$

If we assume harmonic solutions E, x_1, $x_2 \sim e^{iwt}$ then from (2) the dielectric function

is given by

$$\epsilon(w) - \epsilon_\infty = P/E = \frac{z_1^2 G_1 + z_2^2 G_2 + 2z_1 z_2 iw\gamma_{12} G_1 G_2}{1 + w^2 \gamma_{12}^2 G_1 G_2} \tag{3}$$

where

$$G_j = \frac{1}{w_j^2 - w^2 + iw(\gamma_j + \gamma_{12})} \quad (j = 1, 2) \tag{4}$$

is the response function of the uncoupled mode.

The dielectric function for the case of reactive "spring" coupling is similarly obtained using (1). For the analysis of our KDP c axis spectra we take $j = 1$ to designate the ferroelectric soft mode and $j = 2$, the optic mode.

The model described by (3) has seven parameters. We use the sets w_1^2, w_2^2, $(\gamma_1 + \gamma_{12})$, $(\gamma_2 + \gamma_{12})$, γ_{12}, z_1, $-z_2$ for resistive coupling and $(k_1 + k_{12})$, $(k_2 + k_{12})$, k_{12}, Γ_1, Γ_2, e_1, $-e_2$ for reactive coupling following Barker and Hopfield. The effective charges are of opposite sign and to indicate this we have attached a minus to e_2 and z_2.

There are in fact an infinite number of mathematically correct solutions to the diagonalization of the force constant matrix each with its corresponding set of seven parameters. The "spring" and "dashpot" couplings are two particular choices.

We have performed both "spring" and "dashpot" coupling fits to our KDP spectra and the parameters obtained are listed in Tables 1 and 2. For both sets of parameters we took the value $\epsilon_\infty = 3.2$ from Gauss *et al.*[5] and only used the results above 40 cm^{-1} in the fits. Also included in these tables is the equivalent notation for the parameters as used by other workers who employed the same coupling model.

The use of Barker and Hopfield notation clearly illustrates the problem that arises when the resistive coupling model is employed. This problem, encountered by Barker and Hopfield, has since become obscured by the different notation adopted by other workers.[5,6] It is immediately evident from Table 2 that $(\gamma_2 + \gamma_{12}) < \gamma_{12}$ in all cases, hence $\gamma_2 < 0$ and so we have the unphysical occurrence of a negative resistance in the high frequency mode. We should thus treat the resistive model simply as a mathematical curve fitting exercise and not as a description of the physical situation. Consequently we prefer to use reactive coupling as did She *et al.*[9]

In this version we find that in two cases the spring constant k_1 is negative, but this simply means that the low frequency oscillator would be unstable by itself, and that the overall stability is maintained by the spring coupling to the other oscillator.

The clue to what is happening is the very small value of ϵ'' at $\sim 135\,cm^{-1}$ [Fig. 2(b)]. This dip can be described as follows. The heavily damped soft mode is not being driven here because the direct coupling to the radiation field is cancelled by the indirect coupling through the high frequency mode. The low value of ϵ'' caused by this "interference" requires firstly that any damping in the coupling and in the high frequency mode must be small, and secondly that the effective charges must have opposite signs, since the interference takes place below the frequency of the high frequency mode. Any attempt to describe the situation by using resistive coupling leads to the use of an unphysical compensating negative damping in the high frequency mode. The reactive model, how-

Table 1. Parameters obtained from theoretical fits to the experimental data using the reactive "spring" coupling model

Barker & Hopfield analysis parameters	e_1 (cm^{-1})	e_2 (cm^{-1})	$k_1 + k_{12}$ (cm^{-2})	$k_2 + k_{12}$ (cm^{-2})	Γ_1 (cm^{-1})	Γ_2 (cm^{-1})	k_{12} (cm^{-2})
Equivalent notation of She *et al*[9]	P_a	P_b	w_a^2	w_b^2	Γ_a	Γ_b	$\Delta^2(\Gamma_{ab} = 0)$
T = 300°K	526	181	19,500	25,600	228	7.2	15,000
200°K	589	182	18,200	26,300	229	2.3	16,500
175°K	581	181	15,800	26,200	211	4.0	16,100
150°K	589	181	13,100	25,900	180	4.1	15,600

Table 2. Parameters obtained from theoretical fits to the experimental data using the resistive "dashpot" coupling model

Barker & Hopfield analysis parameters	z_1 (cm^{-1})	z_2 (cm^{-1})	w_1^2 (cm^{-2})	w_2^2 (cm^{-2})	$\gamma_1 + \gamma_{12}$ (cm^{-1})	$\gamma_2 + \gamma_{12}$ (cm^{-1})	γ_{12} (cm^{-1})
Equivalent notation of Gauss *et al.*[5]	M_1	M_2	w_1^2	w_2^2	γ_1	γ_2	$\Gamma\ (\Delta = 0)$
$T = 300°K$	293	472	7300	37,800	140	96	108
200°K	352	507	5300	39,200	143	88	110
175°K	363	488	4100	37,900	139	76	99
150°K	388	478	2700	36,300	125	59	81

ever, only requires a low value of Γ_2 and opposite signs for the effective charges. There may be some damping in the coupling but it cannot be very large; a recent paper by Wehner and Steigmeier[18] discusses the need for more information before the choice of one set of parameters can be physically justified.

COMPARISONS AND ERRORS

The resistive parameters are listed so that comparison can be made with results obtained by other workers.[5,6] The main difference is that our w_1^2 values, the square of the ferroelectric mode frequency, are consistently larger due perhaps to a lack of accurate data below $40\,cm^{-1}$. However, the trend in these values does exhibit the soft behaviour of this mode.

The parameters obtained for the reactive model can be compared with those of She *et al.*[9] Here the $(k_1 + k_{12})$ values are higher than those of She but show the expected "softening" whereas the $(k_2 + k_{12})$ values are temperature independent to $\sim \pm 1\%$.

Fits using the reactive model were also performed on three modified 300°K spectra. These spectra were obtained by $\pm 1\%$ changes in the experimental r curve and by shifting the ϕ curve by the equivalent of -0.020 of a sampling step (i.e. $0.020 \times 5\,\mu m$). This corresponds to a phase shift which is linearly proportioned to the frequency and typically produces a change of $-1°$ at $136\,cm^{-1}$ in the ϕ spectrum. In this way, the effects on the parameter values of errors in the measured spectra could be observed.

The parameters changed by only $\sim 1\%$ due to the modifications in the amplitude. However the model appeared to be sensitive to shifts in the phase spectrum. The phase shift used gave the following parameter values. The figures in brackets showing the difference between these values and those given in Table 1, obtained from the unmodified spectra.

$$e_1 = 551\,(+5\%);\ e_2 = 186\,(+3\%);\ k_1 + k_{12} = 21600\,(+11\%);$$
$$k_2 + k_{12} = 26100\,(+2\%)$$
$$\Gamma_1 = 248(+9\%);\ \Gamma_2 = 4.3(-40\%);\ k_{12} = 15900(+6\%).$$

One of the important regions in the spectra is the phase minimum between the two modes. The division of field technique gave $3.2 \pm 0.5°$ at 300°K, $2.5 \pm 0.5°$ at 200°K and $2.3 \pm 0.5°$ at 175°K and 150°K as the phase at $136\,cm^{-1}$. Simulated curves show no significant variation of the phase ϕ at this point with $(k_1 + k_{12})$. Measurements by Gauss *et al.*[5] at 300°K show almost zero phase at this point indicating decoupling of the soft mode to the electric field.

Because of the limit on the accuracy of the phase measurements the uncorrected ϕ curves, obtained by replacement of the crystal by the mirror were "phased up" to 3° at 300°K and 2.5° at 200, 175 and 150°K at $136\,cm^{-1}$.

Due to the minimum in ϵ'' (~ 1 at $136\,cm^{-1}$) and the corresponding low value for the absorption coefficient,[19] this point in the spectrum is particularly suited to investigations by transmission spectroscopy. Such measurements are far more sensitive to changes of phase than those obtained by reflection techniques.

Initial transmission measurements on a 0.17 mm thick crystal of KDP at 300°K displayed the 'c' axis transmission as a sharp spike peaking at $\sim 135\,cm^{-1}$. They also gave

indication of a similar phase value to the 3.2° obtained by the reflection studies.[20]

Further such measurements at lower temperatures are planned to give a good fix on the behaviour of ϕ in this spectral region, and hence accurate phase reference points for calibrating the reflection data.

CONCLUDING REMARKS

The trends in the curves of Figs. 1 and 2 below 40 cm^{-1} illustrate the importance of obtaining better low frequency data, for most of the effects produced by cooling manifest themselves in this region. The overdamped ϵ'' band, associated with the ferroelectric transition, which peaks at $\sim 50\,cm^{-1}$ at 300°K, peaks at lower frequencies as T drops towards the transition temperature.[11] To resolve this band at these lower temperatures necessitates the use of a Helium cooled detector. It is hoped that such measurements will commence shortly, enabling the spectra to be extended down to at least $\sim 5\,cm^{-1}$ and consequently better theoretical fits to be made.

Initial results have been obtained at 125°K, just above the transition temperature $T_c = 122$°K, but a further problem was encountered. On cooling the crystal to 125°K the temperature sometimes overshot and fell below T_c before the thermostat heater restored the system to equilibrium at 125°K. Thus, the crystal undergoes the transition from its paraelectric to ferroelectric phase. The stresses in the crystal that accompany this transition have caused one sample to crack. However, this "overshoot" can now be prevented by taking extra precautions with the cooling process.

Acknowledgements—This work is supported in part by the Science Research Council. The authors also wish to thank the technical staff of the Physics Department and Computer Unit for their valuable assistance, and Mr J. R. Birch of the National Physical Laboratory, Teddington, for the loan of equipment.

REFERENCES

1. PARKER, T. J., D. A. LEDSHAM & W. G. CHAMBERS, *Infrared Phys.* **16**, 293 (1976).
2. PARKER, T. J. & W. G. CHAMBERS, *Infrared Phys.* **16**, 349 (1976).
3. LEDSHAM, D. A., W. G. CHAMBERS & T. J. PARKER, *Infrared Phys.* **16**, 515 (1976).
4. BIRCH J. R., G. D. PRICE & J. CHAMBERLAIN, *Infrared Phys.* **16**, 311 (1976).
5. GAUSS, K. E., H. HAPP & G. ROTHER, *Phys. Stat. Sol.* (*b*) **72**, 623 (1975).
6. LAGAKOS, N. & H. Z. CUMMINS, *Phys. Rev.* **B10**, 1063 (1974).
7. KATIYAR, R. S., J. F. RYAN & J. F. SCOTT, *Phys. Rev.* **B4**, 2635 (1971).
8. KAMINOV, I. P. & T. C. DAMEN, *Phys. Rev. Lett.* **20**, 1105 (1968).
9. SHE, C. Y., T. W. BROBERG, L. S. WALL & D. F. EDWARDS, *Phys. Rev.* **B6**, 1847 (1972).
10. KAWAMURA, T., A. MITSUISHI & H. YASHINAGA, *J. Phys. Soc. Japan* **28**, Supp. 227 (1970).
11. SUGAWARA, F. & T. NAKAMURA, *J. Phys. Soc. Japan* **28**, 158 (1970).
12. ONYANGO, F., W. SMITH & J. F. ANGRESS, *J. Phys. Chem. Solids* **36**, 309 (1975).
13. BARKER, A. S. & M. TINKHAM, *J. Chem. Phys.* **38**, 2257 (1963).
14. PARKER, T. J., W. G. CHAMBERS & J. F. ANGRESS, *Infrared Phys.* **14**, 207 (1974).
15. BARKER, A. S. & J. J. HOPFIELD, *Phys. Rev.* **135**, A1732 (1964).
16. REESE, R. L., I. J. FRITZ & H. Z. CUMMINS, *Phys. Rev.* **B7**, 4165 (1973).
17. BRODY E. M. & H. Z. CUMMINS, *Phys. Rev. Lett.* **21**, 1263 (1968).
18. WEHNER, R. K. & E. F. STEIGMEIER, *RCA Rev.* **36**, 70 (1975).
19. See for example: BORN, M. & E. WOLF, *Principles of Optics*, pp. 613–614. Pergamon Press, Oxford (1970).
20. GLEDHILL, G. A., J. F. ANGRESS, R. W. MARTIN & W. G. CHAMBERS, *J. Phys. C: Solid State Phys.* **9**, L01 (1976).